On the Full Lagrangian Approach and Thermophoretic Deposition in Gas-Particle Flows

David Patrick Healy

Clare College

A dissertation submitted for the

degree of Doctor of Philosophy

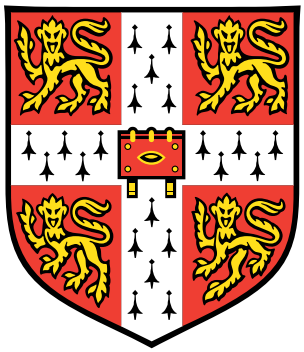

University of Cambridge

Department of Engineering

September 2003

Preface

This should not be the last time that I thank my supervisor, Prof. John Young. I have learned more from him than will be apparent from this thesis, the completion of which owes much to his patience, encouragement and inspiration. During the course of our (longer than expected) association, I could not have asked for a better academic role model.

I owe a great debt to my predecessors on this project, Dr. Shane Slater and Dr. Angus Leeming. Besides beating the path from Limerick to Cambridge, Shane provided guidance in my early days, and the original Lagrangian tracking code from which the Osiptsov version emerged. Angus's phone calls were a great source of support and experimental clues at a time when I was as likely to take an axe to the rig as I was to run *another* experiment. He also provided the Eulerian pipe flow code, which formed the basis of the annulus code. I am grateful to Dr. John Fackrell for his technical advice, and help with the provision of experimental equipment.

I would like to thank the inhabitants of the Whittle and Hopkinson Labs for various contributions over the years, with special thanks to Dr. Michael Brear for his astute observations on the 'bucking-annulus' phenomenon. I should also mention Prof. Mark Davies of the University of Limerick (and formerly the Whittle Lab) for his encouragement with my initial application, and on our many chance meetings since then.

I do not underestimate the contribution of Anne Stillman, for her friendship throughout, and my parents John and Patricia, for their support and everything that went with that.

Without the ingenuity of Roy Slater, the experimental rig would not have been of very much use to anyone. Thanks also go to Mick Underwood, Trevor Parsons, Dr. Zhilei Wu, Steve and Anna Almond, and anyone who I managed to persuade to pull on the end of a ten metre rope until a uranine covered pipe was suspended high above the lab.

I am grateful for financial support received from a Cambridge University Domestic Research Studentship, a British Chevening Scholarship, and the maintenance contributions from the PowerGen Power Technology Centre, Ratcliffe-on-Soar, and the Ford of Britain Trust and Rex Moir Fund of the Cambridge University Engineering Department.

The work described in this dissertation was undertaken between October 1998 and September 2003, initially at the Whittle Laboratory and then at the Hopkinson Laboratory, Cambridge University Engineering Department. This dissertation is my own work and contains nothing which is the outcome of work done in collaboration with others, unless explicitly stated otherwise. It has not been submitted for any purpose to any other University or place of learning.

This dissertation does not exceed the regulation length. It contains approximately 64,700 words (including appendices, bibliography, footnotes, tables and equations), and 74 figures.

David Healy
September, 2003

Summary

Theoretical and experimental studies of particle deposition in turbulent pipe flow have been carried out for over forty years, but some of the most important transport mechanisms are still not well understood. The **first part** of this thesis is concerned with the calculation of particle density when using Lagrangian methods to predict inertial particle transport in two-dimensional laminar fluid flows. Traditionally, Lagrangian calculations involve integrating the particle equations of motion along particle pathlines, and the particle density is obtained by applying a statistical averaging procedure to those pathlines which intersect a particular computational grid cell. Unfortunately, extremely large numbers of particles are required to reduce the statistical errors to acceptable levels, and this makes the method computationally expensive.

Recently, the Full Lagrangian approach has been developed, which allows the direct calculation of the particle density along particle pathlines. This method had previously been applied only to simple analytical flow fields. The application of the method to CFD generated fluid velocity fields was shown to be possible, and the results obtained using the Full Lagrangian approach were compared to those from a traditional Lagrangian approach. It was found that better quality solutions could be obtained with the use of far fewer particle pathlines. An analysis of the manner in which the Full Lagrangian approach deals with particles whose paths cross each other (and the resulting discontinuity in particle density) was also undertaken, and this illustrates the sophistication of the method.

The **second part** of the thesis comprises an experimental and theoretical study of the deposition of small particles in turbulent flows by thermophoresis. Thermophoresis is the phenomenon whereby small particles suspended in a gas in which there exists a temperature gradient experience a force in the direction opposite from that of the temperature gradient. Previous researchers have attempted to impose a radial temperature difference in pipe flow experiments, but have not yet succeeded in attaining a constant thermophoretic force along the length of the pipe. This limits the accuracy and usefulness of the data for the validation of theoretical expressions for the thermophoretic fluxes.

An experimental rig has been designed to achieve a constant thermophoretic force. This was done by using an annular geometry with a cold inner wall and hot outer wall. The particle size was varied and the deposition flux was measured for turbulent flow with three temperature differences. The deposition fluxes for small particles were found to be independent of dimensionless particle size, with each increase in temperature difference resulting in an increase in magnitude of the flux. Evidence of a thermophoresis-turbulence coupling was found for intermediate-sized particles, and large particles were not influenced by thermophoresis.

A theory of particle deposition, developed for the case of turbulent pipe flow, was modified to study flow in a turbulent annulus, so that theoretical expressions for the thermophoretic fluxes could be included and compared with the experimental results. Agreement with ex-

perimental data was quite good, but some deficiencies in a widely used theoretical expression for the thermophoretic flux were exposed. An alternative expression was used, which gave much better agreement with the experimental data, and the mechanisms behind the thermophoresis-turbulence coupling were also investigated. The validation of this expression for the thermophoretic force will allow its inclusion in numerical studies of particle deposition in more complex geometries.

Contents

List of Figures

List of Tables

Nomenclature

Symbols which are defined locally are not included here.

Latin Letters

A	Area	I	Volumetric concentration
a	Pipe radius		of the non-volatile impurity
B	Dynamic mobility of a particle	J	Flux vector
C	Concentration of non-volatile	J	Jacobian of the Eulerian-
	solute in the solution		Lagrangian transformation
C_c	Cunningham correction factor	J_B	Brownian mass flux of particles
C_D	Stokes drag coefficient	J_T	Turbulent mass flux of particles
C_f	Skin friction coefficient	J_w	Mass flux of particles to the
C_p	Particle concentration		wall per unit area
$C_{p,out}$	Theoretical particle concentration	K	Similarity parameter describing
	at outlet of aerosol generator		rate of particle depletion
c_c	Continuous phase volume fraction	Kn	Particle Knudsen number
c_d	Dispersed phase volume fraction	K_{TH}	Dimensionless coefficient of
c_p	Specific heat capacity of		thermophoresis
	the particle material	k	Boltzmann's constant
c_u	Mass of uranine per unit	k_g	Gas thermal conductivity
	volume of oleic acid	k_o	Thermal conductivity of oleic acid
$\overline{c}$	Mean gas molecular speed	k_p	Particle thermal conductivity
D_B	Coefficient of Brownian diffusion	k_u	Thermal conductivity of uranine
D_T	Coefficient of turbulent diffusion	kp	Number of grid points
d	Pipe diameter	L	Length of test section
d_d	Droplet diameter		(pipe or annulus)
d_h	Hydraulic diameter of annulus	L_p	Luminosity
d_i	Inner diameter of annulus	M_p	Mass of particles deposited
d_m	Gas molecular diameter	m_p	Mass of a particle
d_o	Outer diameter of annulus	$\dot{m}_p$	Mass flow rate of particle
d_p	Particle diameter	n_p	Number of particles
F, $\mathbf{F}$	Force per unit mass, force vector		per unit volume
f	Force	P	Fractional penetration
f	Friction factor	p	Pressure
G	Geometric progression ratio	p_p	Partial pressure of the
$\mathbf{g}$	Gravitational acceleration		particle phase

Q_a	Volumetric flow rate of air	T_{ow}	Nominal outer wall temperature
Q_{ind}	Volumetric flow rate of air	t	Time
	indicated by rotameter	U, u	Fluid velocity
Q_l	Liquid feed rate	U_m	Mean fluid velocity (averaged over
R	Specific gas constant		a cross-section)
R	Radius	u', u''	Fluid instantaneous velocity
Re	Reynolds number	u_*	Friction velocity
Re_p	Particle Reynolds number	V, v	Particle velocity
Re_{sh}	Shear Reynolds number	v', v''	Particle instantaneous velocity
r	Pipe radius, spatial coordinate	V_d	Deposition velocity
r_i	Annulus inner radius	V_{dp}	Dispersed phase volume
r_o	Annulus outer radius	V_p	Volume of a particle
r_p	Particle radius	W, w	Particle convective velocity
r^*	Annulus radius ratio	w	Partial derivative of J with respect to time τ
Sc	Laminar particle Schmidt number	w',w''	Particle instantaneous convective velocity
Sc_T	Turbulent particle Schmidt number	x	Cartesian direction
St	Stokes number	x_p	Particle position along a pathline
T	Temperature	y	Cartesian direction
T_{grad}	Nominal temperature gradient	y_p	Particle position along a pathline
T_{iw}	Inner wall temperature	z	Spatial coordinate

Greek Letters

Γ	Function	ρ_o	Density of oleic acid
Ψ	Stream function	ρ_p	Particle density, particle phase bulk density
α_L	Lift coefficient	$\overline{\rho}_{pm}$	Time-mean particle density
α_{TH}	Thermophoretic coefficient		averaged across the annulus
β	Reciprocal of τ_p	$\rho_{p,mat}$	Particle material density
δ	Spatial extent, uncertainty	ρ_u	Density of uranine
η_d	Deposition efficiency	τ	Lagrangian time
η_{TH}	Coefficient of thermophoresis	τ_f	Fluid time-scale
θ	Spatial coordinate	τ_g	Gas time-scale
κ_w	Wall boundary condition	τ_p	Particle momentum response time,
λ_g	Mean free path of gas molecules		inertial relaxation time
μ_g	Gas dynamic viscosity	$\tau_{p,T}$	Particle thermal response time
ν_{ART}	Artificial viscosity	τ_w	Wall shear stress
ν_g	Gas kinematic viscosity	$\overline{\tau}_w$	Mean wall shear stress
$\nu_{g,T}$	Turbulent kinematic viscosity of the	ϕ	Scalar function of position
	gas, eddy viscosity	ϕ	Function
ρ_c	Continuous phase bulk density	ϕ_D	Correction to the Stokes drag coefficient
ρ_g	Gas density	ϕ^*	Annulus geometric shape factor
ρ_I	Density of non-volatile impurity	$\overline{\psi}$	Dimensionless time-mean particle density

Symbols

Δ	Discrete change
∇	Vector gradient operator
D	Substantive derivative
∂	Partial derivative
$\lvert \cdot \rvert$	Absolute Value
$\mathcal{S}$	Sign
$\times$	Cross Product
∞	Infinity
$\overline{A}$	Reynolds average of A
$\overline{\overline{A}}$	Density-weighted average of A

Abbreviations

CFD	Computational Fluid Dynamics
CFL	Courant-Friedrichs-Levy
DNS	Direct Numerical Simulation
erf	Error function
lpm	litres per minute
min	Minimum value
NaOH	Sodium hydroxide
ppmw	Parts per million by weight
VOAG	Vibrating Orifice Aerosol Generator

Superscripts

$'$, $''$	Instantaneous Value
$+$	Dimensionless Value
$*$	Dimensionless value
^{A}	Dimensionless value (in an annulus)

Subscripts

avg	Average
app	Approach pipe
B	Brownian
cal	Calibration
$conv$	Convective
D	Drag
d, dp	Dispersed phase
$diff$	Diffusive
g	Gas
I	Non-volatile impurity
ISO	Isothermal conditions
$inlet$	Inlet of test section
i	Inner wall
L	Lift
m	Mean
nom	Nominal
o	Oleic acid
o	Outer wall
p	Particle
p	Propan-2-ol
$pipe$	Pipe
rot	Rotameter
$saff$	Saffman
S	Solution
$test$	Test section
TH	Thermophoretic
$turbo$	Turbophoretic
u	Uranine
w	Value at wall
∞	Freestream value
0	Initial value

Chapter 1

Introduction

Atmospheric pollution by particulate matter presents a risk to human health and the health of the environment, damaging respiratory and cardiovascular systems in humans, interfering with photosynthesis in plants, causing the deterioration of building facades, and smog in the air.

The main sources of particulate matter in the atmosphere are from combustion for heating and power generation, and motor vehicle traffic. These *primary* pollutants are harmful not just in the vicinity of the source, but they can travel long distances and engage in chemical reactions as they do so, producing *secondary* pollution such as ozone and acid rain. The transport and deposition of particles (or droplets) in the atmosphere may be considered a dispersed two-phase flow, where the particles constitute the dispersed phase and the atmosphere the continuous phase.

Dispersed two-phase flows are a subset of a wider category of flows, known as multi-phase flows (gas-liquid, gas-solid, liquid-solid and three-phase flows). Industrial applications involving multiphase flows include the production of food and pharmaceuticals through spray drying; the pneumatic transport of cement, grains, and coal; the solid propellant rocket; fire suppression and control; and fluidised beds for coal gasification, combustion and liquefaction (Crowe *et al.*, 1998).

1.1 Dilute gas-particle flow in a gas turbine

The main motivation for this work comes from the power generation industry. Combined-cycle gas turbine (CCGT) power stations have been the subject of much recent interest, mainly due to the increase in gas turbine temperature (and subsequent increase in specific work) and the availability of natural gas, which results in greater efficiency and a reduction in the production of CO_2, SO_x and NO_x. Aside from the environmental benefits, the overall efficiency of the best stations are just below 60% compared with 40% for a traditional coal-fired power station. These factors have led to CCGT stations replacing coal-fired stations throughout the United Kingdom.

CCGT plants can operate with distillate oil or natural gas, but cannot burn coal since the products of combustion cannot be accepted by the gas turbine. Concerns regarding the long-term availability of natural gas supplies have led to the development of new technologies to allow the modification of such plants to operate using coal. Coal gasification involves the mixing of pulverised coal and hot air under pressure, to produce a 'synthetic gas' which is cleaned by being cooled and passed through a ceramic filter, before undergoing combustion and expansion through a gas turbine.

Hot filtration of the gas before entry to the gas turbine results in the removal of most particles in the $10 - 20$ μm range, but the gas still contains greater levels of contaminants than in a natural gas-fired system. Particles in the gas stream may deposit on the turbine blades and accumulate to cause blockages and gradually reduce the power output; particles may cause erosion of the blades and affect their aerodynamic properties eventually leading to mechanical failure; alkali vapours released from the coal may condense on the blade surface and cause enhanced corrosion resulting in reduced blade lifetimes.

A combination of cyclone and high temperature filters may be used to reduce the dust levels present in the gas to just a few ppmw (parts per million by weight), and the use of a standard gas turbine may be possible (although more frequent cleaning than with other fuels and corrosion resistant blade coatings may be required). However, such excessive filtration can result in high pressure loss and inefficiency. If only a cyclone filter is used, then the dust loading can be of the order of a few hundred ppmw, and the gas turbine must be designed to minimise damage caused by particles and the uneconomically short cleaning/replacement intervals that would be required. These low mass loadings mean that the gas-particle flow may be considered dilute, and it is the influence of the gas on the particles (rather than particle-particle interactions or particle modification of gas turbulence) that is important.

A typical approach to such a design taken by a major turbine manufacturer was as follows: two stages of high cyclone filtering were used to reduce the dust loading to between 200 and 400 ppmw, and to restrict the particle size to less than about 10 μm, with only 1 ppmw above 5 μm. This limit on particle size is significant, as small particles follow the curved flow through the turbine more closely than large particles, so that fewer deposit and with lower impact energy, resulting in minimal erosion. The load and turning angle of the turbine was also modified to resist erosion, which resulted in an increase in the number of stages from four to five. The average velocity in the turbine was reduced, as was the combustor bed temperature (to reduce alkali release and subsequent corrosion), and hence the turbine inlet temperature. As a result, blade cooling (to protect the blade from excessively high temperatures) was not required, and solid blades could be used, giving more structural integrity in the event of erosion. Blade coatings were also used to prevent corrosion, and the blade profile was thickened in areas sensitive to deposition.

Some of these steps represent an over-cautious approach to protecting the turbine against the effects of particles, the result being that the turbine is operated at off-design conditions, and at a reduced efficiency. A greater knowledge of particle behaviour would help to achieve

more of a balance between turbine efficiency and limiting the damage caused by particle deposition, corrosion and erosion. Such knowledge can be obtained through experimentation, but the expense and difficulty of conducting experiments in gas turbines precludes comprehensive variational studies, and as a result there are very few such experiments (Parker & Ryley, 1970; Wenglarz, 1981). Consequently, experiments are often conducted in simpler geometries (such as pipe flows), and the experimental results are used to validate numerical models, which are then developed to predict particle behaviour in more complex geometries. The work in this thesis comprises both experimental and numerical work. There has been a great deal of research into gas-particle flows, and the aim of this research was to address two areas which have been largely neglected to date. Although they both pertain to dilute gas-particle flows and will feature together in future numerical work, they are best treated as two separate, fundamental problems. As a consequence, the thesis is divided into two parts.

1.2 Part I - Numerical study of the direct calculation of particle density using the Full Lagrangian approach

Numerical methods are usually divided between Eulerian and Lagrangian approaches. The more intuitive Lagrangian approach tracks individual particles as they move through a fluid, and tracking many such particles yields representative information about the whole particle field. The Eulerian approach treats the particles as a continuum 'fluid' with properties representative of averaged particle behaviour; for this reason it is also known as the 'two-fluid' approach.

The choice of modelling approach depends on the class of particles in question, and particles are best classified using the Stokes number, St, which is a ratio of particle and fluid time-scales:

$$St = \frac{\tau_p}{\tau_f} \tag{1.1}$$

τ_p is a time-scale representative of particle motion, and is sometimes known as the inertial relaxation time. A large dense particle will have a larger response time (and higher inertia) than a smaller, less dense particle. τ_f is a time-scale which reflects the temporal rate of change of the fluid, and may be chosen in a number of ways depending on the flow conditions and geometry. When $St \gg 1$, the inertial particles will ignore the fluid flow, while for $St \ll 1$, the particles have plenty of time to respond to changes in the fluid flow, which now has a much greater influence on particle motion.

The Eulerian approach solves the particle momentum and mass conservation equation for particle density and particle velocity. This approach works best for small Stokes numbers. At intermediate and large St, the method is less suitable, and effects such as crossing trajectories

(particles pathlines intersecting each other) are not well represented, because the particle velocity cannot be multi-valued at a single point.

The Lagrangian approach involves the integration of the particle equation of motion along particle pathlines to yield the particle velocity. Traditionally, the particle density (where particle density is equivalent to the particle concentration) is found by applying an averaging procedure to those particles which cross a particular Eulerian cell (the fluid flow field is solved using an Eulerian approach). However, large numbers of particles are required to reduce the statistical errors to acceptable levels (although comparatively few are needed to find the particle velocity field accurately). The Lagrangian approach works best for large Stokes numbers. In the limit of $St \to \infty$, crossing trajectories are well represented, and a large integration time-step can be used, resulting in computational efficiency. However, at intermediate and small St, fluid motion becomes important and the integration time-step must be of the same order of magnitude as the fluid time-scale, and the number of particles required also increases. These factors make the method computationally expensive.

In order to produce a numerical code that can be integrated in the gas turbine design process, the method must be computationally efficient and capable of representing the correct physical behaviour. As the majority of real gas-particle flows fall somewhere between the limits of high and low Stokes numbers (where the choice of either Lagrangian or Eulerian approach could be made), a natural target would appear to be a method that combines both approaches, exploiting the advantages while avoiding the disadvantages of each. Most numerical studies are carried out in two-dimensions, but as extension of this joint Eulerian-Lagrangian approach to three-dimensions is desired, particular emphasis is placed on computational efficiency.

While it is beyond the scope of this thesis to complete such a joint Eulerian-Lagrangian approach, one of its aims is to develop the Lagrangian side of the approach. A recent work by Osiptsov (1998) allows the direct calculation of the particle density along particle pathlines (which is known as the Full Lagrangian approach), thus reducing the large number of particles required. The ensuing increase in computational efficiency allows the application of the approach to smaller Stokes numbers than before, and extension to three-dimensional calculations is possible. Osiptsov (1998) only applied his method to simple analytical flow fields, and the workings of his method are established in **chapter 2** (with particular attention paid to the treatment of crossing trajectories), along with a study into the suitability of using this Full Lagrangian approach with a computationally generated solution for the fluid flow field.

1.3 Part II - Experimental and numerical study of the influence of thermophoresis on particle deposition

There have been many experimental studies into the relationship between particle size and deposition rate in fully-developed turbulent pipe flow, as exemplified by the work of Liu & Agarwal (1974). The attractiveness of these experiments is that this relatively simple flow field features many of the characteristics of particle behaviour found in more complex geometries. Modern industrial gas turbines may have mean free-stream temperatures of up to 1420 °C, but material considerations require that the turbine blade temperature does not rise much higher than 800 °C. This results in high temperature gradients near the blade surfaces, and small particles experience a force in the opposite direction from that of the temperature gradient. This phenomenon is known as thermophoresis, and causes small particles to deposit on the turbine blades. While the free-stream temperature could be reduced, this would result in reduced turbine efficiency and, depending on the particle size, may not even be necessary (large particles are comparatively insensitive to thermophoresis). Hence, the variation of deposition rate for particles of different sizes in a flow field in which a temperature gradient exists, is of great importance. **Chapter 3** provides an explanation of the various particle transport mechanisms that will be encountered throughout this work, and also provides a comprehensive review of experimental work in turbulent pipe flow, and a detailed assessment of experimental and theoretical work on the form of the thermophoretic force, and its use in studies of turbulent pipe flow.

The magnitude of the thermophoretic force depends mainly on the particle diameter (through the Knudsen number) and the magnitude of the temperature gradient. Ideally, experiments would feature a range of particle sizes under the influence of a range of temperature differences. One of the most comprehensive set of experiments was carried out by Romay *et al.* (1998), who studied particle deposition in turbulent pipe flow with a cross-stream temperature gradient. The temperature gradient was established by heating the particle-laden flow before entry to the pipe, whose wall was cooled. However, the temperature of the particle-laden flow decreased as it travelled through the pipe so that a constant temperature difference (and constant thermophoretic force) was not maintained. Leeming (1995) also carried out experiments on thermophoresis in a turbulent pipe flow, and while managing to maintain a constant temperature difference, the drawback was that only a single, low temperature difference was achieved.

The aim of the experimental work in this thesis, was to perform similar experiments in a turbulent flow, but with a constant temperature difference (which could be varied), and a constant mean temperature. **Chapter 4** describes the design of an experimental rig and the procedures to carry out such experiments. A concentric annulus was chosen as the geometry. It is a close geometric relative of the pipe, and the inner wall was cooled with a flow of water,

while the outer wall was heated with a heating tape. The result was a test section with a constant temperature difference, and a near-constant mean temperature. The power to the heating tape could be varied, allowing a number of different temperature differences to be imposed on the flow. **Chapter 5** describes the results of these experiments. In order to provide a datum against which to compare the effects of thermophoresis, and to provide a link with the pipe flow experiments of other researchers, isothermal experiments were also carried out. Some interesting results from these are also presented.

There have been many theoretical and experimental studies of thermophoresis (under conditions where thermophoresis is the sole force on the particle), which have attempted to provide (or corroborate) an expression for the thermophoretic force. Considerable controversy existed at one time over the correct expression, and this controversy has subsided with the general acceptance of one particular expression. The validity of this expression will be investigated by including it in a numerical study of deposition in a turbulent annulus with a number of cross-stream temperature gradients, for comparison with the experimental results. Young & Leeming (1997) developed a theory of deposition for the case of fully-developed turbulent pipe flow. The strength of this theory was its relatively simple turbulence closure models which did not obscure the underlying physical behaviour of the particles. This approach was modified for the case of a turbulent annulus and, while Young & Leeming (1997) used Reynolds averaging of the particle equations, particle density-weighted averaging was used for the present work. A numerical computer code was produced to study deposition in a turbulent annulus. The modifications for the case of an annulus, for density-weighted averaging, and the numerical details of the creation of the code are described in **chapter 6**.

Chapter 7 presents and discusses the results of the numerical study in a turbulent annulus with isothermal conditions and also with a cross-stream temperature gradient. Comparison is made between these and the experimental results, and solutions using different expressions for the thermophoretic force are evaluated.

Part I

Chapter 2

The Full Lagrangian approach for the calculation of inertial particle transport

2.1 Modelling approaches in gas-particle flows

A large number of numerical methods have been developed for calculating dilute gas-particle flows and comprehensive reviews have been published by Crowe (1982) and Crowe *et al.* (1996). The continuous gas phase equations are usually solved in Eulerian form, and the method of solving the particle phase equations normally takes one of two forms, depending on how the particle flow is observed. Choosing a stationary point and observing the particles as they move past results in an Eulerian description of the flow, while a Lagrangian description may be had if the observer follows the same path as the particle. The Stokes number of the particles largely determines which description is more appropriate. The two categories of modelling approach will be discussed in more detail, along with a number of methods which attempt to combine the best features of Eulerian and Lagrangian descriptions.

2.1.1 The Eulerian approach

Using the Eulerian (or two-fluid) approach, particles are treated as a continuum fluid with properties representative of averaged particle behaviour. The particle momentum and particle mass conservation equations are solved for the particle density and particle velocity fields. Brownian and turbulent diffusion are represented by the addition of modelling terms to the governing equations. The inclusion of turbulent/diffusive effects in the Eulerian approach does not result in a significant increase in computational expense. This approach is most suitable for small Stokes numbers. At intermediate Stokes numbers, when inertial effects start to become important, the equation set may become ill-posed and effects such as crossing trajectories are not well represented, because the particle velocity cannot be multi-valued at one point. It should be noted that this part of the thesis is concerned with laminar flows, so that the

term 'inertial effects' refers to those effects caused by large-scale streamline curvature, and not turbulent inertial effects, such as turbophoresis.

2.1.2 The traditional Lagrangian approach

The traditional Lagrangian approach involves integrating the particle equations of motion along particle pathlines. While comparatively few pathlines are required to define the particle velocity field with good accuracy, it is not as easy to obtain the particle density field. The normal approach is to apply a statistical averaging procedure to those pathlines which intersect a particular Eulerian cell (particles are tracked through the Eulerian grid on which the gas phase equations have been solved). Unfortunately, extremely large numbers of pathlines are required to reduce the statistical errors to acceptable levels. For example, to reduce the local error in particle density to less than 1% in a two-dimensional calculation (a very modest target in CFD), *each* cell must be intersected by more than 10,000 pathlines (Crowe, 1982). The Lagrangian approach is most suitable for large Stokes numbers, as it can represent inertial effects such as crossing trajectories and rebounding, while a large integration time-step can be used, thus making the method computationally efficient. However, at intermediate St when turbulent/diffusive effects become important, the time-step must be of the same order of magnitude as the time-scale of fluid turbulence. The background turbulent fluid flow must be modelled, and this increases the required number of particle trajectories dramatically. The reduction in size of the time-step and the increase in the required number of trajectories combine to make the method computationally expensive. The computational cost (particularly for three-dimensional flow fields) is prohibitive even on modern computers.

2.1.3 Other methods

There are also a range of methods that attempt to either combine Eulerian and Lagrangian approaches, or to relax the restriction on the range of Stokes numbers for which they are applicable. A number of the most promising are described below.

Joint Eulerian-Lagrangian approach

While Eulerian methods are most appropriate when $St \ll 1$ and Lagrangian methods when $St \gg 1$, the use of either method when $St \approx 1$ results in the loss of either computational efficiency or the representation of inertial effects. A method that combines the two approaches, and exploits the advantages of each method while avoiding the disadvantages, would provide an ideal approach for such situations. There have been a number of attempts at such a combined approach.

The model of Elsden & Hutchinson (1996) begins with a Lagrangian component in the form of a stochastic simulation, which calculates the particle diffusion coefficients required for an Eulerian calculation, and allows the representation of effects such as crossing trajectories.

Advantage is taken of the smoothly varying nature of the diffusion coefficient, and a 'look-up' table for the diffusion coefficient is compiled for a range of velocity and length scales. An Eulerian calculation is then performed, and the mass and momentum equations are solved with reference to the table of diffusion coefficients. The model's agreement with experiment was at least as good as other calculation methods, but it is computationally expensive, and lacks elegance.

Menguturk *et al.* (1983) investigated the inertial and diffusive motion of particles in gas turbines. They found that, for very small particles, an Eulerian model considering laminar and turbulent diffusion inside the blade boundary layer was sufficient, because the inertial deviation of particles from mean streamlines could be neglected. For large particles, diffusion could be neglected and it could be assumed that the particles had large enough relaxation times so that the viscous boundary layer around the blade did not affect particle trajectories, allowing the use of a Lagrangian approach based on inviscid flow data. However, there is an intermediate particle size that may respond equally to both inertia and diffusion, and it is this problem that was addressed. The method takes the initial particle conditions at the edge of the boundary layer from a Lagrangian solution for inviscid flow, and then proceeds with an Eulerian boundary layer calculation which considers laminar and turbulent diffusion.

This approach assumes little interaction between diffusive and inertial transport mechanisms. This represents a significant simplification, as the different mechanisms may act in unison. For example, Konstandopoulos & Rosner (1995a,b) have shown that inertial effects on small particles in boundary layer flows with streamwise curvature, and in which a temperature gradient exists, can be significant. While this combined approach is promising, the 'cut-off point' between the relevant mechanisms cannot be considered to be as extreme without significant loss of accuracy, and a more gradual 'transition' between them needs to be found. This could involve extending the limits of applicability of the Eulerian part of the calculation to deal with inertial effects due to streamwise curvature.

Eulerian diffusion-inertia approach

Slater & Young (1998) extended the region of validity of the Eulerian method to higher Stokes numbers, by addressing some of the problems associated with inertial effects due to streamwise curvature. An absorbing boundary condition was used to produce solutions for inertial deposition on solid boundaries without discontinuities in particle density (incorrect boundary conditions often allow $\rho_p \to \infty$). A new artificial dissipation scheme for capturing spatial discontinuities, along with a new damping technique to guarantee positivity of particle density, allowed the accurate prediction of 'shadow zones' (regions devoid of particles when particle pathlines separate from solid boundaries due to their inability to follow the surface curvature) without any new numerical or stability issues. While a general solution to the representation of crossing trajectories was not found, a particular test case involving crossing trajectories was undertaken successfully. Favourable comparisons were made between the

solutions from the new approach and those from a traditional Lagrangian approach. The method also has the potential for including turbulent/diffusive mechanisms without a heavy computational penalty.

The Osiptsov Lagrangian approach

Recently, a new approach has been developed by Osiptsov (1998) which allows the direct calculation of the particle density along particle pathlines. This is a major development, as the direct calculation of the particle density removes the need for the use of an averaging procedure and the 'counting' of a large number of particles. This is achieved by integrating differential equations for the components of the Jacobian of the Eulerian-Lagrangian transformation. Knowing the Jacobian yields the particle density via the Lagrangian form of the particle continuity equation. Calculating the particle density directly removes the need for the large number of particles required to reduce the local error to an acceptably small value, and vastly improves the computational efficiency.

A requirement of the Osiptsov Lagrangian method is that the gradient of the fluid velocity field be known. Osiptsov only applied his method to simple flow fields which could be described analytically and which therefore had smooth and continuous fluid velocity gradients. CFD generates velocity fields which are inherently 'noisy' and it needs to be established whether the method can be used when the fluid velocity gradients have been obtained from a CFD solution. The fact that equations are solved for particle density as well as particle velocity means that the Osiptsov Lagrangian approach belongs to a wider category that has become known as the 'Full Lagrangian' approach.

Other Full Lagrangian approaches

Attention should also be drawn to the method of Tarasova & Tsirkunov (2000), which was developed independently to, but is essentially the same as, what has been termed the 'Osiptsov Lagrangian' approach over the course of this work. The authors find that the additional ordinary differential equations for the elements of the Jacobian, can be extremely cumbersome when studying flows that require additional forces acting on a particle from a carrier gas (e.g. Saffman lift force, thermophoresis) to be taken into account. Instead, the elements of the Jacobian are calculated from finite-difference formulae with the use of several (typically two) additional particle trajectories close to the basic one.

The origins of the Full Lagrangian approach are obscure but the first overt derivation of a relevant set of equations was given by Fernandez de la Mora & Rosner (1981). The authors did not exploit the method further as they were primarily concerned with an Eulerian rather than a Lagrangian solution to their problem. Superficially, this method appears similar to that of Osiptsov, but closer examination of the mathematics highlights some important differences. Fernandez de la Mora & Rosner (1981) viewed the particle continuity equation equation as an Eulerian equation which could, with advantage, be solved along Lagrangian trajectories

by working with the substantive derivative. The Osiptsov approach, on the other hand, is firmly rooted in a Lagrangian framework, with the particle density being obtained from the Lagrangian form of the particle continuity equation by computing the change in volume of a 'particle cluster' along its trajectory. This allows the calculation to handle certain types of singularity when the particle density becomes infinite, because the Jacobian (from which the particle density is calculated) passes smoothly through zero. However, the method of Fernandez de la Mora & Rosner (1981) requires the calculation of the divergence of the particle velocity field to obtain the particle density, which itself becomes infinite when the particle density is infinite, leading to problems if a numerical solution is attempted. A more detailed comparison of these two methods can be found in Healy & Young (2003). The Osiptsov Lagrangian approach is found to be more suitable due to its wider range of applicability. To avoid confusion with other 'Full Lagrangian' approaches, the term 'Osiptsov Lagrangian' approach will be used over the course of this chapter.

2.1.4 Proposed direction towards a numerical method covering the complete range of Stokes numbers

One of the motivations of this work is quantifying particle deposition and erosion in gas turbines, so that new turbine designs can be tested for these effects prior to manufacture. Three-dimensional effects may also be significant (end wall boundary layers, passage vortices, radial flows - Ulke & Rowleau (1976)). For reasons of practicality, this three-dimensional analysis would need to be completed in a matter of hours rather than months.

The objective of this chapter is to assess the potential of the Osiptsov Lagrangian method for use with two-dimensional CFD generated flow fields, to predict inertial particle transport. If successful, the computational time for such calculations would be greatly reduced as far fewer particles would be required for an accurate solution. Extension to three-dimensional cases would then become computationally feasible.

For cases where both large-scale inertial and turbulent/diffusive effects are important, a joint Eulerian-Lagrangian approach (similar to that of Menguturk *et al.* (1983)) would be the long term numerical objective. The Osiptsov Lagrangian approach could be used to provide a solution of the particle flow field up to the edge of the boundary layers (outside of which the turbulence has little effect on the particles), from which point the Eulerian diffusion-inertia approach (with turbulent/diffusive effects included) could be used to complete the calculation. For cases where either inertial or turbulent/diffusive effects are important, the appropriate component (Lagrangian or Eulerian) could be used. As both components would be computationally efficient and capable of representing almost all of the necessary transport mechanisms, accurate and quick three-dimensional analyses would then be possible.

The investigation into the Osiptsov Lagrangian method will take the following form:

- development of the method in its simplest, one-dimensional form, so that its basic operation becomes obvious. It will be applied to some simple test cases.

- two-dimensional development.

- application to the case of two-dimensional fluid-particle stagnation point flow, using an analytical fluid flow field, and comparison between a numerical solution and the analytical particle solution that exists for this case.

- development of a special treatment of the equations at low Stokes numbers, to relieve mathematical stiffness when the time-step is required to be less than the particle relaxation time in order to maintain numerical stability.

- application to two-dimensional fluid-particle flow over a cylinder, using an analytical fluid flow field and a CFD-generated fluid flow field, and comparison with a traditional Lagrangian approach. A method is developed for the calculation of fluid velocity gradients, and validated.

- quantification of the improvement in computational time compared with a traditional Lagrangian approach, using the case of fluid-particle flow over a cylinder.

- testing the reaction of the method to crossing particle pathlines.

- application to two-dimensional fluid-particle flow in an industrial gas turbine is demonstrated, along with a simple test of accuracy of the calculated particle density field.

2.2 The Osiptsov Lagrangian method in one-dimension

Consider a one-dimensional dilute gas-particle flow satisfying the usual dusty-gas approximations. In the Lagrangian formulation (see figure 2.1) attention is focused on an element of 'particle fluid', which, at time $t = 0$, is situated at position $x = a$. At a later time $t = \tau$ the *same* element has moved to position $x = x_p$ and the particle density and velocity associated with it are denoted ρ_p and V. Fixing a and τ is therefore sufficient to define the values of x_p, ρ_p and V through relationships of the form:

$$x_p = x_p(a, \tau) \qquad \rho_p = \rho_p(a, \tau) \qquad V = V(a, \tau) \tag{2.1}$$

The Lagrangian coordinate a identifies a particular particle pathline and the Lagrangian time τ identifies a point on that pathline.

The spatial extent δx_p of the element at time τ is generally different from its spatial extent δa at time zero. This is because the element becomes stretched or compressed by local variations of particle velocity, caused by acceleration or deceleration of the background fluid flow field. Nevertheless, in the absence of Brownian or turbulent diffusive fluxes, the element always comprises the same particles. The conservation of particle mass therefore

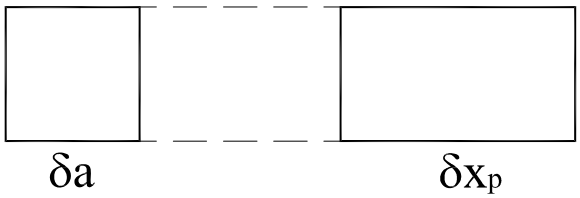

Figure 2.1: A one-dimensional element of 'particle fluid' at times $t = 0$ and $t = \tau$

requires,

$$\rho_p(a,\tau)\delta x_p = \rho_p(a,0)\delta a \tag{2.2}$$

In the limit as $\delta a \to 0$ this may be written,

$$|J(a,\tau)|\rho_p(a,\tau) = |J(a,0)|\rho_p(a,0) = \text{constant} \tag{2.3}$$

where J is the Jacobian of the Eulerian-Lagrangian transformation,

$$J(a,\tau) = \frac{\partial x_p(a,\tau)}{\partial a} \tag{2.4}$$

and $J(a,0) = 1$. Note that the partial differentiation is at constant τ.

Equation 2.3 is the Lagrangian form of the particle continuity equation. The absolute value of J is used in order to cover the possibility that the 'back' of the element overtakes the 'front' with the result that J becomes negative. Calculation of the particle density therefore reduces to the equivalent problem of finding the variation of the Jacobian J along the particle pathline.

Assuming that the only force experienced by the particles is that due to steady-state drag, Newton's second law of motion (the Lagrangian form of the particle momentum equation) is written,

$$\frac{\partial V(a,\tau)}{\partial \tau} = \beta(U - V) \tag{2.5}$$

where the partial differentiation is at constant a. U is the local fluid velocity at the position of the particle element and β is the reciprocal of the particle relaxation time τ_p:

$$\tau_p = \frac{\rho_{p,mat} d_p^2}{18\mu_g} \tag{2.6}$$

where $\rho_{p,mat}$ is the particle material density, d_p is the particle diameter, and μ_g is the gas dynamic viscosity.

The variation of J with time along a pathline is described by $\frac{\partial J}{\partial \tau}$ (at constant a) and is

denoted by the variable w,

$$w = \frac{\partial J}{\partial \tau} \tag{2.7}$$

Introducing equation 2.4, switching the order of differentiation and noting that $V = \frac{\partial x_p}{\partial \tau}$ (at constant a),

$$w = \frac{\partial J}{\partial \tau} = \frac{\partial}{\partial \tau}\left(\frac{\partial x_p}{\partial a}\right) = \frac{\partial}{\partial a}\left(\frac{\partial x_p}{\partial \tau}\right) = \frac{\partial V}{\partial a} \tag{2.8}$$

Differentiating w with respect to Lagrangian time, again switching the order of differentiation, and substituting equation (2.5) gives,

$$\frac{\partial w}{\partial \tau} = \frac{\partial}{\partial \tau}\left(\frac{\partial V}{\partial a}\right) = \frac{\partial}{\partial a}\left(\frac{\partial V}{\partial \tau}\right) = \frac{\partial}{\partial a}[\beta(U - V)] \tag{2.9}$$

Treating β as a constant (more precisely assuming $\frac{\partial \beta}{\partial a} = 0$), equation 2.9 becomes,

$$\frac{\partial w}{\partial \tau} = \beta\left(\frac{\partial U}{\partial a} - \frac{\partial V}{\partial a}\right) = \beta\left(\frac{\partial U}{\partial a} - w\right) \tag{2.10}$$

$\frac{\partial U}{\partial a}$ (at constant τ) in equation 2.10 is a Lagrangian derivative and is to be interpreted as follows. Consider a particle element that starts at time zero at location a and arrives at time τ at location x_p where the fluid velocity is U. Now consider an adjacent element that starts at time zero at location $a + \delta a$ and arrives at time τ at location $x_p + \delta x_p$ where the fluid velocity is $U + \delta U$. $\frac{\partial U}{\partial a}$ is then equal to the limit of $\frac{\partial U}{\partial a}$ (at constant τ) as $\delta a \to 0$.

$\frac{\partial U}{\partial a}$ is awkward to evaluate because U is generally only known in Eulerian coordinates. However, using the chain rule,

$$\frac{\partial U(a,\tau)}{\partial a} = \frac{\partial x_p(a,\tau)}{\partial a}\frac{\partial U(x,t)}{\partial x} = J\frac{\partial U(x,t)}{\partial x} \tag{2.11}$$

$\frac{\partial U}{\partial x}$ can, in principle, be evaluated from the fluid velocity field specified in Eulerian coordinates. Practical problems that arise in calculating $\frac{\partial U}{\partial x}$ will be discussed later.

Equations 2.5, 2.7 and 2.10 are three first-order ordinary differential equations giving the variation of the three unknowns V, J and w along the particle pathline defined by a particular value of a. Equation 2.5 is uncoupled from the other equations and can be solved for V in the usual way. Equations 2.7 and 2.10 must be solved simultaneously for J and its derivative w. The variation of particle density along the pathline can then be obtained from equation 2.3.

Initial conditions must be specified for V, J and w. $V_0 = V(a,0)$ is defined by the initial gas-particle slip velocity which must be prescribed. $J_0 = J(a,0) = 1$, as mentioned above.

From equation 2.8,

$$w_0 = w(a,0) = \left(\frac{\partial V}{\partial a}\right)_0 = J_0 \left(\frac{\partial V}{\partial x}\right)_0 = \frac{J_0}{V_0}\left(\frac{\partial V}{\partial \tau}\right)_0 = \frac{J_0}{V_0}\beta(U_0 - V_0) \tag{2.12}$$

w_0 is therefore related to the initial slip velocity.

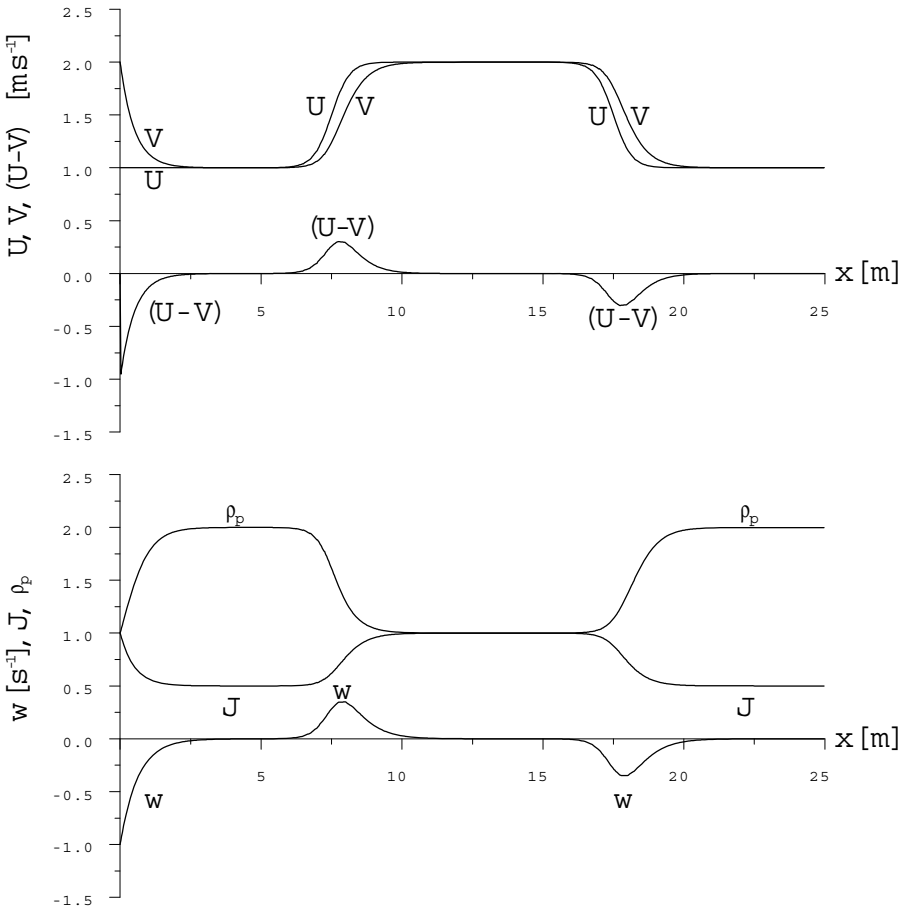

Figure 2.2: Gas velocity, particle velocity, slip velocity, Jacobian time derivative, Jacobian and particle density for an accelerating/decelerating 1-D gas flow field. J and ρ_p are non-dimensionalised by J_0 and $\rho_{p,0}$.

2.2.1 One-dimensional examples

It is appropriate to examine some simple one-dimensional examples, in order to illustrate the behaviour of 'new' quantities such as J and w when there are changes in U, V and ρ_p.

A gas with a constant initial velocity of $U_0 = 1$ ms^{-1}, accelerates to 2 ms^{-1}, and its velocity remains constant before deceleration back to 1 ms^{-1} occurs, followed by another period of constant velocity (figure 2.2). The initial particle velocity ($V_0 = 2$ ms^{-1}) takes little time to attain the gas velocity of $U = 1$ ms^{-1}, due to its small relaxation time of $\tau_p =$ 0.5 s. During the periods of gas acceleration and deceleration, V can be seen to lag behind

U, and the extent to which it does this is shown by the slip velocity $(U - V)$. Also shown are similarities between the behaviour of the slip velocity and w, the time derivative of the Jacobian. J can be seen to increase (decrease) with the acceleration (deceleration) of the gas, as stated earlier, while it is inversely proportional to ρ_p.

If a gas with a constant initial velocity of $U_0 = 1$ ms^{-1}, decelerates at a constant rate until $U = 0$ ms^{-1}, it can be seen from figure 2.3 that V will also tend towards 0 ms^{-1}. J decreases until it reaches zero, and consequently, ρ_p rises rapidly, tending to infinity where U reaches zero. ρ_p always tends to infinity when J becomes very small (or zero). This happens in two-dimensions when particle trajectories cross, and will be discussed later in more detail. Osiptsov (1984) also discusses some interesting one-dimensional particle flows, including singular situations when $J \to 0$ and $\rho_p \to \infty$.

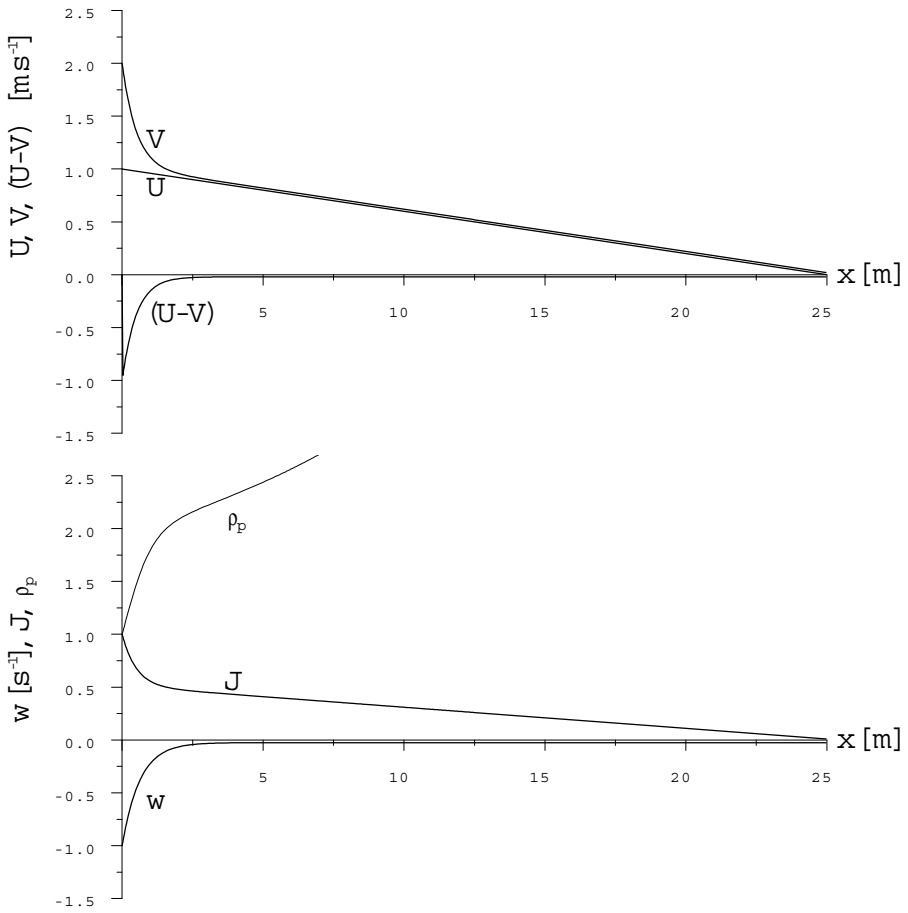

Figure 2.3: Gas velocity, particle velocity, slip velocity, Jacobian time derivative, Jacobian and particle density for a 1-D gas flow field decelerating to a halt. J and ρ_p are non-dimensionalised by J_0 and $\rho_{p,0}$.

Figure 2.4: A two-dimensional element of 'particle fluid' at times $t = 0$ and $t = \tau$

defined by,

$$w_{xa} = \frac{\partial J_{xa}}{\partial \tau} = \frac{\partial V_x}{\partial a}, \quad w_{yb} = \frac{\partial J_{yb}}{\partial \tau} = \frac{\partial V_y}{\partial b}, \quad w_{xb} = \frac{\partial J_{xb}}{\partial \tau} = \frac{\partial V_x}{\partial b}, \quad w_{ya} = \frac{\partial J_{ya}}{\partial \tau} = \frac{\partial V_y}{\partial a} \tag{2.16}$$

Carrying out similar manipulations as in the one-dimensional case then leads to four differential equations analogous to equation (2.10),

$$\frac{\partial w_{xa}}{\partial \tau} = \beta \left(\frac{\partial U_x}{\partial a} - w_{xa} \right) \tag{2.17a}$$

$$\frac{\partial w_{xb}}{\partial \tau} = \beta \left(\frac{\partial U_x}{\partial b} - w_{xb} \right) \tag{2.17b}$$

$$\frac{\partial w_{ya}}{\partial \tau} = \beta \left(\frac{\partial U_y}{\partial a} - w_{ya} \right) \tag{2.17c}$$

$$\frac{\partial w_{yb}}{\partial \tau} = \beta \left(\frac{\partial U_y}{\partial b} - w_{yb} \right) \tag{2.17d}$$

The chain rule expressions which relate the Lagrangian and Eulerian derivatives of U_x and U_y are a little more complicated,

$$\frac{\partial U_x(a,b,\tau)}{\partial a} = J_{xa} \frac{\partial U_x(x,y,t)}{\partial x} + J_{ya} \frac{\partial U_x(x,y,t)}{\partial y} \tag{2.18a}$$

$$\frac{\partial U_x(a,b,\tau)}{\partial b} = J_{xb} \frac{\partial U_x(x,y,t)}{\partial x} + J_{yb} \frac{\partial U_x(x,y,t)}{\partial y} \tag{2.18b}$$

$$\frac{\partial U_y(a,b,\tau)}{\partial a} = J_{xa} \frac{\partial U_y(x,y,t)}{\partial x} + J_{ya} \frac{\partial U_y(x,y,t)}{\partial y} \tag{2.18c}$$

$$\frac{\partial U_y(a,b,\tau)}{\partial b} = J_{xb} \frac{\partial U_y(x,y,t)}{\partial x} + J_{yb} \frac{\partial U_y(x,y,t)}{\partial y} \tag{2.18d}$$

For a given particle pathline, equations (2.15), (2.16) and (2.17) represent ten ordinary differential equations for the ten unknowns (two components of V, four components of J and four components of w). They can be integrated numerically if the components of the fluid velocity gradient in Eulerian coordinates, required for equation (2.18), can be computed at each point along the pathline. It is also necessary to know the values of V, J and w at the start of each pathline.

Figure 2.5: A two-dimensional element of 'particle fluid' at time $\tau = 0$ to illustrate the derivation of initial conditions

2.16, some consideration shows that:

$$w_{xa,0} = \lim(\delta a \to 0)\left(\frac{V_{x,2} - V_{x,1}}{\delta a}\right) = \lim(\delta a \to 0)\left(\frac{(V_{x,2} - V_{x,1'}) + (V_{x,1'} - V_{x,1})}{\delta a}\right)$$

$$= \lim(\delta a \to 0)\left(\frac{(\partial\tau)_{1'-2}(\frac{\partial V_x}{\partial\tau})_0 - (y_{p1} - y_{p1'})(\frac{\partial V_x}{\partial y})_0}{\delta a}\right) = \frac{1}{V_{x,0}}\left(\frac{\partial V_x}{\partial\tau}\right)_0 - \frac{V_{y,0}}{V_{x,0}}\frac{dV_{x,0}}{db} \quad (2.22a)$$

$$w_{ya,0} = \lim(\delta a \to 0)\left(\frac{V_{y,2} - V_{y,1}}{\delta a}\right) = \lim(\delta a \to 0)\left(\frac{(V_{y,2} - V_{y,1'}) + (V_{y,1'} - V_{y,1})}{\delta a}\right)$$

$$= \lim(\delta a \to 0)\left(\frac{(\partial\tau)_{1'-2}(\frac{\partial V_y}{\partial\tau})_0 - (y_{p1} - y_{p1'})(\frac{\partial V_y}{\partial y})_0}{\delta a}\right) = \frac{1}{V_{x,0}}\left(\frac{\partial V_y}{\partial\tau}\right)_0 - \frac{V_{y,0}}{V_{x,0}}\frac{dV_{y,0}}{db} \quad (2.22b)$$

2.3.2 Computational cost considerations

It should be pointed out, that for an incompressible and irrotational flow in two-dimensions,

$$\frac{\partial U_x}{\partial x} = -\frac{\partial U_y}{\partial y} \qquad \text{and} \qquad \frac{\partial U_x}{\partial y} = \frac{\partial U_y}{\partial x} \quad (2.23)$$

and the result of this, is that $w_{xa} = -w_{yb}$ and $w_{xb} = w_{ya}$. There are now just four additional equations, instead of eight.

Although three-dimensional flow fields will not be considered here, it is worth noting that the Osiptsov Lagrangian method can, in principle, be extended to such flows. V now has three, and J and w each have nine, components. A total of 21 differential equations (18 additional equations) can be derived corresponding to the 21 unknown dependent variables. Again, for an incompressible and irrotational flow, the number of additional equations is reduced (10 additional equations are required in three-dimensions with these simplifications).

2.3.3 A two-dimensional example: stagnation point flow

Two-dimensional, inviscid, incompressible stagnation point flow is a good example with which to assess the potential of the Osiptsov Lagrangian method because analytical solutions exist for both fluid and particle flow fields.

The fluid flow field is shown in figure 2.6, and the stream function $\Psi = -Axy$ (where A is a positive constant) describes the flow in the upper-left quadrant of the flow field. The velocity components and their spatial derivatives are then given by,

$$U_x = \frac{\partial\Psi}{\partial y} = -Ax, \qquad \frac{\partial U_x}{\partial x} = -A, \qquad \frac{\partial U_x}{\partial y} = 0 \quad (2.24a)$$

$$U_y = -\frac{\partial\Psi}{\partial x} = Ay, \qquad \frac{\partial U_y}{\partial x} = 0, \qquad \frac{\partial U_y}{\partial y} = A \quad (2.24b)$$

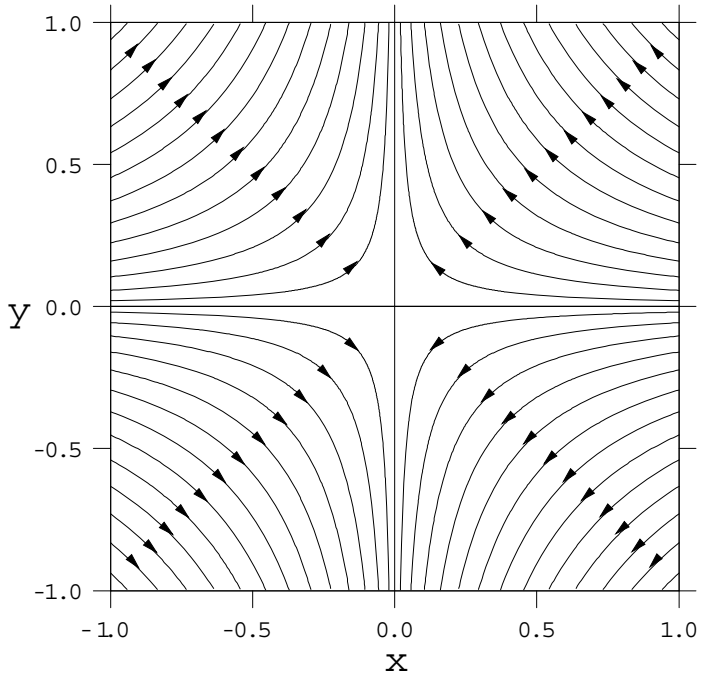

Figure 2.6: 2-D stagnation point flow.

The analytical solution for the particle velocity field is obtained by substituting $V_x = \frac{\partial x_p}{\partial \tau}$ and $V_y = \frac{\partial y_p}{\partial \tau}$, together with equation 2.24 for U_x and U_y, into equation 2.15 to give two integrable second order differential equations for the particle pathlines in parametric form, $x_p = x_p(\tau)$, $y_p = y_p(\tau)$, (Osiptsov, 1984). Details of this process can be found in appendix A.1, along with the derivation of an analytical expression for the Jacobian, from which the particle density can be found.

The particular case of interest corresponds to particles injected at $\tau = 0$ at points along the $x = -1$ line with zero y-direction velocity ($V_{y,0} = 0$) and zero x-direction slip velocity ($V_{x,0} = U_{x,0}$). With these initial conditions, it can be shown that both V_x and ρ_p are independent of y and depend only on x, i.e. $V_x = V_x(x)$ and $\rho_p = \rho_p(x)$. Substituting these initial conditions into equations 2.21 and 2.22, gives $w_{xa,0} = w_{xy,0} = w_{yb,0} = 0$ and $w_{yx,0} = \beta U_{y,0}/U_{x,0}$.

The Osiptsov Lagrangian solution is obtained by time-integrating equations 2.15, 2.16 and 2.17 numerically along particle pathlines starting from the same initial conditions. For the present calculations, a predictor-corrector algorithm was used for all the equations. At each time-step, the components of the fluid velocity and the spatial derivatives were obtained directly from equation 2.24.

Examination of the analytical solution shows that, when non-dimensionalised, it can be expressed in terms of just one parameter, the Stokes number, defined by,

$$St = \frac{A}{2\beta} \tag{2.25}$$

This is to be interpreted as the ratio of the particle inertial relaxation time (β^{-1}) to a fluid time-scale ($2/A$). Figure 2.7, shows fluid streamlines, particle pathlines and the particle density variation, in the upper-left quadrant of the flow field for several Stokes numbers, when $A = 1$. In virtually all cases, the Osiptsov numerical and analytical solutions are indistinguishable and hence only the numerical solution has been plotted.

The analytical solution for V_x (see appendix A.1), has three types of solution depending on the roots of its auxiliary equation. The roots change their nature at $St = 0.125$. In the subcritical regime, $St < 0.125$ (figure 2.7a), particles approach the y-axis asymptotically as $y \to \infty$, while the particle density remains finite. Particles do not cross other particles pathlines nor the $y-$axis. At the critical condition, $St = 0.125$ (figure 2.7b), the solution is singular and $\rho_p \to \infty$ as $x \to 0$. In the supercritical regime, $St > 0.125$ (figure 2.7c), particles reach the y-axis with a finite velocity and density. The situation shown is equivalent to replacing the y-axis by a perfectly absorbing wall.

If the y-axis is not replaced by such a wall, the finite x-direction velocity of the particles means that they can penetrate into the upper-right quadrant of the stagnation flow. When particles do this, they oscillate about the $y-$axis with decaying amplitude, and this leads to the crossing of particle trajectories, and an increase in the local particle density. The regions of crossing trajectories are bounded by lines of infinite particle density.

For the case of $St = 0.5$ (figure 2.7d), the decay occurs relatively quickly. The particles penetrate across to $x \approx 0.3$, and return across the y-axis before turning once more back across the $y-$axis. At the extent of particle penetration into the upper-right quadrant, the particle density becomes infinite. An infinite value of particle density is also found at each 'turning point' where the particles reverse direction and head back towards the $y-$axis. The $x-$coordinates of these 'turning points' are coincident with lines of infinite particle density, and these define the boundaries within which particle trajectories cross. The ability of the Osiptsov Lagrangian method to deal with this behaviour, and other types of crossing trajectories, will be discussed later. Healy & Young (2003) compared the behaviour of the Jacobian and the divergence of the particle velocity field (from which the particle densities are calculated) under these circumstances, to demonstrate the advantages of using the Osiptsov Lagrangian approach over that of Fernandez de la Mora & Rosner (1981), for situations where particle trajectories cross.

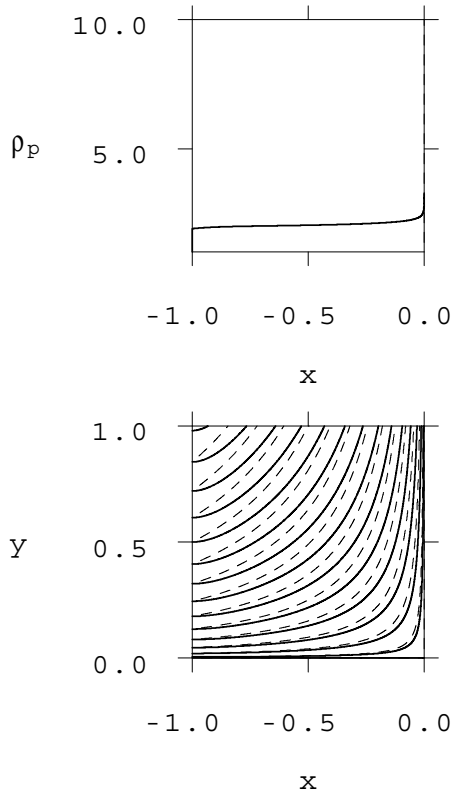

a) Subcritical $St = 0.05$

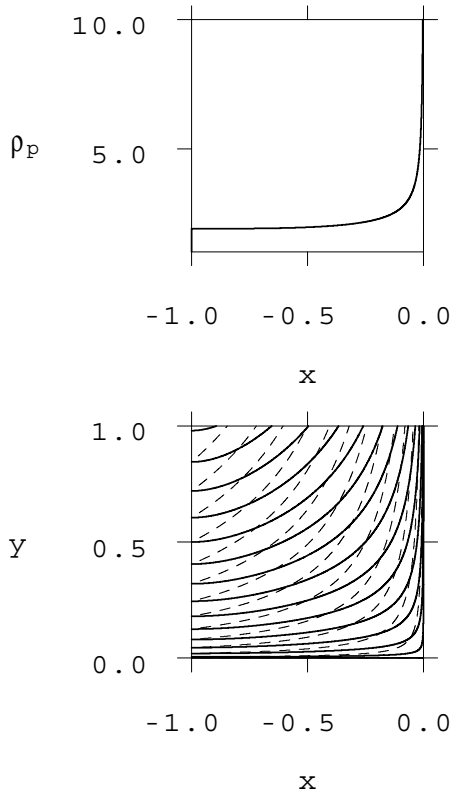

b) Critical $St = 0.125$

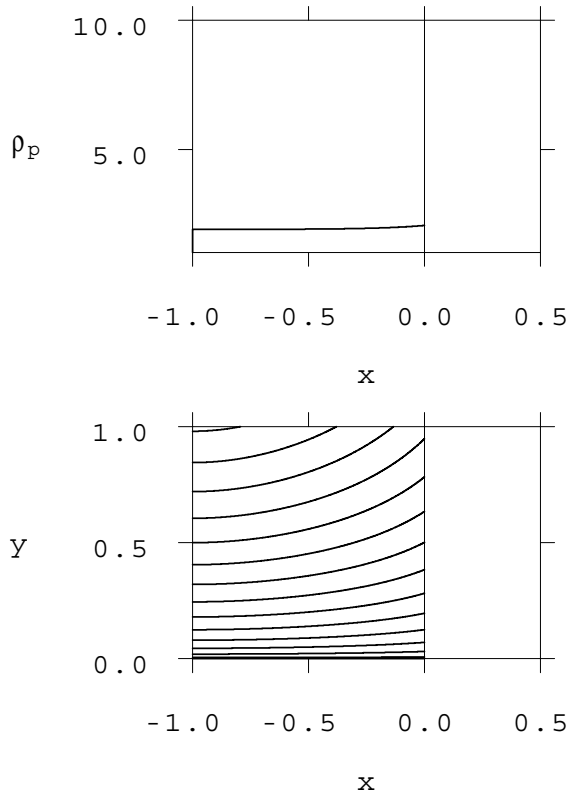

c) Supercritical $St = 0.5$ (absorbing wall)

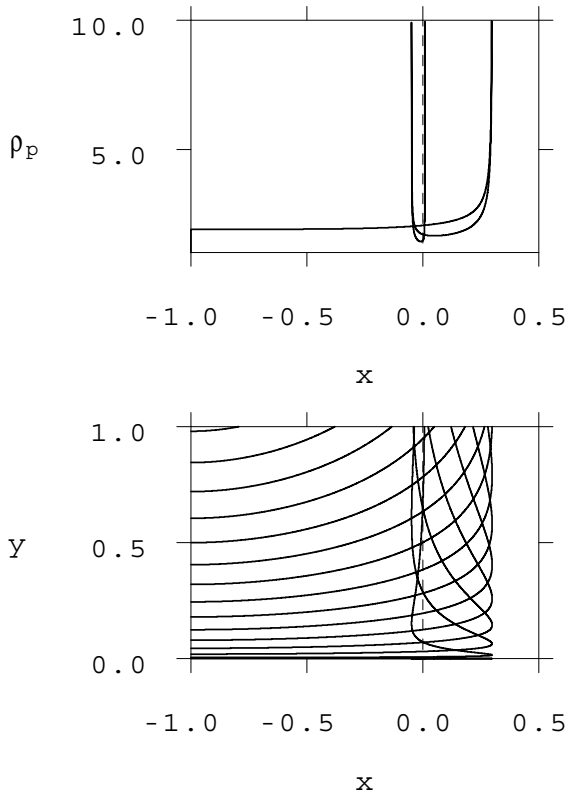

d) Supercritical $St = 0.5$

Figure 2.7: Particle pathlines (solid) and fluid streamlines (dashed - a) and b) only), and particle density for flow near a stagnation point

2.4 Special treatment at low Stokes numbers

A serious computational problem arises at low Stokes numbers if an explicit numerical scheme is used to integrate the equations. As is well-known, the time-step of an explicit scheme must be less than the particle relaxation time in order to maintain numerical stability. At low Stokes numbers, the equations become mathematically 'stiff', very small time-steps are required, and the computational time becomes excessive. One method of overcoming this problem is to use a semi-analytical approach whereby the Lagrangian equations are integrated analytically over a time interval which is long compared to β^{-1} but short compared with the time-scale of flow changes. This approach is simpler and more transparent than traditional backwards-difference numerical methods for stiff ordinary differential equations. The method is described below with reference to the one-dimensional equations but the extension to two-dimensions is straightforward.

The particle equation of motion (equation 2.5) can be rewritten,

$$\frac{\partial(V-U)}{\partial\tau}+\beta(V-U)=-\frac{\partial U}{\partial\tau} \tag{2.26}$$

Multiplying by the integrating factor $e^{\beta\tau}$ and rearranging,

$$\frac{\partial(V-U)}{\partial\tau}e^{\beta\tau}+\beta(V-U)e^{\beta\tau}=\frac{d}{\partial\tau}\left[e^{\beta\tau}(V-U)\right]=-\frac{\partial U}{\partial\tau}e^{\beta\tau} \tag{2.27}$$

Then, integrating analytically (from $\tau=0$ to $\tau=\Delta\tau$) while assuming $\frac{\partial U}{\partial\tau}$ to remain constant gives,

$$(V-U)=(V-U)_0e^{-\beta\Delta\tau}-\frac{1}{\beta}\overline{\frac{\partial U}{\partial\tau}}(1-e^{-\beta\Delta\tau}) \tag{2.28}$$

The first term on the right hand side represents the exponential decay, with time constant β^{-1}, of the slip velocity at the start of the current time-step. The second term represents the exponential approach (also with time constant β^{-1}) to the local 'steady-state' slip velocity $\beta^{-1}\overline{\frac{\partial U}{\partial\tau}}$.

An identical approach can be used to integrate out the stability restriction in equation 2.10. Thus, multiplying by $e^{\beta\tau}$ and integrating analytically, assuming $\frac{\partial U}{\partial a}$ to remain constant,

$$w=w_0e^{-\beta\Delta\tau}+\overline{\frac{\partial U}{\partial a}}(1-e^{-\beta\Delta\tau}) \tag{2.29}$$

A further integration gives an expression for J to replace equation 2.7,

$$J=J_0+w_0\left(\frac{1-e^{-\beta\Delta\tau}}{\beta}\right)+\overline{\frac{\partial U}{\partial a}}\left(\Delta\tau-\frac{1-e^{-\beta\Delta\tau}}{\beta}\right) \tag{2.30}$$

The full set of equations for two-dimensions is given in appendix A.2.

Equations 2.28, 2.29 and 2.30 can be applied using a predictor-corrector algorithm (this is necessary as x_p is needed to find U and thus V, while V must be known in order to find x_p). Now, however, there are no stability restrictions and the time increment $\Delta\tau$ is only limited by the accuracy of the assumptions that $\frac{\partial U}{\partial \tau}$ and $\frac{\partial U}{\partial a}$ remain constant. In this way, calculations for flows at very low Stokes numbers can be performed accurately with no increase in computational time.

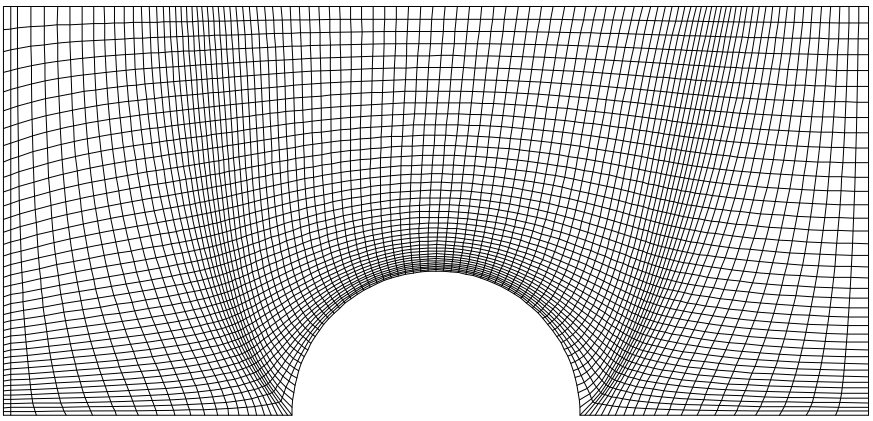

Figure 2.8: Near-cylinder grid for inviscid CFD calculations

2.5 Fluid-particle flow over a cylinder

2.5.1 Calculation of the fluid velocity field

Inviscid, incompressible fluid-particle flow over a cylinder has been investigated by Morsi & Alexander (1972), Fernandez de la Mora & Rosner (1981), and others. The flow is unphysical because there are no boundary layers but it is still a useful test case because of the existence of an analytical solution for the fluid (although not the particle) velocity field. The stream function Ψ is given by,

$$\Psi = U_\infty y\left(1 - \frac{R^2}{x^2 + y^2}\right) \tag{2.31}$$

where U_∞ is the velocity of the oncoming flow and R is the radius of the cylinder. Analytical expressions for the fluid velocity components can easily be obtained by differentiating equation 2.31. The Stokes number for the cylinder calculations is defined by $St = U_\infty/(R\beta)$.

The fluid velocity field can also be obtained from a CFD calculation and this can then be used to determine whether or not the Osiptsov Lagrangian method can function with a

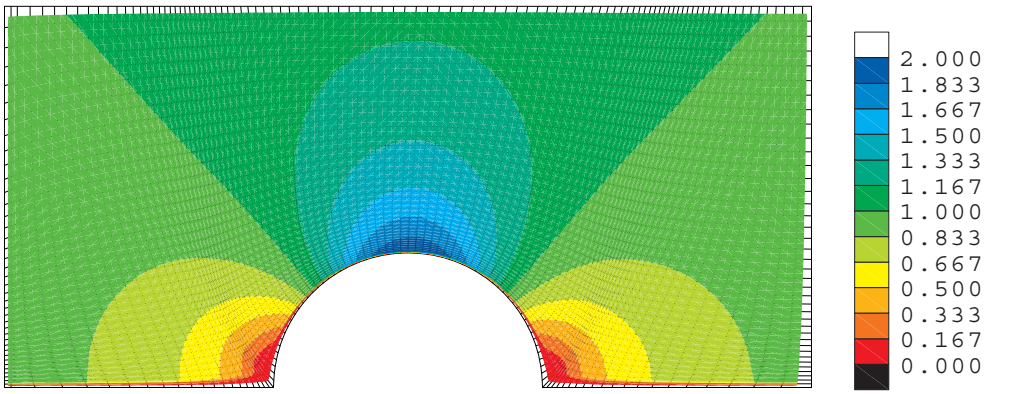

a) Analytical fluid velocity x-component

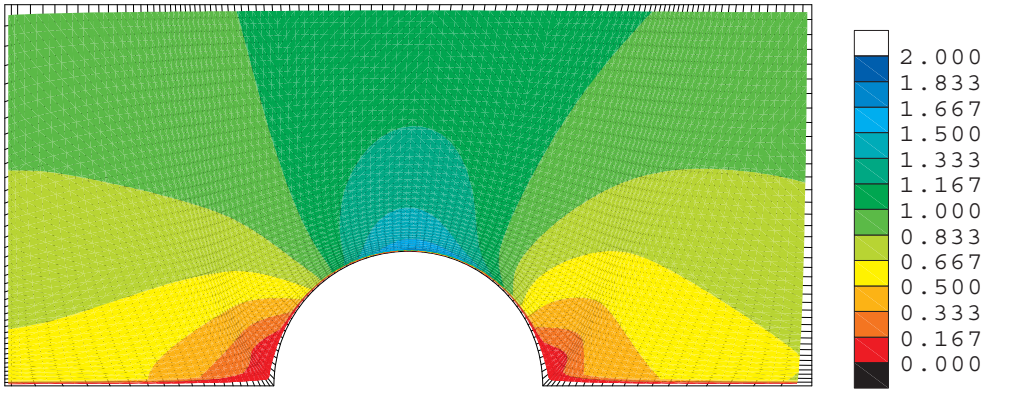

b) CFD fluid velocity x-component

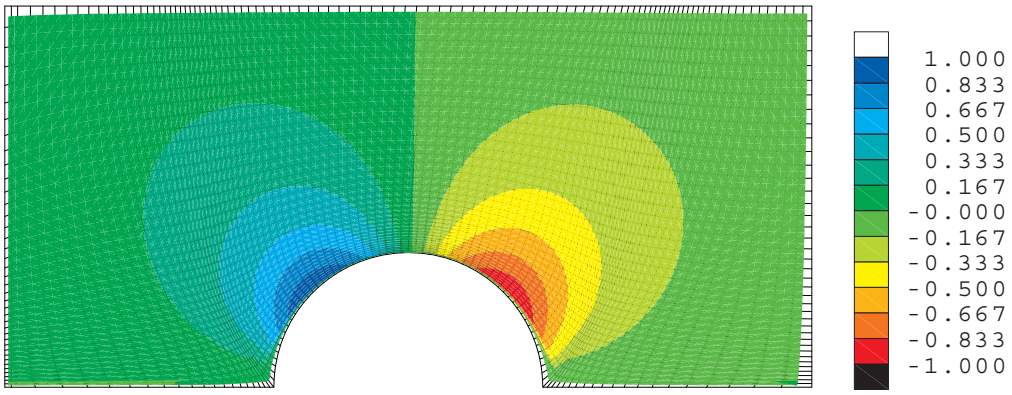

c) Analytical fluid velocity y-component

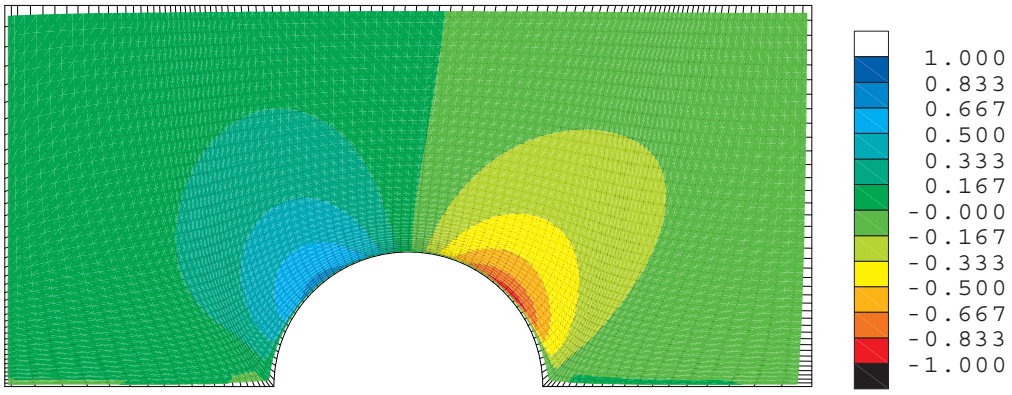

d) CFD fluid velocity y-component

Figure 2.9: Comparison between analytical and CFD fluid velocity fields

non-analytical fluid flow field. The outcome is crucial because if the method is restricted solely to analytical flow fields it is of little practical value.

The inviscid CFD solver used was actually written for duct flows but equation 2.31 represents the flow around an isolated cylinder. In order to model the far-field boundary as realistically as possible, the duct height was made very large in comparison to the cylinder diameter. The near-cylinder CFD grid is shown in figure 2.8 but the actual extent in the y-direction was five times greater. A comparison between the analytical and CFD generated velocity fields is shown in figure 2.9. The agreement is rather better than a comparison of the contour plots suggests, as the method of presentation tends to exaggerate errors.

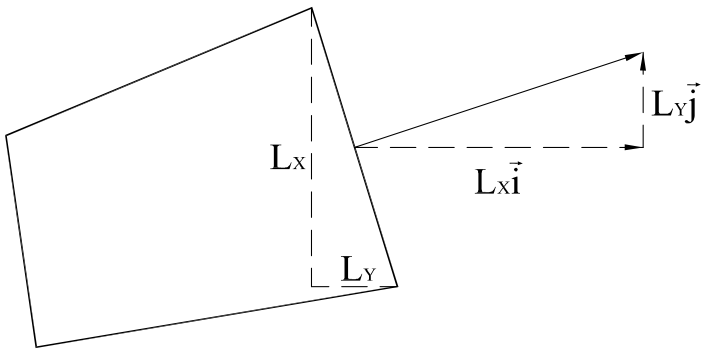

Figure 2.10: A cell of the Eulerian grid showing the projections L_x and L_y

2.5.2 Calculation of the fluid velocity gradient field

It is well-established that particle velocity fields can be computed accurately using CFD generated flow fields, but integration of the equations for the Jacobian requires a knowledge, not only of the fluid velocity components, but also of their gradients. It is quite feasible that numerical differentiation of a 'noisy' CFD velocity field may generate unacceptable errors. A special technique was therefore developed to obtain the velocity derivatives from a CFD solution generated on a non-uniform grid. As numerical differentiation enhances errors, a method based on numerical integration was used.

The so-called 'gradient theorem' (a special case of Gauss' theorem) is expressed by,

$$\oint_S \phi d\vec{S} = \int_{vol} \nabla\phi d(vol) \tag{2.32}$$

where vol is a finite volume enclosed by a surface S and ϕ is any scalar function of position. When the theorem is applied in finite-difference form to the single two-dimensional quadrilat-

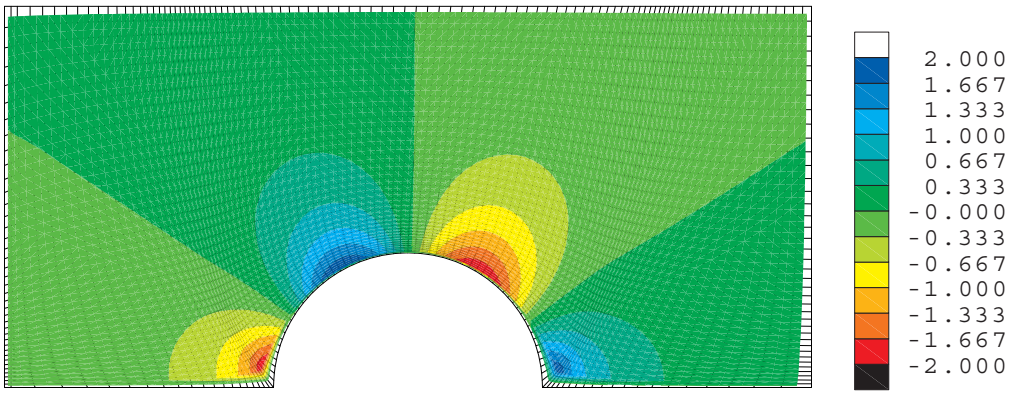

a) Analytical $\frac{dU_x}{dx}$

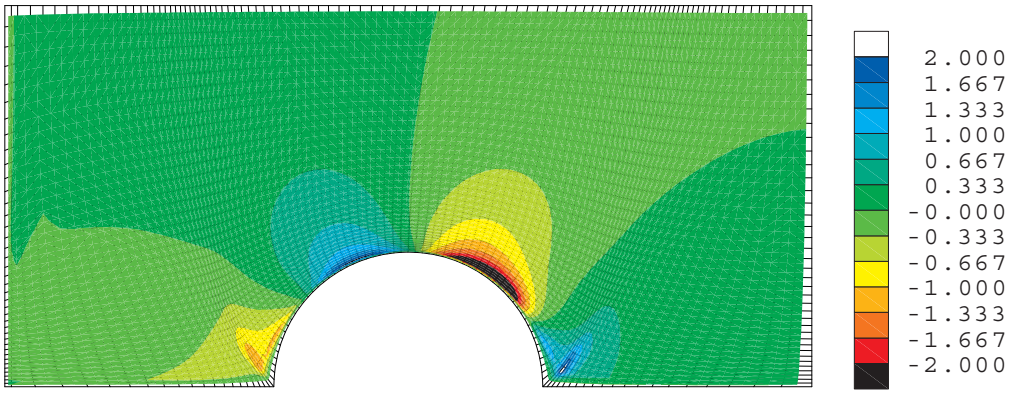

b) CFD $\frac{dU_x}{dx}$

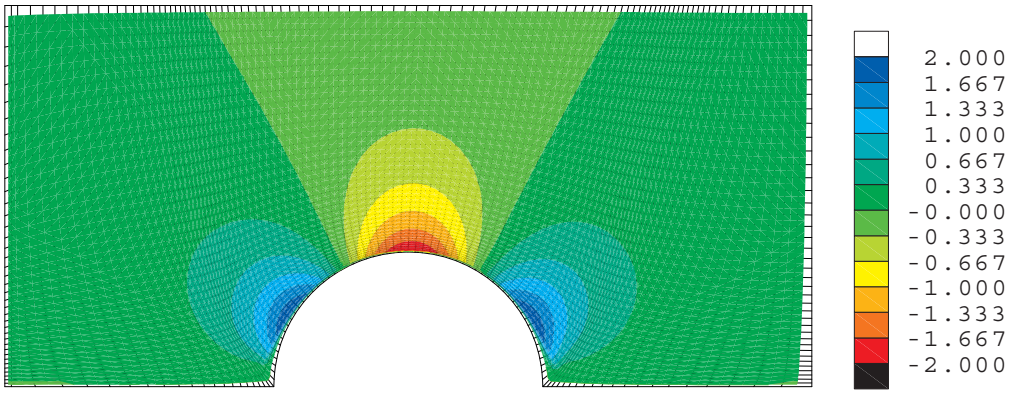

c) Analytical $\frac{dU_x}{dy}$

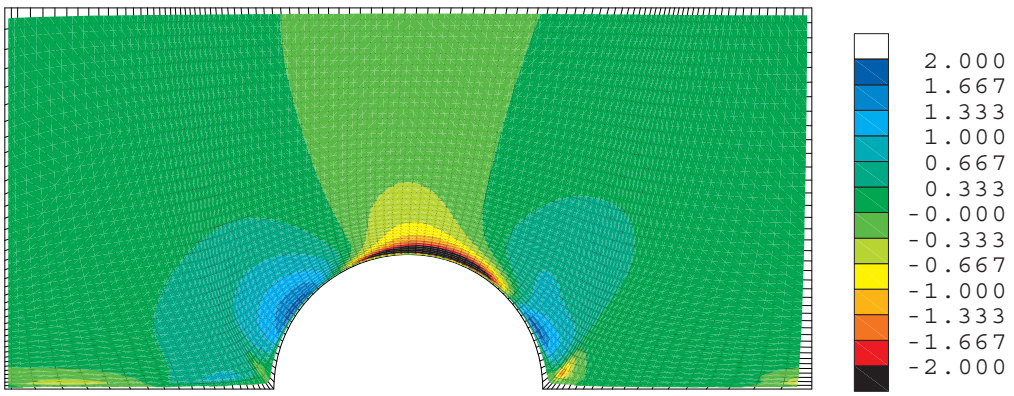

d) CFD $\frac{dU_x}{dy}$

Figure 2.11: Comparison between analytical and CFD fluid velocity gradient fields

eral cell of the Eulerian grid shown in figure 2.10, the following relationship is obtained,

$$\sum_{sides} \phi(L_x\vec{i} + L_y\vec{j}) = \left(\frac{\partial\phi}{\partial x}\vec{i} + \frac{\partial\phi}{\partial y}\vec{j}\right)A \tag{2.33}$$

On the left hand side, L_x and L_y are the projections of a side normal to the $x-$ and $y-$directions and ϕ represents a mean value along the side. On the right hand side, $\frac{\partial\phi}{\partial x}$ and $\frac{\partial\phi}{\partial y}$ are mean values of the derivatives, averaged over the cell which is of area A. Setting $\phi = U_x$ and then $\phi = U_y$ and separating into components gives four scalar equations,

$$A\frac{\partial U_x}{\partial x} = \sum_{sides} U_x L_x \qquad A\frac{\partial U_x}{\partial y} = \sum_{sides} U_x L_y \tag{2.34a}$$

$$A\frac{\partial U_y}{\partial x} = \sum_{sides} U_y L_x \qquad A\frac{\partial U_y}{\partial y} = \sum_{sides} U_y L_y \tag{2.34b}$$

Equation 2.34 can be used to calculate the four required velocity gradients from the CFD generated velocity field. Values along particle pathlines are then obtained by interpolation. The method can easily be adapted for either cell centre or cell vertex storage schemes.

Figure 2.11 provides a comparison between the analytical and CFD-based calculations of $\frac{\partial U_x}{\partial x}$ and $\frac{\partial U_x}{\partial y}$. The agreement is not perfect but the main features are reproduced reasonably well by the numerical calculation. Similar agreement is obtained for $\frac{\partial U_y}{\partial x}$ and $\frac{\partial U_y}{\partial y}$ but these are not shown here (as $\frac{\partial U_x}{\partial x} = -\frac{\partial U_y}{\partial y}$ and $\frac{\partial U_x}{\partial y} = \frac{\partial U_y}{\partial x}$). The real test, however, is whether or not this level of accuracy will generate unacceptable errors in calculating the particle density field.

2.5.3 Calculation of the particle density field

Particles were computationally injected along a line $x_{p,0} = -3R$ (the centre of the cylinder is at $x = 0$) with uniform density $\rho_{p,0}$, zero $y-$direction velocity ($V_{y,0} = 0$) and zero $x-$direction slip velocity ($V_{x,0} = U_{x,0}$). As before, $J_{xa,0} = J_{yb,0} = 1$ and $J_{xb,0} = J_{ya,0} = 0$. From equations 2.21 and 2.22,

$$w_{xa,0} = w_{yb,0} = 0 \qquad w_{xb,0} = \frac{\partial U_{x,0}}{\partial b} \qquad w_{ya,0} = \frac{\beta U_{y,0}}{U_{x,0}} \tag{2.35}$$

The Lagrangian equations 2.15, 2.16 and 2.17 for the components of the particle velocity, the Jacobian and its derivatives were then integrated along particle pathlines through the flow field (see appendix A.3 for details). The fluid velocity gradients required for equation 2.18 were obtained either analytically from equation 2.31 or numerically from the CFD solution (using equation 2.34). For low Stokes numbers, the special treatment described in section 2.4 was applied in a two-dimensional form.

Contour plots of the particle density fields for four different Stokes numbers are shown in figure 2.12 (a-p). For each Stokes number, a traditional Lagrangian calculation (again see appendix A.3) was performed on the analytical and CFD generated fluid flow field, and 10,000 particles were used in the calculation. An Osiptsov Lagrangian calculation was also carried out on both the analytical and CFD generated fluid flow field, and just 500 particles were used. In each case, the integration time-step was chosen so that about five steps were needed for a particle to cross the smallest Eulerian cell.

The traditional Lagrangian method calculates the particle density by counting the number of particles crossing a particular Eulerian cell, dividing by the area of that cell, and normalising using the inlet particle density. The particle density is then known at the centre of each Eulerian cell. The Osiptsov Lagrangian method calculates the particle density directly along each particle pathline at each integration time-step. To produce the Osiptsov Lagrangian contour plots of figure 2.12, the particle density was interpolated onto the CFD mesh of quasi-streamlines and orthogonals. This was achieved, firstly by interpolating along pathlines to give a set of off-mesh values on each orthogonal, and then by interpolating along the orthogonals to give a set of on-mesh values, suitable for contouring. This independently developed method is very similar to that of Geller *et al.* (1993) (see appendix A.4).

Results for a particle flow with $St = 10$ are shown in figure 2.12 (a-d). The particles have high inertia and their pathlines are almost straight. Particles launched directly upstream of the cylinder deposit on the surface (a perfectly absorbing boundary is assumed) and a 'shadow-zone', devoid of particles, forms behind the cylinder. The Osiptsov Lagrangian solutions on either flow field show very good agreement. The traditional Lagrangian solutions deviate from each other, and from the Osiptsov Lagrangian solutions.

For $St = 1.0$ (figure 2.12 (e-h)), the particles follow the fluid streamlines more closely, resulting in pathline 'bunching' near the particle 'separation' point at the top of the cylinder. The shadow-zone is larger than before and there is a steep particle density gradient close to the 'separation pathline'. All the solutions show close agreement.

For $St = 0.1$ (figure 2.12 (i-l)), the particle separation point moves upstream. Agreement between the methods is still very good.

Figure 2.12 (m-p) shows the results for $St = 0.01$. This is a difficult test case because the particle pathlines deviate only slightly from the fluid streamlines, as indicated by the very small shadow-zone behind the cylinder. As for the $St = 10$ case, the Osiptsov Lagrangian solutions show very good agreement with each other, while the traditional Lagrangian solutions deviate from each other, and from the Osiptsov Lagrangian solutions.

Depending on the limits used in constructing contour plots, information may be obscured, and the results may be misleading. Therefore, figure 2.13 (a-d) shows plots of particle density at the outlet of the flow field (right hand side of plots in figure 2.12) for the different schemes used, over a range of Stokes numbers. In all cases, the Osiptsov Lagrangian calculations on a CFD and analytical flow field, are in close agreement, with slight differences occurring in the location of the beginning of the shadow-zone. This is a result of slight differences in the

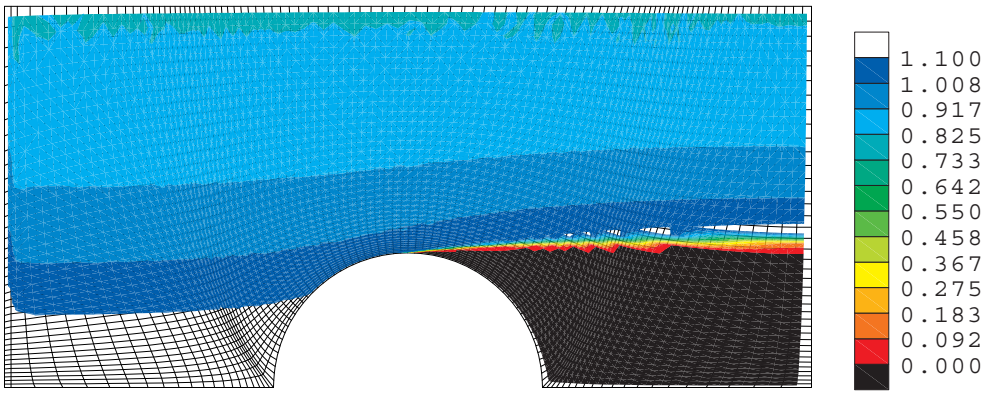

a) Stokes number = 10: traditional Lagrangian CFD solution

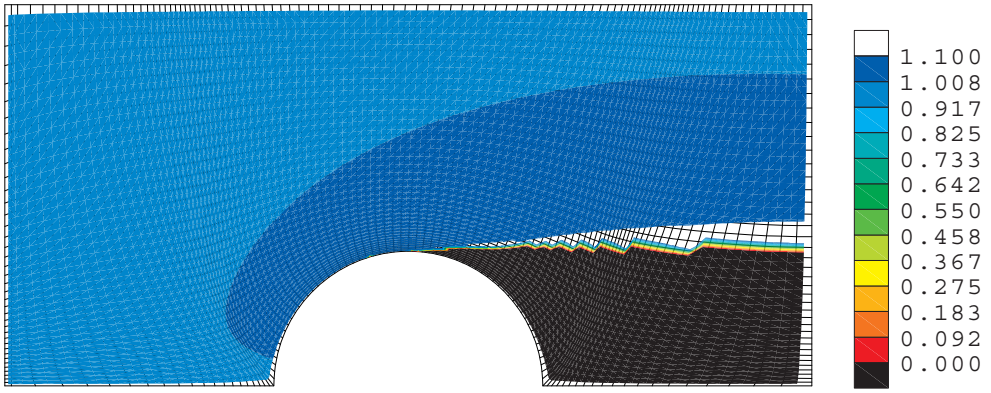

b) Stokes number = 10: Osiptsov Lagrangian CFD solution

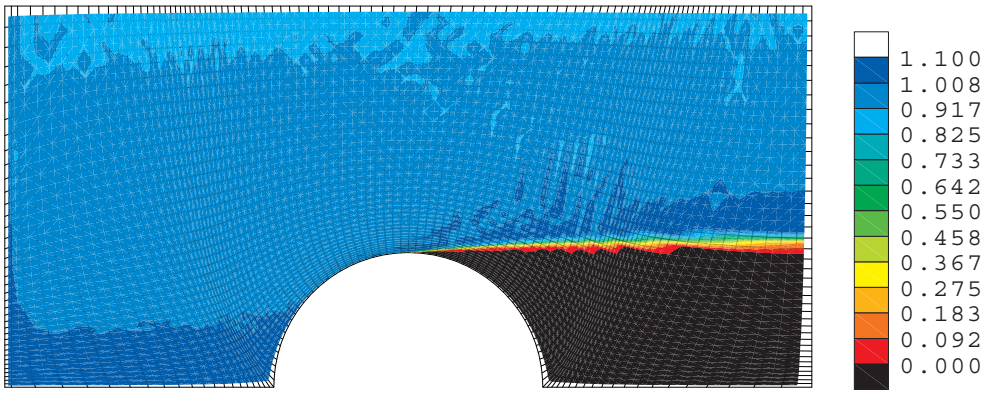

c) Stokes number = 10: traditional Lagrangian analytical solution

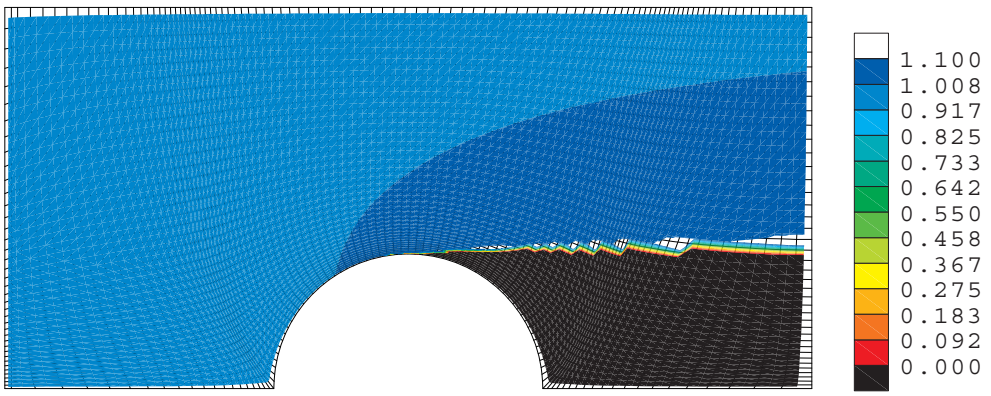

d) Stokes number = 10: Osiptsov Lagrangian analytical solution

Figure 2.12: Fluid-particle flow over a cylinder in two-dimensions - comparison between traditional Lagrangian and Osiptsov Lagrangian calculations using analytical and CFD solutions for the fluid flow field with St=10

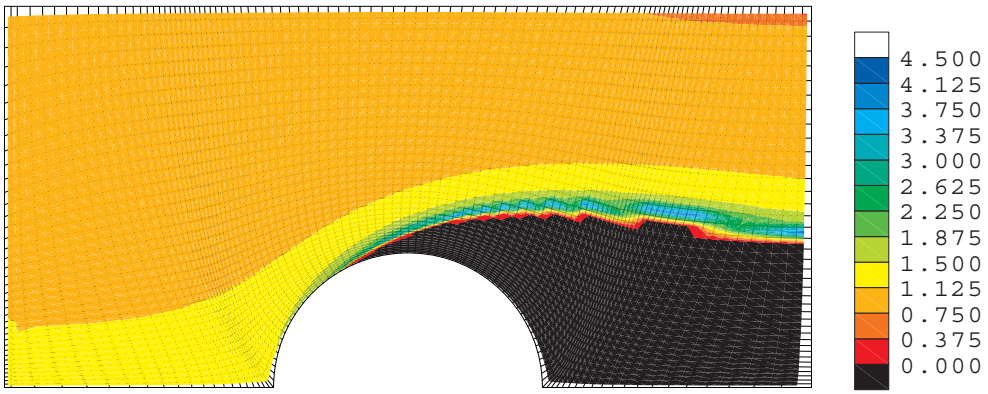

e) Stokes number = 1: traditional Lagrangian CFD solution

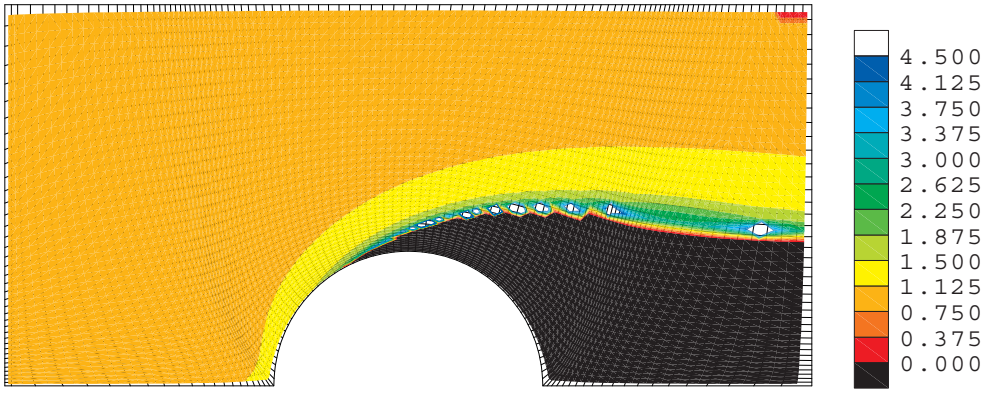

f) Stokes number = 1: Osiptsov Lagrangian CFD solution

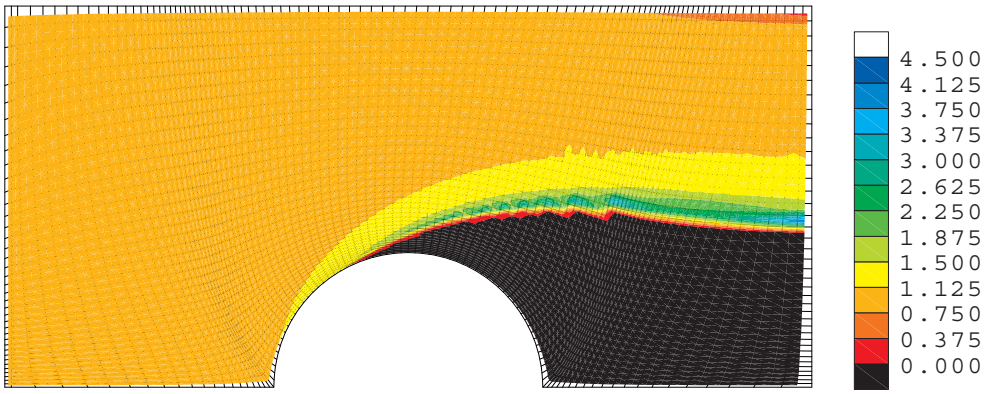

g) Stokes number = 1: traditional Lagrangian analytical solution

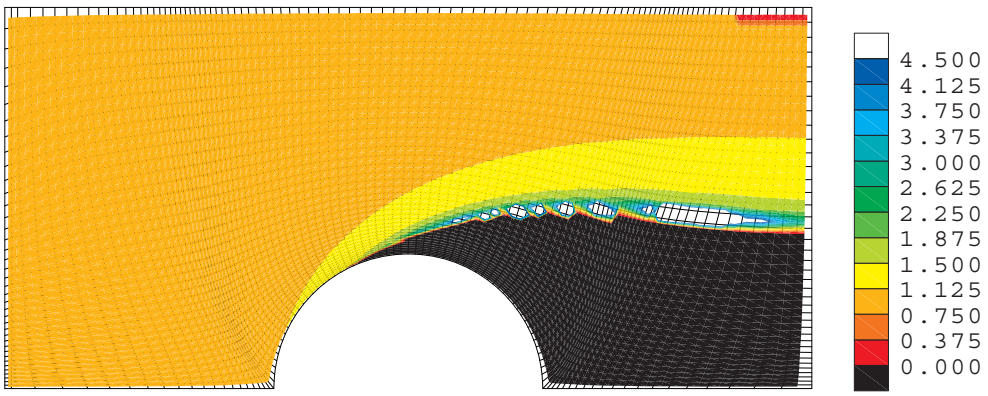

h) Stokes number = 1: Osiptsov Lagrangian analytical solution

Figure 2.12: Fluid-particle flow over a cylinder in two-dimensions - comparison between traditional Lagrangian and Osiptsov Lagrangian calculations using analytical and CFD solutions for the fluid flow field with St=1

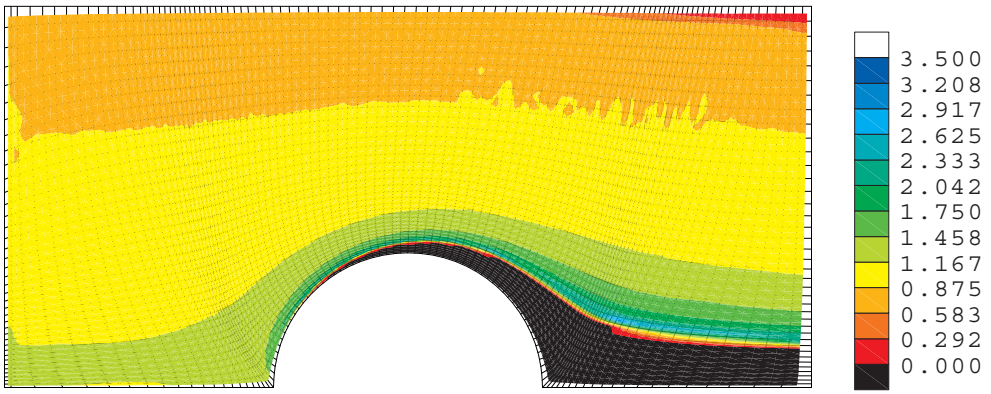

i) Stokes number = 0.1: traditional Lagrangian CFD solution

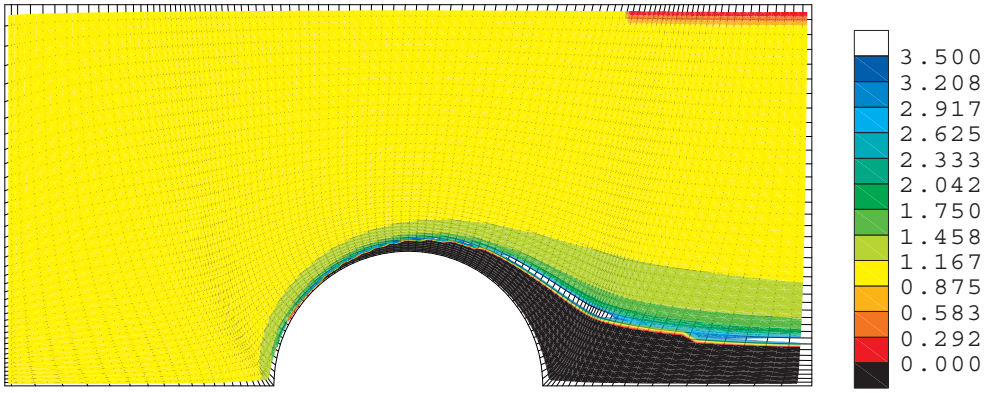

j) Stokes number = 0.1: Osiptsov Lagrangian CFD solution

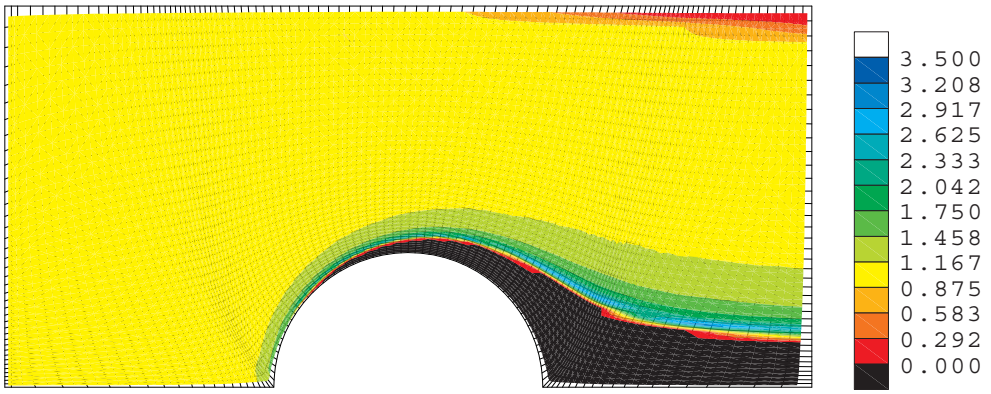

k) Stokes number = 0.1: traditional Lagrangian analytical solution

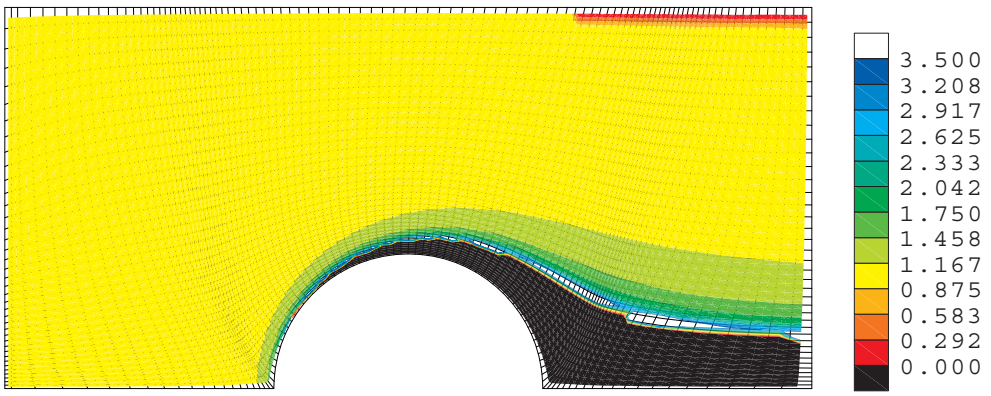

l) Stokes number = 0.1: Osiptsov Lagrangian analytical solution

Figure 2.12: Fluid-particle flow over a cylinder in two-dimensions - comparison between traditional Lagrangian and Osiptsov Lagrangian calculations using analytical and CFD solutions for the fluid flow field with St=0.1

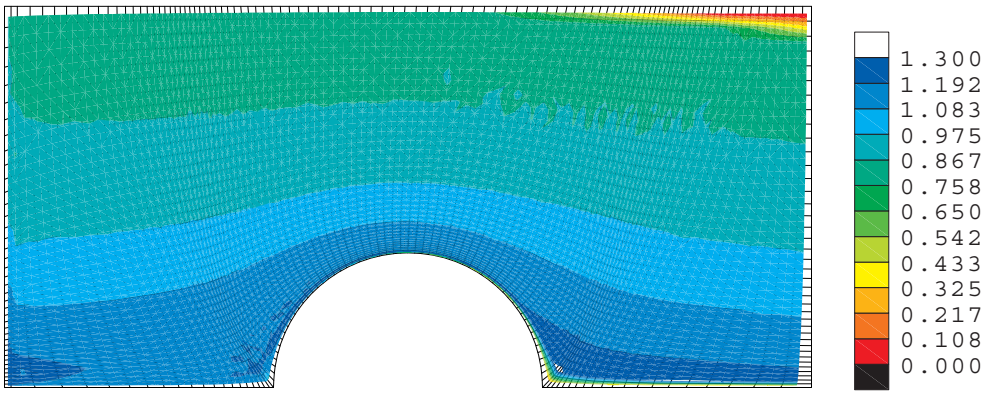

m) Stokes number = 0.01: traditional Lagrangian CFD solution

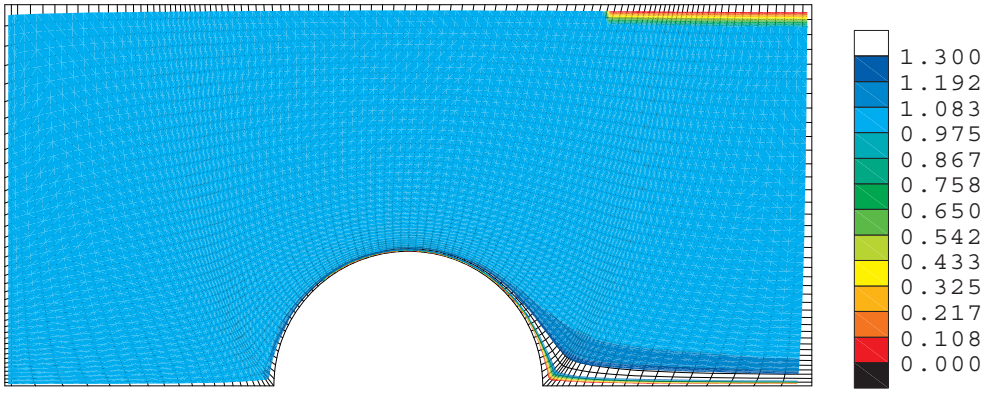

n) Stokes number = 0.01: Osiptsov Lagrangian CFD solution

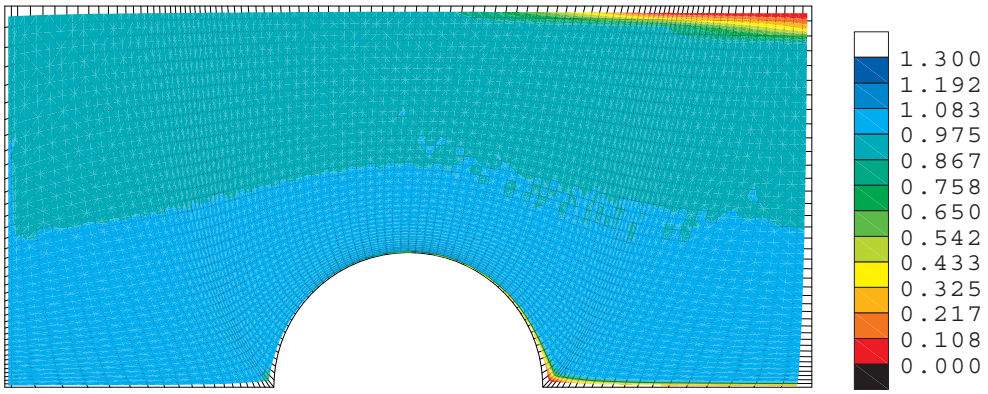

o) Stokes number = 0.01: traditional Lagrangian analytical solution

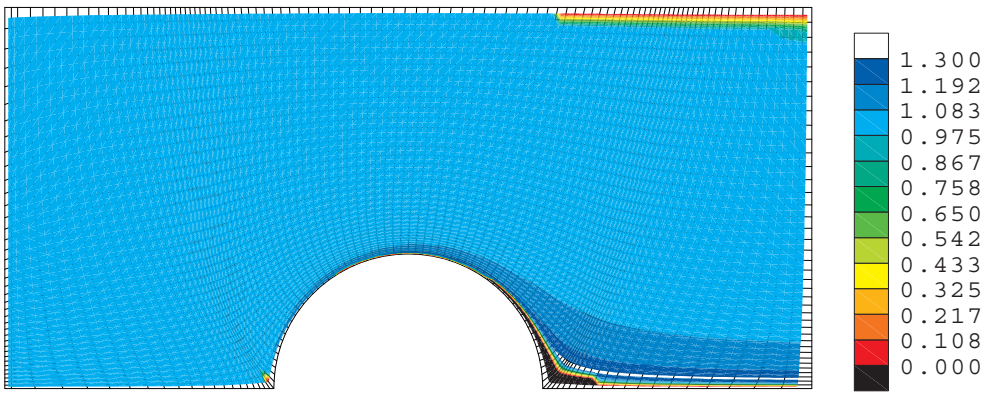

p) Stokes number = 0.01: Osiptsov Lagrangian analytical solution

Figure 2.12: Fluid-particle flow over a cylinder in two-dimensions - comparison between traditional Lagrangian and Osiptsov Lagrangian calculations using analytical and CFD solutions for the fluid flow field with St=0.01

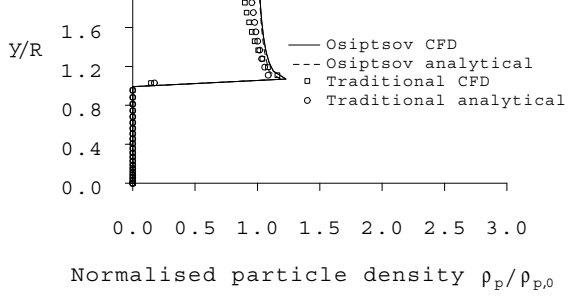

a) Stokes number = 10

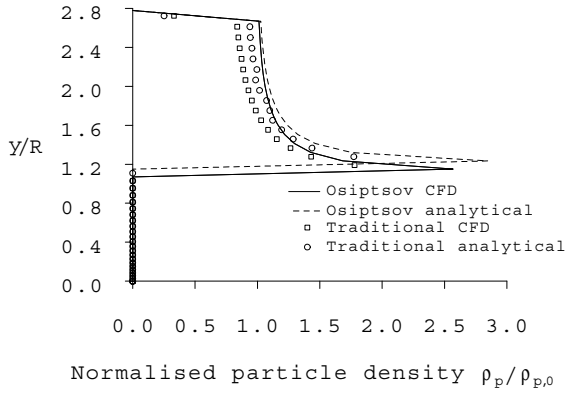

b) Stokes number = 1

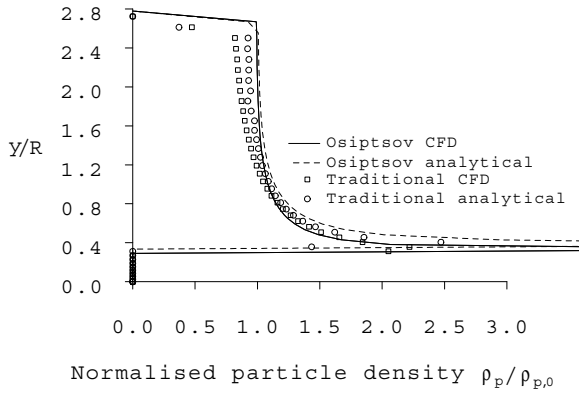

c) Stokes number = 0.1

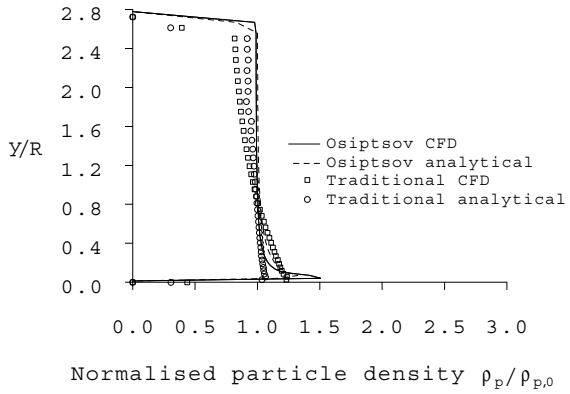

d) Stokes number = 0.01

Figure 2.13: Particle density profiles at outlet of flow field for fluid-particle flow over a cylinder - comparison between traditional Lagrangian and Osiptsov Lagrangian calculations using analytical and CFD solutions for the fluid flow field

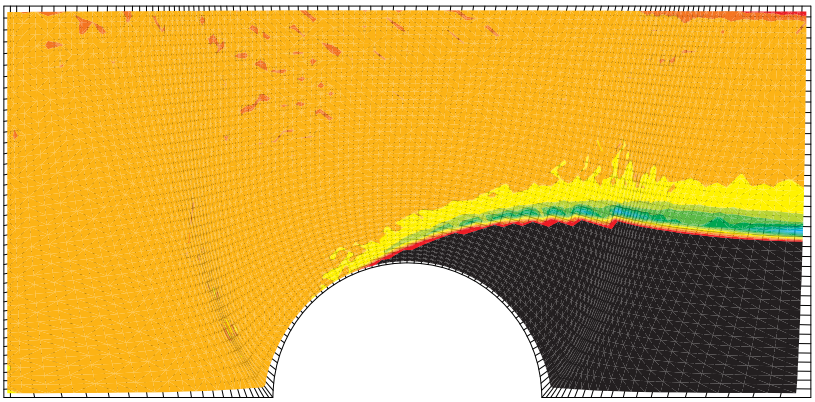

Figure 2.14: 'Noisy' particle density contour plot as a result of reducing the number of particles used in a traditional Lagrangian calculation for fluid-particle flow over a cylinder (analytical flow field with 200 particles and Stokes number = 1)

fluid flow fields, but agreement is close enough to support the use of the method when an analytical solution for the fluid flow is not available.

Using either method, there are differences between the solutions for the analytical and CFD flow fields, but more significantly there are greater differences between the traditional Lagrangian solution and the Osiptsov Lagrangian solution regardless of the flow field used. This will be shown to be as a result of the method of calculation of particle density.

2.5.4 Number of particles required for the calculation of the particle density field

The calculations presented in figures 2.12 and 2.13 were carried out using 500 particles for the Osiptsov Lagrangian method, compared to 10,000 for the traditional Lagrangian method. The number of particles chosen for the respective calculations was based on the minimum number required for the particle density to reach a stationary average, i.e. the number of particles that result in a particle density field that does not change with a further increase in the number of particles. The effect of using too few particles in a calculation is shown in the contour plot of figure 2.14, which is extremely 'noisy' compared to figure 2.12g, which is the equivalent case but with 10,000 particles instead of just 200.

Figure 2.15a shows particle density values at the outlet of the flow field, for the two methods using a range of particle numbers. The Osiptsov Lagrangian calculations of the previous section were carried out using 500 particles, but it can be seen that the result is unaffected when just 200 particles were used. The traditional Lagrangian calculations used 10,000 particles, and it can be seen that these results do not coincide with those for 200 and 500 particles. Above 10,000 particles, the solution was found to remain unaltered.

It has been established that the Osiptsov Lagrangian and traditional Lagrangian methods give solutions for particle density that differ from each other. Lagrangian calculations attempt

to solve for the particle properties at every point in a domain, but use a finite number of particle trajectories. The Osiptsov Lagrangian approach views the particle density between adjacent pathlines as being an intermediate value which can be estimated by interpolation. Thus an exact value of particle density can be found at any point. The traditional Lagrangian approach finds an average value for particle density in each Eulerian cell through which particles pass. Hence, the quality of the traditional Lagrangian solution is limited by the quality of the computational grid (i.e. the grid from the fluid flow calculation), even when large numbers of particles are used. By using an extremely fine grid with a very large number of particles passing through each cell, the traditional Lagrangian method should give the same result as the Osiptsov Lagrangian method. Such a hypothesis is difficult to test due to computational expense, but figure 2.15b examines the effect of doubling the number of y-direction grid cells. This has no effect on the Osiptsov Lagrangian solution. However, the traditional Lagrangian method (with twice as many particles to keep up with the increase in grid cells), gives a

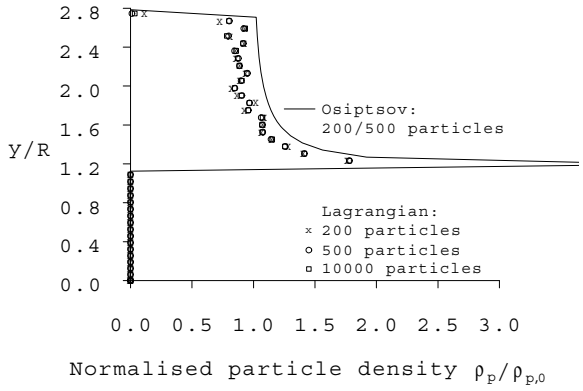

a) Particle density profiles at outlet of flow field - comparison between number of particles required for traditional Lagrangian and Osiptsov Lagrangian calculations

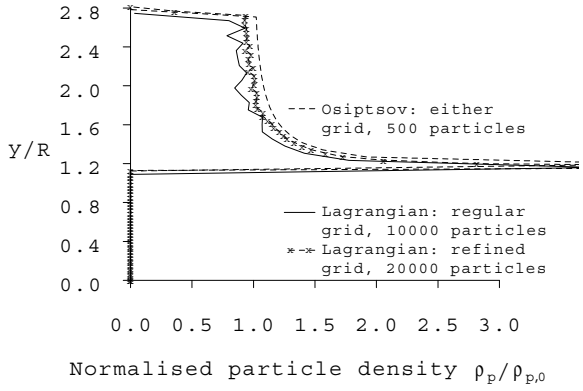

b) Particle density profiles at outlet of flow field - Comparison between traditional Lagrangian method using a more refined grid with Osiptsov Lagrangian and traditional Lagrangian methods on the original grid

Figure 2.15: The effect of particle numbers and computational grids on traditional Lagrangian and Osiptsov Lagrangian calculations using an analytical flow field for fluid-particle flow over a cylinder with Stokes number = 0.5

different result, that is much closer to the Osiptsov solution.

The Osiptsov Lagrangian method solves ten ordinary differential equations, while the traditional Lagrangian method solves just two. Hence, for the same number of particles, the Osiptsov Lagrangian calculation requires five times as much CPU time. However, it has been shown that the Osiptsov calculation can be performed accurately with just 200 particles, compared with 10,000 particles which are needed using the traditional calculation. This more than offsets the cost of the extra equations, with the result that the Osiptsov Lagrangian approach is almost ten times faster than the traditional Lagrangian approach, for two-dimensional problems. It should be pointed out that for this particular problem, the flow field is both incompressible and irrotational, so that (as pointed out in section 2.3) there are just six different ordinary differential equations to be solved using the Osiptsov method. In this case, the Osiptsov approach is therefore almost twenty times faster than the traditional Lagrangian approach. These savings would be even more pronounced in three-dimensions.

In summary, these calculations demonstrate that the Osiptsov Lagrangian method can be applied reliably using a CFD-generated fluid flow field. To highlight the accuracy and speed of this method, the particle density fields were calculated using the traditional Lagrangian method of computing a very large number of pathlines and applying an averaging procedure to those intersecting each Eulerian cell in turn. The CPU times for the Osiptsov method were less by factors ranging from ten to twenty, and gave a better quality solution. Further improvements in computational time could be achieved by use of an improved algorithm for locating the Eulerian grid cell in which the particle resides. Zhou & Leschziner (1999) recently developed a new algorithm that claims to be about 30% faster than the most efficient scheme available at that time.

2.6 Crossing particle pathlines

The ability to model crossing particle pathlines is a feature of Lagrangian methods and it is interesting to see how the Osiptsov method copes with such difficulties. It should be noted that the concern of this work is dilute suspensions of particles in fluid, and hence particle-particle interactions are neglected.

Several different types of pathline intersection can occur in 2-D flows. One example is when the distance between initially adjacent pathlines decreases to zero. This, of course, never happens with fluid streamlines, but particle pathlines are not restricted by the same continuity requirement. Intersecting pathlines do occur when the fluid velocity gradients enforce such behaviour, but only when the particles are of a small enough Stokes number to respond. At the crossing point itself, the Jacobian vanishes and the particle density becomes infinite. The Osiptsov Lagrangian method handles this well because, in actual computation, the Jacobian simply changes sign in passing through the crossing point (see figure 2.16). Osiptsov (1984) discusses a number of examples to illustrate different types of unbounded growth of particle density.

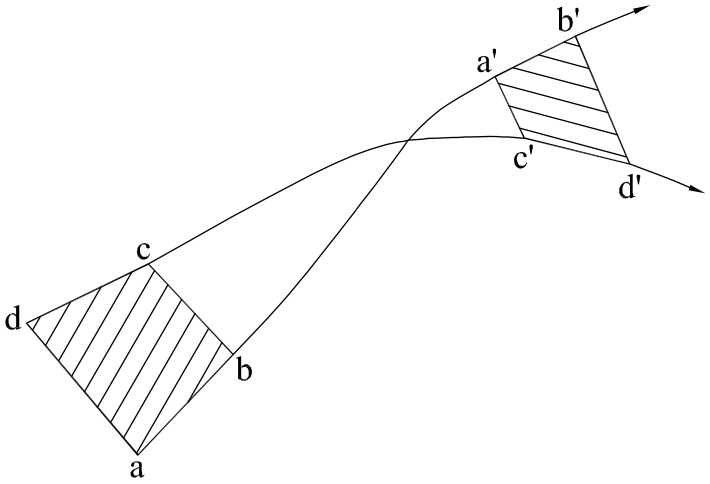

Figure 2.16: An element of 'particle fluid' compressing to zero and expanding as pathlines cross

2.6.1 Crossing particle pathlines in fluid-particle flow over a cylinder

When St is less than a critical value, St_{crit}, particles do not deposit on the cylinder surface. For a cylinder flow, $St_{crit} > 0.125$ (the value for stagnation-point flow) because the surface curvature acts to reduce deposition. It was found that deposition occurred for $St > 0.15$, but also that particles crossed (using either the Osiptsov or traditional Lagrangian approach) in the range $0.2 < St < 2$. However, there have been very few (if any) mentions of crossing particle pathlines in fluid-particle flow over a cylinder, despite the many studies that have been carried out (e.g. Fernandez de la Mora & Rosner, 1981; Geller *et al.*, 1993).

Figure 2.17 shows an example from fluid-particle flow over a cylinder of some initially adjacent particles which cross each other under the influence of fluid velocity gradients. Figure 2.17a is plotted with pathline 2 (used as a reference pathline) projected onto the abscissa. The centre of the cylinder is at $x/R = 3$ and the leading edge at $x/R = 2$, and $St = 0.2$. 200 particles were injected, and particle pathlines 1, 3, 4, 5, 6, 7 and 8 are plotted so that the ordinate represents their displacement from the reference pathline. Figure 2.17b has the same abscissa scale but the ordinate scale is expanded to show the trajectory intersections in greater detail.

Pathline 1 deviates downwards from the reference pathline before impacting the cylinder surface. The particle pathlines numbered 2, 3, 4 ,5 and 6 cross the trajectory that had initially been above them, and some of their other neighbouring trajectories. Pathlines 7 and 8 do not cross their upper neighbouring trajectories, although some other neighbouring trajectories are crossed.

Figure 2.17c shows the variation of the Jacobian along each particle pathline. The Jacobians of pathlines 7 and 8 approach zero, because they almost cross. The Jacobians of

pathlines which do cross, pass smoothly through zero (and the particle density becomes infinite) but only when a pathline passes one which had previously been located above it. The Jacobian of a pathline that crosses an additional neighbouring pathline does not pass through zero again. This behaviour can be expected, because the Jacobian was defined in terms of a very small element of 'particle fluid', which is consequently only 'aware' of its immediate neighbour. The decrease in J prior to crossing, and subsequent increase in J after crossing, raises questions on the analysis of Robinson (1956) (cited in Fernandez de la Mora & Rosner (1981)), and his result that the particle density cannot decrease (or the Jacobian cannot increase) along a particle pathline in a potential flow (see Healy & Young, 2003).

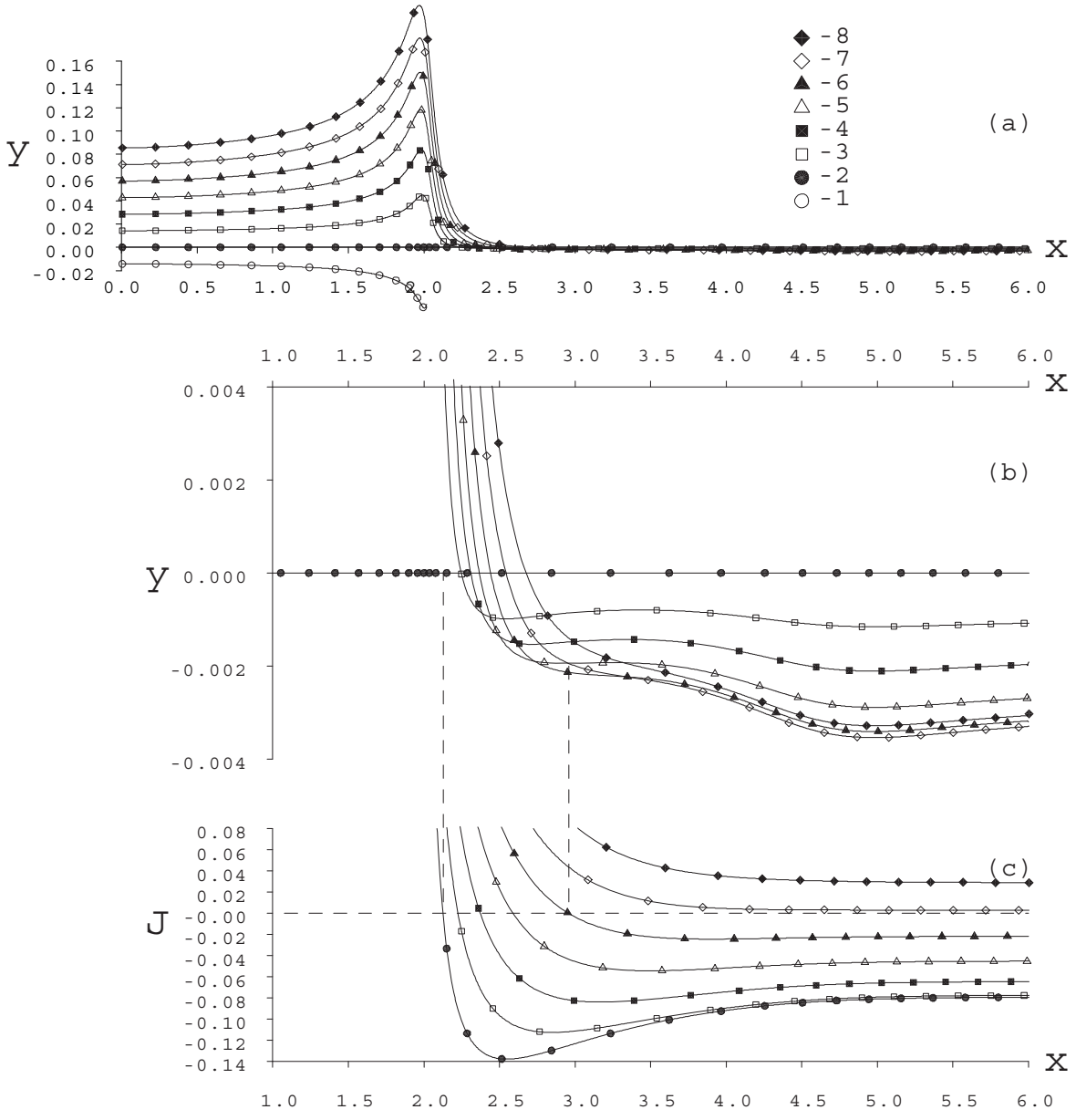

Figure 2.17: Crossing particle pathlines in fluid-particle flow over a cylinder (X=x/R)
a) Deviation y of pathlines 1 and 3-8 from the reference pathline 2
b) As a) but with an expanded ordinate scale
c) Corresponding behaviour of the Jacobian along each pathline

2.6.2 Some further examples of crossing particle pathlines

The crossing of particle pathlines in the previous section, was caused by the influence of fluid velocity gradients on particles of an intermediate Stokes number, which were initially adjacent to each other. Figure 2.18 shows two different types of pathline intersection, where non-neighbouring particles cross, under the influence of their inertia and initial injection velocities.

In figure 2.18a, two particle streams of low density intersect in a small region. The particles have large inertia (and so do not follow the fluid streamlines) which, combined with their prescribed initial velocities, causes the particle streams to intersect. Within the crossing region, the value of the particle density should be double that in the individual streams. The Osiptsov Lagrangian method, with the data processed as in the previous case, does not deal correctly with this situation. The failure to deal with this type of crossing pathline situation could have been expected from an examination of how non-neighbouring particles cross in figure 2.17.

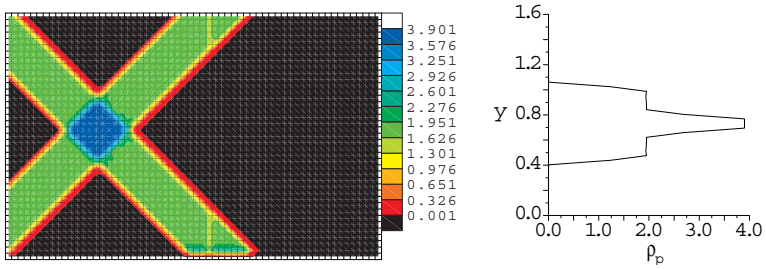

a) Particle density - intersecting, non-interacting particle streams, ρ_p doubles

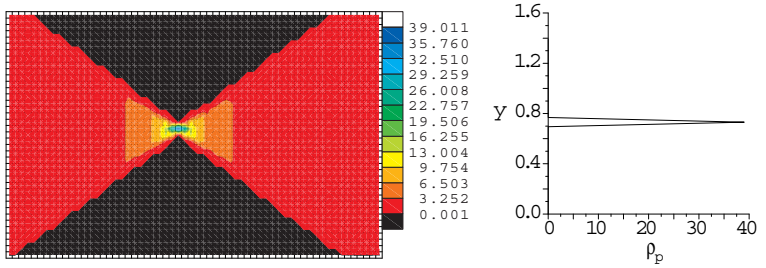

b) Particle density - intersecting, non-interacting particle pathlines, $\rho_p \to \infty$

Figure 2.18: Intersecting particle pathlines in two-dimensional flows

The plotting routine would need to be amended so that, if two particles share the same position, their respective values of particle density are added together. Computationally, it is very difficult to find an exact match in the position of any two particles, so a 'cell' would have to be placed around each particle, to determine coincidence of particles. A much easier method involves the use of a plotting routine similar to that used with the traditional Lagrangian method. The particle densities of every particle that crosses a particular Eulerian cell are added (with an extra contribution for each time-step across a particular cell), divided by the area of the cell, and normalised using the inlet particle density. The values of particle density are known exactly along each pathline, so plotting using this 'averaging' procedure still gives

a stationary solution for particle density, using as few particles as when the 'interpolative' plotting procedure is used. The results from such a plotting procedure can be shown to agree almost exactly with the results from the interpolative procedure for fluid-particle flow over a cylinder (using the Osiptsov Lagrangian approach), but with a slight loss in spatial resolution.

Figure 2.18a shows that the Osiptsov Lagrangian method (with the altered plotting routine) now deals with this situation correctly. Along each pathline, the Jacobian remains essentially constant but the procedure to interpolate the Lagrangian data onto the Eulerian grid recognises the existence of twice the number of pathlines within the crossing region with the result that the particle density is doubled as required (as can be seen from the cross-sectional plot of particle density taken through the crossing point of the particles, on the right hand side of figure 2.18a).

Figure 2.18b shows an extreme example of this type of flow. Particles with high inertia are injected along the inlet plane at varying angles with the intention that their pathlines intersect at the same point resulting in an infinite particle density. Computationally, a sharp density spike is generated. It has finite magnitude because of the finite number of pathlines used in the computation and the fact that the crossing point becomes a small crossing region in numerical reality. The correct behaviour is predicted with the inclusion of a certain amount of 'smoothing', as one would expect with any numerical scheme.

2.7 Flow through a turbine cascade

A more practical application of the Osiptsov Lagrangian method is that of gas-particle flow through a turbine cascade. The gas field was calculated using a viscous CFD solver developed by J.D. Denton at the Whittle Laboratory, Cambridge University. Figure 2.19 shows the particle density fields for $St = 1.0$ and 0.1. As expected, a shadow-zone forms behind the blade in both cases and the particle separation point is closer to the leading edge with greater pathline 'bunching' for $St = 0.1$.

A useful check on the accuracy of the calculations can be made in the limit $St \to 0$ when particle pathlines and gas streamlines coincide. Writing $\frac{D}{Dt}$ for the convective derivative, the Eulerian forms of the particle and gas continuity equations are,

$$\frac{D(ln\rho_p)}{Dt} + \nabla \cdot \vec{V} = \frac{D(ln\rho_g)}{Dt} + \nabla \cdot \vec{U} = 0 \tag{2.36}$$

which, in Lagrangian form with zero velocity slip, becomes,

$$\frac{\partial(ln\rho_p)}{\partial\tau} = \frac{\partial(ln\rho_g)}{\partial\tau} \tag{2.37}$$

Equation (2.37) can be integrated to give,

$$\frac{\rho_p}{\rho_{p,0}} = \frac{\rho_g}{\rho_{g,0}} \tag{2.38}$$

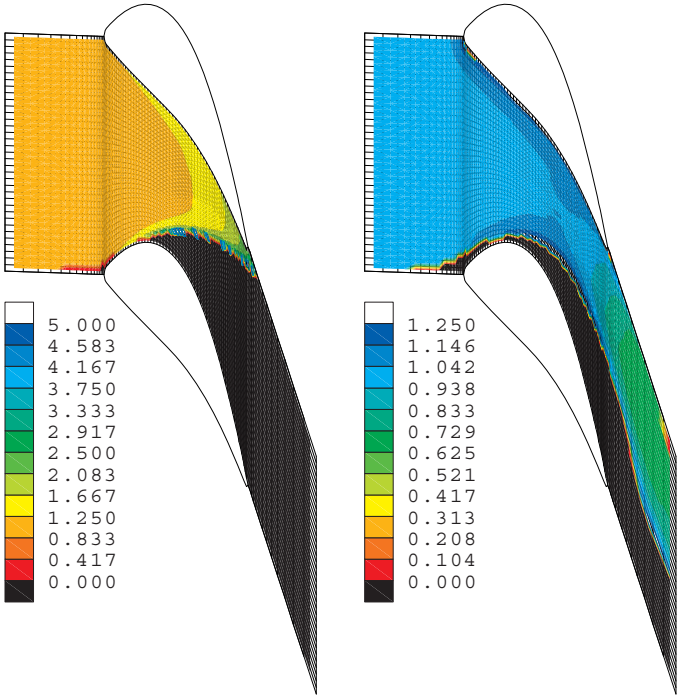

a) b)

Particle density fields for a) $St = 1.0$, and b) $St = 0.1$ (right)

Figure 2.19: Gas-particle flow through a turbine cascade

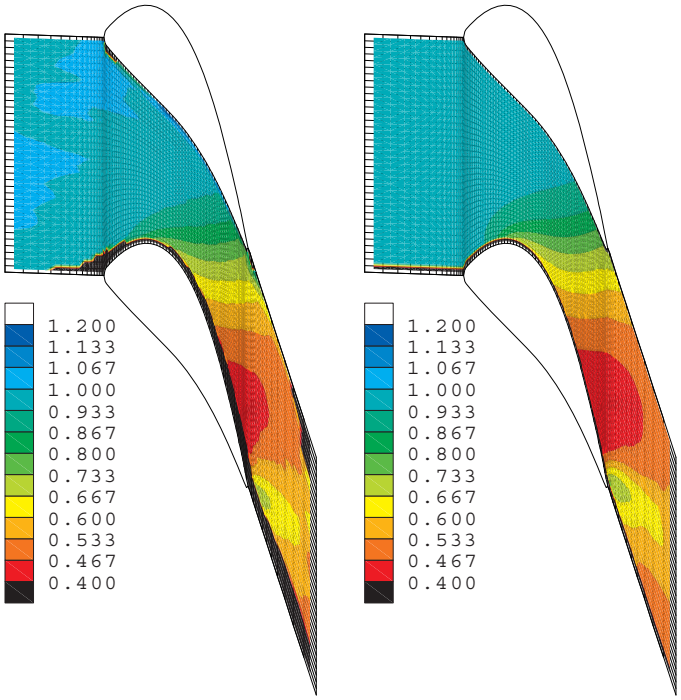

a) b)

Particle density fields for a) $St \cong 0$, and b) gas density field

Figure 2.20: A check on the accuracy of the calculations

which shows that, when suitably non-dimensionalised, the particle and gas density fields should be identical in the limit $St \to 0$. For the flow through the turbine cascade, the exit Mach number was 1.12, which results in significant variations in gas density. A comparison between the gas and particle density fields at very low Stokes number therefore provides a sensitive test of computational accuracy. Figure 2.20 shows that the Osiptsov Lagrangian method performs well in this respect.

2.8 Conclusions

The theory and calculations presented in this chapter have shown that Osiptsov's elegant Full Lagrangian approach for calculating the particle density field in two-dimensional non-turbulent flows has great potential for dramatic reductions in computational time and improvements in accuracy. A special technique has been developed for flows at low Stokes number which relieves the mathematical stiffness of the equations and allows their solution to proceed without increase in CPU time. It has been established that Osiptsov's method can be used with CFD-generated flow fields and a procedure for calculating the spatial velocity derivatives from 'noisy' velocity fields without introducing unacceptable errors has been developed. Particle density calculations in three-dimensional flows, a target previously precluded by prohibitive computational expense, now appear feasible.

Part II

Chapter 3

Literature Review

3.1 Introduction to dispersed two-phase flows

Various forms of multiphase flows are encountered in industrial applications, such as convective boiling, separated flows where the component phases may be considered continuous (such as slug flow and film flow), and dispersed two-phase flows consisting of particles or droplets in a continuous carrier phase (gas or liquid). Dispersed gas-particle flows (such as ash particles in air flowing through a gas turbine) are the concern of this work.[†]

The first aim of this chapter is to define the scope of the investigation that has been undertaken, and to provide an explanation of the various particle transport mechanisms that will be encountered in later chapters. Fully-developed turbulent pipe flow features all of these mechanisms, and in order to obtain as much understanding as possible from the pipe (and annulus) flow experiments that will be presented later, a comprehensive review of previous experimental studies is undertaken. The focus of the turbulent annulus experiments is to investigate the transport mechanism of thermophoresis, which is the phenomenon whereby small particles suspended in a gas in which there exists a temperature gradient, experience a force in the direction opposite to that of the temperature gradient. Accordingly, a detailed assessment is made of the theoretical and experimental studies that have been carried out on thermophoresis, in order to establish the need for such experiments and to appreciate the strengths and weaknesses of the available theories.

There are a number of different properties used for the characterisation of dispersed two-phase flows. The dispersed phase volume fraction is the limit of the ratio of the particulate phase volume to the total volume:

$$c_d = \lim_{\delta V \to \delta V^0} \frac{\delta V_{dp}}{\delta V} \tag{3.1}$$

where V_{dp} is the volume of the dispersed (particulate) phase, and δV^0 is the limiting volume.

[†]In this introduction, many of the statements made with regard to a 'particle' may also be applied to a 'droplet'.

The continuous (fluid) phase volume fraction c_c may be similarly defined by the use of V_c, the volume of the continuous phase, in place of V_{dp}. These definitions involve averaging over a volume, as that volume approaches zero. Crowe (1982) points out that for a gas-particle flow, the limiting volume must be large enough to contain sufficient particles to obtain a stationary average. However, the dimension of the limiting volume must also be many times smaller than the characteristic dimension of the flow, in order for the volume to be treated as a 'point' and the dispersed phase to be treated as a 'continuum'.

The particle phase bulk density (subsequently referred to as the particle density) is the mass of the particulate phase per unit volume of the mixture, and may be expressed in terms of its volume fraction and material density ($\rho_{p,mat}$), such that:

$$\rho_p = c_d \rho_{p,mat} \tag{3.2}$$

The continuous (fluid) phase bulk density is given by:

$$\rho_c = c_c \rho_g \tag{3.3}$$

where ρ_g is the density of the continuous phase (g is used as the continuous phase in this work is a gas).
The particle mass ratio (Crowe *et al.*, 1998) is then defined as:

$$C = \frac{\rho_p}{\rho_c} \tag{3.4}$$

A suspension of particles in a fluid may be described as dilute if the particles have no interaction with each other. At high mass loadings, the particles interact with each other in what is considered a dense suspension. According to Elghobashi (1994), a dispersed two-phase flow may be considered dilute if $c_d < 10^{-3}$. If the condition $c_d < 10^{-6}$ also holds, then the interaction between the particle and fluid phases constitutes a 'one-way coupling', as the fluid phase is not affected by the presence of the particles. When $10^{-6} < c_d < 10^{-3}$, 'two-way coupling' is said to exist. There is sufficient momentum transfer between the phases for the motion of the fluid phase to be altered by the presence of the particles. For $c_d > 10^{-3}$, the flow is considered dense, and there is a 'four-way coupling' consisting of two-way coupling between the phases as well as further coupling due to momentum transfer within the particulate phase, i.e. particle-particle collisions.

However, a theoretical prediction of the relative significance of particle-particle collisions and the reverse effect of the particle phase on the carrier gas by Tsirkunov (2001), shows that particle-particle collisions become important at volume fractions almost ten times lower than those at which two-way coupling becomes important. This implies that the use of a two-way coupling model, together with a collisionless particle phase, is physically incorrect.

The dispersed gas-particle flows of concern to this work may be classified by using the low mass ratio criterion proposed by Johansen (1991), and making reference to the experiments

of Fackrell *et al.* (1994). Johansen (1991) found that when $C \ll 1$, the flow is dilute and one-way coupling may be assumed. Fackrell *et al.* (1994) investigated particle deposition in a coal-fired gas turbine, representative of the flows of interest to this work. The gases from the combustor were first cleaned with a cyclone system to reduce particulate loading. Particles of 10 to 20 μm passed through this clean-up, and the resulting total dust loading was 100 parts per million by weight (ppmw). The low mass loading of such flows means that in the work to follow, the influence of particles on the fluid phase can be considered negligible, and that particle-particle interactions can also be neglected (i.e. the flow is dilute with one-way coupling).

3.1.1 Particle response times

The non-dimensional parameters used to characterise a flow are often defined in terms of the response time of a particle or droplet to changes in flow velocity or temperature. Assuming Stokes flow, the particle momentum response time (or inertial relaxation time) is defined by:

$$\tau_p = \frac{\rho_{p,mat} d_p^2}{18 \mu_g} \tag{3.5}$$

where d_p is the particle diameter, and μ_g is the gas dynamic viscosity. The particle momentum response time is the time required for a particle released from rest in a uniform flow to achieve 63% $(1 - \frac{1}{e})$ of the flow velocity. Although Stokes flow may not apply, τ_p (as defined by equation 3.5) is, nevertheless, used to non-dimensionalise data. The thermal response time (once more assuming Stokes flow) is:

$$\tau_{p,T} = \frac{\rho_{p,mat} c_p d_p^2}{12 k_g} \tag{3.6}$$

where c_p is the specific heat capacity of the particle material, and k_g is the thermal conductivity of the gas. In gases, the thermal response time is of the same order of magnitude as the momentum response time (because the Prandtl number $\cong 1$), hence the assumption of one-way coupling between gas and particle momentum equations also holds good for the energy equations. In any case, the particle conservation of energy equation can usually be omitted from consideration, particularly when the differences in temperature between particle and gas are slight.

By choosing some characteristic fluid time-scale τ_f, the Stokes number may be defined as:

$$St = \frac{\tau_p}{\tau_f} \tag{3.7}$$

τ_f is a time-scale which reflects temporal rates of change of the fluid, and may be chosen in a number of ways, depending on the fluid flow conditions (e.g. a laminar or turbulent gas time-

scale). For $St \ll 1$, the response time of the particles is much less than the characteristic time-scale of the fluid, giving them plenty of time to respond to changes in fluid velocity, and resulting in an inter-phase slip velocity approaching zero. If $St \gg 1$, the particles have significant inertia, which impedes their response to the changing fluid flow field, and the particle phase develops a velocity relative to the fluid phase.

Gas-particle flows may be observed in two ways. By choosing a stationary point and observing the particles as they move past it, an Eulerian view of the flow may be taken. However, a reference point which moves with a particle may also be chosen, so that the observer follows the same path as the particle and is given a Lagrangian view of the flow. In the modelling of gas-particle flows, it is necessary to adopt either an Eulerian or a Lagrangian description, and, as was shown in chapter 2, the Stokes number of the particles will largely determine which description is more appropriate.

3.2 Particle transport in laminar flows

3.2.1 The drag force on a particle

The steady-state viscous drag force on a particle is related to the relative velocity between the particle and the fluid. The particle Reynolds number is defined as:

$$Re_p = \frac{d_p|\mathbf{u}-\mathbf{v}|}{\nu_g} \tag{3.8}$$

where $\mathbf{u}$ and $\mathbf{v}$ are the fluid and particle velocities, and ν_g is the gas kinematic viscosity. When a particle moves relative to a gas, vorticity is generated at its surface. For very low values of Re_p, energy is dissipated by viscosity. In the viscous limit, as $Re_p \to 0$, the Navier-Stokes equation can be linearised and solved. The drag force in this limit is known as Stokes drag.

In the limit as $Re_p \to 0$, the equation of motion for a small rigid sphere in a viscous quiescent fluid is the Basset-Boussinesq-Oseen (BBO) equation. Crowe *et al.* (1998) expressed it as:

$$\begin{aligned} m_p\frac{d\mathbf{v}}{dt} =& \overbrace{3\pi d_p\mu_g(\mathbf{u}-\mathbf{v})}^{\text{Stokes drag}} + \overbrace{V_p(-\nabla p + \nabla\tau)}^{\text{pressure gradient \& shear stress}} + \overbrace{\frac{\rho_g V_p}{2}\frac{d}{dt}(\mathbf{u}-\mathbf{v})}^{\text{virtual mass}} \\ &+ \underbrace{\frac{3}{2}d_p^2\sqrt{\pi\rho_g\mu_g}\int_0^t \frac{(\mathbf{u}-\mathbf{v})}{\sqrt{t-t'}}dt'}_{\text{Basset history}} + \underbrace{m_p\mathbf{g}}_{\text{gravity}} \end{aligned} \tag{3.9}$$

where m_p is the mass of a single particle, V_p is the particle volume, p is the pressure and τ is the shear stress in the vicinity of the particle, and $\mathbf{g}$ is the gravitational acceleration. The Faxen relations accounting for velocity curvature have been neglected. The pressure gradient and shear stress terms are related to the fluid acceleration and gravitational force so that equation 3.9 becomes:

$$\left(1+\frac{1}{2}\frac{\rho_g}{\rho_{p,mat}}\right)\frac{d\mathbf{v}}{dt} = \frac{18\mu_g}{\rho_{p,mat}d_p^2}(\mathbf{u}-\mathbf{v}) + \frac{3}{2}\frac{\rho_g}{\rho_{p,mat}}\frac{d\mathbf{u}}{dt} + \left(\frac{9}{2\pi\tau_p}\frac{\rho_g}{\rho_{p,mat}}\right)^{\frac{1}{2}}\int_0^t \frac{(\mathbf{u}-\mathbf{v})}{\sqrt{t-t'}}dt' + \left(1-\frac{\rho_g}{\rho_{p,mat}}\right)\mathbf{g} \tag{3.10}$$

The ratio of the gas phase density to the particle material density is often small in gas-particle flows (e.g. for a particle of uranine and oleic acid in air, as used in the pipe (and annulus) flow experiments to be described later, $\rho_g/\rho_{p,mat} \approx 10^{-3}$), and under these circumstances equation 3.10 may be simplified to:

$$\frac{d\mathbf{v}}{dt} = \frac{18\mu_g}{\rho_{p,mat}d_p^2}(\mathbf{u}-\mathbf{v}) + \mathbf{g} = \frac{(\mathbf{u}-\mathbf{v})}{\tau_p} + \mathbf{g} \tag{3.11}$$

This is the origin of the definition of particle inertial relaxation time (equation 3.5). As $Re_p \to 0$,

$$\mathbf{f}_D = 3\pi d_p \mu_g (\mathbf{u}-\mathbf{v}) \tag{3.12}$$

where $\mathbf{f}_D$ is the drag force on the particle. The Stokes drag coefficient for small Re_p is then defined as:

$$C_D = \frac{|\mathbf{f}_D|}{\frac{1}{2}\rho_g|(\mathbf{u}-\mathbf{v})|^2\frac{\pi}{4}d_p^2} = \frac{24}{Re_p} \tag{3.13}$$

When a particle moves relative to a gas with a finite Re_p, eddies are formed in the region behind the particle. As a result, the pressure (or form) drag on the particle increases and the drag force is larger than that predicted by the expression for Stokes drag. The Stokes expression can be extended to finite Re_p, however, by using an empirical curve fit to experimental data for the drag coefficient, to account for the increase in total drag (Morsi & Alexander, 1972). The drag term over the range of particle Reynolds numbers ($0 < Re_p < 50000$) is:

$$\mathbf{F}_D = \frac{\phi_D(Re_p)}{\tau_p}(\mathbf{u}-\mathbf{v}) \tag{3.14}$$

where $\mathbf{F}_D$ is the drag force per unit mass on the particle, and $\phi_D(Re_p)$ is a correction containing an empirical curve fit to experimental data for C_D [$\phi_D(Re_p) = C_D(Re_p/24)$], details of which can be found in appendix B.1.

When the molecular mean free path of the gas molecules (λ_g) becomes comparable with the linear dimension of a particle (its radius r_p), the gas becomes rarefied with respect to the particle. The extent of this rarefaction is given by the particle Knudsen number, $Kn = \lambda_g/r_p$. Stokes drag was derived in the limit of $Kn \to 0$, where there is no slip between the gas and the surface of the particle. This is not the case when $Kn \approx 1$, and the gas then slips relative

to the surface of the particle. The drag on such a particle will be less than that predicted by Stokes drag, so equation 3.14 must be altered to take account of this. An accurate empirical correction factor, is that derived by Cunningham (1910):

$$\mathbf{F}_D = \frac{\phi_D(Re_p)}{\tau_p C_c}(\mathbf{u} - \mathbf{v}) \quad \text{where} \quad C_c = (1 + 1.35Kn) \tag{3.15}$$

The expression used for C_c is not Cunningham's original expression, but an approximate curve fit to more refined kinetic theory.

The assumption of a spherical particle in a uniform flow and in a domain of infinite extent has been made in the derivations described above. A particle in a flow near a planar surface, will find itself in a simple shear flow, with the velocity varying from its free-stream value to zero at the wall. The numerical results of Dandy & Dwyer (1990) show that the drag force is independent of the presence of a wall. However, the particle in the shear flow will not only experience a drag force acting parallel to the direction of its motion relative to the flow; there will also be a force due to shear, which acts perpendicular to the relative motion, known as the lift force.

3.2.2 The lift force on a particle

Particles moving in a shear flow experience a non-uniform relative velocity and consequently, a non-uniform pressure distribution. The resultant force acts in the transverse direction and is called the Saffman lift force. There will also be a Magnus lift force due to the rotation of the particle. Saffman (1965) showed that the force due to rotation was an order of magnitude less than that due to shear, for small particle Reynolds numbers.

Saffman (1965, 1968) found that the lift force on a small sphere in an unbounded slow shear flow was given by:

$$m_p \mathsf{F}_L = 1.61 \mu_g d_p |u - v| \sqrt{Re_{sh}}, \qquad Re_{sh} = \frac{d_p^2}{\nu_g} \frac{du}{dy} \tag{3.16}$$

where F_L is the lift force per unit mass on the particle, and Re_{sh} is the shear Reynolds number, based on the fluid velocity change in a distance d_p. Figure 3.1 shows two particles suspended in a gas flowing downwards in a vertical pipe. One particle leads the gas while the other lags behind it. It can be seen that the particle leading the gas experiences a force towards the pipe wall, while the particle lagging the gas experiences a force away from the pipe wall. Saffman's expression was only valid when $Re_p \ll Re_{sh}$, and both Re_p and Re_{sh} are small compared to unity.

McLaughlin (1989) performed a DNS study of olive oil droplets in turbulent air flowing vertically between two parallel walls which showed that the condition of $Re_p \ll Re_{sh}$ was rarely satisfied. In his study, Re_{sh} was of the order 0.04, and Re_p was of the order unity. McLaughlin (1991) removed this restriction of Saffman's expression, and Dandy & Dwyer

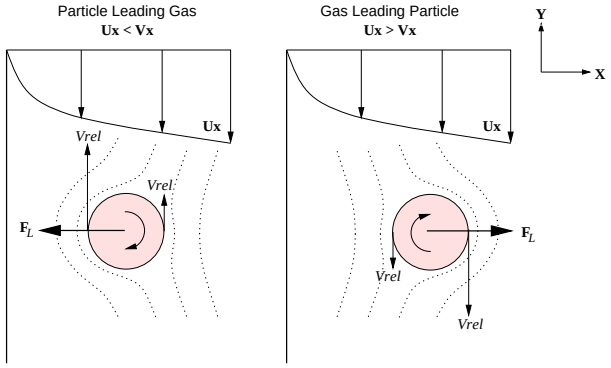

Figure 3.1: The effect of lift on a particle lagging or leading the fluid in a vertical pipe

(1990) extended its validity up to $Re_p = 100$. Mei (1992) produced a curve fit incorporating both of these improvements (see appendix B.2). For a pipe flow, equation 3.16 may be rewritten as (Slater *et al.*, 2003):

$$\mathsf{F}_{L,y} = 0.725 \left(\frac{\rho_g}{\rho_{p,mat}} \tau_p \frac{\partial u_x}{\partial y} \right)^{1/2} \frac{(u_x - v_x)}{\tau_p} \tag{3.17}$$

Studies have also been carried out on the lift force acting on a particle in a wall-bounded shear flow, and Wang *et al.* (1997) found that accounting for the wall had the effect of reducing the lift force predicted using the Saffman expression by a factor of three.

3.2.3 Thermophoresis

Small particles suspended in a gas in which there exists a temperature gradient, will experience a force in the opposite direction to that of the temperature gradient, and this behaviour is known as thermophoresis. Gas molecules impinging obliquely on the particle surface deliver more tangential momentum if they arrive from a hotter region of the flow, than those arriving from a cooler region. This unequal momentum transfer leads to the gas exerting a shear stress on the particle which accelerates it towards the cooler region. The particle exerts an equal and opposite shear stress upon the gas, so that in the region adjacent to the particle surface, there is a flow in the opposite direction. This is known as thermal creep.

Modern industrial gas turbines may have mean free-stream temperatures of up to 1420 °C, but material considerations require that the turbine blade temperature does not rise to much higher than 800 °C. The cooling techniques implemented to meet this requirement result in huge temperature gradients in the boundary layer adjacent to the blade surface, and the resulting thermophoretic force may be so large that thermophoresis becomes the dominant deposition mechanism for small particles.

The thermophoretic force per unit mass ($\mathbf{F}_{TH}$) on a spherical particle is given by:

$$m_p \mathbf{F}_{TH} = -\eta_{TH} \nabla (lnT) \tag{3.18}$$

where T is the absolute temperature of the surrounding gas and η_{TH} is the coefficient of thermophoresis. It should be noted that η_{TH} has the dimensions [kgm^{2}s^{-2}]. A dimensionless thermophoretic coefficient may be defined as:

$$K_{TH} = \frac{\eta_{TH} \tau_p}{\nu_g m_p} \tag{3.19}$$

This allows the thermophoretic force per unit mass to be written as:

$$\mathbf{F}_{TH} = \frac{K_{TH} \nu_g}{\tau_p} \nabla (lnT) \tag{3.20}$$

Thermophoresis is central to this work, and the determination of η_{TH} will be examined in much greater detail later in this chapter. η_{TH} is the thermophoretic coefficient commonly used in the literature, and is used in place of the dimensionless K_{TH} to enable comparison.

3.2.4 Brownian motion

In a laminar gas flow, the transport of particles is determined by the drag, lift and thermophoretic forces. Small particles in particular will follow the fluid streamlines almost exactly. If the particles are extremely small, however, they will respond to the random collisions of the gas molecules, and this gives rise to a diffusive transport mechanism known as Brownian diffusion. The result is a net transport of particles, from regions of high particle density to regions of low particle density.

Fick's law of diffusion relates the mass flux of particles, $\mathbf{J}_B$, to the particle density gradient, $\nabla \rho_p$:

$$\mathbf{J}_B = -D_B \nabla \rho_p \tag{3.21}$$

where D_B is the coefficient of particle Brownian diffusion. A large value of D_B represents more vigorous Brownian motion and more rapid mass transfer in a gradient of particle density. Einstein's treatment of diffusion as a random walk (see Kennard, 1938, pg. 286) resulted in the determination of the coefficient as:

$$D_B = kTB \tag{3.22}$$

where k is Boltzmann's constant, T is the absolute temperature of the surrounding gas, and $B = \tau_p / m_p$ is the dynamic mobility of the particle, which may include Cunningham's correction factor in the case of a rarefied gas.

Ramshaw (1979) considered Brownian motion in relation to the partial pressure of the

particle phase, p_p, associated with the random thermal movement of the particles. Assuming that the particles and gas are in thermal equilibrium, equipartition of energy gives:

$$p_p = n_p kT = \frac{\rho_p kT}{m_p} \tag{3.23}$$

where n_p is the number of particles per unit volume. Hence:

$$\nabla p_p = \frac{kT}{m_p}\nabla\rho_p + \frac{k\rho_p}{m_p}\nabla T = \frac{kT}{m_p}\nabla\rho_p + \frac{kT\rho_p}{m_p}\nabla(lnT) = \frac{D_B}{\tau_p}\Big(\nabla\rho_p + \rho_p\nabla(lnT)\Big) \tag{3.24}$$

The $\nabla(lnT)$ term will tend to create a net particle drift down a temperature gradient, but it is neglected as this flux is about five orders of magnitude smaller than that associated with thermophoresis. The Brownian force per unit mass is now given by:

$$\mathbf{F}_B = -\frac{D_B}{\tau_p}\nabla(ln\rho_p) \tag{3.25}$$

The laminar particle Schmidt number relates the gas kinematic viscosity, ν_g, to the particle diffusivity, D_B:

$$Sc = \frac{\nu_g}{D_B} \tag{3.26}$$

The particle diffusivity is many orders of magnitude less than the gas kinematic viscosity, reflecting the greater mobility of the gas molecules, and resulting in $Sc \gg 1$. Typically, particles in air may have Schmidt numbers of $10^4 \sim 10^6$. In a pipe flow, deposition due to Brownian motion will consequently lead to localised reduction of particle density, only in a very thin region adjacent to the pipe wall. In the limit of $D_B \to 0$, the thickness of the particle density boundary layer will tend to zero, and no deposition will occur. It will later be shown that the dimensionless deposition velocity of very small particles depositing under the influence of Brownian motion depends only on the particle Schmidt number.

3.3 Particle transport in turbulent flows

In a turbulent flow, the mechanisms of particle transport that occur in a laminar flow will all be present, in addition to some others caused by the turbulence. The random interactions of a particle with turbulent eddies is somewhat similar to the random molecular collisions of Brownian motion. This has led to a modified version of Fick's law of diffusion being used to describe the transport of particles in a turbulent flow, known as the 'gradient diffusion' model. The turbulent mass flux of particles is then assumed to be given by:

$$\mathbf{J}_T = -D_T\nabla\rho_p \tag{3.27}$$

where D_T is the coefficient of particle turbulent diffusion.

When the particles are very small, they follow the turbulent eddies almost exactly. The diffusion of particles is essentially the same as the diffusion of large molecules, and the model of simple Fickian diffusion is valid. In these circumstances, it is a good approximation to assume that the turbulent particle Schmidt number ($Sc_T = \nu_{g,T}/D_T$) is about unity, i.e. $D_T \cong \nu_{g,T}$, where $\nu_{g,T}$ is the turbulent kinematic viscosity (eddy viscosity) of the gas.

As the particles become larger, however, the effect of particle inertia becomes important and the model of simple Fickian diffusion is no longer realistic. A particle with significant inertia is unable to respond to the changing motion of the fluid, and a large relative velocity may develop which results in the particle drifting out of the fluid eddy.

3.3.1 Homogeneous and inhomogeneous turbulence

Consider a solid particle caught up in a turbulent eddy centred at an arbitrary position O within the flow. The particle may remain entrained by this eddy until it decays, at which time the particle will be picked up by another eddy, centred elsewhere in the flow. However, if the particle's inertial relaxation time, τ_p, is large compared with a characteristic time for the eddy, the particle may be ejected from the eddy before it has decayed. It will then be picked up by another eddy. Although each successive eddy will impart a random velocity on the particle, in homogeneous turbulence the particle will have a zero mean displacement from O.

If the turbulence is inhomogeneous, the particle-eddy interaction will be locally similar to the homogeneous case. However, because of differences in the mean-square fluctuating gas velocity ($\overline{u'u'}$) throughout the flow, a net particle flux may be generated. In homogeneous turbulence, a particle being thrown from an eddy is as likely to be thrown back in the direction from whence it came as it is to be thrown in any other direction. But when the turbulence is inhomogeneous, it may find itself transported to another part of the flow where $\overline{u'u'}$ is lower. The random velocity imparted by the eddies in this more quiescent region will probably be insufficient to return the particle up the gradient of turbulent gas velocity from whence it came. For inhomogeneous turbulence, there is consequently a net particle flux which is driven by the gradient of turbulent gas velocity, for particles that have sufficient inertia to 'slip' out of the eddies. This effect has been termed 'turbophoresis' (Caporaloni *et al.*, 1975; Reeks, 1983). It is important to appreciate that this is a convective drift flux of particles and is not a diffusive flux driven by a particle density gradient, as in equation 3.27.

By Reynolds averaging equation 3.11 (without gravity, or lift and thermophoresis) and invoking the principle of conservation of mass, Young & Leeming (1997) showed that for a pipe flow the radial momentum equation may be written:

$$\overline{V}_y \frac{\partial \overline{V}_y}{\partial y} = -\frac{\phi_D \overline{V}_y}{\tau_p} - \frac{\partial \overline{v'_y v'_y}}{\partial y} \tag{3.28}$$

where the final term on the right hand side is the turbophoretic force per unit mass:

$$\mathsf{F}_{turbo} = -\frac{\partial \overline{v_y' v_y'}}{\partial y} \tag{3.29}$$

The particle acceleration (left hand side of equation 3.28) is therefore enhanced by turbophoresis and opposed by steady-state drag.

The term $\overline{v_y' v_y'}$ is the mean-square fluctuating particle velocity normal to the pipe wall. In the core of the pipe, the mean-square fluctuating gas velocity in the wallward direction ($\overline{u_y' u_y'}$), has an almost constant value, and its value decreases through the buffer layer becoming zero at the wall. This results in a large gradient of $\overline{u_y' u_y'}$ near the wall, so that particles thrown into this region are unlikely to make their way back into the core of the flow, and instead deposit on the wall.

By manipulating the equations it can be shown that an alternative interpretation is to consider the turbophoretic term as an addition to the diffusive term, to give an expression for the particle mass flux to the wall in a turbulent pipe flow as:

$$J_y = -(D_T + D_B)\frac{\partial \overline{\rho}_p}{\partial y} - \rho_p \tau_p \frac{\partial \overline{v_y' v_y'}}{\partial y} \tag{3.30}$$

In the core of the flow, $D_T \gg D_B$, and turbulent diffusion transports the particles towards the wall. However, D_T decreases in the viscous sublayer as the wall is approached (now $D_T < D_B$), and very small particles are deposited by Brownian diffusion. For particles with sufficient inertia to slip out of the eddies, turbophoresis becomes the dominant transport mechanism as the wall is approached (where the fluctuating velocity gradient is high), and deposits the particles on the wall. It has already been stated, that for very small particles $D_T \cong \nu_{g,T}$. The problem of choosing a suitable value of D_T for particles with high inertia is discussed below.

3.3.2 Turbulence modelling

In order to model the behaviour of particles in a turbulent flow, models are required for the mean-square fluctuating particle velocity in the direction of the wall ($\overline{v_y' v_y'}$), and the coefficient of particle turbulent diffusion (D_T).

One of the most detailed considerations of this problem can be found in a series of papers by Reeks (1991, 1992, 1993). The continuum equations were derived by integrating a kinetic equation analogous to the Maxwell-Boltzmann equation for the particle probability density function (PDF), and closure models were then provided for the stochastic terms at this level. A similar approach has also been developed by Zaichik (1997).

Johansen (1991) and Young & Leeming (1997) used a more simple approach to demonstrate the basic physical processes involved, by assuming that the local particle turbulent velocity is a function of the local fluid turbulent velocity, in what is commonly referred to as

the 'local equilibrium' model:

$$\overline{v'_y v'_y} = \Gamma(\overline{u'_y u'_y}, St) \tag{3.31}$$

where $St = \tau_p/\tau_g$ is the Stokes number and τ_g is a suitable time-scale of the fluid turbulence. Γ is a function of the response of a particle to the fluid turbulence around it. This implies that the particle $\overline{v'_y v'_y}$ is related to the local gas $\overline{u'_y u'_y}$ and that the particles do not retain a memory of the turbulent field through which they have just passed (although Shin & Lee (2001) have attempted to account for this 'memory effect' through the use of an additional term). Referring to the data of Mei *et al.* (1991), this would appear to be a reasonable assumption, at least when τ_p is small, but maybe not for larger τ_p. By making various approximations, the turbulent particle velocity fluctuations are related to the turbulent fluid velocity fluctuations by the relationship (e.g. Slater *et al.*, 2003):

$$\overline{v'_y v'_y} = \Gamma \overline{u'_y u'_y} = \frac{\tau_g}{\tau_g + \tau_p} \overline{u'_y u'_y} \tag{3.32}$$

This is a relationship based on theoretical considerations which models the essential features. Equation 3.32 is essentially a curve-fit connecting two extreme cases. When $\tau_p \ll \tau_g$, then the particles respond 'perfectly' to the turbulence, and:

$$\overline{v'_y v'_y} = \overline{u'_y u'_y} \tag{3.33}$$

When $\tau_p \gg \tau_g$, particles respond less to the turbulence and in proportion to the ratio of gas and particle time-scales:

$$\overline{v'_y v'_y} = \frac{\tau_g}{\tau_p} \overline{u'_y u'_y} \qquad \text{and} \qquad \overline{v'_y v'_y} \to 0 \quad \text{as} \quad \tau_p \to \infty \tag{3.34}$$

Consider now the modelling of D_T. Even for particles of high inertia, it is probably a reasonable assumption in homogeneous turbulence that the turbulent particle Schmidt number is near unity. This was a conclusion from the analyses of Tchen (1947), Reeks (1977) and Pismen & Nir (1978). The surprising outcome that particle and fluid diffusive coefficients are nearly equal may be explained as follows: a particle of large inertia will have a lower turbulent velocity than a small particle, but this velocity is more persistent, because the integral length scale of turbulence for the large particle is longer than that for the small particle. The result is that D_T remains approximately independent of particle size, and is therefore given for homogeneous turbulence, by:

$$D_T \cong \nu_{g,T} \tag{3.35}$$

Difficulties arise in inhomogeneous turbulence when there is significant particle drift: particles entrained by eddies in one region of the flow acquire sufficient inertia to drift into regions with

very different turbulence characteristics. The subsequent reduction in the correlation between the particle velocity and that of the eddy by which it was originally entrained results in a reduction in D_T. D_T can be corrected for this 'crossing trajectory effect' [†] (Simonin *et al.*, 1993). Again, a 'local equilibrium' model may be adopted, where D_T is assumed to be unaltered from its homogeneous (isotropic) value (Young & Leeming, 1997).

An alternative formulation for D_T is:

$$D_T = \tau_g \overline{u'_y u'_y} \tag{3.36}$$

where τ_g is a suitable eddy time-scale. This arises from the following prescription of τ_g:

$$\tau_g = \frac{\nu_{g,T}}{\overline{u'_y u'_y}} \tag{3.37}$$

This type of prescription was found to be the most reliable by Rambaud *et al.* (2002), who compared a number of methods for obtaining the Lagrangian integral time-scale in a channel flow with DNS data.

In a turbulent pipe flow, τ_g (as prescribed in equation 3.37) varies across the pipe. However, for turbulent pipe flow experiments, non-dimensionalisation is usually performed using a characteristic eddy time-scale in the core (and there is no variation across the pipe) which is approximated by:

$$\tau_g = \frac{\nu_g}{u_*^2} \tag{3.38}$$

(the friction velocity u_* is defined below). In order to avoid confusion, ν_g and u_*^2 (rather than τ_g) will be used explicitly for the case of turbulent pipe flow.

3.4 Pipe flow experiments

A relatively simple flow field, which features all of the transport mechanisms described earlier in the chapter, is fully-developed turbulent gas-particle flow in a vertical pipe. The importance of the various mechanisms varies with particle size but, as a general rule, particles with small Stokes numbers are heavily influenced by diffusion, while inertial effects dominate the transport of particles with large Stokes numbers. Pipe flow experiments have been carried out for over forty years, and it is the rate of deposition of particles from the bulk flow onto the pipe walls which bound it, that is of primary interest.

The dimensionless deposition velocity is defined as:

$$V_d^+ = \frac{V_d}{u_*} = \frac{J_w}{\rho_{p,m} u_*} \tag{3.39}$$

[†] Not be confused with the crossing trajectories of chapter 2.

where V_d is the deposition velocity, u_* is the friction velocity ($u_* = \sqrt{\tau_w/\rho_g}$, and τ_w is the wall shear stress), J_w is the mass flux of particles to the wall per unit area, $\rho_{p,m}$ is the mean particle density across the pipe.

Neglecting entrance effects, electrical effects, and the roughness of the pipe wall, the deposition velocity is a function of the following parameters:

$$V_d = f(\rho_{p,mat}, \rho_g, u_*, d_p, \mu_g, d, D_B) \tag{3.40}$$

where d_p is the particle diameter, and d is the pipe diameter. Choosing appropriate dimensionless groups yields

$$V_d^+ = f(\tau_p^+, Sc, Re, \frac{\rho_{p,mat}}{\rho_g}) \tag{3.41}$$

where the dimensionless particle relaxation time is given by:

$$\tau_p^+ = \Big(\frac{\rho_{p,mat} d_p^2}{18\mu_g}\Big) \Big/ \Big(\frac{\nu_g}{u_*^2}\Big) \tag{3.42}$$

and ν_g/u_*^2 is the gas relaxation time based on a characteristic eddy time-scale. Re is the pipe Reynolds number, based on pipe diameter and mean flow velocity (U_m):

$$Re = \frac{\rho_g U_m d}{\mu_g} \tag{3.43}$$

The results of experimental studies of particle deposition in turbulent pipe flows, are usually presented as plots of V_d^+ against τ_p^+. A small particle obeying Stokes law of resistance while moving through a stationary fluid from an initial velocity u_s, will stop after a distance:

$$S = \Big(\frac{\rho_{p,mat} d_p^2}{18\mu_g}\Big) u_s = \tau_p u_s \tag{3.44}$$

S is known as the stopping distance, and τ_p^+ can be interpreted as a dimensionless stopping distance S^+. The concept of a stopping distance played a central role in the earlier theories of particle deposition.

3.4.1 The factors influencing particle deposition in vertical pipe flows

Figures 3.2 and 3.3 show some of the available experimental data, which are plotted on a number of separate graphs for clarity. Conventionally, the data is divided into three regimes.

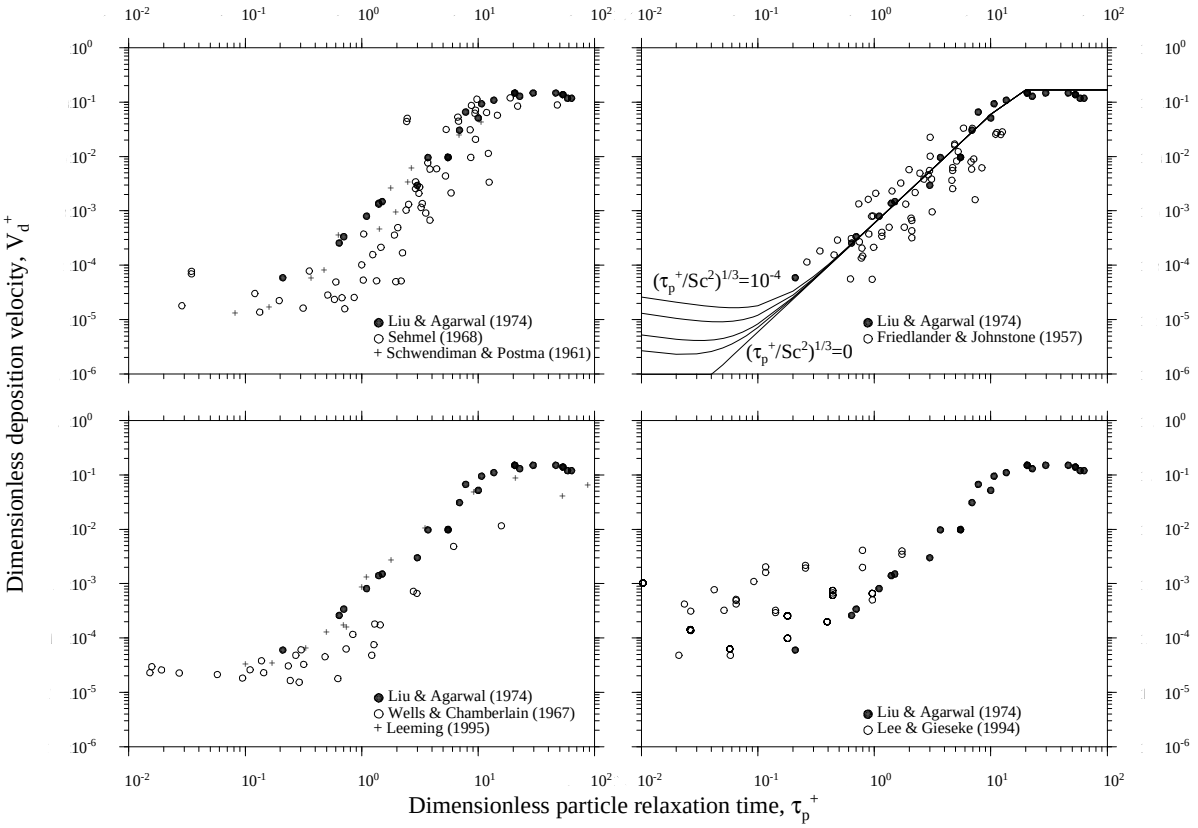

Figure 3.2: The variation of dimensionless deposition velocity with dimensionless particle relaxation time for a range of different experiments in vertical turbulent pipe flow

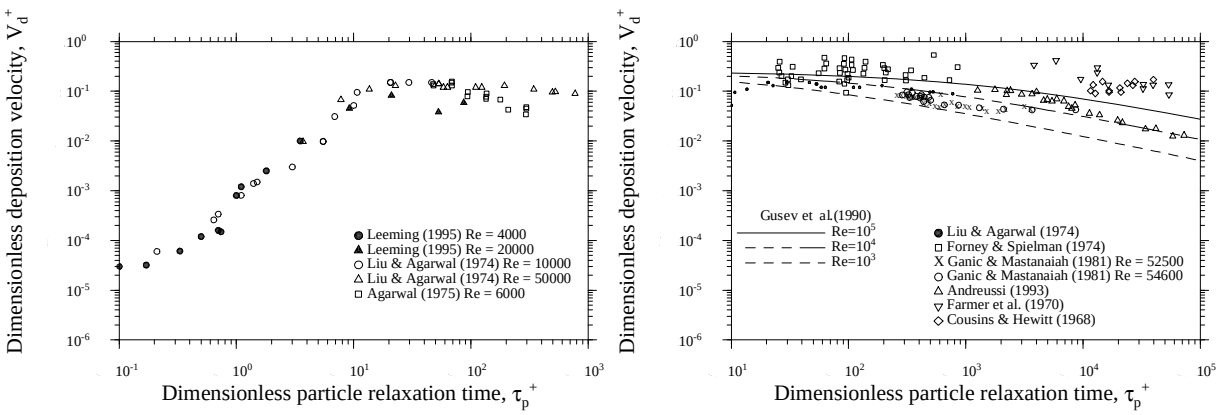

a) b)

Figure 3.3: The variation of dimensionless deposition velocity with dimensionless particle relaxation time for a range of different experiments in vertical turbulent pipe flow: a) The data of Liu & Agarwal (1974), Agarwal (1975) and Leeming (1995); b) Data for the 'inertia moderated' regime

'Diffusional deposition' regime

Below $\tau_p^+ \approx 0.2$, is the 'diffusional deposition' regime. Particles follow the streamlines of the fluid motion almost exactly. The lift force is negligible and deposition is by turbulent and Brownian diffusion. Turbulent diffusion dominates over Brownian diffusion in the core of the flow and carries particles well into the viscous sublayer, from which point Brownian diffusion becomes dominant, and is responsible for particle deposition. Analysis shows that in the diffusional deposition regime, V_d^+ is a function only of the laminar particle Schmidt number, Sc. The laminar Schmidt number for particles is very high, resulting in a 'concentration sublayer' that is much thinner than the 'viscous sublayer'. Hence, Brownian diffusion only comes into play very close to the wall.

As shown by the solid lines in figure 3.2 (top right hand graph), it is customary to plot V_d^+ against τ_p^+, not for constant Sc (which would give horizontal lines) but for constant $(\tau_p^+/Sc^2)^{1/3}$ (e.g. Wood, 1981b). This group is chosen because it is independent of particle diameter but varies with flow conditions. Experimentally, the condition of constant Sc is extremely difficult to obtain, but achieving a constant value of $(\tau_p^+/Sc^2)^{1/3}$ is much more straightforward. Thus, for the same flow conditions, two particles of different diameter (and different τ_p^+), will have equal values of $(\tau_p^+/Sc^2)^{1/3}$, and lie on the same line of almost constant V_d^+.

Now consider two particles of different diameters in flows of different Reynolds numbers, but with the same τ_p^+. The particle in the higher Reynolds number flow will be physically smaller and have a greater molecular diffusivity, and a lower Sc. This will result in a higher value of $(\tau_p^+/Sc^2)^{1/3}$, and from figure 3.2, an increase in V_d^+ would be expected. The greater diffusivity (and lower Sc) results in an increase in the thickness of the narrow diffusion layer, and an increase in V_d^+. This dependence on the particle Schmidt number illustrates the controlling influence of diffusion on small particles. Pershukov *et al.* (1995) found that V_d^+ could be represented by $(0.115/Sc^{3/4})$ for this regime, and this led to the possibility of determining a boundary value of τ_p^+ for which the use of a simple diffusion model is valid.

'Turbulent diffusion-eddy impaction' regime

Between $\tau_p^+ \approx 0.2$ and $\tau_p^+ \approx 20$ is the 'turbulent diffusion-eddy impaction' regime. As the particle inertia is increased, the deposition velocity increases by several orders of magnitude. Particles slip relative to the turbulent eddies and the mechanism of turbophoresis causes a drift flux towards the wall. In this region, the empirical relationship $V_d^+ = k\tau_p^{+2}$ approximately holds, where k is a constant.

'Inertia moderated' regime

Above $\tau_p^+ \approx 20$ is the 'inertia moderated' regime, where the particles are no longer as responsive to the eddy motion of the fluid. The deposition velocity has reached its maximum, and

gradually decreases with increasing τ_p^+.

Equation 3.41 expressed the dependencies of V_d^+. The direct numerical simulation of Zhang & Ahmadi (2000) has shown that a variation of $\rho_{p,mat}/\rho_g$ between values of 1000 and 2000 has little effect on V_d^+. Consequently, for the 'diffusional deposition' regime, $V_d^+ = f(Sc)$, and for the 'turbulent diffusion-eddy impaction' regime, $V_d^+ = f(\tau_p^+)$. The experimental deposition velocities in the 'inertia moderated' regime are often represented by a straight line at $V_d^+ = 0.17$, but there is an obvious decrease as τ_p^+ increases. Pershukov *et al.* (1995) and Gusev *et al.* (1990) have performed analyses that find that $V_d^+ = f(\tau_p^+, Re)$, which becomes significant above $\tau_p^+ \approx 10^3$. Using the analytical expression of Gusev *et al.* and assuming that the pipe wall is perfectly absorbing, the solid lines of figure 3.3b show the variation of V_d^+ with τ_p^+ for Reynolds numbers of 10^3, 10^4 and 10^5. The data do not match these lines for the various Reynolds numbers very well.

Figure 3.2 shows data collected for $\tau_p^+ < 100$, which is well into the start of the 'inertia moderated' regime. The data of Liu & Agarwal (1974) is included on each graph as a datum for comparison, as these experiments covered a large range of τ_p^+ and are the most frequently cited. This is probably because much of the data follows the empirical relationship $V_d^+ = k\tau_p^{+2}$ (where $k = 6 \times 10^{-4}$) with very little scatter. Figure 3.3a compares the data of Liu & Agarwal (1974), Agarwal (1975) (cited in Ganic & Mastanaiah, 1981) and Leeming (1995). A range of Reynolds numbers have been used in these studies, and the experimental methods are similar to that used by the author for the work reported later in this thesis. Figure 3.3b shows the available data for very large τ_p^+.

3.4.2 Measurement of deposition velocity in vertical turbulent pipe flow

These experiments will now be critically discussed to assess the reliability of the data presented in figures 3.2 and 3.3, and to shed light on the practicalities involved with such experiments. Table 3.1 summarises the experimental conditions of all the presented data.

Friedlander & Johnstone (1957)

Friedlander & Johnstone (1957) carried out one of the first such experiments, using glass and brass tubes. They calculated the amount of deposition by removing the particles from the pipe wall with Scotch tape, or applying pressure-sensitive tape or glycerol jelly to the wall for the duration of the experiment, and then counting the particles on the tape or jelly under a microscope. Microscopic examination of several experiments allowed checks for re-entrainment (removal of particles which had already deposited on the wall). The pressure-sensitive tape or glycerol jelly were applied to avoid re-entrainment, and it was found that without them, re-entrainment began at Reynolds numbers between 12500 and 20000, depending on the

experimental conditions. Results for the brass and glass tubes compared favourably, indicating that rebounding was not significant, as the different materials would have had different coefficients of restitution, and thus a different propensity for rebound.

In order to allow comparison of experimental data with theory, most experiments employed a transition length of pipe as well as a test section, so that a fully-developed turbulent flow existed, before the measurements were made. The distance taken for this transition to turbulence to occur may be defined by the Reynolds number based on distance from the inlet (Re_x), and this must be between 10^5 and 10^6 for transition to occur (Schlichting, 1968, pg. 435). The deposition rate as a function of distance from inlet is plotted by Friedlander & Johnstone, and no deposition is found until $Re_x \approx 10^5$. The rate of deposition then increased until a constant value was reached at $Re_x \approx 2 \times 10^5$, indicating that the flow here was fully-developed. This illustrates the importance of turbulent eddies on deposition rates, as the deposition rate near the inlet follows the development of the boundary layer. The distance required for the transition to turbulence to occur may also be based on the number of pipe diameters. Friedlander & Johnstone found that between 25 and 45 diameters was sufficient. Table 3.1 gives the total pipe length to diameter (L/d) ratios used by other researchers.

In an attempt to explain their results, they proposed the stopping distance model. This also formed the basis of many other early theoretical studies. The central idea of the model is that turbulent diffusion carries the particles from the turbulent core to within one stopping distance of the wall, and the particles have enough wallwards momentum to make a 'free-flight' across to the wall. If a particle comes within one particle radius of the wall it will deposit, and if it comes within one stopping distance of the wall it will also deposit. Therefore, the stopping distance can be viewed as the effective radius of the particles due to their inertia, and is the distance which a particle with a given initial velocity will move through a stagnant gas. The initial velocity is assumed to be equal to the root mean square of the fluctuating gas velocity. As noted by Young & Leeming (1997), the theory was a crude attempt to explain the fact that both diffusive and convective effects contribute to particle deposition in pipe flow. The flow field is divided into a diffusive region in the core of the pipe, and a region close to the wall where convective effects, although arbitrarily specified, are active.

Wells & Chamberlain (1967)

Wells & Chamberlain (1967) used radioactive-tagged particles to measure the deposition rate. Their geometry was an annular arrangement consisting of a brass rod placed axially in a copper tube. This arrangement is of particular interest with regard to the experiments carried out in this work. It also allowed better access to the deposition surface, in order that it might be roughened by covering it with filter paper.

The authors contended that the surface was still aerodynamically smooth, and that the surface roughness elements were too small to disturb the viscous boundary layer of the airflow, allowing the effect of surface roughness on particle deposition rate to be examined, without

altering the gas flow field. This could be interpreted as follows: Schlichting (1968, pg. 511) found that the critical height of roughness below which transition to turbulence is unaffected is given by $(u_* h)/\nu_g = 20$, where h is the height of the roughness elements; and $(u_* h)/\nu_g < 20$ in Wells & Chamberlain's experiments. It was found that the deposition velocity increased by several orders of magnitude when the deposition surface was covered with filter paper (although only the results for the smooth surface are plotted in figure 3.2). This contrasts with the results of Schwendiman & Postma (1961) for pipe flow, who found no difference in deposition velocity between a grit roughened surface and a polished surface. Clearly, however, the preparation of the inner walls of a pipe has inherent difficulties that are overcome by the novel annular arrangement of Wells & Chamberlain. It should be noted that only the deposition on the inner rod was measured. For a more detailed treatment of the effects of roughness on particle deposition in turbulent pipe flow, see Wood (1981b) and El-Shobokshy (1983).

Sehmel (1968)

Sehmel (1968) used uranine and uranine-methylene blue particles in a variety of pipe diameters, and at various Reynolds numbers. The amount deposited on the pipe wall was determined by cutting the pipe into sections, and washing each section before using fluorimetric techniques to determine the mass deposited (uranine was used as a fluorescent tracer). The mass deposited on each section, together with the mass deposited on a filter at the outlet of the flow, was used to calculate the fraction of particles penetrating through each individual section of the pipe. The deposition velocity in each section was then calculated using the equation:

$$V_d = \frac{Q_a}{\pi d \Delta x} ln\left(\frac{1}{P}\right) \tag{3.45}$$

where Q_a is the volumetric flow rate of air, Δx is the length of the section, and P is the fractional penetration through the section.

Many experimental conditions were investigated and sources of error discussed, such as: pipe roughness, pipe entry and end effects, the effects of pipe joints, re-entrainment, particle dryness (large particles dry more slowly and may be more 'sticky'), and the repeatability of results. These were the main features that led to the order of magnitude scatter observed in Sehmel's experimental results, and understanding their effects is important to producing a 'definitive' set of experimental results, against which theoretical models can be validated.

A criterion for re-entrainment of particles was proposed; particles are re-entrained if turbulent eddies penetrate the laminar sublayer to within one particle diameter, a condition that occurs when the dimensionless particle diameter in wall units d_p^+ $(= d_p u_*/\nu_g) > 0.4$. As well as the result for particle deposition velocity, important supplementary information was presented. Non-uniform radial profiles of particle concentration were found (by placing a filter across the tube center), and axial concentration profiles were also found (from the fractional

penetration P). Log coordinates were used to plot the concentration drop along the axis, and for monodispersed particles a linear profile would be expected. However, the normalised concentration was shown to decrease linearly to 10% of its inlet value within the first 8 foot (of a 50 foot pipe), but the profile then levelled out, due to the existence of what were termed smaller 'satellite' particles.

The plots of deposition velocity against Reynolds number or particle diameter are quite confusing, and show significant amounts of scatter. However, in an earlier paper (Sehmel, 1963), results are plotted as dimensionless deposition velocity (V_d/U_m) against dimensionless stopping distance (S^+), and the various experimental data correlate much better when plotted in this manner, with a subsequent reduction in scatter. This is very similar to the V_d/u_* versus τ_p^+ plots that are now in widespread use, and may be the first instance of such a plot. Some of the data in figures 3.2 and 3.3 have been modified from their original dimensionless forms.

Lee & Gieseke (1994)

Lee & Gieseke (1994) sought to supplement the 'very few' experimental data points for the region between the diffusional deposition and inertia moderated regimes, although figure 3.2 indicates that data is not as scarce as the authors intimate. Three methods were used to determine the deposition velocity: an electrical aerosol detector, a fluorimetric technique with uranine-tagged particles (similar to that of Sehmel, 1968), and the use of upstream and downstream membrane filters. The results compared well for the three different methods. The apparent scatter in the 'diffusional deposition' regime is largely due to the different values of the Schmidt number used.

Liu & Agarwal (1974)

The most popular set of experiments for comparison is that of Liu & Agarwal (1974). This is probably due to the range of τ_p^+ covered, and the self-consistency of the results. Particles of olive oil tagged with uranine were used, and the deposition velocity determined after Sehmel (1968). Physically, the particles consisted of a solid core of uranine surrounded by a liquid coating of olive oil, so that the adhesion of the particles to the wall was not considered a problem. Results in the inertial regime are presented for pipe Reynolds numbers of 10000 and 50000, and this data is well supplemented by that of Agarwal (1975), for Reynolds number of 6000, which suggest that there may be a Reynolds number dependancy above $\tau_p^+ \approx 50$. Also shown are the experiments of Leeming (1995), which were carried out (in a very similar manner to those of Liu & Agarwal) as a datum against which to examine the effect of thermophoresis on particle deposition (which is of direct interest to this work).

Particles and droplets of high inertia

The data of Forney & Spielman (1974) for particles of high inertia shows a much higher peak in the value of deposition velocity, but also displays large scatter. The trend of decreasing

deposition velocity as inertia increases further, is shown by the investigations of Cousins & Hewitt (1968), Farmer *et al.* (1970), Ganic & Mastanaiah (1981) and Andreussi (1983), into the behaviour of water droplets in air. It should be noted that such experiments almost always involve a polydispersed droplet size distribution, rather than one that is monodispersed.

3.4.3 Precautions for future experiments

The experimental data presented above varies by up to an order of magnitude for certain ranges of τ_p^+, and the review of the experimental methods used in these investigations gives a clear indication of pitfalls to be avoided in future experiments. In order to carry out experiments in turbulent pipe flow, and to achieve repeatable and reproduceable results that do not contribute more to the uncertainty and scatter apparent in the data that already exists, a number of precautions must be taken. The particles must be electrically neutral, the pipe wall must be earthed and smooth, and the pipe length to diameter ratio must be sufficient so that entrance effects may be neglected. The use of an aerosol with a liquid component helps in ensuring adhesion and guarding against re-entrainment. Along with these precautions, rigorous experimental techniques are needed in order for the results to be reproduceable and self-consistent.

3.5 Thermophoresis

It has already been stated that thermophoresis may be the dominant deposition mechanism for small particles in a temperature gradient (section 3.2.3). One of the aims of this work is to provide reliable experimental data for the influence of thermophoresis on particle deposition, and to compare this data with theoretical calculations. Accordingly, various theoretical models for the coefficient of thermophoresis are examined in order to identify the most suitable form for inclusion in the theory. In section 3.4, experiments on particle deposition in fully-developed turbulent pipe flow were examined. The popularity of these experiments is due to the presence of all the transport mechanisms previously described, and such experiments also lend themselves to investigations into thermophoresis. Previous turbulent pipe flow experiments featuring thermophoresis will therefore be examined, and suggestions for improvements will be made. These improvements form the basis of the experimental work to be presented.

The magnitude of the thermophoretic force depends on the particle Knudsen number. The particle Knudsen number, Kn, is the ratio of the mean free path of a gas molecule, λ_g, to the particle radius, r_p:

$$Kn = \frac{\lambda_g}{r_p} \tag{3.46}$$

Useful explanations of the phenomena occurring at various Knudsen numbers are given by Rohsenow & Choi (1961) and Eckert & Drake (1959).

Deposition surface	Flow direction	d (cm)	L/d	Particle type	$\rho_{p,mat}/\rho_g$	Reynolds No. range	τ_p^+ range
Friedlander & Johnstone (1957)							
Vertical pipe	Up	0.54-2.5	46-66	Iron & aluminium powder	6100, 2093	7200-40000	0.26-12.6
Schwendiman & Postma (1961)							
Vertical pipe	Up	1.9 & 2.54	Unknown	Zinc sulfide & glass spheres	2744	3000-20000	0.08-10.6
Wells & Chamberlain (1967)							
Vertical annulus	Down	1.27 id & 3.81 od	197	Aitken nuclei, TCP droplets & polystyrene spheres	915 (TCP)	2000-40000	0.015-16
Cousins & Hewitt (1968)†							
Vertical pipe	Up	0.953 & 3.18	369 & 437	Droplets of water in air	775	37380-196000	12000-40000
Sehmel (1968)							
Vertical pipe	Up	0.53-7.14	210-2860	Uranine & uranine-methylene blue	1163	2000-60000	0.03-48
Farmer, Griffith & Rohsenow (1970)							
Vertical pipe	Down	1.27	158	Droplets of water in air	775	14000-28000	1700-48000
Forney & Spielman (1974)							
Vertical pipe	Down	1.3-4.4	70-238	Ragweed pollen, lycopodium spores, polystyrene spheres & pecan pollen	372, 504, 852, 728	4000-60000	25-795
Liu & Agarwal (1974)							
Vertical pipe	Down	1.27	>80	Uranine-olive oil	713	10000-50000	0.21-774
Agarwal (1975)†							
Vertical pipe	Down	0.327 & 1.38	91.7 & 73.9	Uranine-olive oil	713	6000 & 50000	40-449
Ganic & Mastanaiah (1981)							
Vertical pipe	Up	1.27	130	Droplets of water in air	775	52500 & 94600	264-8670
Andreussi (1993)							
Vertical pipe	Down	2.4	208	Droplets of water in air	775	48000-146000	$10^3 - 10^5$
Lee & Gieseke (1994)							
Vertical pipe	Down	0.622 & 0.767	1520 & 1596	Dioctyl phthalate	Unknown	1800-15600	$1.9\text{x}10^{-5}$-1.7
Leeming (1995)							
Vertical pipe	Down	1.0	240	Uranine-oleic acid	931	4000-20000	0.1-87

Table 3.1: A summary of the experimental conditions of vertical turbulent pipe flow data

†Information from Ganic & Mastanaiah (1981).

Under continuum conditions ($Kn \ll 1$), rates of momentum and energy transfer at the particle surface are governed by the equations of continuum fluid flow and the fluid adjacent to the surface assumes the velocity and temperature of the surface with negligible 'slip'. When the molecular mean free path becomes comparable with the particle diameter, however, the gas becomes rarefied with respect to the particle. This results in a velocity 'slip' between the gas and the particle at the particle surface. There is also a 'jump' in temperature between the particle surface and the adjacent gas. The effects of the molecular velocity distribution in the gas now become important, because the rates of momentum and energy exchange are no longer solely governed by intermolecular collisions, but also by the effectiveness of momentum and energy exchange between the gas molecules and the particle. These effects are quantified by parameters known as *accommodation* and *reflection* coefficients, which describe the statistical surface-molecule interactions. This flow regime is known as the *slip-flow regime*, and it occurs when $Kn \approx 0.1$.

When $Kn \gg 1$, intermolecular collisions are negligible compared with surface collisions, as molecules leaving the particle surface do not collide with free-stream particles until they are very far away. The molecular velocity distribution away from the surface can be assumed to be undistorted (Maxwellian), and flow near the body is considered as the interaction between free molecules and the surface. This is known as the *free-molecule* or *Knudsen regime*.

Between the slip-flow and free-molecule regimes lies the *transition regime*, where $Kn \approx 1$. Collisions between molecule and surface, and molecule and molecule are frequent and of equal importance. Analysis of transition flow is very difficult.

3.5.1 Theories of thermophoresis over the range of Knudsen numbers

The thermophoretic force on a spherical particle is given by:

$$\mathbf{f}_{TH} = -\eta_{TH} \nabla(lnT) \tag{3.47}$$

where T is the absolute temperature of the surrounding gas, and η_{TH} is the coefficient of thermophoresis, which depends particularly on the Knudsen number and the ratio of gas to particle thermal conductivities.

In the free-molecule regime ($Kn \gg 1$), kinetic theory was used by Waldmann (1959) (cited in Byers & Calvert, 1969) to give the thermophoretic coefficient as:

$$\eta_{TH} = 2\pi\mu_g\nu_g\frac{r_p^2}{\lambda_g} = 2\pi\mu_g\nu_g\frac{r_p}{Kn} \tag{3.48}$$

where λ_g is the mean free path of a gas molecule and is given by kinetic theory as $\lambda_g = \frac{2\mu_g}{\rho_g\bar{c}}$, where $\bar{c} = \sqrt{8RT/\pi}$ is the mean molecular speed. R is the specific gas constant.

One of the earliest attempts to calculate the thermophoretic force was made by Epstein

(1929) (cited in Talbot *et al.*, 1980), who derived the following expression for use in the slip-flow regime:

$$\eta_{TH} = 9\pi\mu_g\nu_g r_p \left(\frac{\frac{k_g}{k_p}}{1 + 2\frac{k_g}{k_p}} \right) \tag{3.49}$$

where k_p is the thermal conductivity of the particle, and k_g is the thermal conductivity of the gas. Epstein's expression was found to underpredict the thermophoretic force compared to experimental results, especially for particles of high thermal conductivity ($\frac{k_g}{k_p} \ll 1$). It should be noted that in the free-molecule regime, the thermophoretic force varies with r_p^2 (equation 3.48), while in the continuum and slip-flow regimes the variation is with r_p (equation 3.49).

Brock (1962) had two objections to the Epstein expression. These were that the correct boundary conditions for the slip-flow regime may not have been used, and that the continuum energy equation had been solved neglecting the convective terms. Taking these into account, he arrived at the expression:

$$\eta_{TH} = \frac{12\pi\mu_g\nu_g r_p C_s \left(\frac{k_g}{k_p} + C_t Kn \right)}{\left(1 + 3C_m Kn \right) \left(1 + 2\frac{k_g}{k_p} + 2C_t Kn \right)} \tag{3.50}$$

where C_m, C_s and C_t are constants whose order of magnitude can be established by kinetic theory. This is the best established equation, and is favoured by many researchers, but the values C_m, C_s and C_t as suggested by Brock are usually replaced by those suggested by Talbot *et al.* (1980). Note that equation 3.50 reduces to equation 3.49 in the limit $Kn \to 0$ if $C_s = 0.75$ (the value suggested by Brock). It also reduces to equation 3.48 in the limit $Kn \to \infty$, if $C_s = C_m$.

Cha & McCoy (1974) adapted their own analysis for the thermophoretic force to present a theory that would span all values of Knudsen number. Their findings were modified by Wood (1981) and presented by He & Ahmadi (1998) as the Cha-McCoy-Wood theory:

$$\eta_{TH} = \frac{Kn}{4\sqrt{2}\alpha \left(1 + \frac{\pi_1}{2} Kn \right)} \left[1 - exp\left(-\frac{\alpha}{Kn} \right) \right] \left(\frac{4}{3\pi} \phi \pi_1 Kn \right)^{\frac{1}{2}} kT \frac{(2r_p)^2}{d_m^2} \tag{3.51}$$

where T is the mean gas temperature in the vicinity of the particle, k is the Boltzmann constant, and d_m is the molecular diameter. ϕ depends on the gas properties, π_1 is a function of the normal and tangential momentum accommodation coefficients, and α is a function of ϕ, π_1 and Kn. It will be shown later that this expression is at variance with both theoretical and experimental results.

Another theory that merits examination is that of Bakanov & Roldugin (1977), for small Knudsen numbers. It claims to represent the behaviour of particles of high thermal conductivity better than other theories, but it will be seen that this theory is highly dependent on

the choice of the energy accommodation coefficient.

3.5.2 Determination of accommodation coefficients

The constants C_t (associated with the temperature jump) and C_m (associated with the velocity slip) are complex functions of the energy (a_t) and momentum (a_m) accommodation coefficients respectively. For the case of incident molecules achieving complete thermodynamic equilibrium (accommodation) with the surface before leaving, $a_t = a_m = 1$; and for the case of complete specular reflection of the molecules, $a_t = a_m = 0$.

Brock assumed the case of complete momentum and energy accommodation, resulting in $C_m = 1.0$ and $C_t = 1.875$. According to Talbot *et al.* (1980), the best kinetic theory values for complete accommodation appear to be $C_m = 1.14$, $C_t = 2.18$ (from Loyalka & Ferziger (1967) and Loyalka (1968)).

However, for the thermal slip coefficient, Brock used the value $C_s = 0.75$, first used by Maxwell (see Kennard, 1938, pg. 295) on the assumption that the distribution function in the bulk of the gas held all the way to the wall. Talbot found that $C_s = 1.17$ for complete thermal accommodation from the more refined kinetic theory analysis of Ivchenko & Yalamov (1971), a value in substantial agreement with other analyses.

Talbot was seeking a fitting formula that would give an expression for the thermophoretic force that was valid over the entire range of Knudsen number. He chanced upon the fact that in the limit $Kn \to \infty$, the Brock result and the Waldmann free-molecule result are identical, except for the factor C_s/C_m. But $C_s/C_m = 1.17/1.14 = 1.03$ (using Talbot's constants), giving an error of just 3%. The Brock result, with the constants recommended by Talbot *et al.*, has been taken by many authors as the definitive formula and has been widely shown to agree with experiments (as will be discussed in a subsequent section).

According to Talbot, drag measurements carried out on the various aerosols used in thermophoretic experiments support the assumption of perfectly diffuse reflection ($a_m = 1.0$ and $C_m = 1.14$). The validity of the assumption of complete thermal accommodation has also been examined. Brock found evidence that for unprepared surfaces, a_m is usually very close to 1 and a_t varies between 0.5 and 1.0; and that for air on various surfaces a_t is very near 1. Talbot examined the effect of a reduction in the value of a_t to less than unity. In the near-continuum regime, a reduction in the magnitude of C_s results in a slight reduction in the thermophoretic force. However, in the slip-flow regime this reduction of C_s was offset by changes in the ratio of the two terms containing C_t. A lowering of a_t results in an increase in the thermophoretic force in the free-molecule regime. It was concluded that there would be no significant improvement to the fitting formula by abandoning the assumption of complete thermal accommodation.

3.5.3 Additional considerations for particles of high thermal conductivity

Brock's expression was found to give poor agreement with experiment for particles of high thermal conductivity (Bakanov, 1992), although there is improvement over the results using the Epstein expression. Examining the case for particles of low thermal conductivity in the near-continuum regime ($k_g/k_p \gg \lambda_g/r_p$), the Epstein and Brock expressions are equivalent. Epstein's formula is the formal limit as $Kn \to 0$ of Brock's theory.

Bakanov (1992) recognised the limiting case of Epstein's result, and described it as the first term of a series in powers of Kn. He reasoned that it was the omission of higher powers of the Knudsen number that led to the theory under-predicting experiment. Bakanov & Roldugin (1977) proposed an expression for the thermophoretic velocity at small Knudsen numbers that was similar to that of Epstein, but with a multiplier of $(1 + Kn\phi)$, where ϕ is a complex function of the momentum and energy accommodation coefficients, and the curvature of the surface. The $Kn\phi$ term was included to account for mechanisms other than thermal slippage that contribute to thermophoresis of solid particles. For particles of high thermal conductivity ($\frac{k_g}{k_p} \ll 1$), the $Kn\phi$ term dominates. Bakanov interpreted this as reflecting the physical fact that for particles of high thermal conductivity, the temperature of the particle will be very nearly uniform regardless of the temperature distribution of the gas, and that the thermal slippage is close to zero. The origin of thermophoresis in this case is from thermal stresses in the gas, and the nonuniformity of the normal flux of heat on the surface of the solid.

Bakanov (1991) argued that because reliable theoretical results were derived mainly in the $Kn \ll 1$ domain, that comparison with experiment is justified only at these Knudsen numbers. He found little experimental work in this domain, and those experiments that were carried out at sufficiently small Knudsen numbers, only provided a result at one point, and consequently gave no information regarding the effect of Knudsen number. According to Bakanov, for particles of high thermal conductivity, the more rigorous condition $Kn \ll \frac{k_g}{k_p}$ must be fulfilled in order for a justifiable comparison with theory to be made.

There have been several other attempts at theoretically quantifying the thermophoretic force, using approaches other than the hydrodynamic analysis of Brock. Dwyer (1968) used the relationships derived from the Grad molecular velocity distribution, and it was found that when $\frac{k_g}{k_p} \ll 1$ that the thermophoretic velocity can alter its sign, resulting in a positive thermophoretic force (usually the force is in the opposite direction to the temperature gradient and the sign is negative). Bakanov (1991) reports that Gorelov (1976) solved the linearised Boltzmann equation for the cases where $\frac{k_g}{k_p} = 0.2$ and $\frac{k_g}{k_p} = 0.002$, typical of low and high thermal conductivity particles. For the high thermal conductivity particle, Gorelov found that close to $Kn \approx 0.1$, the thermophoretic force may be very slightly positive. A similar reversal of the thermophoretic force was found by Sone & Aoki (1981).

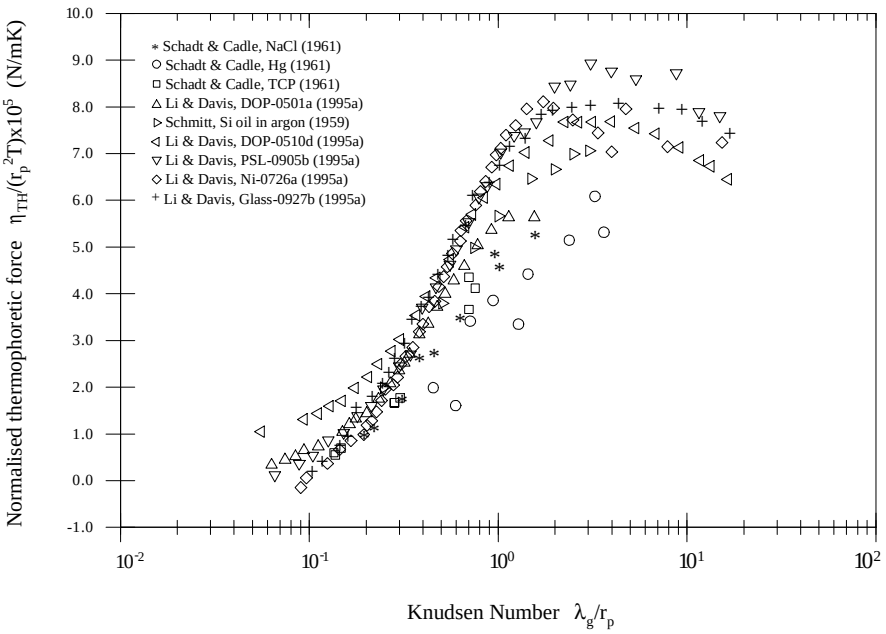

Figure 3.4: The variation of normalised thermophoretic force with Knudsen number: a selection of experimental data

3.5.4 Experimental work

The experimental data collected in figure 3.4 shows the variation of the normalised thermophoretic force with Knudsen number. The normalised thermophoretic force is:

$$\frac{|\mathbf{f}_{TH}|}{r_p^2|\nabla T|} = \frac{\eta_{TH}}{r_p^2 T} \tag{3.52}$$

Based on the various theoretical formulations, $\eta_{TH}/(r_p^2T)$ can be expected to be a unique function of the Knudsen number for a specific gas-particle system, and Li & Davis (1995a) found that this normalisation of the force substantially reduces the scatter in the data. It was earlier noted that $\mathbf{f}_{TH}$ varies with r_p (from equation 3.50) for the continuum and slip-flow regimes, and it follows that $\eta_{TH}/(r_p^2T)$ varies inversely with r_p. Thus, for a given flow field, $\eta_{TH}/(r_p^2T)$ varies directly with Kn. Experimental data supports this linear dependence of the normalised thermophoretic force on Knudsen number.

The experiments of Schmitt (1959)† (silicon oil droplets in argon) and Schadt & Cadle (1961)† (mercury and tricresyl phosphate (TCP) droplets and sodium chloride (NaCl) particles in air) were carried out using the Millikan oil drop experimental technique. Li & Davis (1995a) used electrodynamic levitation to maintain a microsphere in the space between heated and cooled plates (for dioctyl phthalate (DOP) droplets and polystyrene latex (PSL), nickel and glass particles in air). A potential difficulty in such experiments is that the gas may be

†Data from Li & Davis (1995a).

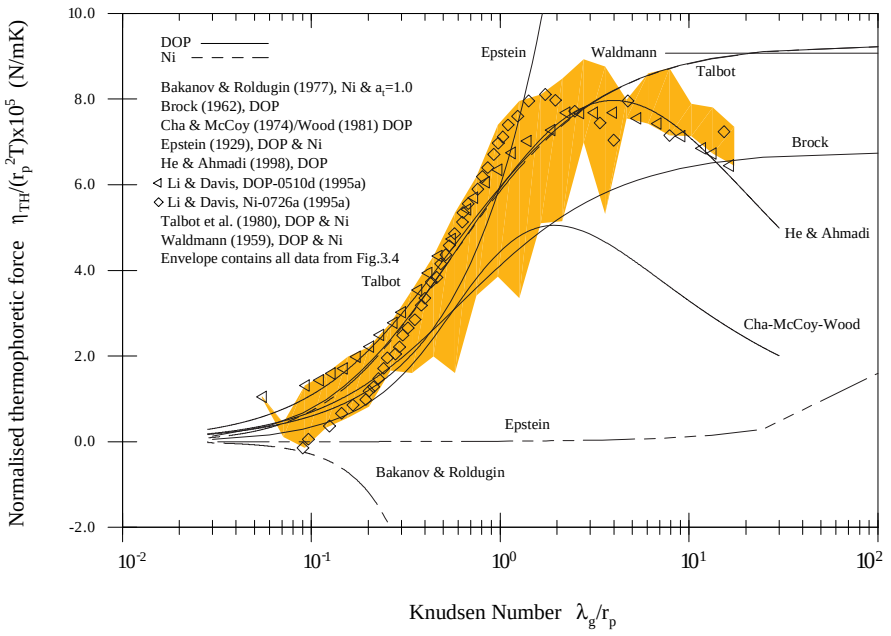

Figure 3.5: The variation of normalised thermophoretic force with Knudsen number: a representative comparison between theory and experiment

subject to free convection and thermal creep effects. Li & Davis (1995b) also carried out experiments to determine the effect of gas properties. Figure 3.4 shows a representative sample of experimental data for various materials in air.

The data of Li & Davis (1995a) shows an increase in $\eta_{TH}/(r_p^2 T)$ with an increase in Knudsen number. For $Kn > 3$, $\eta_{TH}/(r_p^2 T)$ is seen to decrease, even though, for free-molecule flow, a constant value would be expected from the Waldmann theory. The authors explain that this is due to the fact that the temperature gradient used to calculate these points is not the effective temperature gradient for large values of Kn. As the mean free path of the gas approaches the distance between the heated and cooled plates, the temperature gradient at the center of the chamber deviates from the assumed continuum value, because temperature jumps exist at the solid surfaces. Thus, there is a second Knudsen number (Kn_2) based on the distance between the heated and cooled surfaces, which must be taken into account. By using a correction term for the temperature gradient, the data was shown to approach a constant asymptotic value for $5 < Kn < 20$ (in agreement with the Waldmann expression for the free-molecule regime), and the data for $Kn > 20$ has been ignored. The possibility of reverse thermophoresis was also investigated for particles of high thermal conductivity at low Knudsen numbers. It was concluded that due to scatter in the data for $Kn < 0.1$, there was insufficient evidence of such a reversal.

3.5.5 Comparison of experimental data with theory

Figure 3.5 shows the comparison between theoretical models and the data of Li & Davis (1995a) for DOP and nickel. These experimental data sets are plotted as they are representative of low and high particle thermal conductivity (for DOP $k_p = 0.125\ Wm^{-1}K^{-1}$, and for nickel $k_p = 90.9\ Wm^{-1}K^{-1}$, resulting in $\frac{k_p}{k_g} \approx 5$ and $\frac{k_p}{k_g} \approx 3600$ respectively). The expression of Talbot *et al.* is plotted for the two cases. For $Kn < 1$, both sets of data are represented fairly well, but at $Kn \approx 1$ the theoretical expressions merge and follow the data for DOP (underpredicting the data for nickel in this region) before reaching an asymptote, corresponding to the Waldmann expression for the free-molecule regime. The theories of Epstein and Brock are also plotted. The extent to which the Epstein theory underpredicted $\eta_{TH}/(r_p^2 T)$ for particles of high thermal conductivity is evident. Brock's theory does not represent the data well when $Kn > 0.1$.

He & Ahmadi (1998) presented the Cha-McCoy-Wood equation, and this shows $\eta_{TH}/(r_p^2 T)$ increasing with increasing Knudsen number until $Kn \approx 3$, and thereafter decreasing with increasing Knudsen number. The amplitude and other parameters (α, π_1) were then modified to improve agreement with the experimental data. The authors find good agreement between the data of Li & Davis and their modified Cha-McCoy-Wood equation, but do not seem aware that Li & Davis have themselves pointed out that the trend of decreasing $\eta_{TH}/(r_p^2 T)$ for $Kn > 3$ is due to experimental conditions. The fact that the theory follows the experimental data at all, is probably due to the fact that the original Cha & McCoy (1974) theory was developed for a spherical particle suspended in a gas midway between two planes at different temperatures; an arrangement similar to the experiments of Li & Davis. Cha & McCoy were also aware of the existence of a second Knudsen number based on the distance between the plates. Wood (1981a) attempted to remove the dependence on a second Knudsen number Kn_2 from the expression by assuming that $Kn_2 \ll 0$, but this does not appear to have been sufficient to correct the deficiencies in the theory.

The theory of Bakanov & Roldugin (1977) is shown for a particle of high thermal conductivity (nickel), and with $a_t = 1$. The normalised force due to thermophoresis decreases with increasing Knudsen number, and it is not until $a_t < 0.9$ that the force increases with Knudsen number, though it still does not represent the experimental data well. Bakanov (1991) thought that the possibility existed to assess the value of the energy accommodation coefficient of gas molecules undergoing collisions with the surface of a particle, according to the variation of the thermophoretic force at small Knudsen numbers using the theory of Bakanov & Roldugin. However, Li & Davis (1995a) report that a_t strongly depends on the type of surface, the cleanliness of the surface, its temperature, and the composition of any adsorbed gas. The theory of Bakanov & Roldugin (1977) would seem to be too sensitive to the value of a_t to be of practical use. The reversal of the sign of $\eta_{TH}/(r_p^2 T)$ for a slight change in the value of a_t at $a_t \approx 0.9$ suggests that the theory is far removed from the actual physical process. The obvious failings of this theory may explain Bakanov's subsequent rejection of

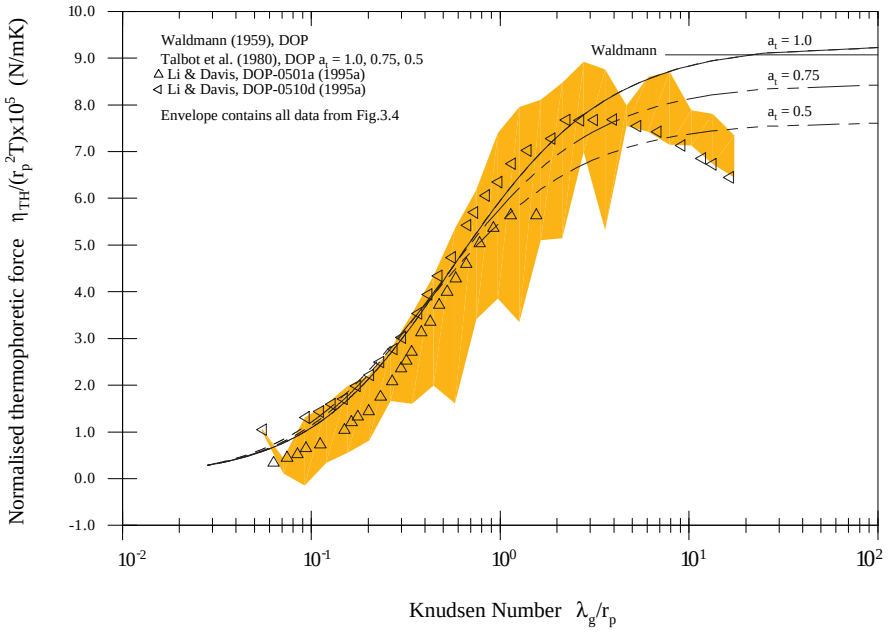

Figure 3.6: The effect of variation of the thermal accommodation coefficient on the normalised thermophoretic force across the range of Knudsen numbers

comparisons between experimental data and theoretical analyses.†

The effect of a coefficient of energy accommodation that deviates from unity on the expression of Talbot *et al.* is shown in figure 3.6. It can be seen that below $Kn \approx 1$, the value of a_t has no significant effect on $\eta_{TH}/(r_p^2 T)$, as would be expected from continuum theories. It should be pointed out that the Waldmann theory also assumes complete accommodation. Talbot *et al.* (1980) have managed to match the near-continuum result of Brock, and the free-molecule result of Waldmann, while representing the experimental data between these limits fairly well. The assumption of complete accommodation has been shown to be reasonable, and even if this is not the case, the effects of a varying energy accommodation coefficient are negligible below $Kn \approx 1$ (0.01< Kn <0.1 is the range of interest in this work). It is clear that the most suitable formulation is that of Brock, using the constants recommended by Talbot *et al.*.

3.6 The effect of thermophoresis on particle deposition

Particle transport and deposition in fully-developed turbulent pipe flow is a relatively simple flow field which still features particle transport by nearly all of the mechanisms described in sections 3.2 and 3.3. Since Friedlander & Johnstone (1957) first carried out experiments on

†Bakanov & Roldugin (1977) is reconsidered in chapter 7 in the light of a newly discovered paper by Beresnev & Chernyak (1995).

isothermal and turbulent vertical pipe flows, there have been many other investigations of this type. The influence of thermophoresis (acting either alone or in unison with other mechanisms) on particle deposition may be studied by imposing a temperature gradient across the pipe. Most experiments involving a temperature gradient have been conducted in laminar pipe flows, but the present work aims to deal with the case of turbulent pipe flow.

Montassier *et al.* (1991) performed experiments by heating a laminar flow of air, laden with uranine particles, and then directing this upwards through a vertical pipe. The outer wall of the pipe was kept at a constant temperature by a flow of cold water, and the nominal temperature gradient at entry to the deposition pipe (difference in temperature between the wall and the flow at entry divided by the pipe radius) was approximately 8000-9000 Km^{-1} (80-90 K in a 2 cm diameter pipe). The nominal temperature gradient will be denoted by T_{grad}.† Experiments were performed for a number of different particle sizes, and the deposition efficiencies were determined by cutting the deposition pipe into sections, washing these sections, and then measuring the fluorescence of the solution with a photometer.

Romay *et al.* (1998) carried out experiments on sodium chloride (NaCl) and polystyrene latex (PSL) particles in a downward turbulent flow through a vertical pipe. The particle-laden flow had a temperature of between 298 K and 410 K at the entrance to the deposition pipe, compared to a temperature of 20 K at the water-cooled pipe wall. For a 0.49 cm diameter pipe, this corresponds to a nominal temperature gradient at entry to the deposition pipe of approximately 2000-48000 Km^{-1}. Condensation nucleus counters upstream and downstream of the deposition pipe were used to measure the deposition efficiency. Having derived a theoretical expression for thermophoretic deposition efficiency in turbulent pipe flow, this was compared with the turbulent expressions of Byers & Calvert (1969), Nishio *et al.* (1974), Batchelor & Shen (1985), and the laminar expression of Stratmann *et al.* (1994). All the expressions (including that for laminar flow) were found to be within 2% of each other, except for that of Byers & Calvert. This expression predicted much higher deposition rates, due, it was thought, to the particular treatment of the temperature gradient at the gas-wall boundary.

Leeming (1995) performed similar experiments with particles of oleic acid and uranine, in a turbulent pipe flow. The particle-laden flow was directed downwards through a vertical pipe. The quantities deposited on the pipe walls were then determined by cutting the pipe into sections and using fluorescence spectrometry. As well as experiments in isothermal flow, experiments were carried out where the flow was heated and passed through a pipe with water-cooled walls. However, it was found that when the flow had travelled far enough along the pipe for the temperature profile to be fully-developed, the temperature difference between the flow and the walls of the pipe was only 4 K in a 1 cm diameter pipe ($T_{grad} = 800$ Km^{-1}).

While Montassier *et al.* (1991) and Romay *et al.* (1998) plotted their results as deposition efficiencies, Leeming plotted dimensionless deposition velocities, as used for the results from the many isothermal pipe flow experiments. The dimensionless deposition velocity is (from

†The limitations of using a nominal temperature gradient will be explained in chapter 4.

equation 3.45):

$$V_d^+ = \frac{dU_m}{4Lu_*} ln\left(\frac{1}{P}\right) \tag{3.53}$$

where L is the length of the pipe (or section), d is the pipe diameter, U_m is the mean flow velocity, u_* is the friction velocity, and the fractional penetration of each section $P = 1 - \eta_d$, where η_d is the deposition efficiency of that section. The deposition efficiencies were converted to dimensionless deposition velocities using the parameters shown in equation 3.53, with the parameters evaluated at a representative mean temperature (taken as the mean of the wall temperature and the temperature of the flow at entry to the deposition pipe) for the experiments of Montassier *et al.* (1991) and Romay *et al.* (1998). The experiments of Leeming (1995) calculated the deposition velocities themselves, based on the mean temperature in the section of the pipe where the temperature field was fully-developed.

The results are shown in figure 3.7. The data taken from the experiments of Romay *et al.* was for sodium chloride particles at flow rates of 5 lpm and 35 lpm, corresponding to a laminar flow with $Re \approx 1400$ and a turbulent flow with $Re \approx 9500$, respectively. The upper lines bounding this data represents the case when the nominal temperature gradient at entry to the deposition pipe $T_{grad} = 48000$ Km^{-1}, and the lower bounding lines represent the case when $T_{grad} = 2000$ Km^{-1}.

It should be noted that τ_p^+ for the data of Romay *et al.* is defined by equation 3.5 multiplied by the Cunningham correction factor of equation 3.15, to account for the rarefaction of the gas with respect to the particle. At standard conditions, the error involved in the omission of this correction factor is only significant for particles less than 1 μm in diameter (Hinds, 1998, pg. 49). Romay *et al.* used particle diameters in the range 0.1-0.7 μm, making the use of this correction factor necessary. Montassier *et al.* used particles of diameter both greater and less than 1 μm, so although the Cunningham correction factor was included in the expression for τ_p^+, it use was only significant for the submicron particles. This correction was not used in Leeming's data as all the particles were greater than 1 μm in diameter.

The shaded area in figure 3.7 represents the scatter of experimental data for isothermal turbulent pipe flow. The isothermal data of Leeming is within these limits, while the data of Romay *et al.* is slightly higher, but demonstrates a similar trend. Leeming's data for turbulent flow with only a 2000 Km^{-1} nominal temperature gradient across the pipe shows an increase in V_d^+ from the isothermal case for $\tau_p^+ < 1$, but there is no apparent effect on particles of higher inertia. It should be expected that, outside of the inertia-moderated regime, the effect of thermophoresis would decrease as particle size increased. Leeming's data shows this as a reduction in the increase in V_d^+ of the heated experiments over the isothermal experiments. The fact that there is still an increase in V_d^+ for the heated experiments at these values of τ_p^+ is due to the additional deposition mechanism of turbophoresis, which becomes increasingly important in this particular size range.

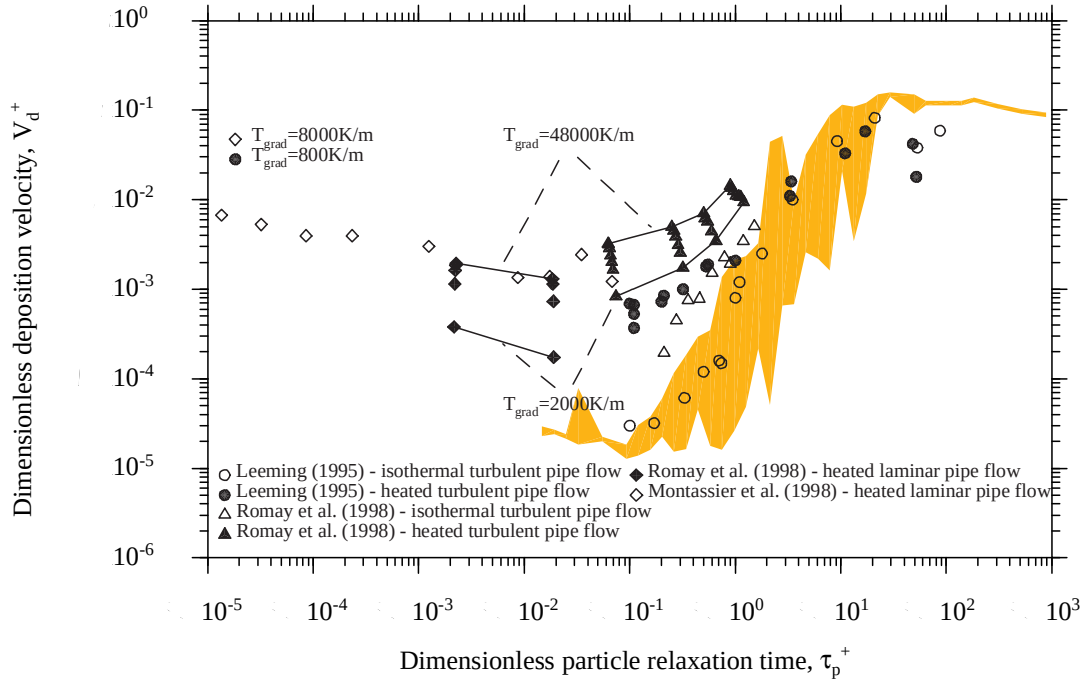

Figure 3.7: The influence of thermophoresis on the variation of dimensionless deposition velocity with dimensionless particle relaxation time in pipe flows

The trend of decreasing thermophoretic effect with increasing particle size may be seen in the data of Montassier *et al.* for laminar flow. They found that deposition was negligible in the absence of a temperature gradient for laminar flow at this range of τ_p^+, so that the deposition measured is almost completely due to thermophoresis. There is agreement between this data for laminar pipe flow (T_{grad} = 8000 Km^{-1}), and that of Romay *et al*, also for laminar pipe flow (T_{grad} = 48000 Km^{-1}). The difference between T_{grad} for the two cases does not produce significantly different values of V_d^+, which can be attributed to the approximate method of calculating V_d^+, and the decreasing effect of further increases of T_{grad} on V_d^+.

The turbulent heated pipe flow data shows an increase in deposition as T_{grad} is increased. It should be noted that the greatest increase in deposition velocity in the data of Romay *et al.* occurs when T_{grad} = 2000 Km^{-1}, and that these values are very close to those of Leeming with T_{grad} = 800 Km^{-1}. This agreement is very good when the approximations made in converting the data from deposition efficiencies to deposition velocities is considered. The Knudsen numbers for all these experiments were in the range 0.01 to 1.5.

Some problems with the available thermophoretic data

The conversion from deposition efficiency to deposition velocity is only approximate as the mean temperature of the flow decreases with distance from the inlet of the deposition pipe. When a cross-stream temperature gradient exists, the gas properties vary across the pipe, and mean values are used to calculate the Reynolds and Knudsen numbers. However, the existence

of an axial temperature gradient means that the mean gas properties also vary in the axial direction, along with the Reynolds number and Knudsen number. The thermophoretic force also decreases along the length of the pipe as the mean gas temperature approaches the (cooled) wall temperature. Leeming's experimental data is more useful, as the mass flow rates of the particle-laden flow and the counterflow cooling water were chosen so that there was a constant heat flux from the particle-laden flow to the cooled pipe wall. This resulted in a constant temperature difference, and thus a constant thermophoretic force in the section of the pipe where the measurements were made (although the mean temperature still varied axially, the variation was small enough not to alter the thermophoretic force or influence the gas properties significantly).

3.6.1 Comparison of experimental data with theory

In order to compare these experimental results with the available theories for the thermophoretic force, the thermophoretic contribution to the deposition velocity must first be separated from the contributions due to other deposition mechanisms. However, a coupling between thermophoresis and one or more of the other mechanisms may exist, in which case the separation of these contributions would not be trivial.

Comparison is possible using the results of Montassier *et al.* (1991), as they found that deposition was negligible for the isothermal laminar case. Their experimental data has been compared with the theories of Walker (1979) and Stratmann & Whitby (1989) (cited in Montassier *et al.*, 1990), both of which use the coefficient of thermophoresis η_{TH} as given by Brock (1962), with the constants suggested by Talbot *et al.* (1980). The experimental data showed good agreement with these theories, especially considering that the expression for the thermophoretic coefficient was originally derived only for small temperature gradients.

Such a comparison is not as straightforward using the turbulent results of Leeming and Romay *et al.*, as it can be seen that other deposition mechanisms were involved in the isothermal case. Romay *et al.* sought to decouple the thermophoretic component of deposition efficiency from the overall deposition efficiency through the use of the expression:

$$\eta_{combined} = \eta_1 + \eta_2 + f_{1,2} \tag{3.54}$$

where η_1, η_2 are the deposition efficiencies due to mechanisms 1 and 2, and $f_{1,2}$ is a function of the dimensionless parameters for mechanisms 1 and 2. As the value of $f_{1,2}$ will depend on the exact nature of the mechanisms involved, it was assumed to be equal to zero as a first approximation, and the same assumption was made by Nishio *et al.* (1974), i.e. complete decoupling of the mechanisms was assumed. When Leeming treated his deposition velocity data in the same way, he found too much scatter in the plots of V_d^+ against T_{grad} for the results to be meaningfully compared.

Romay *et al.* found that, once the thermophoretic component had been extracted for the turbulent pipe flow, the experimental results were a factor of 1.4-2.0 times greater than

theoretical predictions (again based on Brock's theory using Talbot's constants). They also showed that theory underpredicted the experimental data of Byers & Calvert (1969) and Nishio *et al.* (1974) by similar amounts. While a negative $f_{1,2}$ would only enhance the discrepancy, a positive value would have improved agreement, and such a value would indicate a coupling between thermophoresis and turbophoresis. Leeming (1995) also presented the results of a numerical study that showed a non-linear coupling between the isothermal and temperature dependent deposition of particles in the turbulent diffusion-eddy impaction regime. It was also found that numerical calculations (using the same expression for the thermophoretic force as Romay *et al.* (1998)) underpredicted the experimental results by a factor of two.

The experiments carried out on thermophoresis in laminar pipe flows show good agreement with available theoretical expressions, which use the expression for the thermophoretic force recommended by Talbot *et al.* (1980). The results from turbulent pipe flows indicate that there may be a coupling between the mechanisms of thermophoresis and turbophoresis for certain classes of particles, and that this coupling further enhances deposition.

3.6.2 Other experimental and theoretical work

Rosner & Fernandez de la Mora (1982) developed a theory of particle transport across turbulent boundary layers in the presence of a temperature gradient, and examined the interaction between turbulent diffusion, Brownian diffusion and thermophoresis, for small particles. Konstandopoulos & Rosner (1995a,b) carried out a theoretical and experimental study of inertial effects on thermophoresis of small particles in laminar boundary layer flows with streamwise curvature. While the important role of inertial transport of large particles is well recognised, the indirect effects of particle inertia on small particles have been widely overlooked. The authors report how particle inertia has been shown to affect deposition rates by local enrichment or depletion of the particle concentration in the vicinity of the collector.

As well as pipe flow experiments, there have been many experiments to examine the influence of thermophoresis in other applications. Nomura *et al.* (1997) and Vermes (1979) have investigated enhanced deposition to air-cooled turbine blades, while Ryley & Davies (1983) examined how thermophoresis could be used to discourage the deposition of fog droplets on steam turbine guide blades.

Chen (1999) and Chen & Xu (2002) have carried out studies on the effect of the presence of a wall on the thermophoresis of particles at small and large Knudsen numbers. For the case of small Knudsen numbers (of more interest to this work), the effect only becomes significant when the ratio of the particle radius to the distance from the wall is less than 0.5. Gallis *et al.* (2002) studied this effect over the entire range of Kn and found that the force increased slightly (less than 5%) near the wall, with the greatest increase being for the smallest Kn.

3.6.3 Proposed work

Previous pipe flow experiments have involved heating the particle-laden flow before passing it through a pipe with a cooled outer wall. The temperature of the gas and particles then decreases along the length of the pipe. The result of this is that the conversion of the pipe flow data from deposition efficiency to deposition velocity (shown in figure 3.7) was only approximate, and the thermophoretic force was not constant. Under such conditions, a constant thermophoretic force may be achieved by a constant heat flux from the pipe walls to the flow, but only if the axial variation in mean temperaure is small and the temperature field is fully-developed. However, only the data of Leeming takes note of this, and measures deposition in the part of the pipe where the temperature field is fully-developed with a constant thermophoretic force. Unfortunately, a nominal temperature gradient of just 800 Km^{-1} existed in this part of the pipe. The requirement for a constant heat flux (∇T = constant) and a constant mean temperature for a constant thermophoretic force comes from the fact that $\mathbf{f}_{TH} \propto \nabla(lnT) = \nabla T/T$.

The recommendations of Leeming (1995) were adopted for the present work. Thus, an annular arrangement like that of Wells & Chamberlain (1967) for isothermal flow was used, but with the inner wall cooled and the outer wall heated, so that once the temperature field is fully-developed, the flow experiences a constant temperature difference, and thermophoretic force. The particle-laden gas will not decrease in temperature as it flows down the annulus as happened in previous pipe flow experiments. It will flow between two walls maintained at constant temperatures, and hence it will now be possible to achieve a fully-developed temperature field with large temperature differences, and with very limited axial variations in mean gas properties.

Owen *et al.* (1989) and Chiou & Cleaver (1996) carried out experiments on thermophoresis in annular arrangements. However, Chiou & Cleaver (1996) investigated the case of laminar flow, and Owen *et al.* (1989) used only particles with very small τ_p^+ ($\approx 10^{-2}$). It is worth noting that both studies used uranine particles and a fluorimetric analysis technique, and that both studies seem only to have measured the deposition to the inner pipe of the annulus (in common with Wells & Chamberlain (1967)). As will be seen when the method of calculating the deposition velocity in an annulus is presented later, it should not be possible to calculate the deposition velocity on one surface, without analysing the deposit on the other surface, unless the deposition velocity to the omitted surface is negligible . It is hoped that the annular arrangement will improve the accuracy of the experiments by providing a range of constant thermophoretic forces in fully-developed temperature fields with constant mean temperatures, resulting in a datum against which any potential coupling between thermophoresis and other deposition mechanisms may be investigated, and expressions for the thermophoretic force may be validated.

Chapter 4

Experimental study of thermophoresis in a turbulent annular flow - design and procedure

4.1 Introduction

There have many experimental studies of the relationship between particle size and deposition rate, and most of these have been carried out in a fully-developed turbulent pipe flow, in which no temperature gradient exists (reviewed in section 3.4). This relatively simple flow field, featuring many of the transport mechanisms previously discussed, was understandably attractive to researchers.

With the large of amount of experimental data available for such flows (and results which are well established), attention has now turned to studying the mechanism of thermophoresis in fully-developed turbulent pipe flow. One possibility is that the gas-particle flow is heated before it enters the pipe, and the wall of the pipe is cooled, so that a temperature difference exists between the flow at the centre of the pipe and the pipe wall. However, as the gas-particle flow moves through the pipe its temperature decreases, and this detracts from the usefulness of the data obtained because the thermophoretic force varies along the length of the pipe. Experimental conditions can be arranged in such a way that the wall temperature also decreases so that a constant temperature difference, and hence a constant thermophoretic force, is maintained (Leeming, 1995). The disadvantage of such an arrangement is that high temperature differences are difficult to achieve. Alternatively, high temperature differences may be achieved, but without a constant temperature difference (Romay *et al.*, 1998). If the cold wall is maintained at a constant temperature while the hot gas-particle flow loses heat as it moves along the pipe, then the gas properties (such as density and dynamic viscosity) also change along the pipe as the temperature changes, and this leads to variations in the thermophoretic coefficient, Knudsen number and Reynolds number. This makes it difficult to reliably non-dimensionalise the results in the traditional (and most useful) manner, involving

dimensionless deposition velocity and dimensionless particle relaxation time.

The experiments described here involve the study of turbulent flow in an annulus, subsequently referred to as turbulent annular flow (this is definitely not to be confused with annular gas/liquid flows where part of the liquid moves as a film on the pipe wall and part is entrained as droplets in the high-velocity gas core). The inner wall of the annulus is cooled and the outer wall heated, in such a way that the temperature of each is (almost) constant. A near constant thermophoretic effect along the length of the annulus is then achieved (although the thermophoretic force varies across the annulus), without a variation in gas properties, and in such a way that high temperature differences may be achieved. The first part of the study involved a set of isothermal experiments, to provide a datum against which to compare the thermophoresis experiments, and a link to the turbulent pipe flow experiments of other researchers. The thermophoresis experiments were carried out for a range of particle sizes, with a number of temperature differences.

This chapter deals with the many factors which were considered during the design of the experiment, and the establishment of a procedure for performing an experiment and analysing the measurements to obtain a result. The complete set of results are presented and discussed in the next chapter, and will be shown to provide invaluable new data on the influence of thermophoresis on particle deposition, against which computational models containing theoretical expressions for thermophoresis (and the other transport mechanisms) may be assessed.

4.2 Experimental overview

The experiment is best described by dividing it into a number of parts:

1 Aerosol particles tagged with a fluorescent tracer were generated and entrained by a flow of air.

2 The particle-laden flow then underwent a series of preparations on its journey to the test section.

3 The particle-laden flow then entered an annular region between two pipes. The inner wall of the annulus was cooled by a flow of water, and the outer wall was heated by a heating tape wrapped around its outer side. The particle-laden flow passed through this annular arrangement and a fraction of the particles deposited on the pipe walls. The remainder of the particles were removed from the flow by a filter at the end of the annular section, and the air was exhausted to the atmosphere.

4 Temperature and pressure measurements were taken to determine the conditions under which deposition occurred.

5 At the end of a run, the annular test section was removed. The inner and outer pipes and the filter paper were washed, and the washings were analysed using a luminescence spectrometer.

6 The quantity of fluorescent tracer (and hence the fraction of particles) deposited on each pipe wall was determined from an analysis of the washings, and this information was used to determine the rate of deposition to each pipe wall for the particular size of particle generated.

4.2.1 Particle generation

The TSI model 3450 vibrating orifice aerosol generator (VOAG) (TSI Inc, 1998) produces a spherical, near monodisperse aerosol of known particle size and concentration from any material in solution form. A syringe pump forces an aerosol solution from a syringe, at constant flowrate, through an extremely small orifice in a disk, so that the solution forms a liquid jet. Such a jet is naturally unstable and tends to break up into droplets. Left uncontrolled, non-uniform droplets would be produced, but the application of a periodic disturbance of an appropriate frequency to the jet results in the production of extremely uniform droplets. This is done by applying a signal across a piezoelectric ceramic, which produces a mechanical vibration in the orifice disk. The aerosol generator is shown in figure 4.1.

One droplet is produced per cycle of disturbance, so that if the liquid feed rate of the aerosol solution and the frequency of the applied disturbance are known, the volume of a single droplet may be accurately calculated. Then, the droplet diameter, d_d (in cm), is calculated from:

$$d_d = \left(\frac{6Q_l}{\pi f} \right)^{\frac{1}{3}} \tag{4.1}$$

where Q_l is the liquid feed rate ($cm^3 s^{-1}$) and f is the frequency of the disturbance (Hz).

A number of different sized orifices are available for use with the aerosol generator, and 10, 20 and 35 μm diameter orifices were used in these experiments. Apart from the upper size limit that the diameter of the orifice places on the particle to be generated, the diameter of the orifice only affects the droplet diameter through the limitations that it places on the choice of liquid feed rate and disturbance frequency. These limitations are that there is a minimum liquid velocity needed to form a liquid jet, and that uniform droplets can only be produced if the frequency of the disturbance is within a certain range. The minimum liquid velocity and the limits of this frequency range are determined by the orifice diameter.

The droplet diameter (d_d) does not represent the diameter of the final aerosol particle. The aerosol solution components were a non-volatile solute (oleic acid, uranine and any non-volatile impurities initially present in the solvent) in a volatile solvent (propan-2-ol and deionised water). When this solution passed through the orifice and had been broken up into

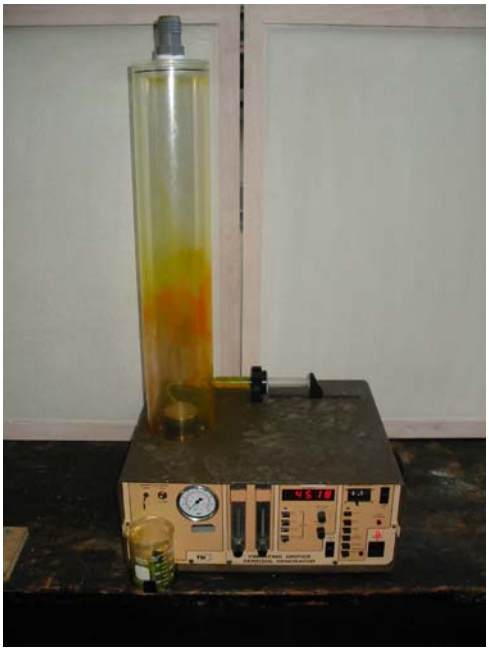

Figure 4.1: The TSI model 3450 VOAG (note the drying column on top)

droplets, it was dispersed and then diluted with air in a drying column above the aerosol generator. This prevented agglomeration (the joining of one or more droplets into a single larger droplet), and allowed the solvents to evaporate, leaving a final aerosol particle which consisted of a solid core of uranine surrounded by a liquid coating of oleic acid, with a diameter d_p. This liquid coating helped to ensure that when a particle deposited on the pipe wall, the adhesive forces were sufficient to prevent re-entrainment. Uranine was used as a fluorescent tracer.

Once an orifice had been chosen and a suitable frequency and liquid feed rate selected, the diameter of the final aerosol particle, d_p, depended only on the volumetric concentration of the solute in the aerosol solution. The final particle diameter is found using:

$$d_p = \left(\frac{6 Q_l C}{\pi f} \right)^{\frac{1}{3}} \qquad \text{where} \qquad C = \frac{V_o}{V_s} \left\{ 1 + \frac{c_u}{\rho_u} + I \frac{V_p}{V_o} \right\} \tag{4.2}$$

C is the volumetric concentration of non-volatile solute in the solution, V is the volume of a solution constituent, and subscripts o, p, s and u refer to oleic acid, propan-2-ol, the entire solution and uranine, respectively. c_u is the mass of uranine per unit volume of oleic acid, ρ_u is the density of uranine, and I is the volumetric concentration of the non-volatile impurity in the particular grade of propan-2-ol used in these experiments.

Manipulation of equation 4.2 with the substitution of some basic volumetric relationships allows the particle material density to be calculated using:

$$\rho_{p,mat} = \frac{1}{C V_s} \left\{ V_o (\rho_o + c_u) + \rho_I V_p I \right\} \tag{4.3}$$

where ρ_I is the mean density of the non-volatile impurities in the grade of propan-2-ol used. The physical properties of these reagents are given in table 4.1. c_u was chosen as 0.1 gcm^{-3} to match previous experimental studies (Liu & Agarwal, 1974; Leeming, 1995), and this fixed $\rho_{p,mat}$=931 kgm^{-3}. V_s was chosen to be large enough for the experiment to be run for long enough that a measurable quantity of uranine could deposit (ranging from thirty minutes for large particles to thirty six hours for the smallest).

The theoretical particle concentration at outlet from the aerosol generator, $C_{p,out}$, is given by:

$$C_{p,out} = \frac{f}{Q_a} \tag{4.4}$$

where Q_a is the total volumetric flow rate of air through the aerosol generator. The actual particle concentration at entry to the deposition annulus was less than $C_{p,out}$ due to particle deposition in the drying column and in the flexible tubing and pipes through which the particle-laden flow of air passed on its way to the annular test section.

Reagent	Property	Value	Source
Uranine	ρ_u	1.53 gcm^{-3}	Olan-Figueroa *et al.* (1982)
	k_u	0.43 Wm^{-1}K^{-1}	Al-Azzawi & Owen (1984)
Oleic acid	ρ_o	0.892 gcm $^{-3}$ @ 20°C	Weast (1988, pg. C-385)
	k_o	0.230 Wm^{-1}K^{-1} @ 26.5°C	Weast (1967)
Non-volatile propan-2-ol impurity	ρ_I	1.0 gcm $^{-3}$	Fisher Scientific UK (2001)
	I	0.001 %	Fisher Scientific UK (2001)

Table 4.1: Physical properties of aerosol solution reagents

Validation of particle generation

It is of great importance that the size of the particles generated is known accurately. Berglund & Liu (1973) have shown that the use of equation 4.2 to determine particle diameter is much more accurate (as well as easier) than 'conventional microscopic sizing techniques'. However, even if the particle diameter can be calculated with confidence without the use of microscopic techniques, the quality of the particles generated must still be assessed. A particular operating frequency may be within the limits of the frequency range for a particular orifice, and still produce droplets that are not monodispersed. Smaller 'satellite' particles may be produced, or larger 'doublets' and 'triplets' (twice and three times the intended size). Insufficient dispersion or dilution air may result in particle agglomeration. Any of these effects would result in a discrete number of particles of different diameter from that calculated using equation 4.2, and this would affect both τ_p^+ and V_d^+.

One method of collecting oil particles (oleic acid in this case) is through the use of an oleophobic surfactant (e.g. Liu & Agarwal, 1974). A sampling jet (located before the test

section) was opened and particles were collected on a 6mm diameter microscope slide cover-glass coated with the surfactant. However, the particles on the slide were 'flattened' due to the action of surface tension and interfacial forces, resulting in an observed size that was larger than the particle diameter prior to collection. A flattening coefficient is defined to relate the observed size to the true size, and a different flattening coefficient exists for each particle-surfactant combination (Olan-Figueroa *et al.*, 1982). In the past, as surfactants were replaced with newer ones, flattening coefficients were determined for the replacement surfactants. The withdrawal from the market of the widely used FC-721 (3M Co.) has not coincided with the determination of a flattening coefficient for any new surfactant that can be used in conjunction with oleic acid. Hence, the surfactant used in these experiments (Certonal TL6x(J), Layton plc) had an unknown flattening coefficient. As this made determination of the exact particle diameter impossible, microscopic analyses were carried out only to assess the mondispersivity of the particles, the level of agglomeration and to give an indication of the particle diameter. Figure 4.2 shows a comparison between two slides representative of poor quality and good quality aerosols. A number of discrete particle diameters (approximately 3.6, 4.5 and 6.8 μm) can be seen in figure 4.2a, as well as a number of non-spherical particles, indicating a poor quality aerosol). Figure 4.2b shows a monodisperse aerosol with a particle diameter of approximately 9.2 μm. Note that the uranine core surrounded by a liquid coating of oleic acid is clearly visible.

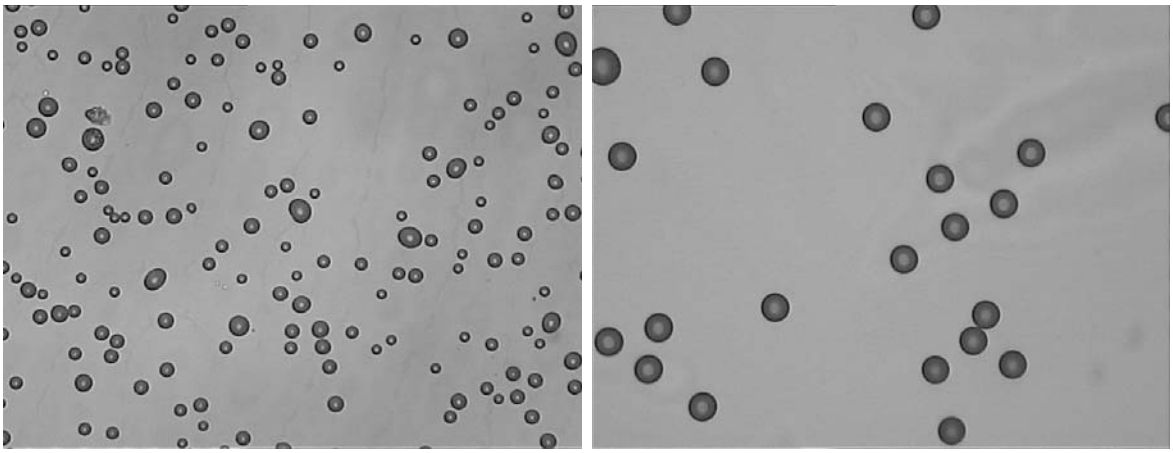

a) b)

Figure 4.2: Particles of uranine and oleic acid collected on slide cover-glasses coated with an oleophobic surfactant: a) poor quality aerosol; b) good quality aerosol

4.2.2 Preparation of particles for the deposition pipe

Before a particle-laden flow can be used to study deposition, certain precautions must be taken so that the mechanisms causing deposition can be identified. Clean dry compressed air entered the aerosol generator and left it carrying an electrically charged cloud of aerosol

particles. An electrical charge would have enhanced deposition (Montgomery & Corn, 1970), so the flow was directed past a 10 mCi Krypton-85 radioactive source (TSI model 3054 aerosol neutraliser). The ionizing Beta radiation left a bipolar residual charge on the particles, but the aerosol cloud as a whole was electrically neutral (Liu & Agarwal, 1974).

The particle-laden flow was then mixed with a secondary flow of air because the air flow required was higher than the rated output of the aerosol generator (which is just 100 lpm). In certain cases, it was necessary for the particle-laden flow to be heated before entry to the test section (for the heated runs to investigate the effects of thermophoresis, this reduced the length of annulus required to attain a fully-developed temperature field). The aerosol generator was not designed for high temperature air flows, so the temperature of the particle-laden flow was increased through mixing with the secondary flow which had passed through a 1600W threaded inline heater (Hawco Ltd.) (see figure 4.3 for a schematic diagram of the rig).

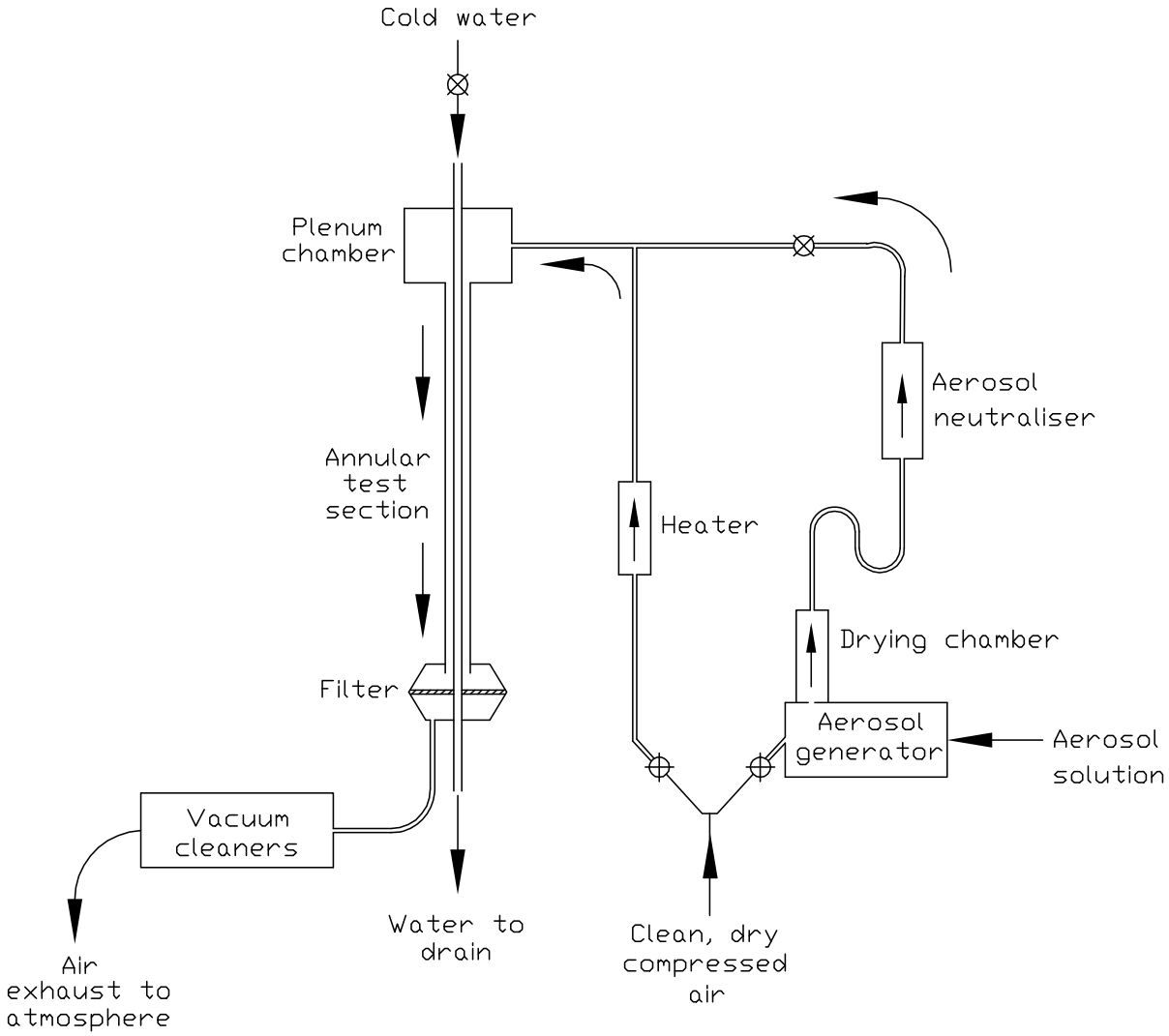

Figure 4.3: A schematic diagram of the experimental rig

As a precaution against swirl in the deposition annulus, and to allow thorough mixing of the two component flows, the flow was directed into a plenum chamber (see figure 4.4). When the flow entered the plenum chamber, a baffle placed in front of the inlet forced it to circulate throughout the chamber, rather than proceeding directly into the deposition annulus. A circular header tube with a spiral arrangement of holes was located around the exit from the plenum chamber (and extended to the roof of the chamber), so that the flow entered the header from all sides before proceeding in a uniform non-swirling manner to the deposition annulus. The baffle and header geometries were designed so as to remove as few particles as possible from the flow.

Figure 4.4: Plenum chamber measuring 280mm x 175mm x 120mm (note that the baffle and a header have been removed - the rig was originally designed to operate with an additional 'bypass' pipe)

4.2.3 Deposition annulus

The deposition annulus represented the test section in this experiment (although the entry and exit regions were neglected as the flow may not have been uniform here). The schematic diagram of figure 4.5 is intended to complement the following description. The deposition annulus consisted of a 15 mm outside diameter (d_i) stainless steel tube placed concentrically in a 23 mm inside diameter (d_o) brass pipe. The brass pipe extended from the bottom of the plenum chamber to the top of the filter assembly. The brass pipe (and deposition annulus) was 2.4 m in length. The stainless steel tube was longer and passed through the top of the plenum chamber (through the centre of the header) and the bottom of the filter assembly. Cold water could be directed downwards through the stainless steel tube, while the particle-laden flow passed from the plenum chamber, vertically downwards between the stainless steel tube and brass pipe, and into the filter assembly. A 110 mm diameter Whatman

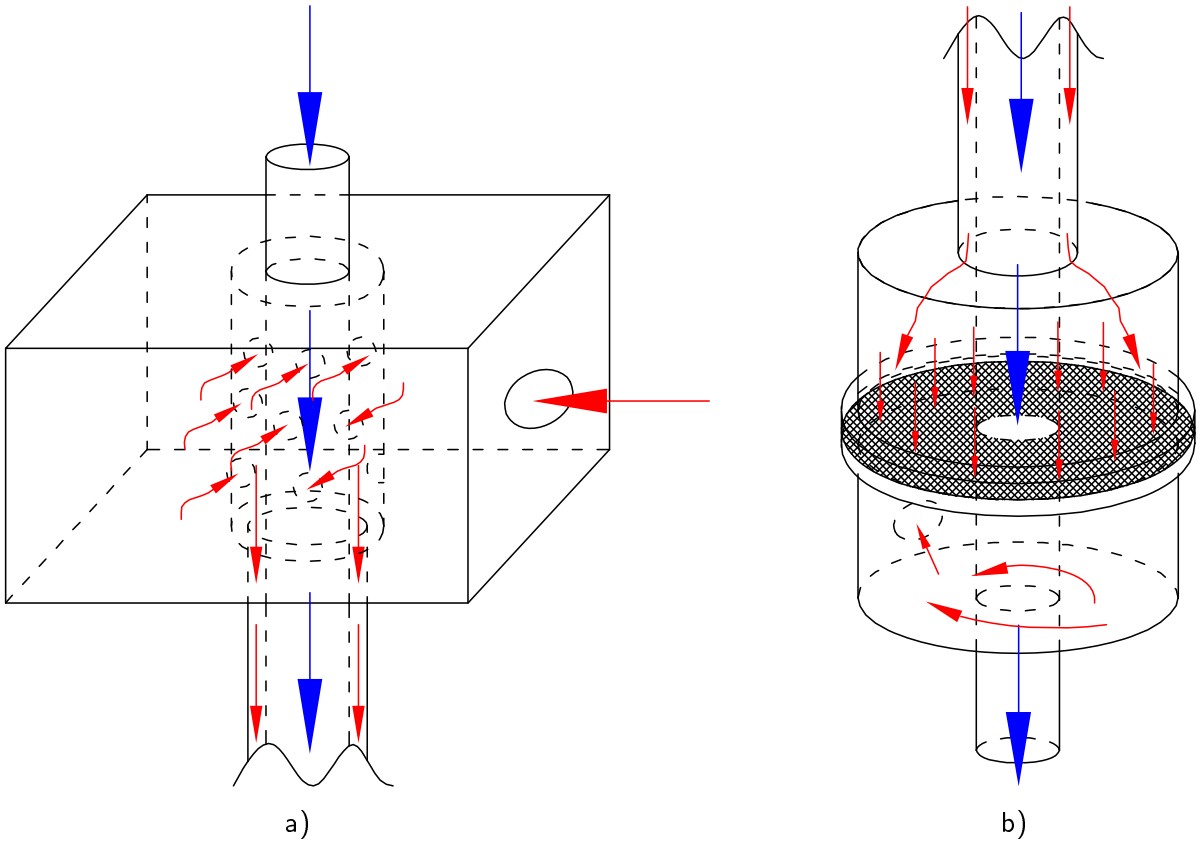

Figure 4.5: A schematic diagram of the particle-laden flow and cooling water as they enter and exit the annular test section: a) entrance via the plenum chamber; b) exit via the filter assembly. Blue arrows represent the flow of water, and red arrows the particle-laden flow. The hatched area of b) represents the filter paper, and the air exits the filter below this, towards the rear of the bottom half of the filter assembly.

glass microfibre (GF/A) filter with 1.6 μm retention was placed across the flow in the filter assembly, to capture any particles which remained suspended in the flow (when using particles smaller than 1.6μm, GF/B filter paper with 1.0 μm retention was used). It was supported by a circular steel mesh, and the stainless steel tube passed through the centre of the filter paper and its supporting mesh. A nitrile rubber o-ring ensured that there was no flow between the stainless steel tube and the filter paper. An 800 W (16 ft x 1 in) heating tape (Electrothermal Engineering Ltd) was wrapped around the outside of the brass pipe, and a controller was used to control the power to the heating tape, maintaining it at a constant temperature. The plenum chamber, filter assembly, heating tape and brass tube were wrapped in aluminium foil, and lagged with Armaflex insulating sheets (Armacell UK Ltd) and Rocklap 800 pipe insulating section (Rockwool Ltd) to prevent heat loss. Both the tube and the pipe were earthed to remove any electrical charge that might have affected deposition.

It has already been stated that the use of a plenum chamber helps in preventing swirl in the deposition annulus. It is well known (e.g. Liu & Agarwal, 1974) that the existence of secondary flows in pipes can influence particle deposition rates, particularly for small particles.

If swirl is present in a turbulent pipe flow, the rotation of the flow as it moves down the pipe subjects the particles to centrifugal forces which cause them to deposit at a much higher rate than expected, as seen in certain experiments of Leeming (1995). A further precaution to prevent swirl was the use of a flow straightener (see figure 4.6) at the entrance to the deposition annulus. A twelve-finned 25 mm long flow straightener was attached to this end of the deposition annulus, and a similar flow straightener was also attached to the lower end of the annulus. Together, they also served the purpose of locating the inner tube concentrically within the outer pipe. They also prevented the removal of deposited particles from either surface when the inner tube was removed from within the outer pipe for washing. These flow straighteners were omitted from figure 4.5 for clarity. Both deposition surfaces were confirmed to be aerodynamically smooth.

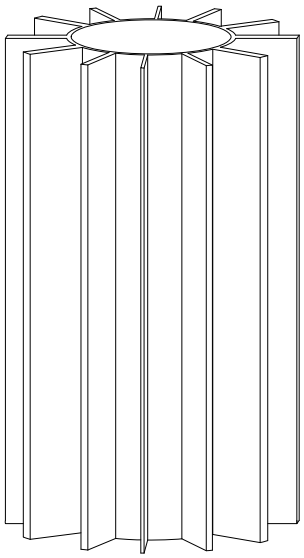

Figure 4.6: A schematic diagram of a flow straightener

Experimental limitations

There were certain limitations on particle size and the flow conditions attainable. The maximum pressure in the system was limited to approximately 1.1 bar by the fact that, at higher pressures, the drying column would lift off the aerosol generator. While the hydraulic diameter of the deposition annulus ($d_h = d_o - d_i = 0.8$ cm) was close to the 1.27 cm diameter pipe used by Liu & Agarwal (1974) and the 1 cm diameter pipe of Leeming (1995), the flow area was much greater, and so compressed air would need to have been supplied at pressures far in excess of 1.1 bar in order to reach some of the higher flow rates and Reynolds numbers used in these other experiments (The highest Reynolds number used by Leeming was 20000 while Liu & Agarwal used 50000). Two vacuum motors were arranged in parallel downstream

of the filter assembly to draw the air through at higher flow rates. The maximum possible Reynolds number attainable was still limited to 6000.

One of the consequences of using vacuum motors was that the pressure fell below the atmospheric level in much of the system, so that use of the sampling jet in the plenum chamber to collect particles on a slide (see figure 4.2) resulted in air being drawn into the system, rather than a sample emerging from the jet. Therefore, sampling had to take place at the end of the run, with the vacuum motors switched off, and with a lower air flow rate than was used during the experiment. This was not ideal when trying to test the quality of the aerosol produced, as agglomeration may have occurred at the lower flow rate, but not during the actual experiment. Sampling was therefore used as an indication of the worst case, so that if the sample were free from agglomeration, the experiment was also considered to be free from agglomeration. If only a small amount of agglomeration was observed, then it was assumed that this occurred due to the sampling method and that there was no agglomeration during the experiment (when higher air flow rates were used).

The dimensionless quantity τ_p^+ has been previously defined (equation 3.42) as the ratio of the particle to the gas relaxation times. For turbulent pipe flow, the gas relaxation time is traditionally based on a characteristic eddy time-scale (given by ν_g/u_*^2). It follows that τ_p^+ can be increased by increasing the particle diameter d_p (and hence τ_p), or by increasing u_* through an increase in the pipe Reynolds number. There were limitations on the size of particle that could be generated by the aerosol generator. Its operating conditions and the difficulty in measuring out very small quantities of uranine and oleic acid prohibited the generation of particles smaller in diameter than approximately 1 μm, while larger particles requiring greater quantities of uranine and oleic acid resulted in the persistent clogging of the small orifice disks. As a result of these limitations, Liu & Agarwal (1974) and Leeming (1995) achieved large values of τ_p^+ by increasing the pipe Reynolds number, an option not available in these experiments. Consequently, τ_p^+ was limited to the range 10^{-1}-10^2 in the experiments described below.

4.2.4 Determination of the flow conditions

A number of measurements were made so that the gas properties were fully known, allowing calculation of u_*, τ_p^+ and V_d^+, and the determination of the conditions under which deposition had occurred. The volumetric flow rate of air was measured using a Platon rotameter (with a 20-180 lpm range) downstream of the filter assembly, and at the same point pressure and temperature measurements were made. The rotameter reading was corrected for pressures and temperatures that deviated from calibration conditions. The volumetric flow rate of air was given by $Q_a = Q_{ind}\sqrt{(p_{cal}T_{rot})/(p_{rot}T_{cal})}$, where Q_{ind} is the indicated flow rate, and the subscript cal refers to calibration conditions and rot refers to actual rotameter conditions. The density of the flow at this point was then found using the equation of state for a perfect gas. By making pressure and temperature measurements in the deposition annulus, and using

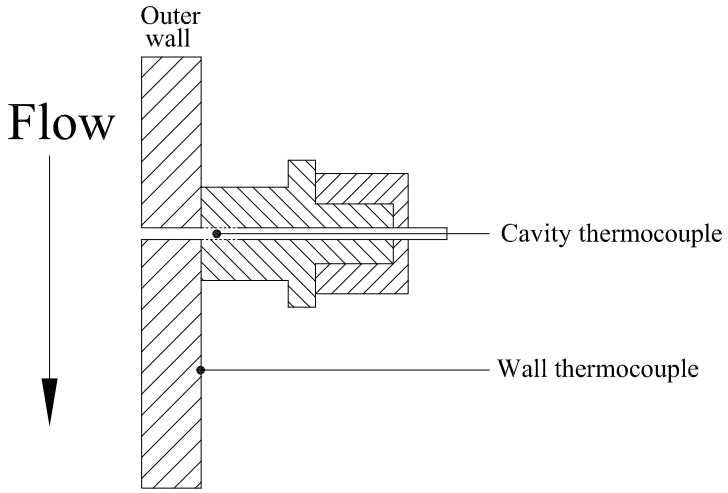

Figure 4.7: A schematic diagram of a thermocouple on the outer wall of the annulus, and a thermocouple in a wall cavity

the principle of conservation of mass, the mean flow velocity was calculated.

Temperature measurement

It was also necessary to have a knowledge of the temperature distribution along the length of the annulus. While there were heat losses at either end of the annulus, the lagging and heating tape controller combined to maintain a constant (high) temperature over a large part of the pipe. By heating the secondary flow of air (see figure 4.3) and thus elevating the temperature of the particle-laden flow supplied to the test section, the distance taken along the deposition annulus to attain a fully-developed temperature profile was reduced. Accordingly, the temperature of the flow after the heater and in the plenum chamber was measured. The temperature of the cooling water before it entered the stainless steel tube and downstream of the filter assembly was also measured to confirm that the flow rate was sufficient to maintain a constant (low) temperature at the stainless steel tube wall.

K-type thermocouples were attached to the outside of the brass pipe to measure the temperature profile along the annulus. It was too difficult to place the thermocouples in such a way that they were all equidistant from the heating tape that spirals around the pipe wall, so that some of the thermocouples may have measured the temperature of the heating tape, rather than the temperature conducted along the brass pipe. To guard against this, further temperature measurements were made by welding a number of bosses onto the wall of the brass tube, each of which held a thermocouple in a cavity between the boss and the pipe wall (see figure 4.7). Each cavity had access to the annular flow area through a 2.5 mm hole, so that these thermocouples measured the approximate temperature of the flow at the wall, and these measurements were used to verify that those taken from the wall thermocouples were correct.

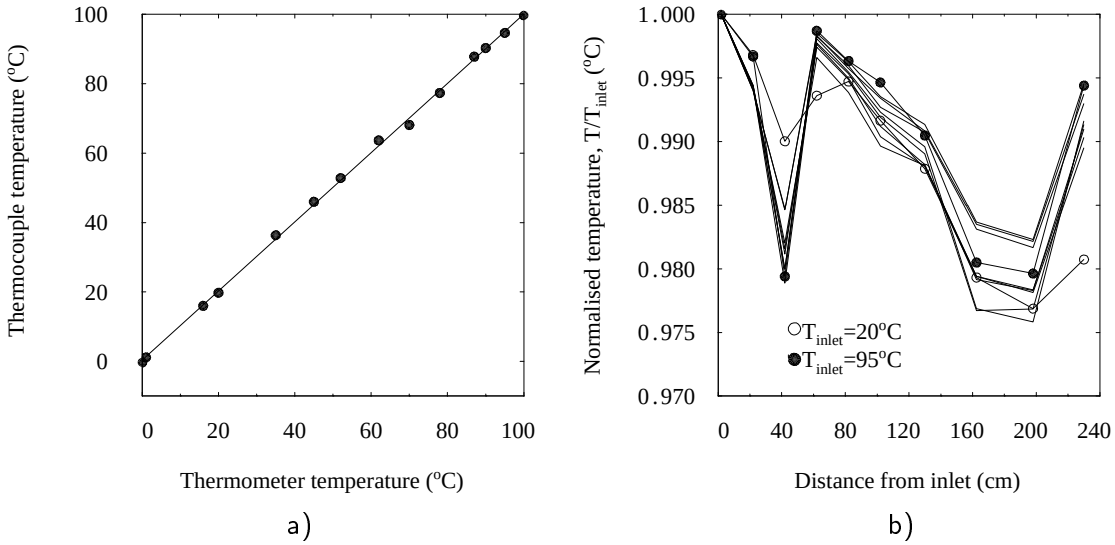

Figure 4.8: Thermocouple calibration: a) TC1 against a mercury thermometer in a water bath; b) TC1 against remaining flow thermocouples in a water bath

The thermocouple temperatures were logged using a personal computer and two TC-16 modules of a Biodata Microlink III mainframe. The TC-16 modules were each connected to an isothermal box housing thermocouple reference junctions and a platinum resistance thermometer to measure the temperature at these junctions.

Calibrating the wall thermocouples before attaching them to the pipe wall would not have been very useful, as a second form of calibration would have been necessary to take into account the proximity (or otherwise) of each thermocouple to the heating tape. Accurate calibration of the 'cavity' thermocouples could have been carried out, but the action of replacing and removing the thermocouples before and after each run resulted in slight alterations to the thermocouples. Therefore, a 'rough' calibration procedure was adopted to check the linearity of the thermocouple readings over the temperature range. This was repeated from time to time.

The results presented in figure 4.8 were taken after the entire set of experiments had been completed. Figure 4.8a shows the variation in the temperature of the inlet 'cavity' thermocouple (TC1) against a mercury thermometer in a water bath. The results are plotted as temperature against temperature, rather than voltage against temperature. The thermocouple temperature was found using a five term power series expansion (incorporated within the logging software) which linearises the variation of thermocouple voltage over a range of temperatures, assuming a 0 °C cold reference junction (Biodata Ltd, 1986). Figure 4.8b shows the variation in temperature of all the 'cavity' thermocouples when placed in a water bath (although the x-axis label in this figure refers to their position when in the annulus). The temperatures were logged at several intervals between 20 and 95 °C, and the temperatures were normalised using the temperature of TC1 (T_{inlet}), at each interval. It can be seen that over

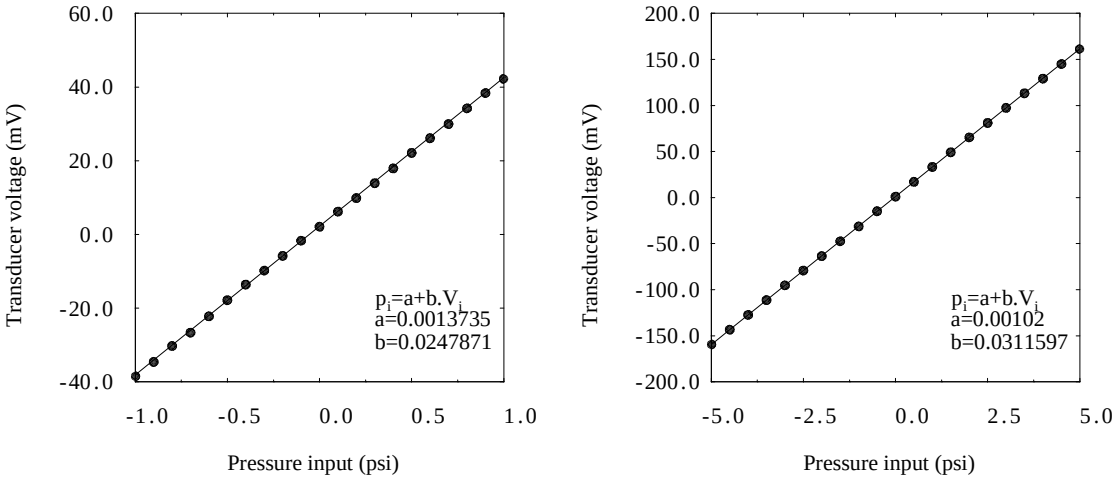

Figure 4.9: Pressure sensor calibration: a) 0-1 psi; b) 0-5 psi

this range of temperature, the greatest deviation from linearity for any of the thermocouples was 2 % of T_{inlet} (°C). Even though the highest temperature (140 °C) that the thermocouples were subjected to was outside of the range of the calibration, the linearity of these thermocouples was assumed to hold. 2 % of the highest temperature is only marginally greater than the 2.5 °C tolerance value associated with K-type thermocouples. The thermocouple readings taken were assumed to be 'true', and the errors were accounted for by including a 2.5 °C bias limit in the uncertainty analysis of the temperature measurement (see appendix C.2).

Pressure measurement

Two pressure sensors (Honeywell Ltd) were used to monitor the pressure in the plenum chamber (0-1 psi range) and at the rotameter (0-5 psi range). The pressure sensor outputs were amplified (with a gain of 100 and 50 respectively) before being input to the PGA-16 module of the Microlink mainframe, as it was found that interference would otherwise corrupt the measurement of such small voltages. The pressure sensors were calibrated using a Druck DPI 610 pressure calibrator, and the results are shown in figure 4.9.

Measurement of pressure drop along the annulus and determination of friction velocity

The friction velocity (u_*) for the annulus must be known, as it is used to find both the dimensionless deposition velocity (V_d^+) and the dimensionless particle relaxation time (τ_p^+). u_* is a function of the pressure drop along the annulus. For fully-developed flow in a pipe, a control volume analysis can be used to show that:

$$\tau_w = \frac{r}{2}\left(-\frac{dp}{dz}\right) \tag{4.5}$$

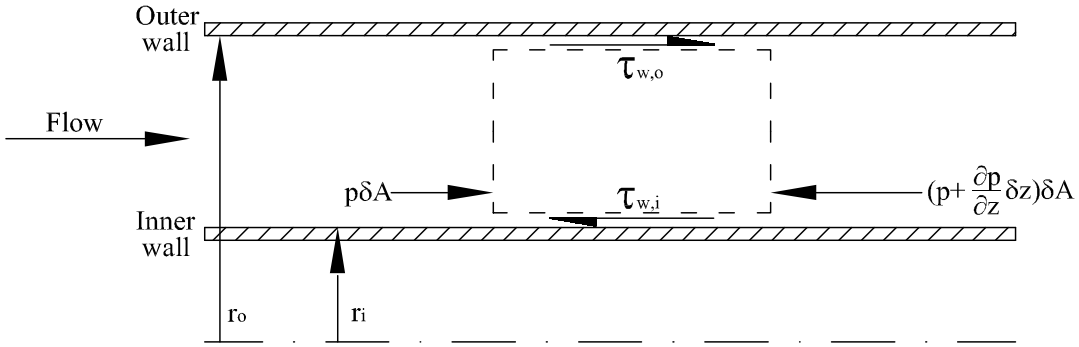

Figure 4.10: A control volume analysis of the pressure drop along an annulus

where τ_w is the wall shear stress, r is the pipe radius, and $-\frac{dp}{dz}$ is the pressure gradient along the pipe. The skin friction coefficient (C_f) is defined by:

$$\tau_w = C_f \frac{\rho_g U_m^2}{2} \tag{4.6}$$

and the friction velocity by:

$$u_* = \sqrt{\frac{\tau_w}{\rho_g}} = U_m \sqrt{\frac{C_f}{2}} \tag{4.7}$$

In the case of the annulus, there is both an inner and outer wall, with associated wall shear stresses ($\tau_{w,i}$ and $\tau_{w,o}$) and wall friction velocities ($u_{*,i}$ and $u_{*,o}$). A control volume analysis of fully-developed flow in an annulus (see figure 4.10) of area $A = \pi(r_o^2 - r_i^2)$ shows that:

$$\frac{r_i \tau_{w,i} - r_o \tau_{w,o}}{r_o + r_i} = \frac{(r_o - r_i)}{2} \left(- \frac{dp}{dz} \right) \tag{4.8}$$

where r_i and r_o are the inner and outer wall radii. It should be noted that $\tau_{w,i}$ is positive, and $\tau_{w,o}$ negative. By comparison with equation 4.5, a mean wall shear stress may be defined as:

$$\overline{\tau}_w = \frac{r_i \tau_{w,i} - r_o \tau_{w,o}}{r_o + r_i} \tag{4.9}$$

The magnitudes of shear stress and friction velocity at the inner and outer walls are very close to each other, so that the mean wall shear stress is representative of the magnitude of the shear stress at either wall. The same point can be made with regard to the friction velocities, where the mean friction velocity is defined in terms of $\overline{\tau}_w$ by $u_* = \sqrt{\overline{\tau}_w / \rho_g}$. It should be noted that $\tau_{w,i}$ is slightly larger in magnitude than $\tau_{w,o}$ (Brighton & Jones, 1964).

In order to obtain the mean friction velocity, the outer wall thermocouple attachments were replaced with pressure tappings, and a water manometer was used to measure the pressure

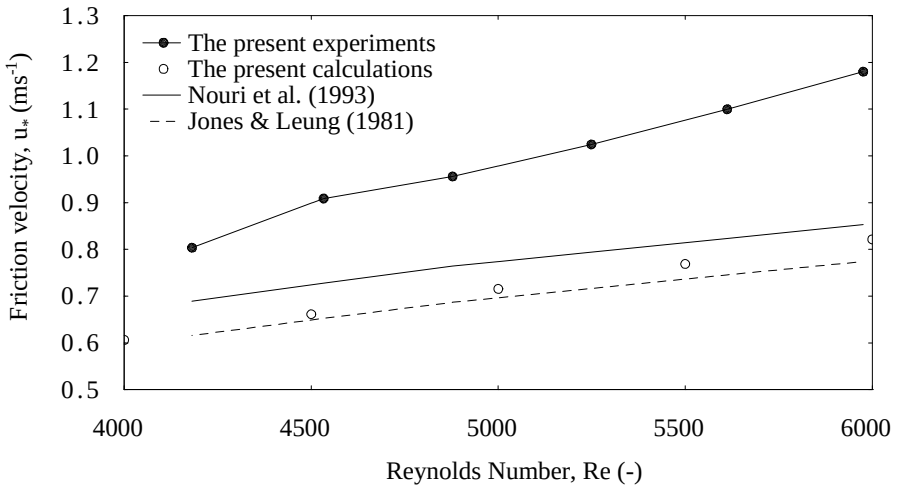

Figure 4.11: The variation of friction velocity with Reynolds number in a turbulent annulus

differences between a point located 120 cm from the top of the annulus, and three other points (at 20 cm intervals further down the annulus). The values of pressure at each of these three points were used to find an average value of $\frac{dp}{dz}$ for that particular Reynolds number. The flow rate was altered, and the measurements repeated until the range of Reynolds number used in the experiments had been spanned. The friction velocity was then calculated for each value of pressure gradient, and the variation of friction velocity with Reynolds number is shown in figure 4.11. Also shown are u_* values found from the least squares fit of Nouri *et al.* (1993) to their own experimental data for C_f:

$$C_f = 0.36Re^{-0.39} \tag{4.10}$$

One of the most complete studies of turbulent flow in annuli is that of Jones & Leung (1981), who found a correlation for the friction factor which was compared against a large number of experimental results over a range of Reynolds numbers and radius ratios ($r^* = r_i/r_o$). Their correlation reduced the observed data scatter to approximately $\pm 5\%$. This correlation was:

$$\frac{1}{\sqrt{f}} = 2\log_{10}(Re\phi^*\sqrt{f}) - 0.8 \quad \text{where} \quad f = 4C_f \tag{4.11}$$

and ϕ^* is a shape factor that takes into account the geometric alterations of the flow by radius ratios which vary between the extreme cases of $r^* = 0$ (pipe) and $r^* = 1$ (flat plate). It is given by:

$$\phi^* = \frac{1}{(1-r^*)^2}\left[1 + r^{*2} + \frac{1-r^{*2}}{\ln r^*}\right] \tag{4.12}$$

u_* was found from this correlation, and also plotted are the values of u_* found from a computer code written by the author (details of this code may be found in appendix D.1). The correlation of Jones & Leung (1981) agrees very well with the author's calculations, and is also close to the least squares fit of Nouri *et al.* (1993). The experimental data shows the correct trend, but its magnitude is considerably larger. However, the pressure differences measured were small and even very small burrs in pressure tappings can cause significant errors. The errors may be of the same order of magnitude as the pressure differences measured (Brighton & Jones, 1964). It was concluded that the correlation of Jones & Leung (1981) represented the most accurate source for values of u_*.

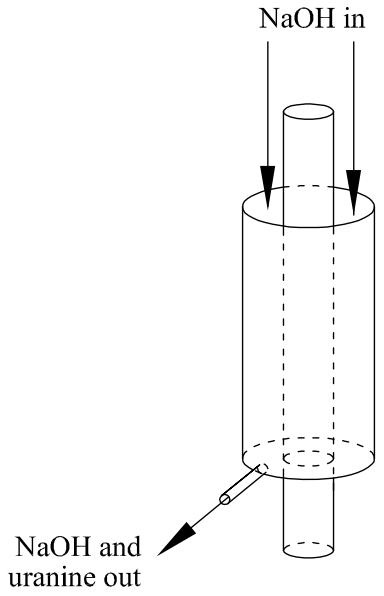

Figure 4.12: A schematic diagram of the washing 'cup' in position around the inner tube

4.2.5 Pipe washing and luminescence spectrometry

After an experimental run, the stainless steel tube, brass pipe and filter assembly were detached from the rig, removed as a unit and dismantled. The filter paper was removed and soaked in a volume of NaOH. NaOH dissolves the deposited uranine, and this was analysed in the luminescence spectrometer, which required an alkaline solution. The analysis gave a measure of the number of particles that did not deposit in the test section. The filter paper and plastic sheets that covered the walls of the upper and lower sections of the filter assembly were also soaked in volumes of NaOH. The lower section washings were downstream of the filter paper, and analysis of these acted as a check that the filter paper captured the particles as intended, and that none were 'leaking' past.

The tube and pipe were placed in a vertical position, and a rope was attached to the top of the inner tube. This was then lifted out of the outer pipe using a pulley system, with the

flow straighteners being used as a guide to ensure that the walls did not touch as the tube was removed. The tube and pipe were then placed in vertical stands to hold them in position for cleaning.

A specially designed 'cup' (see figure 4.12) was then slid onto the bottom end of the stainless steel inner tube. This cup had a hole in the centre of its base, surrounded by a nitrile rubber o-ring which sealed against the tube. It was 10 cm in length and its volume was approximately 50 cm^3. The cleaning cup was filled with NaOH through its open top, and allowed to soak for several minutes. The NaOH/uranine washings were then drained through a tap in the side of the cup at its base, and collected in a graduated cylinder to measure the exact volume. The cup was then slid upwards along the tube and the next 10 cm section was washed. The process was repeated until the entire pipe has been washed in 10 cm sections.

A rubber bung with a drain through its centre was placed in the bottom opening of the brass outer pipe. A funnel was attached to the thermocouple fitting nearest the bottom of the pipe, the pipe was filled up to the level of this fitting with the appropriate amount of NaOH, and allowed to soak. The NaOH/uranine washings were then collected through the drain in the bung (this resulted in the washing of a 20 cm section of the pipe). 50 cm^3 of NaOH was added to remove any residue of NaOH/uranine solution that had gathered around the bung, and collected as before. The funnel was attached to the next fitting up the pipe, the lower fitting was plugged, and again, NaOH was added until the level of this next fitting was reached. The washings collected comprised of the previously washed 20 cm section and a new 20 cm section. This washing technique was continued up along the pipe until the halfway mark was reached, at which point the pipe was inverted, and the washing was continued up the pipe, from what was the top of the pipe as it had been orientated during the experimental run. This was done to reduce the volume of NaOH required to remove the uranine deposit from the central section of the pipe. The volume of each wash increased with distance from the end of the pipe, so this reversal of the pipe ensured that the washings did not become so large as to over-dilute the uranine with NaOH, which would have resulted in negligible luminosity readings (over-dilution was a particular problem for runs with low deposition rates, necessitating very long runs).

The NaOH/uranine washings from the stainless steel tube, brass pipe, and filter assembly were than analysed using the luminescence spectrometer. Finding the luminosity of these washings of known volume (and thus the amount of uranine present) allowed the determination of the amount of particle material that deposited on the annulus walls compared to the amount that was captured by the filter.

The washings were sampled by an LS-30 luminescence spectrometer (Perkin Elmer Ltd). The principle behind luminescence spectrometry is the excitation by irradiation at a characteristic wavelength of an electron in a molecule of some fluorescent substance. After excitation, the electron emits a photon of light at another wavelength to release energy and return to its natural state. The optimum excitation and emission wavelengths for uranine are 475 nm and 514 nm respectively.

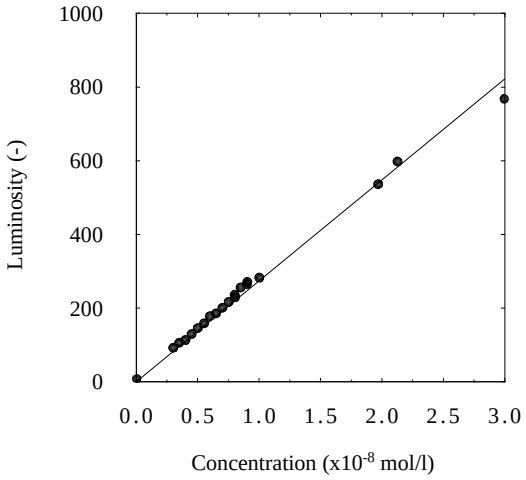

Figure 4.13: LS-30 luminescence spectrometer calibration

The LS-30 can detect uranine at concentrations as low as 1x10^{-14} mol/l. A high concentration sample would be off the scale of the spectrometer, but dilution by a known volume allows the luminosity to be determined, and the original luminosity can then be calculated. This was the case with the washings from the filter paper, or sections of pipe on which a large amount of deposition occurred. The washings were diluted by taking a small volume of the NaOH/uranine washings (measured with a 10 cm^3 burette) and adding a large known volume of NaOH (measured in a graduated cylinder). For extremely high concentrations (such as that at the filter paper), the dilution was repeated a number of times, to avoid the errors inherent in measuring tiny volumes. Averages of these were then taken to give a more accurate luminosity value.

When moving from a section of high deposit to a section of lower deposit (such as near the bottom of the annulus), the washing of the high-deposit section was repeated, to make sure that all of the particle deposit had been dissolved and drained from the cup. Even a small fraction of the deposit from a previous section (if the amount of deposit was high enough), could contaminate the result from a subsequent section. When moving between sections with similar amounts of deposit, it was found that there was no need for a second washing of the section.

The calibration curve for the spectrometer is shown in figure 4.13. The concentration values shown are nominal in that large dilutions were required to obtain a solution with a low enough concentration to be on the scale of the LS-30. This solution was used as a starting point for the calibration and the solution was diluted to different levels to span the scale of the instrument (these dilutions were smaller and of less uncertainty than those required to produce the 'starting point' solution). The linear behaviour of luminosity with concentration is shown. The ratio of the masses deposited was required to determine V_d^+, but the exact concentration of uranine in NaOH (and thus mass of uranine in the sample) was unknown.

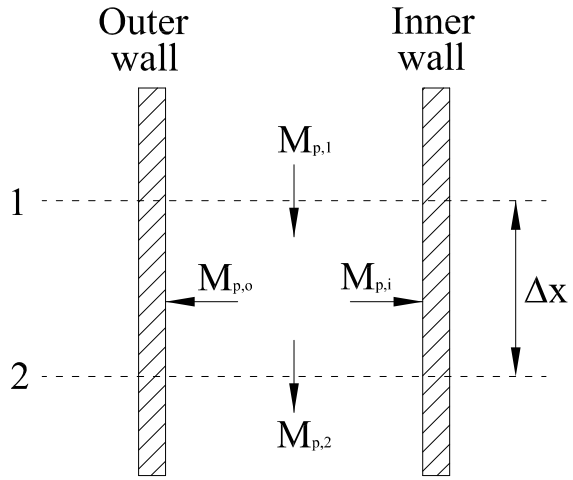

Figure 4.14: Control volume containing a section of the annulus

This was of no consequence once the existence of a linear relationship had been established, as the ratio of luminosities is equivalent to the ratio of masses.

4.2.6 Analysis of experimental washings

The aim of the experiment was to determine the variation of dimensionless particle deposition velocity, V_d^+, with dimensionless particle relaxation time, τ_p^+. The analysis for an annular flow is very similar to that developed for pipe flow by Sehmel (1968).

As the particle-laden flow moves downwards through the annulus, particles deposit and are removed from the flow, resulting in an axial decrease in particle concentration. This concentration drop is related to V_d^+, which can be related to the mass of particles deposited during an experimental run. The principle of conservation of particle mass is applied to a control volume containing a section of the annulus of length Δx (see figure 4.14). The mass flow rate of particles through the section, $\dot{m}_p$, is defined by:

$$\dot{m}_p = \rho_{p,m} U_m A = m_p C_{p,m} U_m A = m_p \int_{r_i}^{r_o} 2\pi r U C_p dr \tag{4.13}$$

where m_p is the mass of a single particle, U_m is the mean gas velocity (it is assumed that the mean particle axial velocity is approximately equal to that of the gas) , $C_{p,m}$ is the mean particle concentration in the section (number of particles per unit volume), $\rho_{p,m}$ is the mean particle density, and A is the cross-sectional area. The change in particle mass flux between the beginning and end of a section can be related to the mass deposited on the walls in that section:

$$\frac{d}{dx}\left(m_p C_p U_m A\right)\Delta x = -\pi\left(d_i J_{w,i} + d_o J_{w,o}\right)\Delta x \tag{4.14}$$

where J_w is the mass flux of particles to the wall per unit area, and C_p is the particle concentration at any point in the section. The subscripts i and o refer to the inner and outer deposition surfaces respectively. Manipulating this and substituting the definition of V_d^+ (equation 3.39) yields an expression for the ratio of the mean concentration leaving the section to the mean concentration entering, $C_{p,m2}/C_{p,m1}$:

$$Q_a ln\frac{C_{p,m2}}{C_{p,m1}} = -\pi\big(d_i u_{*,i}(V_d^+)_i + d_o u_{*,o}(V_d^+)_o\big)\Delta x \tag{4.15}$$

where Q_a is the volumetric flow rate of air, and the subscripts 1 and 2 refer to the beginning and end of the section under consideration. The actual mass of particles deposited on the inner and outer walls ($M_{p,i}$ and $M_{p,o}$) over a section of length Δx can be related to the mass of particles at the beginning and end of the section by:

$$M_{p,1} = M_{p,i} + M_{p,o} + M_{p,2} \tag{4.16}$$

where $M_{p,1} = m_p C_{p,m1} U_m A \Delta t$ and $M_{p,2} = m_p C_{p,m2} U_m A \Delta t$. Δt is the time over which the deposition occurs. Dividing by $M_{p,2}$ and inverting gives:

$$\frac{C_{p,m2}}{C_{p,m1}} = \frac{M_{p,2}}{M_{p,2} + M_{p,i} + M_{p,o}} \tag{4.17}$$

The fraction $C_{p,m2}/C_{p,m1}$ is known as the fractional penetration, P, of particles through the section. Since:

$$\frac{M_{p,o}}{M_{p,i}} = \frac{(V_d^+)_o u_{*,o} d_o}{(V_d^+)_i u_{*,i} d_i} \tag{4.18}$$

equation 4.15 can be rewritten as:

$$Q_a ln\frac{C_{p,m2}}{C_{p,m1}} = -\pi\Delta x d_i u_{*,i}(V_d^+)_i\left(1 + \frac{M_{p,o}}{M_{p,i}}\right) \tag{4.19}$$

By knowing the flow conditions and measuring the mass of particles deposited, V_d^+ can be calculated for each surface. The mass deposited on the filter gives the first value of $M_{p,2}$, and $(V_d^+)_i$ and $(V_d^+)_o$ are then calculated for each section moving up the pipe. As mentioned in section 4.2.5, luminosity readings are not converted into concentration and mass values, due to the uncertainty involved with the spectrometer calibration. However, the linearity of the instrument has been confirmed, so that luminosity readings (L_p) may be substituted in the place of masses deposited (M_p).

The dimensionless deposition velocity for each surface may now be written:

$$(V_d^+)_i = \frac{U_m(d_o^2 - d_i^2)}{4\Delta x u_{*,i} d_i}\frac{M_{p,i}}{M_{p,i} + M_{p,o}} ln\frac{1}{P} \qquad \text{and} \qquad (V_d^+)_o = \frac{U_m(d_o^2 - d_i^2)}{4\Delta x u_{*,o} d_o}\frac{M_{p,o}}{M_{p,i} + M_{p,o}} ln\frac{1}{P} \tag{4.20}$$

In practice, $u_{*,i}$ and $u_{*,o}$ are very close to each other, so u_*, which lies between the two values, may be used without any loss of accuracy.

4.3 Thermophoresis experiments: turbulent annular flow with a cross-stream temperature gradient

Once the depositional behaviour of a range of different sized particles in a turbulent annulus in isothermal flow was known, the effect of imposing a temperature difference across the annulus was studied. Most of the experimental methods that have been described for turbulent flow in an isothermal annulus are also applicable when a temperature difference is imposed. This section aims to describe any deviation from those methods.

4.3.1 Measurement of the temperature flow field

The thermophoresis experiments were executed and analysed in almost exactly the same manner as the isothermal set. The main difference between these experiments and the isothermal set, was that cold water was passed through the central pipe of the annulus at 30 lpm, and the heating tape was switched on so that the outer wall of the annulus was maintained at one of three nominal outer wall temperatures, $T_{ow,nom} = 40°$C, 85°C or 140°C. Although uranine starts to soften at temperatures above 90°C (Al-Azzawi & Owen, 1984), the temperature in the annulus only reached this value very close to the hot wall.

As well as the use of the cold water and heating tape, the experimental runs differed in that a much longer time was required for the rig to reach thermal equilibrium (typically one hour). The secondary flow of air (that supplements the air flow through the aerosol generator) was also heated, to raise the temperature of the flow when it entered the test section and thus reduce the length of annulus required for a constant temperature to be attained. The flow was initially allowed to pass through both the aerosol generator and the secondary supply pipe, and the aerosol jet was started once the flow had reached thermal equilibrium. Although this made starting the aerosol jet more difficult, it meant that no aerosol entered the test section while the temperatures in the rig were still varying.

The heating tape was operated with a controller, which switched power on and off as the temperature of the pipe (monitored by a thermocouple) moved above or below the desired value. The temperature oscillated around $T_{ow,nom}$ by between 2 and 4 °C depending on $T_{ow,nom}$. By averaging the temperature along the pipe over seven readings (representing about thirty minutes), the temperature profile along the outer pipe was found, and this is shown in figure 4.15 for each thermophoresis experiment (grouped together by $T_{ow,nom}$). The outer wall temperatures for each experiment were then averaged to give an average outer wall temperature ($T_{ow,avg}$) profile for each value of $T_{ow,nom}$.

The temperature of the inner pipe was measured after all the experiments had been completed (so as not to deface the deposition surface). Four thermocouples were fixed into

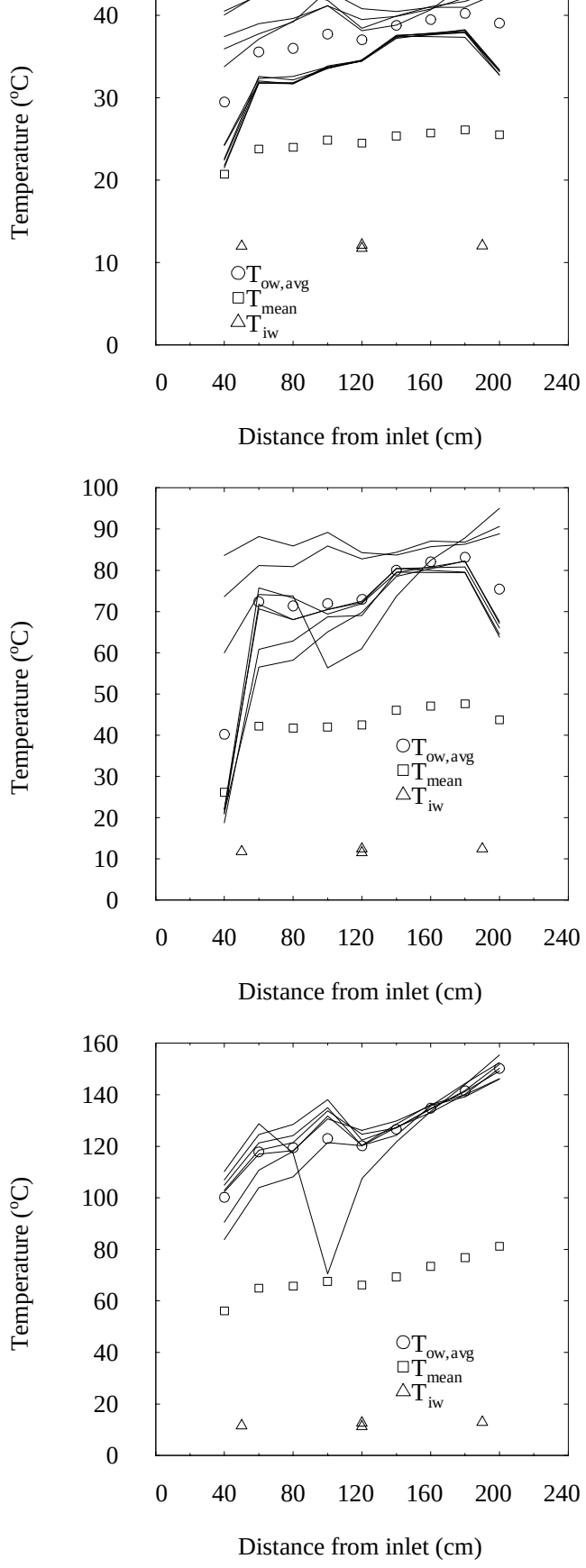

Figure 4.15: Temperature profiles for the three different temperature differences used in the thermophoresis experiments: $T_{ow,nom} = 40°C$ (top), 85°C (middle) and 140°C (bottom). The solid lines represent the outer wall temperature profiles for each individual experiment, and these are averaged to give a $T_{ow,avg}$ profile for each $T_{ow,nom}$. $T_{ow,avg}$ and T_{iw} are then used to find the mean temperature profile T_{mean}.

the inner pipe wall, and the thermocouple leads were fed through the centre of the pipe (where the water flowed). Two of the thermocouples were fixed at the same axial location, but on opposite sides of the pipe, to give an indication of any effects the thermocouples' positions in the pipe wall may have had. The temperature of this wall, T_{iw}, remained constant along the length of the pipe for all values of $T_{ow,nom}$ at $T_{iw} = 12°$C. It was then assumed that the mean temperature of the particle-laden air flow (T_{mean}) was the average of the temperatures at the hot outer wall and cold inner wall, and that flow properties such as μ_g and ρ_g could be evaluated at this temperature.

Although $T_{ow,avg}$ differed from the measured temperature by as much as 15°C in places, the axial variation of T_{mean} (calculated from $T_{ow,avg}$ and T_{iw}) was quite small. The thermophoretic force along the annulus did not deviate significantly either, as this scales with $\nabla(lnT)$, so that a constant temperature difference with small axial variations in temperature ensures a constant thermophoretic force. T_{mean} showed a maximum variation along the annulus (excluding the first and last 40 cm) of 2°C, 5°C and 15°C respectively, for each value of $T_{ow,nom}$. This ensured that the thermophoretic force was almost constant in the area of interest of the test section.

The nominal cross-stream temperature gradient (T_{grad}, as used in chapter 3) can be quite different to the local temperature gradients across the annulus. In a pipe flow, the temperature is highest at the pipe centreline, and decreases all the way to the wall, so that a nominal T_{grad} can be expressed as the temperature difference between the centreline and the wall, divided by the pipe radius. But the largest temperature difference occurs across the boundary layer. In the case of an annulus with a heated outer wall and a cooled inner wall, the temperature is at its highest at the heated wall and drops over the very short distance of the boundary layer to a near-mean temperature, which is almost constant across the annulus. Very near the cooled wall, there is another large temperature drop over another very short distance (another boundary layer). The result is that the nominal temperature gradients are quite approximate, and reflect only the temperature difference between the hottest and coldest points in the flow, and the distance separating them.

Figure 4.15 shows that one experiment for each of $T_{ow,nom} = 85°$C and $T_{ow,nom} = 140°$C experienced a dip in temperature near the middle of the pipe. This was due to the heated outer pipe expanding, and buckling near the middle as it was constrained at each end. To counteract this, the connection between the outer pipe and the plenum chamber was altered from a fixed one, to one which allowed the outer pipe to slide upwards as it expanded, and prevent buckling.

4.3.2 Determination of u_* for a thermophoresis experiment

The friction velocity was measured, with an indicated volumetric flow rate $Q_{ind} = 140$ lpm (and for each value of $T_{ow,nom}$), in the same way as it was for the isothermal experiments. Figure 4.16 collects together the experimental measurements of u_* for isothermal and heated

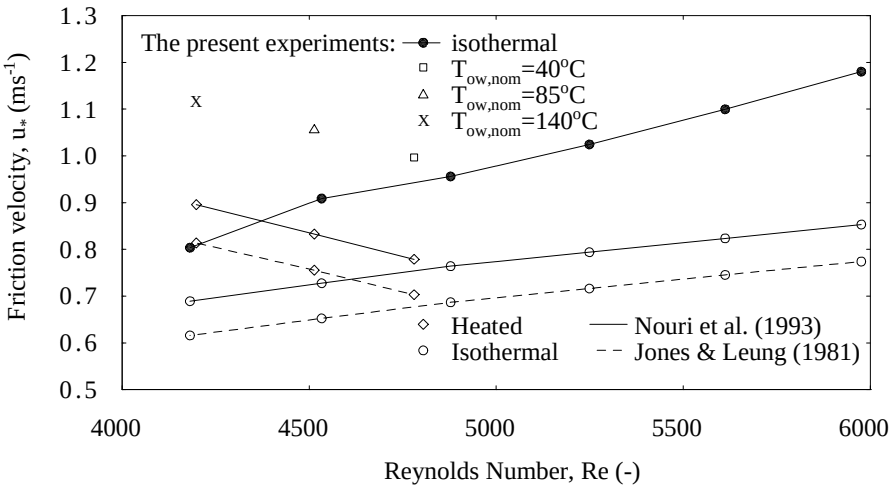

Figure 4.16: The variation of friction velocity with Reynolds number in a turbulent annulus at different temperatures

flow conditions, and compares them with the previously introduced correlations. For the heated runs, u_* increases as $T_{ow,nom}$ increases and Re is reduced, but the isothermal runs experienced an increase in u_* with increasing Re. This seemingly contradictory behaviour may be explained by examining the influence of T_{mean} on U_m. Increasing the temperature of the flow reduces ρ_g and increases μ_g, and this results in an increase in U_m. While two flows with identical Re but different mean temperatures would have the same value of f, an increase in U_m with T_{mean} causes u_* to increase (see equation 4.7). The increase in U_m caused by the large increase in T_{mean} for the heated experiments, is greater than the decrease in C_f (caused by a decrease in Re) and causes u_* to increase.

In figure 4.16, the correlations show the same trend as the experimental data, and the differences in magnitude between them are similar in size to those for isothermal flow. Again, it was decided to use the correlation of Jones & Leung (1981).

4.4 Summary

An annular deposition rig has been designed and built, and an experimental procedure developed, to study the influence of thermophoresis on deposition in turbulent annular flow. An annular geometry was adopted in order that a constant thermophoretic force (and constant mean temperature) existed in the experimental test section. The results from the isothermal and thermophoresis experiments can now be considered.

Chapter 5

Experimental study of thermophoresis in a turbulent annular flow - results

5.1 Introduction

Experimental data for thermophoretic deposition in a turbulent annular flow (with a cross-stream temperature gradient) will be presented in this chapter. First, the results from a number of isothermal turbulent pipe flow experiments are examined, to establish the credibility of the experimental rig and procedures. In order to determine the degree to which thermophoresis influences deposition, experiments were carried out in an isothermal turbulent annular flow. These results also provide a link between the isothermal turbulent pipe flow data of other researchers (e.g Liu & Agarwal, 1974; Leeming, 1995) and the new data for a turbulent annulus with a cross-stream temperature gradient. The thermophoretic experiments were carried out with three different temperature differences, across a range of values of τ_p^+, and the aim was to find the increase in magnitude of V_d^+ at low values of τ_p^+, for each temperature difference. As τ_p^+ increases (and Kn decreases), the thermophoretic force decreases, and the magnitude of V_d^+ is expected to return to that of an isothermal turbulent annular flow.

5.2 Isothermal turbulent pipe flow experiments

In order to develop the experimental techniques, and to test the operation of the experimental rig and equipment, a number of isothermal turbulent pipe flow experiments were attempted. A 2.4 m long 10 mm diameter copper pipe was used for these experiments, and the experimental procedures of the previous chapter (with alterations for the change in test section geometry following Leeming (1995)) were employed. The results are compared with the data of Leeming (1995), Liu & Agarwal (1974) and Agarwal (1975) in figure 5.1. While the agree-

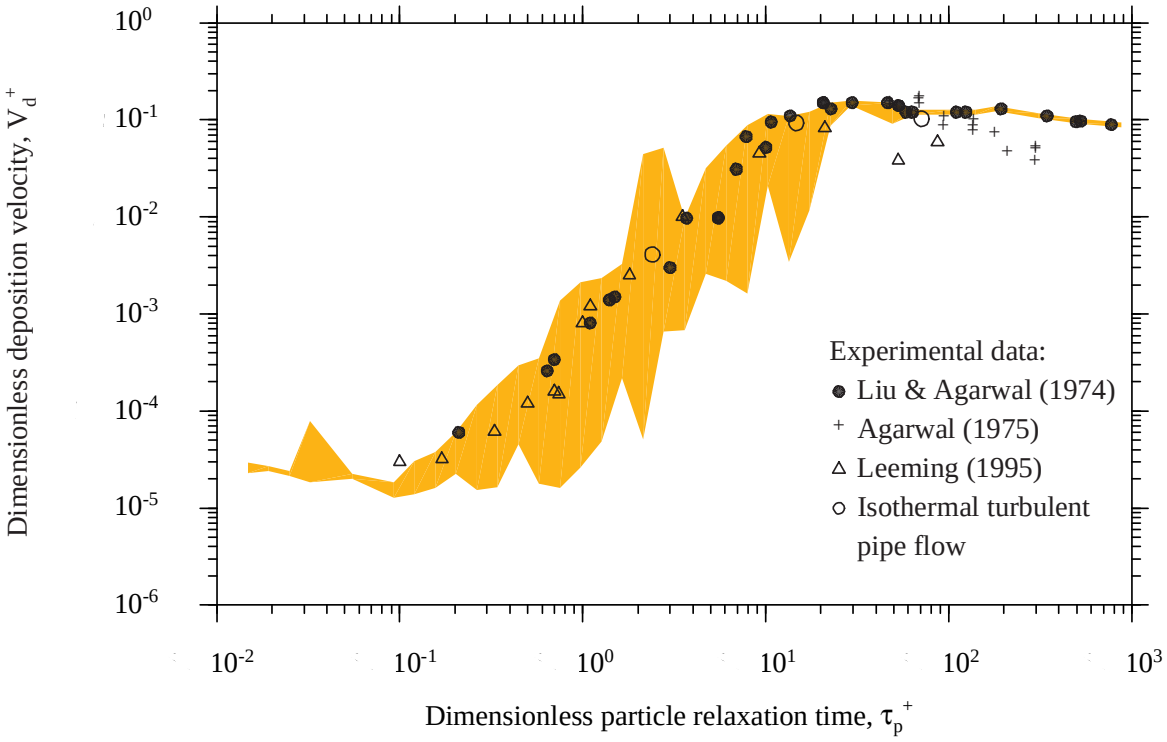

Figure 5.1: Results for the isothermal experiments in turbulent pipe flow
(The shaded envelope contains the data of: Friedlander & Johnstone (1957),Schwendiman & Postma (1961),Wells & Chamberlain (1967),Sehmel (1968) and Liu & Agarwal (1974))

ment is excellent, the analysis involved in achieving these results was also very instructive, and invaluable in understanding some unusual results for the turbulent annulus experiments, which will be discussed later.

5.2.1 The axial variation of V_d^+ for large τ_p^+

Referring to figure 5.1, the data points with $\tau_p^+ = 2.4$ and $\tau_p^+ = 14.7$ were obtained in a straightforward manner. The third point, with $\tau_p^+ = 70.8$, was the result of the experiment 'pipe 7' (run with $d_p = 11.78$ μm and $Re \approx 18000$). Cutting a 2.4 m pipe into 10 cm sections for washing and analysis is very labour intensive; Romay *et al.* (1998) employed more 'modern' techniques, and used a condensation nucleus counter to find the difference in particle concentration between the beginning and end of the test section. However, cutting the pipe into sections allows the variation of V_d^+ (and the mean particle concentration ratio $C_{p,m}/C_{p,m,inlet}$) to be determined along the length of the pipe. This information is illustrated in figure 5.2, and was very useful in determining the conditions under which deposition had occurred.

Figure 5.2a shows the axial variation of V_d^+ along the pipe. There is an order of magnitude difference between V_d^+ at the top and the bottom of the pipe, whereas the other two pipe flow

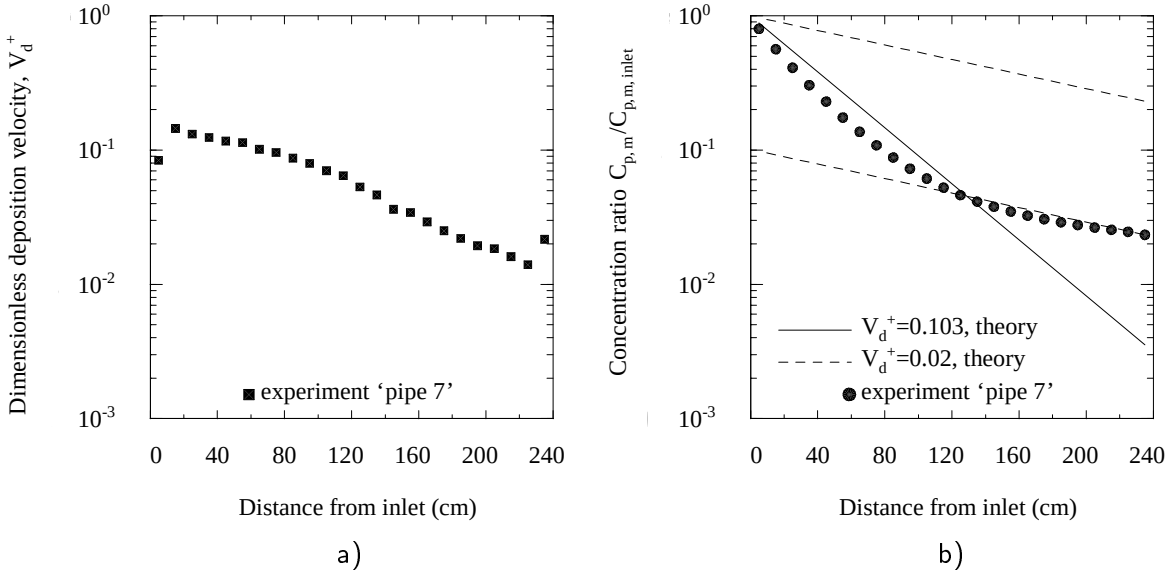

Figure 5.2: Theoretical and experimental values for a) deposition velocity and b) mean particle concentration ratio along the length of a 10 mm diameter pipe with Re=18000 for 'pipe 7'

experiments gave almost constant values of V_d^+ (once the entrance and end effects had been neglected). By averaging values in the top and bottom halves of the pipe separately, $V_{d,top}^+ \approx$ 0.103 while $V_{d,bottom}^+ \approx 0.02$. It is not obvious how to proceed in determining a value for V_d^+ ($V_d^+ \approx 0.1$ is expected from figure 5.1). However, by examining the axial variation in mean particle concentration ratio (figure 5.2b), the reason for the order of magnitude variation of V_d^+ becomes clearer.

The mean particle concentration ratio is initially linear, before curving near the middle of the pipe, and following a second linear trend along the bottom half of the pipe. This sort of behaviour was also found by Sehmel (1968) (and is shown in figure 5.3) in one of the few studies to include detailed information on the axial variation of deposition. Linearity of mean concentration ratio on a logarithmic plot would be expected from monodispersed particles. This non-linear behaviour is indicative of an aerosol with particles of a large diameter (and high τ_p^+ and V_d^+) which are <u>all</u> deposited along the top portion of the pipe, and smaller 'satellite' particles (with much smaller V_d^+) which can penetrate further down the pipe, and dominate deposition once all the larger particles have deposited.

Further confirmation of these experimental observations, may be found through a theoretical analysis of the particle mass flow rate and deposition velocity (see appendix C.1), which yields the expression:

$$V_d^+ = 1.257\alpha\beta\left(\frac{d}{L}\right)Re^{0.125}ln\left(\frac{C_{p,m1}}{C_{p,m2}}\right) \tag{5.1}$$

This expression was used to generate mean particle concentration ratio profiles along the length of the pipe for $V_d^+ = 0.103$ and $V_d^+ = 0.02$ (representative of the average of the measured

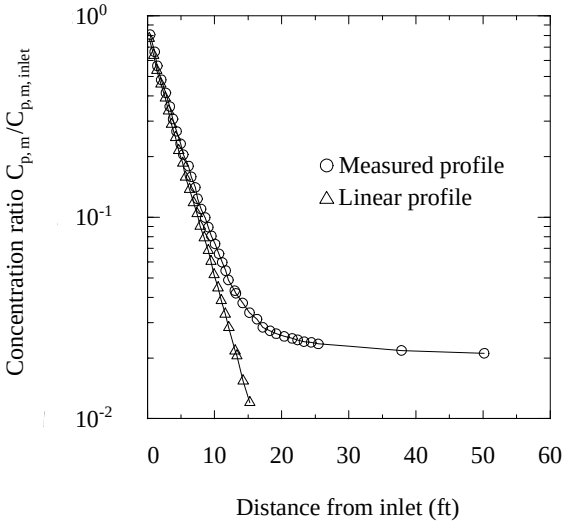

Figure 5.3: Mean particle concentration ratio along a pipe (Sehmel, 1968)
(The linear profile on a logarithmic scale is obtained by subtracting the 'satellite' concentration from the measured profile)

values in each half of the pipe). These are also plotted in figure 5.2b. The $V_d^+ = 0.103$ line passes close to the experimental data for the top half of the pipe, while a line parallel to that for $V_d^+ = 0.02$ passes through the experimental data for the lower half of the pipe.

This behaviour highlights the need for a check on the assumption of a monodispersed aerosol of known diameter, and this may be done through aerosol sampling. It should be remembered that this sort of behaviour is most likely to occur with particles of large τ_p^+. Particles with smaller τ_p^+ are less likely to have their concentration depleted by deposition (because of their lower V_d^+) to the extent that satellite particles influence the value of V_d^+. The value of V_d^+ for a particular experiment is the average of the V_d^+ value for each section where the mean particle concentration ratio is linear - averaging along the entire length of the pipe may not produce the 'correct' result.

5.2.2 Aerosol sampling

The previous chapter pointed out two difficulties with aerosol sampling and microscopic sizing techniques. The first was the unavailability of a surfactant of known flattening coefficient, to determine the 'exact' particle diameter . However, an indication of the level of monodispersivity can still be obtained, along with an 'approximate' particle diameter. The second difficulty was that the aerosol had to be sampled at a lower air flow rate than that used during the experimental run. This increased the chance of particle agglomeration during sampling, and meant that sometimes a 'judgement' would have to be made as to whether agglomeration occurred during the experiment, or only during sampling. The lower air flow rate also altered τ_p^+ of the particles during sampling, through a change in magnitude of u_*.

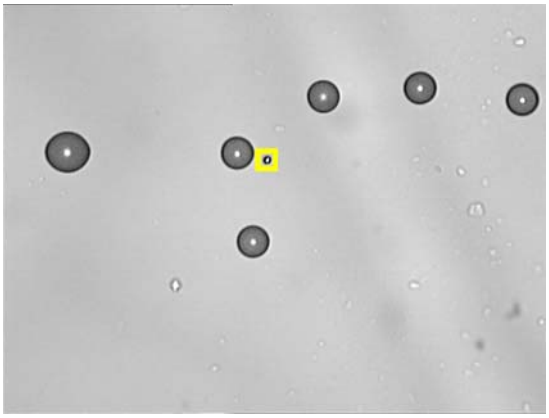

Figure 5.4: Particles of uranine and oleic acid collected on slide cover-glasses coated with an oleophobic surfactant for 'pipe 7'

Aerosol samples from 'pipe 7'

Figure 5.4 shows a sample from this run (taken at 2 cm from the sampling jet). In order to get an approximate indication of d_p from this slide, a flattening coefficient of 1.3 was assumed (this is approximate but not unreasonable when c_u=0.1 gcm^{-3}). In figure 5.4, most particles have d_p =11.4 μm (d_p=11.78 μm using equation 4.2), and there is also one smaller particle (marked with a yellow square) with d_p =1.9 μm. The presence of only one 'small' particle on the slide does not mean that many more were not produced; the deposition rate of small particles onto the slide would have been very low.

The observed particle diameters of 1.9 μm and 11.4 μm correspond to $\tau_p^+ \approx$ 4.5 and 66, respectively. By examining the scatter of experimental data for turbulent pipe flow, particles with these values of τ_p^+ would be expected to have values of $V_d^+ \approx$ 0.02, and $V_d^+ \approx$ 0.1, which provides strong evidence for the validity of the measured values of V_d^+ in each region of the pipe.

5.2.3 Conclusions drawn from isothermal pipe flow experiments

For large values of τ_p^+, high values of V_d^+ may cause the mean particle concentration to be very low in the latter portions of the test section. If small satellite particles are present in the flow, they will dominate depositional behaviour in these latter portions. Their effect would be negligible if the concentration of the large particles remained high. Aerosol sampling can be effective in verifying the calculated particle diameter, and in testing for monodispersivity, satellite particles and agglomeration.

5.3 Isothermal turbulent annular flow experiments

The main reason for carrying out experiments in an isothermal turbulent annulus, is to provide a datum against which to compare the experiments in a turbulent annulus with a cross-stream temperature gradient. Chung *et al.* (2002) found that the turbulence quantities close to the inner wall are similar to those of a turbulent channel flow (for a high radius ratio), and that the outer wall profiles are similar to those of turbulent pipe flow. Since deposition in turbulent channel and pipe flows are very similar, the deposition on each wall of a turbulent annulus is expected to be similar to that of a turbulent pipe flow. The following experiments were intended to validate this assumption.

Experiment were carried out to obtain values of $(V_d^+)_i$ and $(V_d^+)_o$ for a range of different values of τ_p^+. The results, associated uncertainties and experimental conditions are given in table C.1. The values of the dimensionless group $(\tau_p^+/Sc^2)^{1/3}$ for each experiment are given, and these did not vary significantly. Hence, this dimensionless group did not influence the results in the diffusional deposition regime (see section 3.4.1).

The uncertainties associated with V_d^+ (shown in figure C.1) are smaller than those found by Leeming (1995) for a turbulent pipe flow. The uncertainty in V_d^+ scales with $1/lnP$, so that a small uncertainty in P can lead to a large uncertainty in V_d^+. However, the larger surface area of the annulus walls compared to cross-sectional area means that the annulus is more 'efficient' at removing particles from the flow, and the effect of the uncertainty in P on V_d^+ is reduced significantly. Leeming (1995) predicted that such a change in geometry would result in a reduction in the uncertainty of V_d^+.

Figure 5.5 shows V_d^+ (for both walls) plotted against τ_p^+, when d_p is found using equation 4.2. $(V_d^+)_o$ is higher than $(V_d^+)_i$, but this may have been due to uranine soaking into the rubber bung used to plug the outer pipe during washing. This would then increase the luminosity of each outer pipe section by a small amount. The shaded area represents the scatter of experimental data for turbulent pipe flow, and the data for the annulus falls within these limits, but only when $\tau_p^+ \leq 15$. Above this point, V_d^+ decreases with increasing τ_p^+, whereas for a turbulent pipe flow, V_d^+ reaches its peak when $\tau_p^+ > 15$, and remains at this level as τ_p^+ is further increased (the three data points for isothermal turbulent pipe flow are plotted in figure 5.5 for comparison). However, by sampling the aerosol during each experiment, it was found that the particles were not always of the intended d_p, and were sometimes not monodispersed.

5.3.1 Determination of the effective particle diameter in the annular test section

The particle diameter predicted by equation 4.2 for 'annulus 11' was d_p = 13.3 μm, with τ_p^+ = 21.8. From the aerosol sample shown in figure 5.6a, the particles were monodispersed and the particle diameter was measured as d_p=7.12μm, which would result in τ_p^+ = 6.23.

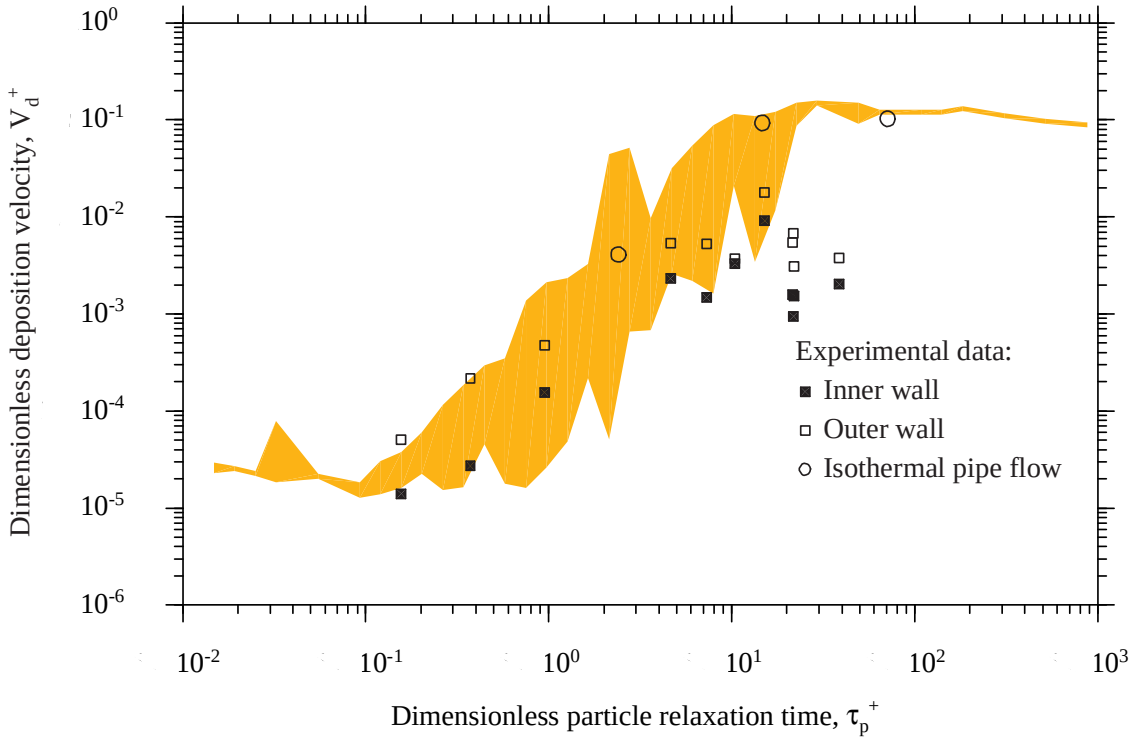

Figure 5.5: Results for the isothermal experiments in turbulent annular flow with d_p calculated using equation 4.2

In some cases, the particles produced were not monodispersed, and an 'effective' particle diameter was calculated based on the equivalence of particle volume (which scales with d_p^3). If two discrete particle sizes were observed, and (frac_1) and (frac_2) represent the fraction of particles of each size, then

$$d^3_{p,\text{effective}} = (\text{frac}_1)d^3_{p,1} + (\text{frac}_2)d^3_{p,2} \tag{5.2}$$

By treating each individual experiment in this way, the results for the isothermal experiments may be replotted, as shown in figure 5.7 (the uncertainty levels are not indicated to maintain clarity, but the same figure with uncertainty levels shown can be found in appendix C.3). When the observed diameter did not vary significantly from the calculated diameter, the calculated value was used, with small deviations from the mean diameter accounted for in the uncertainty associated with the experiment (see appendix C.2). Table C.1 contains information on the variation between 'calculated' and 'observed'/'effective' values of d_p.

Each data point for $\tau_p^+ >$15 has either an observed or effective value of d_p, smaller than its calculated value. There is now no data above $\tau_p^+ \approx$15, and the results fit within the envelope of data for turbulent pipe flow. Also shown is the data of Wells & Chamberlain (1967) for the inner wall of an annulus in an isothermal turbulent flow, and these compare favourably with the inner wall data.

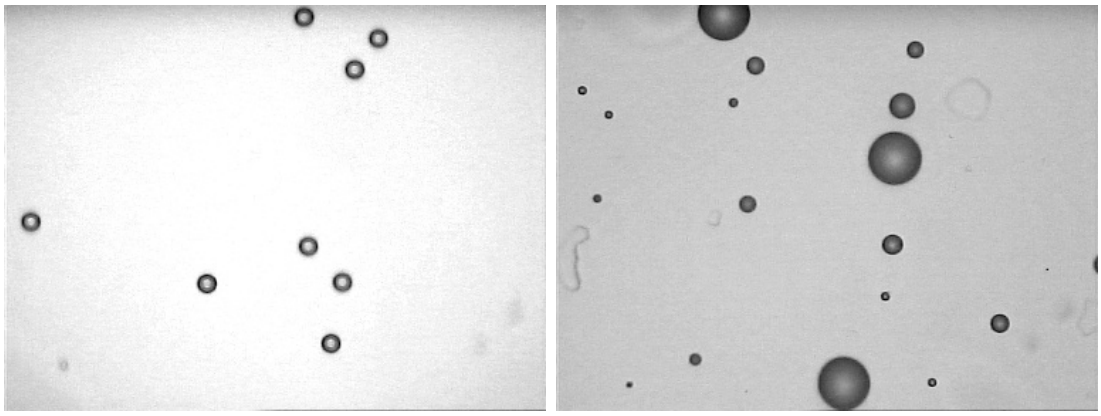

a) b)

Figure 5.6: Particles of uranine and oleic acid collected on slide cover-glasses coated with an oleophobic surfactant; a) 'annulus 11'; b) 'annulus 14'

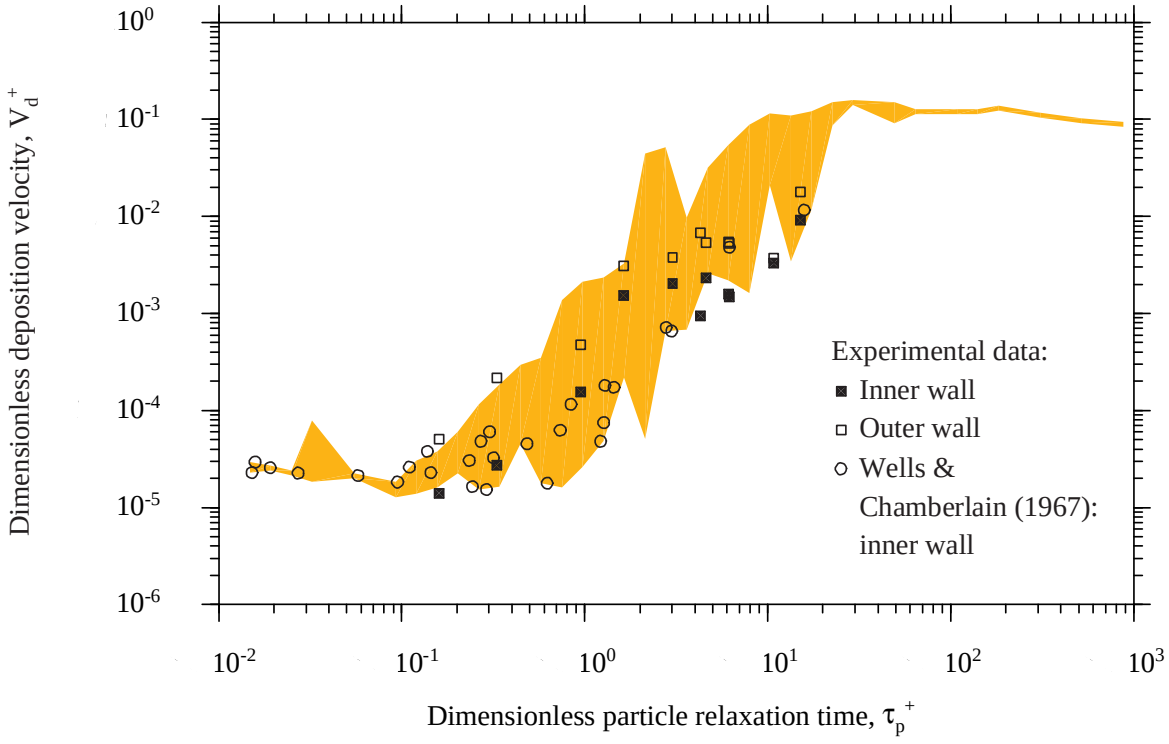

Figure 5.7: Results for the isothermal experiments in turbulent annular flow with d_p found by measuring the particles impacted on a slide

5.3.2 An explanation for the lack of data when $\tau_p^+ > 15$

The experiment 'annulus 14' was run with d_p=22.6 μm and $\tau_p^+ = 58.0$. The aerosol sample taken at the end of the run resulted in no particles being collected. Figure 5.6b shows the particles collected when the airflow rate was reduced to 40 lpm. There are particles of three different diameters: $d_{p,1} = 2.88$ μm, $d_{p,2} = 6.8$ μm, and $d_{p,3} = 19.11$ μm.

It has already been established that the aerosol generator does not always produce a monodispersed aerosol, and that for large τ_p^+, the mean particle concentration can be very low in parts of the test section. The inability to achieve large values of τ_p^+ was a combination of these two factors. Referring back to figure 5.2, the possibility exists that, for very large τ_p^+, most of the particles deposit in the section of the experimental rig between the aerosol generator and the test section, leaving only small satellite particles to deposit in the test section. This would explain the low (and constant axial) values of V_d^+ for experiments run with what was thought to be $\tau_p^+ > 15$.

With 'annulus 11', the 13.3 μm particles deposited before the test section leaving only the 7.12 μm particles to deposit on the annulus walls. With 'annulus 14', nearly all the particles except for the smallest deposited before the test section. The aerosol sampling with a reduced air flow rate was misleading, because u_* was reduced and τ_p^+ consequently decreased (τ_p^+ scales with u_*^2), and the deposition rate of the particles was reduced. This allowed even the large particles to reach the plenum chamber, and deposit on the sampling slide.

The result was an extremely misleading value of V_d^+, or more correctly, a correct (and constant axial) value of V_d^+, but for an unexpected value of τ_p^+ that could not properly be determined by aerosol sampling.

5.3.3 Calculation of τ_p^+ outside of the test section

In order to determine the extent to which particles are removed from the flow as they travel between the aerosol generator and the test section, τ_p^+ must be calculated for this region. From the continuity equation, $(\rho_g U_m A)_{test} = (\rho_g U_m A)_{app}$, where the subscript $_{test}$ refers to the test section, the subscript $_{app}$ refers to the 1 m horizontal approach pipe before the test section, and A is the flow area. Assuming that ρ_g does not vary to a great extent between these two locations:

$$U_{m,test}\frac{\pi(d_o^2 - d_i^2)}{4} = U_{m,app}\frac{\pi d_{app}^2}{4} \tag{5.3}$$

where $d_{app} = 0.019$ m, and $U_{m,app} = 0.8421 U_{m,test}$. Typically, $Re_{test} \approx 5920$, $U_{m,test} = 11.07$ ms^{-1} and $U_{m,app} = 9.32$ ms^{-1}. But before the test section, $Re_{app} \approx 11840$. Using the Blasius formula for a smooth pipe (Schlichting, 1968), $C_{f,app} = 0.0791 Re_{app}^{-0.25} = 7.583x10^{-3}$, and $u_{*,app} = U_{m,app}\sqrt{C_{f,app}/2} = 0.574$ ms^{-1}. Similarly, $u_{*,test} = 0.7713$ ms^{-1}.

τ_p^+ scales with u_*^2, so the dimensionless particle relaxation time of a particle as it approaches

the test section compared to a particle in the test section may be written as:

$$\tau^+_{p,app} = 0.55\tau^+_{p,test} \tag{5.4}$$

Even though $\tau^+_{p,app}$ is just half the size of $\tau^+_{p,test}$, it appears that once $\tau^+_{p,test} > 15$ (and V_d^+ has reached a maximum value that remains almost constant as τ_p^+ increases), the deposition rate in the approach pipe is of a similar magnitude to that in the test section, and is large enough to remove nearly all of the particles before they reach the test section. Between the aerosol generator and the horizontal approach pipe, there is an additional 2 m vertical distance to be travelled (through the aerosol neutraliser and some flexible tubing), where further deposition may occur.

If the test section had been a 10 mm pipe (as used by Leeming (1995)), and the mass flow rates were the same, then $U_{m,pipe}$ = 33.64 ms^{-1}, $Re_{pipe} \approx 22500$ and $u_{*,pipe}$ = 1.911 ms^{-1}. The result of this, is that:

$$\tau^+_{p,app} = 0.09\tau^+_{p,pipe} \tag{5.5}$$

So for this case, even when $\tau^+_{p,pipe}$ is as high as 50, $\tau^+_{p,app}$ will only be 5, and there is almost a whole order of magnitude between the respective values of V_d^+. This would explain why the range of τ_p^+ could be extended to much higher values in the pipe flow experiments of Leeming (1995). However, two data points from these experiments (see figure 5.1) for τ_p^+ >50, are below the expected values of V_d^+.

5.3.4 The decrease in experimental values of V_d^+ with increasing τ_p^+ in the 'inertia moderated' regime

Figure 5.1 shows that in the inertia moderated regime ($\tau_p^+ > 20$), there is a slight decrease in V_d^+ as τ_p^+ increases in the data of Liu & Agarwal (1974) (figure 3.3b shows the data of other researchers who also found this trend). Pershukov *et al.* (1995) and Gusev *et al.* (1990) have performed analyses (again see figure 3.3) suggesting that the decrease in V_d^+ is due to a Reynolds number dependence. However, the analytical expression of Gusev *et al.* does not match experimental data very well.

An alternative explanation may be offered by considering the behaviour of particles with $\tau^+_{p,test}$ >15 in an isothermal annular flow, and the experiments of Liu & Agarwal (1974). Liu & Agarwal (1974) used a 1.27 cm inner diameter pipe as the deposition pipe. The approach to the deposition pipe from the aerosol generator consisted of upward flow through some flexible hosing and a length of 3.2 cm diameter pipe, a plenum chamber, and downward flow through a 3.2 cm diameter transition pipe. By calculating $u_{*,pipe}$ and $u_{*,app}$ for these pipes, it was found that:

$$\tau^+_{p,app} = 0.03\tau^+_{p,pipe} \tag{5.6}$$

and the following then applies:

$$\text{when} \quad \tau^+_{p,pipe} = 100 \rightarrow V^+_{d,pipe} \approx 0.1 \qquad \text{and} \quad \tau^+_{p,app} = 3 \rightarrow V^+_{d,app} \approx 0.003 \tag{5.7a}$$

$$\text{when} \quad \tau^+_{p,pipe} = 1000 \rightarrow V^+_{d,pipe} \approx 0.1 \qquad \text{and} \quad \tau^+_{p,app} = 30 \rightarrow V^+_{d,app} \approx 0.1 \tag{5.7b}$$

The large rise in $V^+_{d,app}$ when 100 $< \tau^+_{p,pipe} <$ 1000, may cause the slight 'roll-off' in $V^+_{d,pipe}$ with increasing $\tau^+_{p,pipe}$ in this region. These experiments were carried out at Re=50000.

The experiments of Agarwal (1975) shown in figure 5.1 were carried out at Re=6000 (the same Re as used for the isothermal annulus), and show an even sharper decrease in V^+_d as τ^+_p increases. The physically larger particle, required to produce similarly large values of τ^+_p for smaller Re, may have encountered additional deposition in the approach pipe, than those used in Liu & Agarwal's experiments. The annulus experiments could be expected to show a greater decrease in V^+_d than pipe flow experiments at the same Re, because of the effect that the much greater flow area has on the ratio $\tau^+_{p,app}/\tau^+_{p,test}$. It could be that there is a Reynolds number dependence in this regime, but that it is a feature of the experimental design, and that the dependence is actually on the ratio of the Reynolds numbers (and u_* and τ^+_p) approaching, and travelling through, the test section.

5.3.5 Additional 'inertial' experiments with modified approach pipes

In order to reduce the ratio $\tau^+_{p,app}/\tau^+_{p,test}$ and thus reduce deposition in the approach to the test section, the approach pipes were altered. From the aerosol generator the flow negotiated a bend through a length of flexible tubing (d = 0.03 m), a 2 m vertical distance through the aerosol neutraliser and then a further bend through some more flexible tubing to the horizontal pipe ($d_{app} = 0.019$ m), and into the plenum chamber. Instead, flexible tubing (d = 0.063 m) came vertically out of the top of the aerosol generator. The aerosol neutraliser was bypassed because it had a small diameter (d = 0.025 m) and any electrical charge would not enhance the deposition of large particles. A second plenum chamber was used to turn the flow in the horizontal direction, and the diameter of the horizontal pipe to the plenum chamber was increased to 0.05 m. The header and baffle were removed from the plenum chamber above the test section. All possible obstructions to the flow which could capture particles were removed, and the ratio $\tau^+_{p,app}/\tau^+_{p,test}$ was now equal to 0.01, which would ensure that most of the particles generated found their way to the test section.

Three further experiments were then carried out, when the rig had been altered for the benefit of the 'inertial' particles, and the results have been added to the others in figure 5.8. Aerosol sampling during the experiment showed that large particles of the correct size were making their way to the plenum chamber, but the values of V^+_d measured were still much lower than expected. On visual inspection of the test section before washing, a huge amount of uranine (visible to the naked eye) could be seen on the inner wall of the annulus, at the

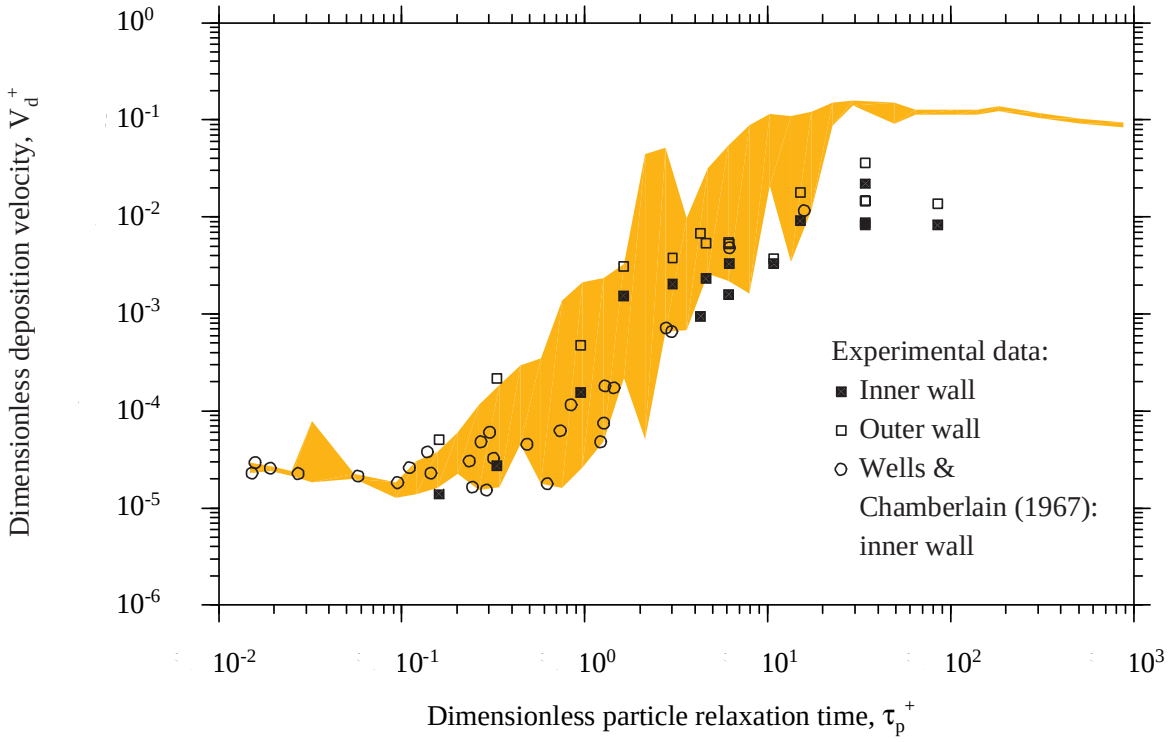

Figure 5.8: Results for the isothermal experiments in turbulent annular flow with d_p found by measuring the particles impacted on a slide, and three further 'inertial' experiments

point where the flow leaves the plenum chamber and enters the test section. The acceleration of the flow at this point was thought to be responsible for this deposition. Again, smaller satellite particles were deposited in the test section. The existence of the satellite particles can be explained as follows: τ_p^+ was increased through increasing particle diameter rather than through increasing Re, and although the final diameter of the particles was always smaller than the orifice diameter, the droplet diameter was comparable to the orifice diameter for large τ_p^+ (see equations 4.1 and 4.2), causing production of the satellite particles.

A relatively large flow area was required by the annular geometry to ensure adequate cooling water through the inner pipe, stiffness of the pipes for concentricity, and ease of removal of the inner pipe from the outer one without the removal of deposited particles. While these requirements facilitated the experiments on thermophoretic deposition, they have placed limitations on the range of τ_p^+ over which experiments can be performed.

5.3.6 Conclusions drawn from the isothermal annular flow experiments

- Particle deposition in a turbulent isothermal annular flow is very similar to that in a turbulent isothermal pipe flow.

- The outer wall dimensionless deposition velocity is consistently higher than the inner wall value, but this may be due to the washing procedure.

- Both $(V_d^+)_o$ and $(V_d^+)_i$ fall within the scatter of experimental data for turbulent pipe flow. $(V_d^+)_o$ agrees well with the data of Liu & Agarwal (1974) and Leeming (1995) for isothermal turbulent pipe flow. $(V_d^+)_i$ agrees well with the data of Wells & Chamberlain (1967) for isothermal turbulent deposition on the inner wall of an annulus.

- Experiments with particles of $\tau_p^+ > 15$ were not possible with this experimental rig, due to the large amount of deposition at the inlet to the test section. The upper limit on τ_p^+ was a consequence of the design requirements of the annular experiments with a cross-stream temperature gradient.

- Experimental conditions in the approach pipes may cause the slight decrease in V_d^+ with increasing τ_p^+ found in the inertia moderated regime, for previous isothermal turbulent pipe flow experiments (especially at low Re).

- The uncertainty in V_d^+ is much less for deposition in a turbulent annular flow than in a turbulent pipe flow.

- In order to perform experiments with large particles, the inlet to the test section needs to be redesigned so that deposition here is reduced to a sufficiently small level that these large particles can actually penetrate through to the test section.

5.4 Thermophoresis experiments - turbulent annular flow with a cross-stream temperature gradient

The aim of these experiments was to find the magnitude of the increase in V_d^+ (for small τ_p^+, with three different temperature differences), compared with isothermal values of V_d^+. While this will provide reliable data against which to validate a numerical scheme with a theoretical expression for thermophoresis, there are also a number of other trends that can be expected, that would provide a stern examination of such a scheme.

At large τ_p^+, thermophoresis should have an almost negligible influence on deposition, and the deposition velocities would be almost equal for the inner and outer walls. The presence of a cross-stream temperature gradient in the annulus means that for small τ_p^+ particles should be driven from the hot outer wall to the cold inner wall, and there would be negligible deposition on the outer wall. For intermediate values of τ_p^+, there is a transition between the two extremes of deposition, and there is also speculation (e.g. Romay *et al.*, 1998) that thermophoresis and eddy impaction-turbulent diffusion mechanisms may interact to enhance deposition. The vastly different depositional behaviour in these three regions makes the results of these experiments of great interest to researchers wishing to test their deposition theories against a new set of experimental data.

5.4.1 Results from the thermophoresis experiments

The tables in appendix C.4 contain the results, uncertainties and experimental conditions of the thermophoresis experiments, and the results are plotted in figure 5.9. This shows the data from the experiments with three different outer wall temperatures. Starting with the set for $T_{ow,nom} = 40°$C, the four smallest values of τ_p^+ resulted in values of $(V_d^+)_i$ which were almost identical to each other, and an order of magnitude greater than the isothermal deposition velocity. $(V_d^+)_o$ was either too low to be measured, or negligible, in these cases. As τ_p^+ was increased (and the eddy impaction-turbulent diffusion regime was entered), $(V_d^+)_o$ became measurable (although with less accuracy than a higher value of V_d^+ would have) but was still much lower than isothermal values, while $(V_d^+)_i$ began to approach isothermal values. Only when $\tau_p^+ \approx 5$ did both $(V_d^+)_o$ and $(V_d^+)_i$ approach their isothermal values. At this stage, $Kn \approx 0.02$, and the effects of thermophoresis are extremely small in comparison with deposition due to turbophoresis. (The largest value of Kn in any of these experiments was $Kn = 0.136$, and inclusion of the Cunningham correction factor would alter τ_p^+ by a factor of only 1.18 in this case. Its omission is also justified as $d_p > 1\mu$m (Hinds, 1998, pg. 49).)

The data sets for $T_{ow,nom} = 85°$C and 140°C show a similar trend. However, the higher temperature difference between outer and inner walls meant that $(V_d^+)_o$ for $T_{ow,nom} = 85°$C appears to be smaller than $(V_d^+)_o$ for $T_{ow,nom} = 40°$C and small particles, and $(V_d^+)_o$ for $T_{ow,nom} = 140°$C is smaller again. The effect on $(V_d^+)_i$ was the opposite, although the increase in $(V_d^+)_i$ with these further increases in temperature difference was not as great

as with the initial increase, because the thermophoretic force increases with $\nabla(lnT)$. With increasing temperature difference (and thermophoretic force), more particles were driven away from the hot outer wall and towards the cold inner wall.

Enhanced deposition by a thermophoresis-turbulence interaction

The difference between the thermophoretic dimensionless deposition velocity on the inner wall, $(V_d^+)_{i,TH}$, and its isothermal equivalent ,$(V_d^+)_{i,ISO}$, decreases as Kn decreases (τ_p^+ increases). However, as $[(V_d^+)_{i,TH}$ - $(V_d^+)_{i,ISO}]$ is decreasing, it is still greater than would be expected unless the interaction between thermophoresis and turbulence in the eddy impaction-turbulent diffusion regime enhanced deposition. Taking a closer look at the experimental results (figure 5.10), the straight lines of V_d^+, as τ_p^+ increases, curve upwards before intersecting the isothermal data, rather than after they intersect it. Thus the results will make an interesting comparison with numerical models in this region. Also of interest is whether these models will predict accurately the level of deposition in the diffusional deposition regime, where thermophoresis is the dominant mechanism. The experimental results in this region are extremely 'self-consistent.' The results at $\tau_p^+ \approx 8$ should be ignored, for the reasons given in the previous section.

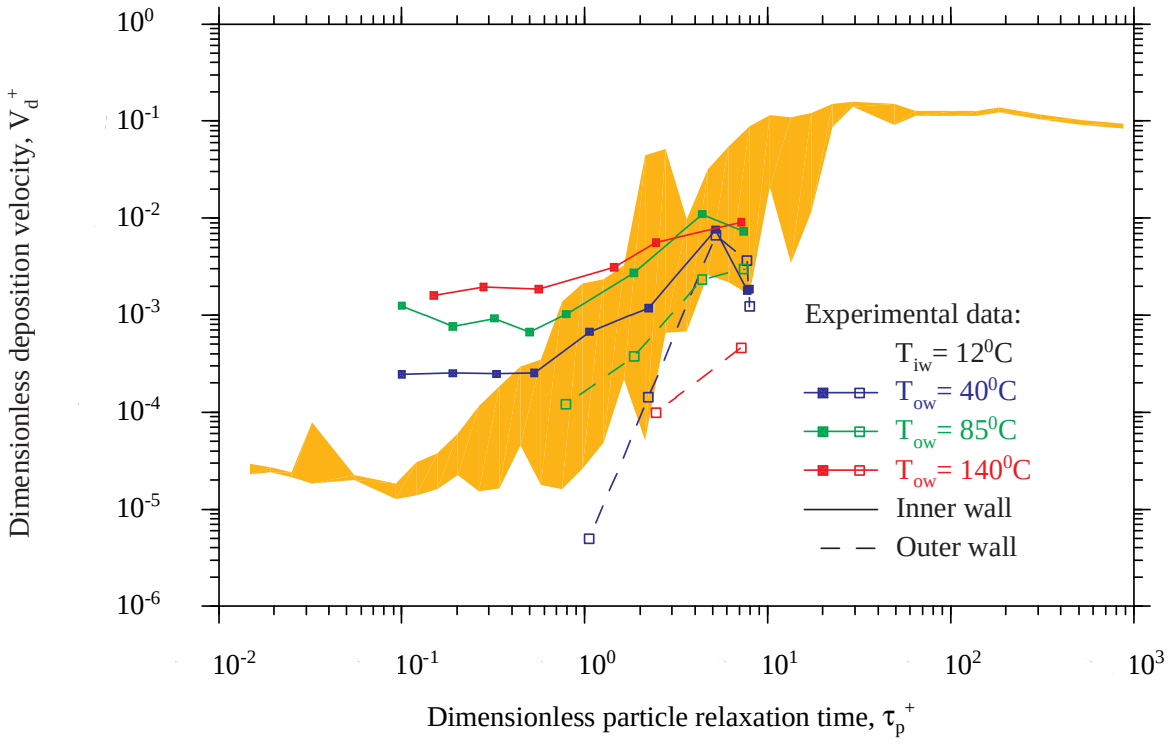

Figure 5.9: Results for the thermophoresis experiments in turbulent annular flow

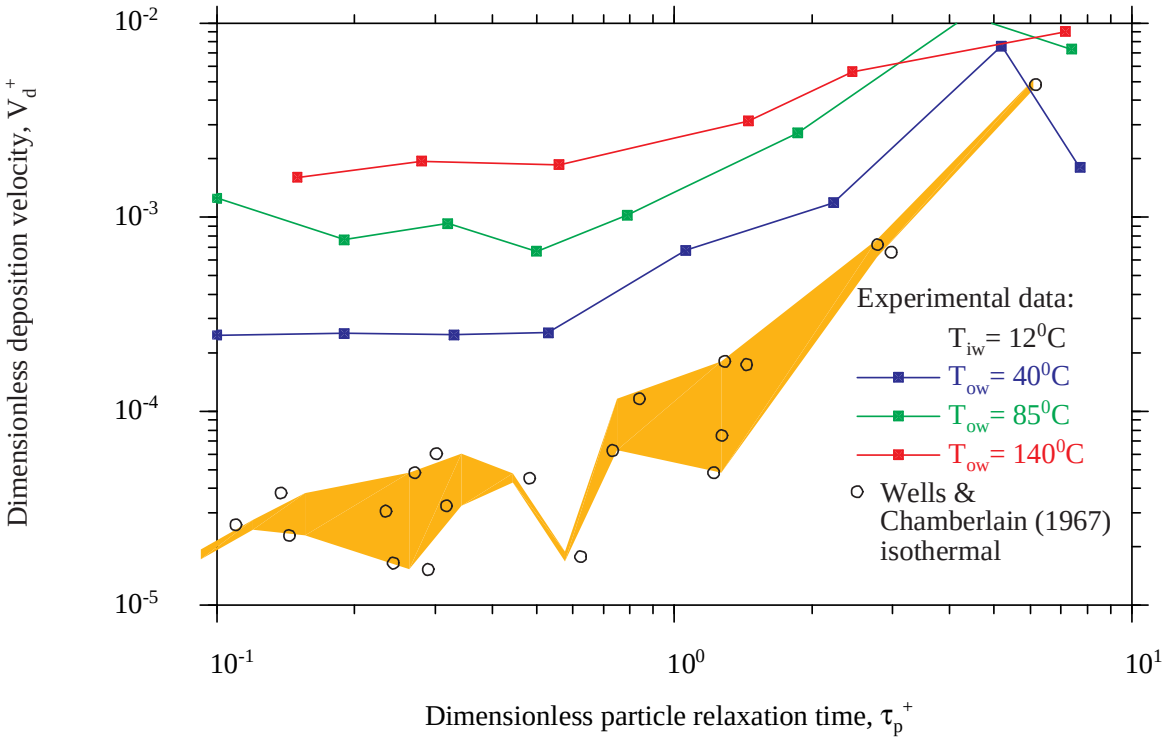

Figure 5.10: Results for the thermophoresis experiments in turbulent annular flow - a closer examination of deposition velocities in the eddy impaction-turbulent diffusion regime (the shaded area highlights the isothermal data of Wells & Chamberlain (1967))

Recovery of deposition to isothermal levels with increasing τ_p^+

As discussed in section 5.3, the rig will not produce particles greater than $\tau_p^+ \approx 15$ (in the test section). While $(V_d^+)_{o,TH}$ for $T_{ow,nom} = 40°$C and 85°C are almost at the same level as $(V_d^+)_{o,ISO}$ for $\tau_p^+ \approx 5$, $(V_d^+)_{o,TH}$ for $T_{ow,nom} = 140°$C has not yet recovered to its isothermal level. At $\tau_p^+ \approx 8$, the thermophoresis experiments have experienced the same problems as the isothermal experiments.

Locating the exact 'cross-over' point (where $(V_d^+)_o$ becomes greater than $(V_d^+)_i$ again, as with the isothermal case) would have been extremely useful, but at least there are still results for both walls at lower values of τ_p^+. This behaviour represents an additional test in the validation of numerical models.

The non-existence of an effective particle diameter in the presence of thermophoresis

Attempts made at generating large particles ($\tau_p^+ > 8$) which failed, are not as useful as those isothermal attempts, where an effective particle diameter can be used to recalculate τ_p^+, and the V_d^+ result then appears reasonable. In a thermophoresis experiment, a flow of small and

large particles cannot be given an 'average' τ_p^+ which will describe their behaviour. Each size of particle will have a different Kn, and the smaller particle size (if small enough) will tend to move away from the hot wall towards the cold wall, while the large particle will have less tendency to do so, and may even be large enough to deposit on the hot wall. Two such runs were 'thermo 16' and 'thermo 26', and while they are not plotted in figure 5.9, the results are included in the tables of appendix C.4.

5.4.2 Conclusions drawn from the thermophoresis experiments

- The thermophoresis experiments have been carried out with an almost zero temperature gradient along the pipe (and almost constant wall and mean temperatures), due to the novel annular arrangement used. The radial temperature difference and gas properties did not vary along the pipe, and thus the Reynolds number, Knudsen number and thermophoretic force also did not vary significantly. The data can be easily non-dimensionalised as τ_p^+ against V_d^+, and represents a vast improvement on previous thermophoresis data, when the flow properties and thermophoretic force were not constant over the length of the test section.

- The results in the diffusional deposition regime shows constant values of deposition velocity as particle size increases, for each particular temperature difference. As the temperature difference increases, the value of the constant deposition velocity also increases.

- There is an area in the eddy impaction-turbulent diffusion regime where the deposition velocity increases further, before reaching the same value as it would have in an isothermal flow. This data provides an opportunity to quantify any interaction between thermophoresis and turbulent deposition mechanisms.

- The outer wall deposition velocity is immeasurable, or negligible, for very small particles but, as particle size increases (and Knudsen number decreases), the outer wall deposition velocity increases again, towards its isothermal value, which is larger than the inner wall isothermal deposition velocity. This feature could be studied more fully if the use of large particle sizes were possible with this rig.

- The thermophoresis experiments with $\tau_p^+ \approx 8$ should be ignored.

Chapter 6

A theory of particle deposition in a turbulent annular flow

6.1 Introduction

One of the aims of this research was to adapt the theory of particle deposition developed by Young & Leeming (1997) and Leeming (1995), which has been successfully applied to the case of fully-developed pipe flow. To complement the experiments of the previous chapter, the theory will eventually be applied to fully-developed turbulent annular flow. The two-dimensional axisymmetric fully Eulerian formulation is similar to that described in Young & Leeming (1997), but particle density-weighted averaging (rather than Reynolds averaging, which is non-density-weighted) is used (as in Slater *et al.*, 2003), because fewer turbulence correlations are generated. The alteration of the boundary conditions to take account of the presence of two walls in the case of the annulus is also considered. This chapter features the derivation of the relevant governing equations of particle motion, and considers the modelling of the turbulence encountered by particles, and the numerical time-marching scheme of the computer code used to solve the particle equations. A detailed study of the results of simulations carried out using this computer code (and comparison with experiments) follows in the next chapter.

6.2 Density-weighted averaged particle conservation equations

6.2.1 Particle conservation equations

The motion of a dilute suspension of particles (under the assumption of 'one-way coupling') is described by the conservation equations of particle mass and momentum. The instantaneous conservation equations for particle mass and momentum using cartesian tensor notation with

the repeated suffix summation convention, may be written as:

$$\frac{\partial \rho_p}{\partial t} + \frac{\partial (\rho_p v_k)}{\partial x_k} = 0 \tag{6.1a}$$

$$\frac{\partial (\rho_p v_i)}{\partial t} + \frac{\partial (\rho_p v_i v_k)}{\partial x_k} = \rho_p (\mathsf{F}_i + g) = \rho_p (\mathsf{F}_{D,i} + \mathsf{F}_{L,i} + \mathsf{F}_{TH,i} + \mathsf{F}_{B,i} + g) \tag{6.1b}$$

where v_i is the i-component of the particle velocity and F_i is the i-component of the force per unit mass acting on the particles. Adopting the usual approximations for dilute-gas particle flows, the most significant forces acting on the particles are due to viscous drag, Saffman lift, Brownian motion, thermophoresis, and gravity. It was shown in section 3.1 that:

$$\mathsf{F}_{L,i} = 0.725 \sum_{k=1,\neq i}^{3} \left[\left(\frac{\rho_g}{\rho_{p,mat}} \tau_p \frac{\partial u_k}{\partial x_i} \right)^{1/2} \frac{(u_k - v_k)}{\tau_p} \right] = \alpha_L \left(\frac{\partial u_k}{\partial x_i} \right)^{1/2} (u_k - v_k)$$

$$\mathsf{F}_{D,i} = \frac{(u_i - v_i)}{\tau_p} \qquad \mathsf{F}_{B,i} = -\frac{D_B}{\tau_p} \frac{\partial (ln \rho_p)}{\partial x_i} \qquad \mathsf{F}_{TH,i} = -\frac{K_{TH} \nu_g}{\tau_p} \frac{\partial (lnT)}{\partial x_i} = -\alpha_{TH} \frac{\partial (lnT)}{\partial x_i}$$

The correction to the drag term for finite values of Re_p has been omitted for now (Re_p is small for all but the largest particles). The coefficients α_L and α_{TH} are defined in order that quantities which do not have a fluid turbulence fluctuating component are grouped together for simplicity.

Combining equation 6.1b with equation 6.1a and manipulating, gives the non-conservative form of the particle momentum equation:

$$\frac{\partial v_i}{\partial t} + v_k \frac{\partial v_i}{\partial x_k} = \frac{(u_i - v_i)}{\tau_p} - \frac{D_B}{\tau_p} \frac{\partial (ln \rho_p)}{\partial x_i} + \mathsf{F}_{L,i} + \mathsf{F}_{TH,i} + g \tag{6.2}$$

6.2.2 Particle convective velocity

Let J_i represent the total mass flux of particles per unit area. v_i is considered to be a mean velocity averaged over the random thermal motions of all the particles, thus treating them as large molecules. Therefore:

$$J_i = \rho_p v_i \tag{6.3}$$

J_i can be represented as the sum of a convective and Brownian diffusive contribution:

$$J_i = J_{conv,i} + J_{diff,i} \tag{6.4}$$

where $J_{diff,i} = -D_B \frac{\partial \rho_p}{\partial x_i}$ (equation 3.21). By writing $J_{conv,i} = \rho_p w_i$, the particle convective velocity, w_i, is defined:

$$\rho_p v_i = \rho_p w_i - D_B \frac{\partial \rho_p}{\partial x_i} \tag{6.5}$$

Substituting this into equations 6.1a and 6.2 has the effect of shifting the diffusive terms from the particle momentum equation into the particle mass conservation equation:

$$\frac{\partial \rho_p}{\partial t} + \frac{\partial (\rho_p w_k)}{\partial x_k} = \frac{\partial}{\partial x_k}\left[D_B \frac{\partial \rho_p}{\partial x_i} \right] \tag{6.6a}$$

$$\frac{\partial v_i}{\partial t} + v_k \frac{\partial v_i}{\partial x_k} = \frac{(u_i - w_i)}{\tau_p} + \mathsf{F}_{L,i} + \mathsf{F}_{TH,i} + g \tag{6.6b}$$

This is helpful in obtaining a clear picture of the different types of transport mechanisms, and also for computational purposes.

Examining equation 6.5, it can be seen that w_i and v_i are only significantly different when diffusive effects are dominant, as happens when τ_p is small. However, inertial effects are then no longer important, and the acceleration term on the left hand side of the particle momentum equation (equation 6.6b) can be neglected in relation to $(u_i - w_i)$ because it is multiplied by τ_p. For large τ_p, the acceleration term cannot be neglected, but because convective effects now dominate, $v_i \cong w_i$. For these reasons it is permissible to replace v_i by w_i in the acceleration term, without serious error, over the whole range of τ_p (see Ramshaw, 1979). A similar approach can be used to advantage with the averaged equations for turbulent flow (see below).

6.2.3 Reynolds and particle density-weighted averaging

The most common method of dealing with the governing equations of turbulent flows is Reynolds averaging, where the instantaneous values of particle phase density and fluid and particle velocity are decomposed into mean and fluctuating components. Decomposing ρ_p and u_i into Reynolds averaged ensemble-mean and fluctuating components:

$$\rho_p = \overline{\rho}_p + \rho'_p \qquad u_i = \overline{U}_i + u'_i \qquad \text{where} \quad \overline{\rho'}_p = \overline{u'_i} = 0$$

While it is more conventional to decompose a velocity as $u_i = \overline{u}_i + u'_i$, the ensemble-mean component is capitalised for visual clarity.

All particle phase density fields are compressible, so it is advantageous to use density-weighted (Favre) averaging for quantities involving v_i. For variable density flows, Reynolds averaging results in significant added complexity in the averaged governing equations, whereas density-weighted averaging leads to a simplified and more easily interpreted set of equations

(Chen *et al.*, 1991). If v_i is the quantity to be averaged (using density-weighting), then decomposing into density-weighted ensemble-mean (denoted by a double overbar) and fluctuating components (denoted by a double prime) gives:

$$\rho_p v_i = \rho_p \overline{\overline{V_i}} + \rho_p v_i''$$

A number of identities that will be used in subsequent derivations will now be defined. The density-weighted average value of any variable ϕ is defined by:

$$\overline{\overline{\phi}} = \frac{\overline{\rho_p \phi}}{\overline{\rho}_p} \tag{6.7a}$$

Decomposing $\rho_p v_i$ and averaging:

$$\rho_p v_i = \rho_p \overline{\overline{V}}_i + \rho_p v_i'' \quad \Rightarrow \quad \overline{\rho_p v}_i = \overline{\rho}_p \overline{\overline{V}}_i + \overline{\rho_p v_i''} = \overline{\rho}_p \overline{\overline{V}}_i \quad \text{which shows that} \quad \overline{\rho_p v_i''} = \overline{\rho_p} \overline{\overline{v_i''}} = 0 \tag{6.7b}$$

Similarly:

$$\overline{\rho_p v_i v_j} = \overline{\rho}_p \overline{\overline{V_i}}\,\overline{\overline{V_j}} + \overline{\rho}_p \overline{\overline{v_i'' v_j''}} \tag{6.7c}$$

Particle mass conservation equation

Decomposing and expanding equation 6.1a:

$$\frac{\partial(\overline{\rho}_p + \rho_p')}{\partial t} + \frac{\partial}{\partial x_k}(\overline{\rho}_p + \rho_p')(\overline{\overline{V}}_k + v_k'') = 0$$

$$\frac{\partial(\overline{\rho}_p + \rho_p')}{\partial t} + \frac{\partial}{\partial x_k}(\overline{\rho}_p \overline{\overline{V}}_k + \overline{\rho}_p v_k'' + \rho_p' \overline{\overline{V}}_k + \rho_p' v_k'') = 0$$

Taking averages, remembering the rules of equation 6.7 and that $\overline{\rho'}_p = 0$, gives the density-weighted averaged particle mass conservation equation as:

$$\frac{\partial \overline{\rho}_p}{\partial t} + \frac{\partial(\overline{\rho}_p \overline{\overline{V}}_k)}{\partial x_k} = 0 \tag{6.8}$$

Particle momentum equation

The drag force is averaged by assuming τ_p to be a local constant evaluated at the local mean slip Reynolds number. By ignoring any correlation between fluctuating particle density and gas velocity in the lift force term, and between fluctuating particle density and gas temperature

in the thermophoretic force term, the averaging of the force terms results in:

$$\overline{\rho_p \mathsf{F}_{D,i}} = \overline{\rho}_p \overline{\overline{\mathsf{F}}}_{D,i} = \frac{\overline{\rho}_p(\overline{U}_i - \overline{\overline{V}}_i) + \overline{\rho_p u_i'}}{\tau_p} = \frac{\overline{\rho}_p(\overline{U}_i - \overline{\overline{V}}_i + \overline{\overline{u_i'}})}{\tau_p} \tag{6.9a}$$

$$\overline{\rho_p \mathsf{F}_{L,i}} = \overline{\rho}_p \overline{\overline{\mathsf{F}}}_{L,i} = \alpha_L \overline{\rho}_p \left(\frac{\partial \overline{U}_k}{\partial x_i} \right)^{1/2} (\overline{U}_k - \overline{\overline{V}}_k) \tag{6.9b}$$

$$\overline{\rho_p \mathsf{F}_{B,i}} = \overline{\rho}_p \overline{\overline{\mathsf{F}}}_{B,i} = -\frac{D_B}{\tau_p} \overline{\rho}_p \frac{\partial (ln \overline{\rho}_p)}{\partial x_i} = -\frac{D_B}{\tau_p} \frac{\partial \overline{\rho}_p}{\partial x_i} \tag{6.9c}$$

$$\overline{\rho_p \mathsf{F}_{TH,i}} = \overline{\rho}_p \overline{\overline{\mathsf{F}}}_{TH,i} = -\alpha_{TH} \overline{\rho}_p \frac{\partial (ln \overline{T})}{\partial x_i} \tag{6.9d}$$

Treating equation 6.1b similarly to the particle mass conservation equation (and substituting equations 6.9a and 6.9c) gives:

$$\frac{\partial(\overline{\rho}_p \overline{\overline{V}}_i)}{\partial t} + \frac{\partial(\overline{\rho}_p \overline{\overline{V}}_i \overline{\overline{V}}_k)}{\partial x_k} = -\frac{\partial(\overline{\rho}_p \overline{\overline{v_i'' v_k''}})}{\partial x_k} + \frac{\overline{\rho}_p(\overline{U}_i - \overline{\overline{V}}_i)}{\tau_p} + \frac{\overline{\rho}_p \overline{\overline{u_i'}}}{\tau_p} - \frac{D_B}{\tau_p} \frac{\partial \overline{\rho}_p}{\partial x_i} + \overline{\rho}_p(\overline{\overline{\mathsf{F}}}_{L,i} + \overline{\overline{\mathsf{F}}}_{TH,i} + g) \tag{6.10}$$

Combining equation 6.10 with 6.8 and manipulating gives the non-conservative form of the particle momentum equation:

$$\frac{\partial \overline{\overline{V}}_i}{\partial t} + \overline{\overline{V}}_k \frac{\partial \overline{\overline{V}}_i}{\partial x_k} = -\frac{\partial(\overline{\overline{v_i'' v_k''}})}{\partial x_k} - \frac{(\overline{\overline{v_i'' v_k''}})}{\overline{\rho}_p} \frac{\partial \overline{\rho}_p}{\partial x_k} + \frac{(\overline{U}_i - \overline{\overline{V}}_i)}{\tau_p} + \frac{\overline{\overline{u_i'}}}{\tau_p} - \frac{D_B}{\tau_p \overline{\rho}_p} \frac{\partial \overline{\rho}_p}{\partial x_i} + (\overline{\overline{\mathsf{F}}}_{L,i} + \overline{\overline{\mathsf{F}}}_{TH,i} + g) \tag{6.11}$$

6.2.4 Turbulence modelling

Closure of the particle momentum equation requires the modelling of the turbulence correlations $\overline{\rho}_p \overline{\overline{v_i'' v_k''}}$ (the particle Reynolds stress) and $\overline{\rho}_p \overline{\overline{u_i'}}$ (the density-velocity correlation). A transport equation for the particle Reynolds stress can be derived in a similar manner to the single-phase Reynolds stress transport equation, and the result is (neglecting lift, thermophoresis, Brownian motion and gravity):

$$\frac{\partial(\overline{\overline{v_i'' v_j''}})}{\partial t} + \overline{\overline{V}}_k \frac{\partial(\overline{\overline{v_i'' v_j''}})}{\partial x_k} = -\frac{1}{\overline{\rho}_p} \frac{\partial(\overline{\rho}_p \overline{\overline{v_i'' v_j'' v_k''}})}{\partial x_k} - \overline{\overline{v_i'' v_k''}} \frac{\partial \overline{\overline{V}}_j}{\partial x_k} - \overline{\overline{v_j'' v_k''}} \frac{\partial \overline{\overline{V}}_i}{\partial x_k} + \frac{\overline{\overline{u_i' v_j''}} + \overline{\overline{u_j' v_i''}} - 2\overline{\overline{v_i'' v_j''}}}{\tau_p} \tag{6.12}$$

In an inhomogeneous turbulent flow, the particles are prevented from attaining local equilibrium by the production of particle fluctuating stress (the second and third terms on the

right hand side of equation 6.12). If the turbulence were homogeneous, the gradients of mean quantities would vanish and:

$$\overline{\overline{v_i'' v_j''}} = \frac{\overline{\overline{u_i' v_j''}} + \overline{\overline{u_j' v_i''}}}{2} \tag{6.13}$$

By adopting the 'local equilibrium' model, equation 6.13 may be used even for inhomogeneous turbulence (especially for small τ_p as all the other terms in the transport equation become very small). The problem of modelling the correlation $\overline{\rho}_p \overline{\overline{v_i'' v_j''}}$ is now replaced by the need to provide a local equilibrium model for $\overline{\rho}_p \overline{\overline{u_i' v_j''}}$. The turbulence modelling adopted for this correlation is detailed in Slater *et al.* (2003), and the result is:

$$\overline{\overline{u_i' v_j''}} = \overline{\overline{u_j' v_i''}} \cong \Gamma \overline{u_i' u_j'} \tag{6.14a}$$

where

$$\Gamma = \frac{1}{\tau_p} \int_0^\infty e^{-s/\tau_p} R(s) ds \tag{6.14b}$$

and $R(s)$ is the gas velocity autocorrelation function. A commonly used approximation is the expression $R(s) = exp(-s/\tau_g)$ where τ_g is the integral time-scale of the turbulence. Substituting this into equation 6.14b gives:

$$\Gamma = \frac{\tau_g}{\tau_g + \tau_p} \tag{6.14c}$$

Combining these results gives:

$$\overline{\overline{v_i'' v_j''}} \cong \Gamma \overline{u_i' u_j'} = \frac{\tau_g}{\tau_g + \tau_p} \overline{u_i' u_j'} \tag{6.14d}$$

It should be noted that, strictly speaking, equation 6.14a requires a density-weighted correlation, but this is ignored in the derivations by Slater *et al.* (2003), Reeks (1991) and others.

Details of the modelling of the density-velocity correlation can also be found in Slater *et al.* (2003). The result is that:

$$\overline{\rho}_p \overline{\overline{u_i'}} \cong -\left(1 - \frac{\tau_p}{\tau_g}\Gamma\right) D_{ik} \frac{\partial \overline{\rho}_p}{\partial x_k} \tag{6.15}$$

where D_{ik} is the turbulent diffusion tensor for a passive scalar. By inserting equation 6.14c and making a further simplification by assuming isotropy of turbulence so that $D_{ik} = \delta_{ik} D_T$ (where D_T is the isotropic turbulent diffusion coefficient):

$$\overline{\rho}_p \overline{\overline{u_i'}} \cong -\Gamma D_T \frac{\partial \overline{\rho}_p}{\partial x_i} \tag{6.16}$$

where $D_T \cong \nu_{g,T}$ (equation 3.35).

These turbulence models (equations 6.14d and 6.16) are quite simple, and some more complex modelling approaches were discussed in section 3.3.2. However, Slater *et al.* (2003) argue that such models cannot be reliably substantiated, and do not necessarily result in improved accuracy. Young & Leeming (1997) have also shown that the local equilibrium assumption can be successful in predicting the gross features, even if the local details are less accurate.

6.2.5 Working form of the particle conservation equations

Combining equations 6.14d and 6.15 with equation 6.11 gives:

$$\frac{\partial \overline{\overline{V}}_i}{\partial t} + \overline{\overline{V}}_k \frac{\partial \overline{\overline{V}}_i}{\partial x_k} = -\frac{\partial(\Gamma \overline{u_i' u_k'})}{\partial x_k} - \frac{(\Gamma \overline{u_i' u_k'})}{\overline{\rho}_p} \frac{\partial \overline{\rho}_p}{\partial x_k} - \left(1 - \frac{\tau_p}{\tau_g}\Gamma\right) D_{ik} \frac{\partial \overline{\rho}_p}{\partial x_k} - \frac{D_B}{\tau_p \overline{\rho}_p} \frac{\partial \overline{\rho}_p}{\partial x_i} + \frac{(\overline{U}_i - \overline{\overline{V}}_i)}{\tau_p} + (\overline{\overline{\mathsf{F}}}_{L,i} + \overline{\overline{\mathsf{F}_{TH,i}}} + g) \quad (6.17)$$

A more general expression of equation 3.36 is $D_{ik} = \tau_g \overline{u_i' u_k'}$. Substituting this into the second term on the right hand side of equation 6.17, rearranging, and again assuming isotropy ($D_{ik} = \delta_{ik} D_T$) gives:

$$\frac{\partial \overline{\overline{V}}_i}{\partial t} + \overline{\overline{V}}_k \frac{\partial \overline{\overline{V}}_i}{\partial x_k} = -\frac{\partial(\Gamma \overline{u_i' u_k'})}{\partial x_k} - \frac{(D_T + D_B)}{\tau_p \overline{\rho}_p} \frac{\partial \overline{\rho}_p}{\partial x_i} + \frac{(\overline{U}_i - \overline{\overline{V}}_i)}{\tau_p} + (\overline{\overline{\mathsf{F}}}_{L,i} + \overline{\overline{\mathsf{F}_{TH,i}}} + g) \quad (6.18)$$

For the purposes of computational work, it is convenient to define an ensemble-mean density-weighted particle convective velocity, $\overline{\overline{W}}_i$. The total mass flux of particles is again divided into convective and diffusive components:

$$\overline{\rho}_p \overline{\overline{V}}_i = \overline{\rho}_p \overline{\overline{W}}_i - (D_T + D_B) \frac{\partial \overline{\rho}_p}{\partial x_i} \quad (6.19)$$

A similar procedure to that described in section 6.2.2 for the instantaneous equations is now followed. Equation 6.19 is substituted into equations 6.8 and 6.18, and $\overline{\overline{V}}_i$ is replaced by $\overline{\overline{W}}_i$ in the acceleration term of equation 6.18 (this is the only approximation):

$$\frac{\partial \overline{\rho}_p}{\partial t} + \frac{\partial(\overline{\rho}_p \overline{\overline{W}}_k)}{\partial x_k} = \frac{\partial}{\partial x_k}\left[(D_T + D_B)\frac{\partial \overline{\rho}_p}{\partial x_i}\right] \quad (6.20\text{a})$$

$$\frac{\partial \overline{\overline{W}}_i}{\partial t} + \overline{\overline{W}}_k \frac{\partial \overline{\overline{W}}_i}{\partial x_k} \cong -\frac{\partial(\Gamma \overline{u_i' u_k'})}{\partial x_k} + \frac{(\overline{U}_i - \overline{\overline{W}}_i)}{\tau_p} + (\overline{\overline{\mathsf{F}}}_{L,i} + \overline{\overline{\mathsf{F}_{TH,i}}} + g) \quad (6.20\text{b})$$

The left hand side of equation 6.20b represents the mean particle convective acceleration, while the terms on the right represent the forces (per unit particle mass) producing this

acceleration, namely turbophoresis, drag, lift and thermophoresis. Equation 6.20b does not involve particle density and can be solved for $\overline{\overline{W}}_i$ independently of equation 6.20a, and this represents a considerable computational simplification.

6.3 Fully-developed axisymmetric turbulent annular flow

6.3.1 Particle momentum equation

The particle mass conservation and momentum equation are transformed into a cylindrical polar coordinate system, where (r, θ, z) are the radial, circumferential and axial components respectively, for steady vertical flow through an annulus. For axisymmmetric flow, the θ-component of the particle momentum equation yields no useful information and is omitted; the circumferential variation of all time-mean quantities is zero; and for non-swirling flow $\overline{\overline{W}}_\theta = \overline{U}_\theta = 0$. The radial and axial momentum equations for steady flow may be written as:

$$\overline{\overline{W}}_r \frac{\partial \overline{\overline{W}}_r}{\partial r} + \overline{\overline{W}}_z \frac{\partial \overline{\overline{W}}_r}{\partial z} = -\frac{\partial(\Gamma \overline{u'_r u'_r})}{\partial r} - \frac{\partial(\overline{v'_r v'_z})}{\partial z} + \frac{\phi_d(\overline{U}_r - \overline{\overline{W}}_r)}{\tau_p} + \overline{\overline{\mathsf{F}}}_{L,r} + \overline{\overline{\mathsf{F}}}_{TH,r} \quad (6.21a)$$

$$\overline{\overline{W}}_r \frac{\partial \overline{\overline{W}}_z}{\partial r} + \overline{\overline{W}}_z \frac{\partial \overline{\overline{W}}_z}{\partial z} = -\frac{\partial(\overline{v'_r v'_z})}{\partial r} - \frac{\partial(\overline{v'_z v'_z})}{\partial z} + \frac{\phi_d(\overline{U}_z - \overline{\overline{W}}_z)}{\tau_p} + \overline{\overline{\mathsf{F}}}_{L,z} + \overline{\overline{\mathsf{F}}}_{TH,z} + g \quad (6.21b)$$

and ϕ_D, which is a function of particle slip Reynolds number, has been introduced in order to take account of non-Stokesian drag.

The following simplifications are made:

- for fully-developed annular flow, the axial variation of the time-mean products of fluctuating components is zero
- for fully-developed annular flow, the time-mean particle velocity field is independent of the axial coordinate
- for fully-developed annular flow, the radial component of the time-mean fluid velocity is zero
- Brownian diffusion, lift and thermophoresis in the axial direction are neglected
- the axial momentum equation is less important than the radial equation, and so the modelling of $\overline{v'_r v'_z}$ is not crucial. It is consequently represented by a gradient diffusion model, and its turbulent viscosity is assumed equal to that of the fluid, such that:

$$-\overline{v'_r v'_z} = \nu_{g,T} \frac{\partial \overline{\overline{W}}_z}{\partial r} \quad (6.22)$$

The equations are non-dimensionalised using: $r^+ = ru_*/\nu_g$ where r is measured from the inner wall radius r_i to the outer wall radius r_o, $\tau_p^+ = \tau_p u_*^2/\nu_g$, $g^+ = g\nu_g/u_*^3$, $\overline{\overline{F}}^+ = \overline{\overline{F}}\nu_g/u_*^3$, $\nu_{g,T}^+ = \nu_{g,T}/\nu_g$ and $t^+ = tu_*^2/\nu_g$. All velocities are non-dimensionalised with the friction velocity, $u_* = \sqrt{\overline{\tau}_w/\rho_g}$.

The dimensionless particle momentum equations are:

$$\boxed{\overline{\overline{W}}_r^+ \frac{\partial \overline{\overline{W}}_r^+}{\partial r^+} = -\frac{\partial(\Gamma \overline{u_r'^+ u_r'^+})}{\partial r^+} + \frac{-\phi_d \overline{\overline{W}}_r^+}{\tau_p^+} + \overline{\overline{\mathsf{F}}}_{L,r}^+ + \overline{\overline{\mathsf{F}}}_{TH,r}^+} \tag{6.23a}$$

$$\boxed{\overline{\overline{W}}_r^+ \frac{\partial \overline{\overline{W}}_z^+}{\partial r^+} = \frac{\partial}{\partial r^+}\left(\nu_{g,T}^+ \frac{\partial \overline{\overline{W}}_z^+}{\partial r^+}\right) + \frac{\phi_d(\overline{U}_z^+ - \overline{\overline{W}}_z^+)}{\tau_p^+} + g^+} \tag{6.23b}$$

6.3.2 Particle mass conservation equation

For fully-developed flow, it has been assumed that $\partial\overline{\overline{W}}_r/\partial z$ and $\partial\overline{\overline{W}}_z/\partial z = 0$, however $\partial\overline{\rho}_p/\partial z$ is not equal to zero, as particles are removed from the flow by deposition to the walls, and $\overline{\rho}_p$ consequently decreases in the axial direction, such that $\overline{\rho}_p = \overline{\rho}_p(r, z)$.

Making the same assumptions as with the momentum equation, the particle mass conservation equation in cylindrical polar coordinates is:

$$\frac{\partial \overline{\rho}_p}{\partial t} + \frac{1}{r}\frac{\partial(r\overline{\rho}_p \overline{\overline{W}}_r)}{\partial r} + \frac{\partial(\overline{\rho}_p \overline{\overline{W}}_z)}{\partial z} = \frac{1}{r}\frac{\partial}{\partial r}\left[r(D_T + D_B)\frac{\partial \overline{\rho}_p}{\partial r}\right] \tag{6.24}$$

A dimensionless time-mean particle density $\overline{\psi}$ is defined by:

$$\overline{\psi} = \frac{\overline{\rho}_p(r, z)}{\overline{\rho}_{p,m}(z)} \qquad \text{and} \qquad \overline{\rho}_{p,m}(z) = \frac{2}{r_o^2 - r_i^2}\int_{r_i}^{r_o} r\overline{\rho}_p(r, z)dr \tag{6.25}$$

where $\overline{\rho}_{p,m}(z)$ is the time-mean particle density averaged across the annulus. The definition of $\overline{\psi}$ is designed to remove the dependency of particle density on axial position, so that the particle conservation of mass equation can be considered as being fully-developed (Young & Leeming, 1997).

For the present, it will be assumed that $\overline{\psi} = \overline{\psi}(r)$, and the mass flux to the wall (where subscript i denotes the inner wall and o the outer wall) is:

$$J_{w,i/o}(z) = \overline{\rho}_{p,m}(z)\left[\overline{\psi}\,\overline{\overline{W}}_r - (D_B + D_T)\frac{d\overline{\psi}}{dr}\right]_{w,i/o} \tag{6.26}$$

A deposition velocity is then defined as $V_{d,i/o} = J_{w,i/o}(z)/\overline{\rho}_{p,m}(z)$ and its dimensionless form

is:

$$(V_d^+)_{i/o} = \frac{J_{w,i/o}(z)}{\overline{\rho}_{p,m}(z)u_*} = \left[\overline{\psi}\,\overline{\overline{W}}_r^+ - (D_B^+ + D_T^+)\frac{d\overline{\psi}}{dr^+}\right]_{w,i/o} \tag{6.27}$$

where D_B and D_T are made non-dimensional using ν_g. It then follows that, if $\overline{\psi} = \overline{\psi}(r)$, V_d^+ is independent of z. This equation is applicable to either wall of the annulus.

The total particle mass flow at any axial location is:

$$\dot{m}_p = \overline{\rho}_{p,m}(z)2\pi \int_{r_i}^{r_o} r\overline{\psi}(r)\overline{\overline{W}}_z(r)dr \tag{6.28}$$

A dimensionless particle mass flow rate (independent of z) can be defined as:

$$\dot{m}_p^+ = \frac{\dot{m}_p(z)u_*}{\overline{\rho}_{p,m}(z)\nu_g^2} = 2\pi \int_{r_i^+}^{r_o^+} r^+\overline{\psi}(r^+)\overline{\overline{W}}_z^+(r^+)dr^+ \tag{6.29}$$

where global conservation of mass imposes the requirement that:

$$\frac{d\dot{m}_p(z)}{dz} = -2\pi(r_o J_{w,o} - r_i J_{w,i}) \tag{6.30}$$

Substituting the definitions of $J_{w,i/o}$ and $\dot{m}_p$ (equations 6.26 and 6.28):

$$\frac{d\overline{\rho}_{p,m}(z^+)}{dz^+} = -K\overline{\rho}_{p,m}(z^+) \tag{6.31}$$

where K is a similarity parameter describing the rate of depletion of particles from the flow (through use of equations 6.27 and 6.29):

$$K = \frac{2\pi[r_o(V_d^+)_o - r_i(V_d^+)_i]}{\dot{m}_p^+} \tag{6.32}$$

If $\overline{\psi} = \overline{\psi}(r)$, then the mean particle density decays exponentially as:

$$\overline{\rho}_{p,m}(z^+) = \overline{\rho}_{p,m}(0)\ \exp(-Kz^+) \tag{6.33}$$

where $\overline{\rho}_{p,m}(0)$ is the value of $\overline{\rho}_{p,m}$ at the inlet of the annulus ($z^+ = 0$).

Introducing equation 6.31 into equation 6.24, the dimensionless particle mass conservation equation becomes:

$$\boxed{\frac{1}{r^+}\frac{d}{dr^+}(r^+\overline{\psi}\,\overline{\overline{W}}_r^+) - K^+\overline{\psi}\,\overline{\overline{W}}_z^+ = \frac{1}{r^+}\frac{d}{dr^+}\left[r^+(D_B^+ + D_T^+)\frac{d\overline{\psi}}{dr^+}\right]} \tag{6.34}$$

6.3.3 Boundary conditions

Boundary conditions for the momentum equations are required at the inner and outer walls, but the purely convective nature of the momentum equations means that the particles have no knowledge of the wall before they deposit. An 'internal' boundary condition is applied at the boundary by upwinding the spatial derivatives, once the equations have been written in finite-difference form.

The wall boundary condition for $\overline{\rho}_p$ given by Young & Leeming (1997) is used for the conservation of mass equation. Although referred to as the 'wall' boundary condition, the finite dimensions of the particles means that it is applied one particle radius from the wall. The boundary condition was derived from a simple kinetic approach based on a Maxwellian distribution of particle velocity. Referring to equation 6.27, the dimensionless deposition velocity is now written as:

$$(V_d^+)_i = \left[\overline{\psi}\,\overline{\overline{W}}_r^+ - (D_B^+ + D_T^+)\frac{d\overline{\psi}}{dr^+}\right]_{w,i} = \overline{\psi}_{w,i}\left[\frac{1}{2}\overline{\overline{W}}_r^+[1+\mathrm{erf}(-M_r)] - \frac{\exp(-M_r^2)}{\sqrt{2\pi Sc\tau_p^+}}\right]_{w,i} \quad (6.35a)$$

$$(V_d^+)_o = \left[\overline{\psi}\,\overline{\overline{W}}_r^+ - (D_B^+ + D_T^+)\frac{d\overline{\psi}}{dr^+}\right]_{w,o} = \overline{\psi}_{w,o}\left[\frac{1}{2}\overline{\overline{W}}_r^+[1+\mathrm{erf}(+M_r)] + \frac{\exp(-M_r^2)}{\sqrt{2\pi Sc\tau_p^+}}\right]_{w,o} \quad (6.35b)$$

where erf is the error function, and $M_r = \overline{\overline{W}}_r^+\sqrt{\frac{1}{2}Sc\tau_p^+}$. The only difference between the expressions for the inner and outer wall is a minus sign in the $erf(\pm M_r)$ term. r_+ is measured from the inner wall, and the result is that $\overline{\overline{W}}_r$ is negative when particles move towards the inner wall and positive when they move towards the outer wall. The opposite signs of $\overline{\overline{W}}_r$ ensure that the signs of $(V_d^+)_i$ and $(V_d^+)_o$ are in opposite directions. The sign changes are subtle, but important, for obtaining the correct values of V_d^+.

6.4 Solution of the particle equations

Equations 6.23a, 6.23b and 6.34 (each with a boundary condition at each wall) comprise the complete set of particle equations to be solved. Although the boundary conditions differ, because of the different geometries, the density-weighted averaged equations are essentially the same as the Reynolds averaged equations obtained by Young & Leeming (1997). The validity of this result (in light of work by Cerbelli *et al.* (2001)) will be discussed in more detail in the next chapter.

The equations are solved numerically using a time-marching approach, and to enable this a time derivative term is added to each equation:

$$\frac{\partial\overline{\overline{W}}_r^+}{\partial t^+} = -\overline{\overline{W}}_r^+\frac{\partial\overline{\overline{W}}_r^+}{\partial r^+} - \frac{\partial(\Gamma\overline{u_r'^+u_r'^+})}{\partial r^+} + \frac{-\phi_d\overline{\overline{W}}_r^+}{\tau_p^+} + \overline{\overline{\mathsf{F}}}_{L,r}^+ + \overline{\overline{\mathsf{F}}}_{TH,r}^+ \quad (6.36a)$$

$$\frac{\partial \overline{\overline{W}}_z^+}{\partial t^+} = -\overline{\overline{W}}_r^+ \frac{\partial \overline{\overline{W}}_z^+}{\partial r^+} + \frac{\partial}{\partial r^+}\left(\nu_{g,T}^+ \frac{\partial \overline{\overline{W}}_z^+}{\partial r^+}\right) + \frac{\phi_d(\overline{U}_z^+ - \overline{\overline{W}}_z^+)}{\tau_p^+} + g^+ \tag{6.36b}$$

$$\frac{\partial \overline{\psi}}{\partial t^+} = -\frac{1}{r^+}\frac{d}{dr^+}(r^+ \overline{\psi}\,\overline{\overline{W}}_r^+) + K^+ \overline{\psi}\,\overline{\overline{W}}_z^+ + \frac{1}{r^+}\frac{d}{dr^+}\left[r^+(D_B^+ + D_T^+)\frac{d\overline{\psi}}{dr^+}\right] \tag{6.36c}$$

By writing the 'non-conservative' form of the particle momentum equations in terms of a particle convective velocity, the momentum equations may be solved for $\overline{\overline{W}}_r^+$ and $\overline{\overline{W}}_z^+$ before the conservation of mass equation is solved for $\overline{\psi}$. Young & Leeming (1997) point out that while conservation of momentum cannot be guaranteed using a non-conservative differencing scheme, this is not actually a physically realistic requirement as the assumption of one-way coupling has already created an unbalanced source of momentum. However, $\overline{\psi}$ may be found using a conservative finite-volume technique, ensuring that particles are not numerically added or removed from the flow field.

6.4.1 Grid generation

In turbulent pipe flows, the grid is usually structured to have greater resolution near the wall than in the core of the flow. This ensures that the rapidly changing gas turbulence near the wall is captured, but without sacrificing computational efficiency by over-resolution of the core region, where the turbulence is nearly homogeneous. In a turbulent annulus, there are two wall regions to be considered. Thus, a computational grid was constructed, with grid spacings that were very small near the inner wall and increased gradually until the annulus half-width was reached, and then decreased again towards the outer wall. If G is the geometric progression ratio, then:

$$(r_{kp/2}^+ - r_1^+)(G-1) = \Delta r_2^+ (G^{kp/2-1} - 1) \tag{6.37}$$

where kp is the number of grid points, and the grid spacing increases from the inner wall ($k = 1$) to half way across the domain ($k = kp/2$). $\Delta r_2^+ = r_2^+ - r_1^+ = r_p^+$ and $r_1^+ = r_p^+$, which reflects the fact that particles deposit when they come within one radius of the wall. The width of the first grid spacing (Δr_2^+) is set equal to r_p^+ to ensure that particle behaviour close to the wall is accurately captured. This equation is solved iteratively using a Newton-Raphson procedure for G. The grid spacing decreases between $k = kp/2$ and the outer wall ($k = kp$) with a geometric progression ratio of G^{-1}, i.e. $\Delta r_2^+ = \Delta r_{kp}^+$.

The pre-determined solution for the gas flow field is then interpolated onto this computational grid, using a variable power spline curve fitting procedure developed by Soanes (1976), the coding for which was implemented by Young (1991).

6.4.2 Particle momentum equation

The particle radial and axial momentum equations are solved by the semi-implicit time-marching integration of equations 6.36a and 6.36b. A second-order accurate central-differencing scheme is used.

Spatial differencing

The centrally-differenced spatial derivatives can be defined for any grid point k (except points $k = 1, kp/2$, and kp) by:

$$\left.\frac{\partial A}{\partial r^+}\right|_k = \frac{A_{k+1} + (G^2 - 1)A_k - G^2 A_{k-1}}{G(G+1)\Delta r_k^+} \tag{6.38}$$

where $\Delta r_k^+ = r_k^+ - r_{k-1}^+$, and A is a property of the flow. G represents either G (from equation 6.37) or G^{-1}, depending on whether k is greater than or less than $kp/2$. When $k = kp/2$,

$$\left.\frac{\partial A}{\partial r^+}\right|_{kp/2} = \frac{A_{kp/2+1} - A_{kp/2-1}}{2\Delta r_{kp/2}^+} \tag{6.39}$$

and at either wall:

$$\left.\frac{\partial A}{\partial r^+}\right|_1 = \frac{A_2 - A_1}{\Delta r_2^+} \qquad \text{and} \qquad \left.\frac{\partial A}{\partial r^+}\right|_{kp} = \frac{A_{kp} - A_{kp-1}}{\Delta r_{kp}^+} \tag{6.40}$$

The upwinding of the spatial derivatives at $k = 1$ and $k = kp$ in equation 6.40 represents the application of two 'internal' boundary conditions to each momentum equation.

Central-differencing of a convective transport equation is inherently unstable when integrated explicitly in time. Artificial viscosity was included through the addition to the right hand side of equation 6.36a of the term:

$$\nu_{ART} \frac{\partial^2 \overline{\overline{W_r}}^+}{\partial r^{+2}} \tag{6.41}$$

Leeming (1995) found that the axial momentum equation did not require the addition of any artificial viscosity.

The centrally-differenced spatial second derivative at any point k (again, $k \neq 1, kp/2, k$) is:

$$\left.\frac{\partial^2 A}{\partial r^{+2}}\right|_k = \frac{2(A_{k+1} - (G+1)A_k + GA_{k-1})}{G(G+1)\Delta r_k^{+2}} \tag{6.42}$$

For $k = 1, kp/2, kp$:

$$\left.\frac{\partial^2 A}{\partial r^{+2}}\right|_1 = \frac{2(A_3 - (G+1)A_2 + GA_1)}{G(G+1)\Delta r_2^{+2}} \tag{6.43a}$$

$$\left.\frac{\partial^2 A}{\partial r^{+2}}\right|_{kp/2} = \frac{A_{kp/2+1} - 2A_{kp/2} + A_{kp/2-1}}{\Delta r_{kp/2}^{+2}} \tag{6.43b}$$

$$\left.\frac{\partial^2 A}{\partial r^{+2}}\right|_{kp} = \frac{2(A_{kp} - (G+1)A_{kp-1} + GA_{kp-2})}{G(G+1)\Delta r_{kp}^{+2}} \tag{6.43c}$$

Time integration

A semi-implicit integration scheme is used for the time-marching of the momentum equations. The radial and axial momentum equations at any point k (for $2 \leq k \leq kp-1$) are:

$$\begin{aligned}\left.\overline{\overline{W}}_r^{+}\right|_k^{i+1} &= \left.\overline{\overline{W}}_r^{+}\right|_k^{i} + \\ &\left\{\frac{\Delta t^+ \tau_p^+}{\Delta t^+ + \tau_p^+}\right\}\left\{\left(- \overline{\overline{W}}_r^{+}\frac{\partial \overline{\overline{W}}_r^{+}}{\partial r^+} - \frac{\phi_D \overline{\overline{W}}_r^{+}}{\tau_p^+} + \mathcal{S}.\alpha_L^+(\overline{U}_z^+ - \overline{\overline{W}}_z^+)\left|\frac{\partial \overline{U}_z^+}{\partial r^+}\right|^{1/2} + \nu_{ART}^+ \frac{\partial^2 \overline{\overline{W}}_r^{+}}{\partial r^{+2}}\right)\right|_k^i \\ &\quad + \left(- \frac{\partial \overline{v_r'^+ v_r'^+}}{\partial r^+} + \alpha_{TH}^+ \frac{\partial ln \overline{T}}{\partial r^+}\right)_k\Bigg\}\end{aligned} \tag{6.44}$$

$$\begin{aligned}\left.\overline{\overline{W}}_z^{+}\right|_k^{i+1} &= \left.\overline{\overline{W}}_z^{+}\right|_k^{i} + \\ &\left\{\frac{\Delta t^+ \tau_p^+}{\Delta t^+ + \tau_p^+}\right\}\left\{\left(- \overline{\overline{W}}_r^{+}\frac{\partial \overline{\overline{W}}_z^{+}}{\partial r^+} + \frac{\phi_D(\overline{U}_z^+ - \overline{\overline{W}}_z^+)}{\tau_p^+} + \frac{\partial}{\partial r^+}\left(\nu_{g,T}^+ \frac{\partial \overline{\overline{W}}_z^{+}}{\partial r^+}\right)\right)\right|_k^i + g^+\Bigg\}\end{aligned} \tag{6.45}$$

where

$$\begin{aligned}\alpha_L^+ &= \frac{\alpha_L \nu_g^{1/2}}{u_*} = 0.725\sqrt{\frac{(\rho_g/\rho_{p,mat})}{\tau_p^+}} \\ \alpha_{TH}^+ &= \frac{\alpha_{TH}}{u_*^2} = \frac{K_{TH}}{\tau_p^+} = \frac{9(\rho_g/\rho_{p,mat})}{r_p^{+2}} \frac{C_s(\frac{k_g}{k_p} + C_t Kn)}{(1 + 3C_m Kn)(1 + 2\frac{k_g}{k_p} + 2C_t Kn)}\end{aligned} \tag{6.46}$$

where $k_g = 3.75\mu_g R$, $\nu^+_{ART} = \nu_{ART}/\nu_g$, and $\mathcal{S}$ is the sign of $\partial\overline{U}^+_z/\partial r^+$. The superscript i represents the value of a property at the current time-step, while $i+1$ represents the value at the next time-step. $ln\overline{T}$ is already non-dimensional.

The drag terms are integrated implicitly with a time-step of $\Delta t^+ \tau_p^+/(\Delta t^+ + \tau_p^+)$. For large values of τ_p^+, this is equal to Δt^+, the time-step of the semi-implicit method and the time-step if the drag terms had been integrated explicitly. However, for small values of τ_p^+, the time-step of the semi-implicit method is scaled by τ_p^+. This avoids the requirement of very small time-steps that would be needed to integrate the drag terms for small τ_p^+ if a purely explicit method had been used. The time-step of the semi-implicit method is defined as:

$$\Delta t^+ = \left. \frac{\mathrm{CFL}\Delta r^+}{\left|\overline{\overline{W}}^+_r\right|} \right|_{min} \tag{6.47}$$

where CFL is a user-specified Courant number, and the subscript min requires that the minimum value across the grid be used.

The turbophoretic, thermophoretic and gravitational forces do not have a superscript as they are unchanged with time. They drive the particles' motion while the other forces are a reaction to these driving forces.

The addition of artificial viscosity is controlled by the cell Reynolds number:

$$Re_c\Big|_k = \frac{\left|\overline{\overline{W}}^+_r\right| \Delta r^+_k}{\nu^+_{ART}\Big|_k} \tag{6.48}$$

with $Re_c = 2$ being sufficient to ensure stability, and $\left|\overline{\overline{W}}^+_r\right|$ is the magnitude of the local convective velocity with which information is transferred across a cell, in the radial direction.

6.4.3 Particle mass conservation equation

The particle mass conservation equation is solved on the same grid as the momentum equations, in contrast with the method of Young & Leeming (1997) where the grid spacing is influenced by the particle density gradient. Apart from this difference, and the choice of boundary conditions, the treatment of the particle mass conservation equation is almost identical to that of Leeming (1995), with some slight changes due to the different coordinate system.

Spatial discretisation

Equation 6.36c is solved by a finite-volume time-marching integration to a steady state, because it is non-linear in $\overline{\psi}$ through K^+. The equation is integrated over a typical control volume, shown in figure 6.1. If J is the flux though each cell face, then $J_z^{net} = J_z^{in} - J_z^{out}$. Thus, the net axial flux J_z^{net} can be related to the rate of depletion of particles from the flow

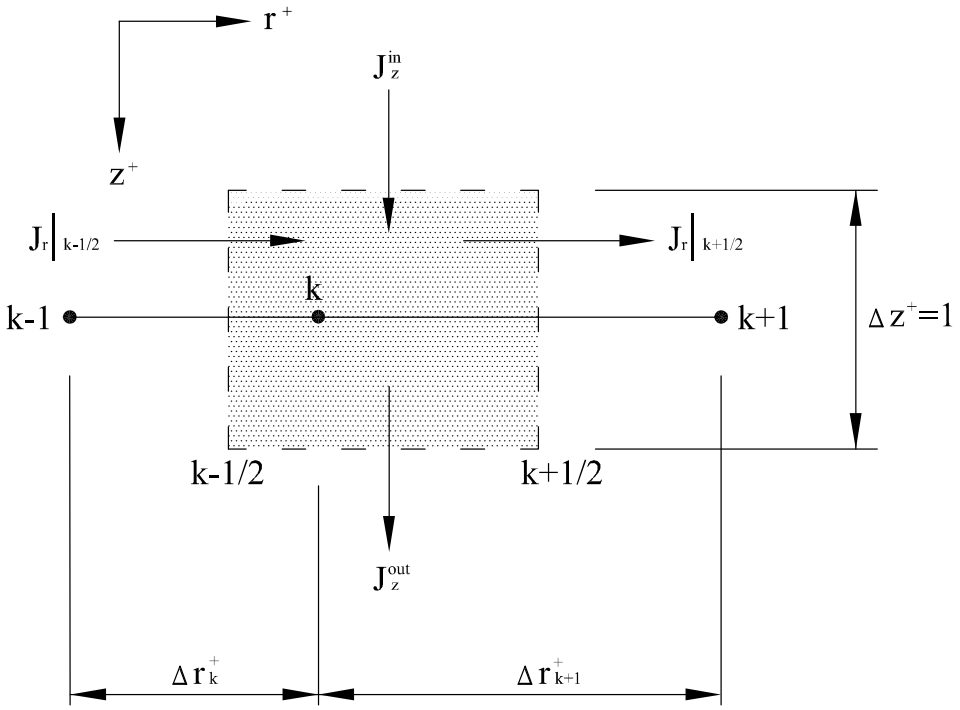

Figure 6.1: Spatial discretisation for the particle conservation of mass equation

(through K^+), and the radial flux J_r is similar in form to the definition of the wall mass flux (equation 6.26), giving:

$$\left[J_z^{net}\right] = -K^+ \overline{\psi}\, \overline{\overline{W}}_z^+ \qquad \text{and} \qquad \left[J_y\right] = \overline{\psi}\, \overline{\overline{W}}_r^+ - (D_B^+ + D_T^+)\frac{\partial \overline{\psi}}{\partial r^+} \tag{6.49}$$

Gauss's theorem then gives:

$$\begin{aligned} &\frac{\partial}{\partial t^+}\left[\,\overline{\psi}\,\right]_k r_k^+ 0.5(\Delta r_k^+ + \Delta r_{k+1}^+) + \left[J_z^{net}\right]_{k+\frac{1}{4}} r_{k+\frac{1}{4}}^+ 0.5\Delta r_{k+1}^+ \\ &+\left[J_z^{net}\right]_{k-\frac{1}{4}} r_{k-\frac{1}{4}}^+ 0.5\Delta r_k^+ + \left[J_y\right]_{k+\frac{1}{2}} r_{k+\frac{1}{2}}^+ - \left[J_y\right]_{k-\frac{1}{2}} r_{k-\frac{1}{2}}^+ = 0 \end{aligned} \tag{6.50}$$

A linear variation of quantites between grid points is assumed.

Time integration

The discretised particle conservation of mass equation (equation 6.50) is of the convection-diffusion type, and is inherently unstable to explicit methods of integration, necessitating the

use of implicit Euler integration. Rewriting equation 6.50:

$$\begin{aligned}
\left[r_k^+(\Delta r_k^+ + \Delta r_{k+1}^+)\right]\left(\frac{\overline{\psi}\,\big|_k^{i+1} - \overline{\psi}\,\big|_k^{i}}{\Delta t^+}\right) = \\
K^+\Big|^i\left(\Delta r_{k+1}^+ r_{k+\frac{1}{4}}^+ \overline{\overline{W}}_z^+\Big|_{k+\frac{1}{4}}\right)\left(0.75\,\overline{\psi}\,\big|_k^{i+1} + 0.25\,\overline{\psi}\,\big|_{k+1}^{i+1}\right) + \\
K^+\Big|^i\left(\Delta r_k^+ r_{k-\frac{1}{4}}^+ \overline{\overline{W}}_z^+\Big|_{k-\frac{1}{4}}\right)\left(0.75\,\overline{\psi}\,\big|_k^{i+1} + 0.25\,\overline{\psi}\,\big|_{k-1}^{i+1}\right) - \\
r_{k+\frac{1}{2}}^+\left[\overline{\overline{W}}_r^+\Big|_{k+\frac{1}{2}}\left(\overline{\psi}\,\big|_k^{i+1} + \overline{\psi}\,\big|_{k+1}^{i+1}\right) - 2(D_B^+ + D_T^+)_{k+\frac{1}{2}}\left(\frac{\overline{\psi}\,\big|_{k+1}^{i+1} - \overline{\psi}\,\big|_k^{i+1}}{\Delta r_{k+1}^+}\right)\right] + \\
r_{k-\frac{1}{2}}^+\left[\overline{\overline{W}}_r^+\Big|_{k-\frac{1}{2}}\left(\overline{\psi}\,\big|_k^{i+1} + \overline{\psi}\,\big|_{k-1}^{i+1}\right) - 2(D_B^+ + D_T^+)_{k-\frac{1}{2}}\left(\frac{\overline{\psi}\,\big|_k^{i+1} - \overline{\psi}\,\big|_{k-1}^{i+1}}{\Delta r_k^+}\right)\right] \qquad (6.51)
\end{aligned}$$

Boundary conditions

The boundary conditions of equation 6.35 along with equation 6.51 (applied for $2 \leq k \leq kp-1$) represent the complete set of equations needed to solve the particle conservation of mass equation. The boundary conditions are re-written in discretised form as:

$$(V_d^+)_i = \overline{\psi}\,\big|_1^{i+1}\overline{\overline{W}}_{r+}\Big|_1 - (D_B^+ + D_T^+)_1\frac{\overline{\psi}\,\big|_2^{i+1} - \overline{\psi}\,\big|_1^{i+1}}{\Delta r_2^+} = \overline{\psi}\,\big|_1^{i+1}\kappa_{w,i} \qquad (6.52a)$$

$$(V_d^+)_o = \overline{\psi}\,\big|_{kp}^{i+1}\overline{\overline{W}}_r^+\Big|_{kp} - (D_B^+ + D_T^+)_{kp}\frac{\overline{\psi}\,\big|_{kp}^{i+1} - \overline{\psi}\,\big|_{kp-1}^{i+1}}{\Delta r_{kp}^+} = \overline{\psi}\,\big|_{kp}^{i+1}\kappa_{w,o} \qquad (6.52b)$$

where

$$\kappa_{w,i} = \frac{1}{2}\overline{\overline{W}}_r^+\Big|_1[1 + \mathrm{erf}(-M_{r,i})] - \frac{\exp(-M_{r,i}^2)}{\sqrt{2\pi Sc\tau_p^+}} \quad \text{and} \quad M_{r,i} = \overline{\overline{W}}_r^+\Big|_1\sqrt{\frac{1}{2}Sc\tau_p^+}$$

$$\kappa_{w,o} = \frac{1}{2}\overline{\overline{W}}_r^+\Big|_{kp}[1 + \mathrm{erf}(+M_{r,o})] + \frac{\exp(-M_{r,o}^2)}{\sqrt{2\pi Sc\tau_p^+}} \quad \text{and} \quad M_{r,o} = \overline{\overline{W}}_r^+\Big|_{kp}\sqrt{\frac{1}{2}Sc\tau_p^+}$$

Equations 6.51 and 6.52 can be written in the general form:

$$c_1\overline{\psi}\,\big|_1^{i+1} + c_2\overline{\psi}\,\big|_2^{i+1} = c_4 \qquad (6.54a)$$

$$b_{1,k}\overline{\psi}\,\big|_{k-1}^{i+1} + b_{2,k}\overline{\psi}\big|_k^{i+1} + b_{3,k}\overline{\psi}\,\big|_{k+1}^{i+1} = b_{4,k} \qquad (6.54b)$$

$$b_{1,kp}\overline{\psi}\,\big|_{kp-1}^{i+1} + b_{2,kp}\overline{\psi}\,\big|_{kp}^{i+1} = b_{4,kp} \qquad (6.54c)$$

where the coefficients are obtained by a simple rearrangement of the equations. The equations 6.54 can be written in matrix-vector form and solved with a single sweep of Gaussian

elimination.

$$\begin{bmatrix} c_1 & c_2 & & & & & & \\ & b_{1,2} & b_{2,2} & b_{3,2} & & & & \\ & & b_{1,3} & b_{2,3} & b_{3,3} & & & \\ & & & \dots & \dots & \dots & & \\ & & & & \dots & \dots & \dots & \\ & & & & & b_{1,kp-1} & b_{2,kp-1} & b_{3,kp-1} \\ & & & & & & b_{1,kp} & b_{2,kp} \end{bmatrix} \begin{bmatrix} \overline{\psi}\big|_1^{i+1} \\ \overline{\psi}\big|_2^{i+1} \\ \overline{\psi}\big|_3^{i+1} \\ \dots \\ \dots \\ \overline{\psi}\big|_{kp-1}^{i+1} \\ \overline{\psi}\big|_{kp}^{i+1} \end{bmatrix} = \begin{bmatrix} c_4 \\ b_{4,2} \\ b_{4,3} \\ \dots \\ \dots \\ b_{4,kp-1} \\ b_{4,kp} \end{bmatrix} \tag{6.55}$$

As the scheme is implicit, it is unconditionally stable and the time-step is set so that the CFL number is 10.

For fully-developed turbulent pipe flow, Leeming (1995) applied boundary conditions at the pipe wall and centre-line. The two wall boundary conditions applied for the case of the annulus mean that while the shape of the particle density profile obtained may be realistic, its actual magnitude may not. The dimensionless time-mean particle density averaged across the annulus is defined as:

$$\overline{\psi}_m = \frac{2}{r_o^{+2} - r_i^{+2}} \int_{r_i^+}^{r_o^+} r^+ \overline{\psi} dr^+ \tag{6.56}$$

The magnitude of $\overline{\psi}$ is controlled by ensuring that $\overline{\psi}_m$ tends towards unity by applying the relationship:

$$\overline{\psi}_k^{i+1} = \frac{\overline{\psi}_k^{i+1}}{\overline{\psi}_m} \tag{6.57}$$

at the end of each time-step.

6.5 Summary

The theory and numerical scheme described in this chapter are based on the work of Leeming (1995), Young & Leeming (1997) and Slater *et al.* (2003) for turbulent pipe flow. The particle equations of motion derived here using particle density-weighted averaging are essentially the same as those derived by Young & Leeming (1997) using Reynolds averaging. They have been extended to the case of turbulent annular flow, and were used to provide the numerical results presented and discussed in the next chapter.

Chapter 7

A numerical study of particle deposition in a turbulent annular flow

7.1 Introduction

The theory of particle deposition and the numerical scheme presented in the previous chapter were used to write a computer code to solve the governing equations of particle motion in a fully-developed turbulent annular flow. The code was written to produce numerical results for comparison with the experimental data for thermophoretic deposition presented in chapter 5. As part of this experimental investigation, data were also obtained for isothermal deposition in a turbulent annulus, as a datum against which the thermophoretic deposition could be compared. The isothermal deposition velocities were expected to be very similar to those in an isothermal turbulent pipe flow. However, as discussed in section 5.3, when $\tau_p^+ > 20$ (the inertia moderated regime), the experimental deposition velocities for the turbulent annulus were almost an order of magnitude lower than those for turbulent pipe flow. While experimental conditions were found to be responsible for some unusual behaviour over this range of τ_p^+, and the order of magnitude deviation in V_d^+ has been attributed to the excessive deposition at the inlet to the test section, this is not the first study to find variations in depositional behaviour in this range of τ_p^+.

The first part of this chapter involves a study of isothermal particle deposition in a turbulent annulus, to illustrate the interaction of the various transport mechanisms without thermophoresis. Attention is paid to the inertia moderated regime in particular, to illustrate the variations in V_d^+ (from both experimental and numerical studies) and to discuss possible explanations for the behaviour mentioned above. Recent works based on the theory of Young & Leeming (1997) are examined, and the results of direct numerical simulations (DNS) in turbulent pipe and channel flows are surveyed. The second part consists of a numerical study of thermophoretic deposition in a turbulent annulus, and comparison with the experimental

results. Thermophoresis does not appear to alter significantly the deposition rates of particles in the inertia moderated regime, and the isothermal results were as expected outside of this regime. Consequently, the study of thermophoresis can proceed with confidence, despite the experimental results obtained for $\tau_p^+ > 20$.

7.2 Isothermal particle deposition

The work of Young & Leeming (1997) (on which this numerical study is based) has been the subject of much recent attention, and has come to be known as both the Advection-Diffusion Equation (ADE) approach, and the unified deposition theory. Shin & Lee (2001) attempted to improve on the local equilibrium assumption by including a non-equilibrium 'memory effect' in the turbophoretic term, valid in the absence of the lift force; Shin *et al.* (2003) extended this non-equilibrium analysis to take account of shear-induced lift, which plays a significant role in the deposition of particles in the inertia moderated regime, and also examined the choice of particle diffusivity and the 'crossing trajectory' effect; Cerbelli *et al.* (2001) estimated the magnitude of a correlation involving the divergence of the particle velocity field that was ignored by Young & Leeming (1997), and found that it can have a significant effect on particle density profiles; and Reeks (2003) conducted an extensive comparison between the approach of Young & Leeming (1997) (with and without the inclusion of the extra correlation from Cerbelli *et al.* (2001)), and an Eulerian model approach based on the probability density function (PDF) method.

Some numerical results found using the computer code described in the previous chapter will now be presented. The success of the theory of Young & Leeming (1997) was the use of comparatively simple theoretical models to represent quantitively the physical processes involved in particle deposition. Before the recent developments (which attempt to provide qualitative improvements) are examined in closer detail, the influence of the Saffman lift force and the prescription of the fluid turbulent properties on particle deposition will first be examined. This is done to demonstrate the large influence that the lift force can have on deposition velocities, and to ascertain the sensitivity of particle deposition to the fluid flow field (the governing equations of particle motion are solved using the fluid flow field as an input). An over-sensitivity to changes in the fluid turbulence characteristics (about which there is some uncertainty), would greatly hinder any attempts at qualitative improvements in particle turbulence modelling, as differences between predicted and measured deposition rates could be attributed to limitations in the modelling of the fluid or the particle turbulence.

7.2.1 The Saffman lift force

As τ_p^+ increases, particles develop a streamwise slip velocity relative to the fluid ($\overline{U}_z - \overline{\overline{W}}_z$). The lift force is related to this slip velocity (see equation 6.9b), and so the deposition velocity changes quite considerably with the inclusion of the lift force, for $\tau_p^+ > 1$. This can be seen

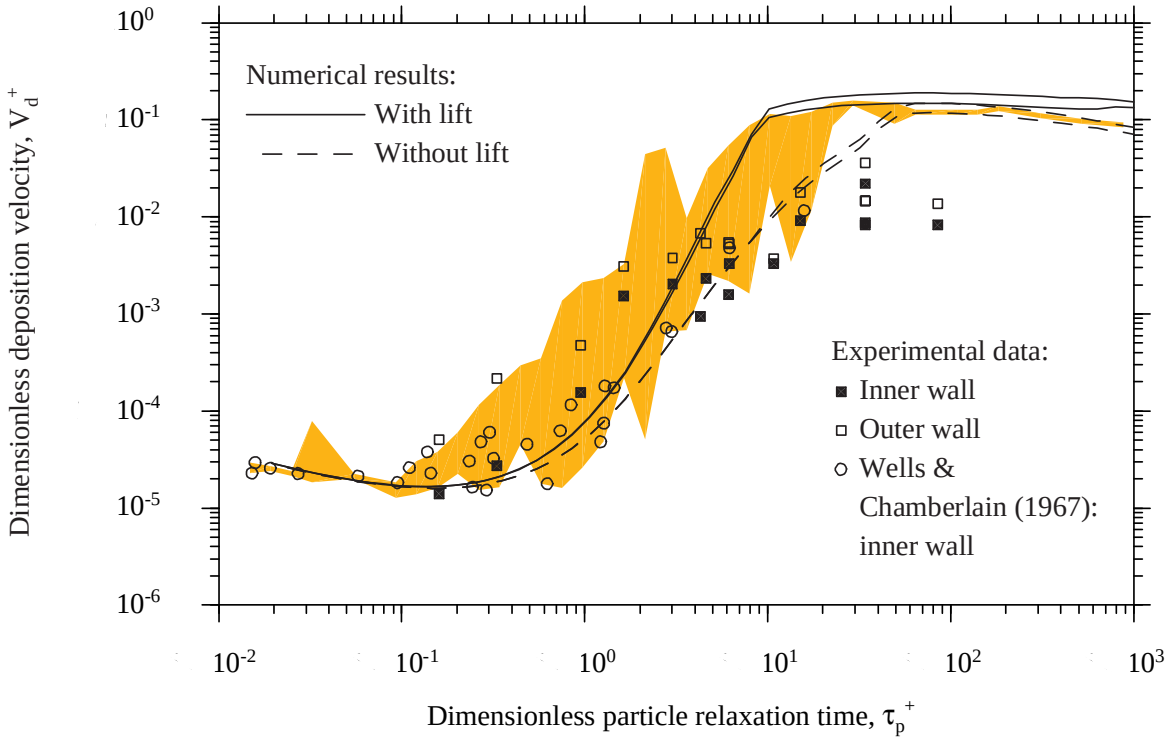

Figure 7.1: Isothermal particle deposition in a turbulent annulus with and without lift (in both cases, the inner wall deposition velocity is slightly higher than that at the outer wall, for large τ_p^+)

clearly in figure 7.1, which shows calculated values of V_d^+ for turbulent flow in an annulus under isothermal conditions with $Re \approx 5900$ (this matches the experimental conditions). The experimental data and numerical results show good agreement, except at large τ_p^+. The inner and outer wall deposition velocities are almost equal in the numerical study, but the experiments showed $(V_d^+)_o$ to be larger than $(V_d^+)_i$, especially for small τ_p^+. However, V_d^+ is much lower at small τ_p^+, and thus more prone to error. The numerical results also show that deposition in an isothermal turbulent annulus is very similar to that in a pipe. The lift force couples the axial and radial momentum equations, so that there is no need to solve the particle axial momentum equation when the lift force is neglected.

Figures 7.2 and 7.3 show the dimensionless profiles of particle velocity in the radial direction (i.e. towards/away from the wall) $\overline{\overline{W}}_r^+$, acceleration and forces per unit mass of particles in the radial direction $\overline{\overline{F}}_r^+$, and dimensionless particle density $\overline{\psi}$, all plotted against dimensionless distance from the inner wall y^+. These profiles are shown for a range of different values of τ_p^+, both with and without lift (figures 7.2 and 7.3 respectively). The vertical axes for the $\overline{\psi}$ profiles are offset from the walls so that the near-wall behaviour is not obscured, and different ordinate scales have been used for each diagram. For the profiles of $\overline{\overline{W}}_r^+$ and $\overline{\overline{F}}_r^+$, a negative value represents a velocity or force towards the inner wall, while a positive value is representative of a velocity/force towards the outer wall.

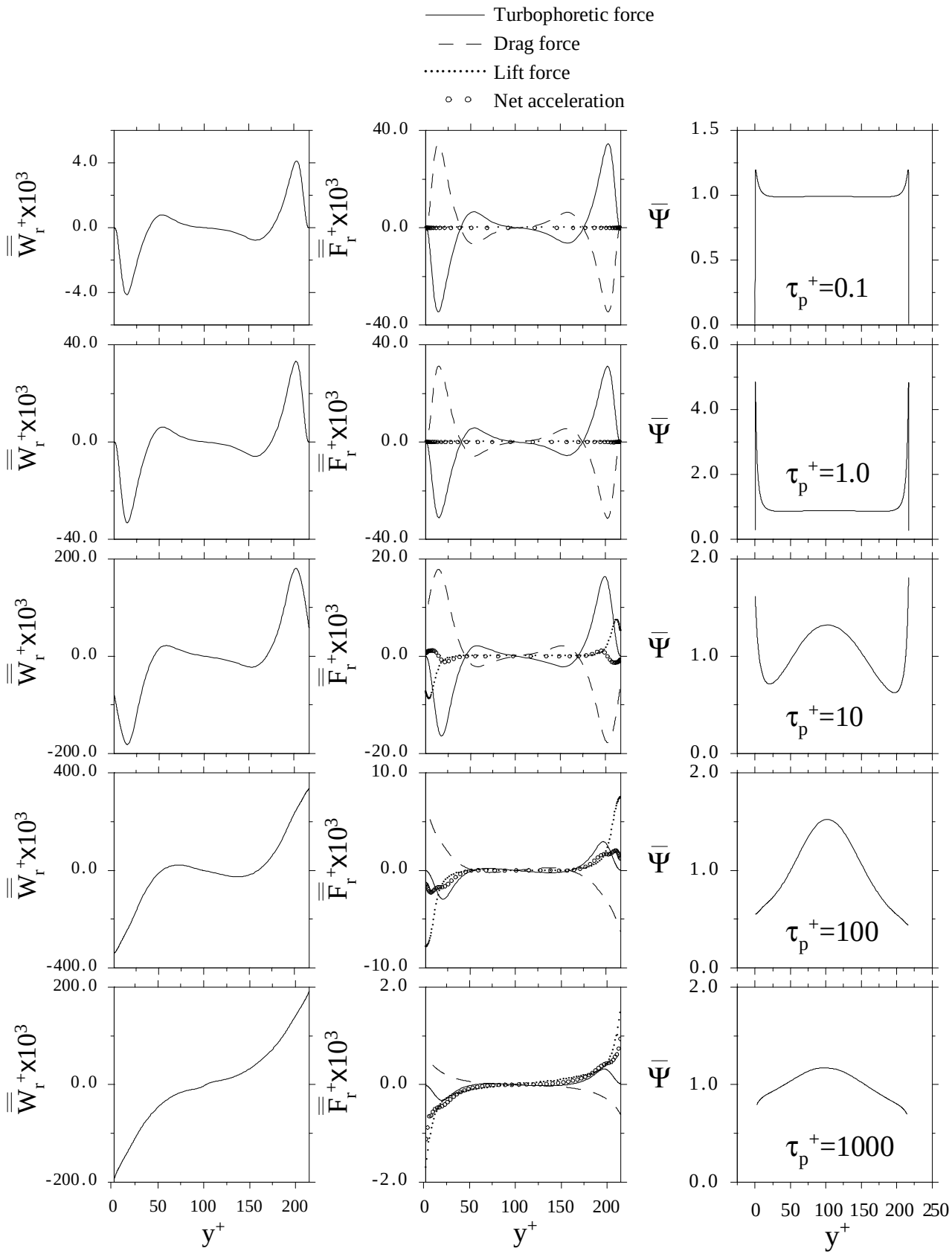

Figure 7.2: Particle behaviour including the Saffman lift force: dimensionless profiles of radial particle velocity, radial forces and acceleration, and particle density

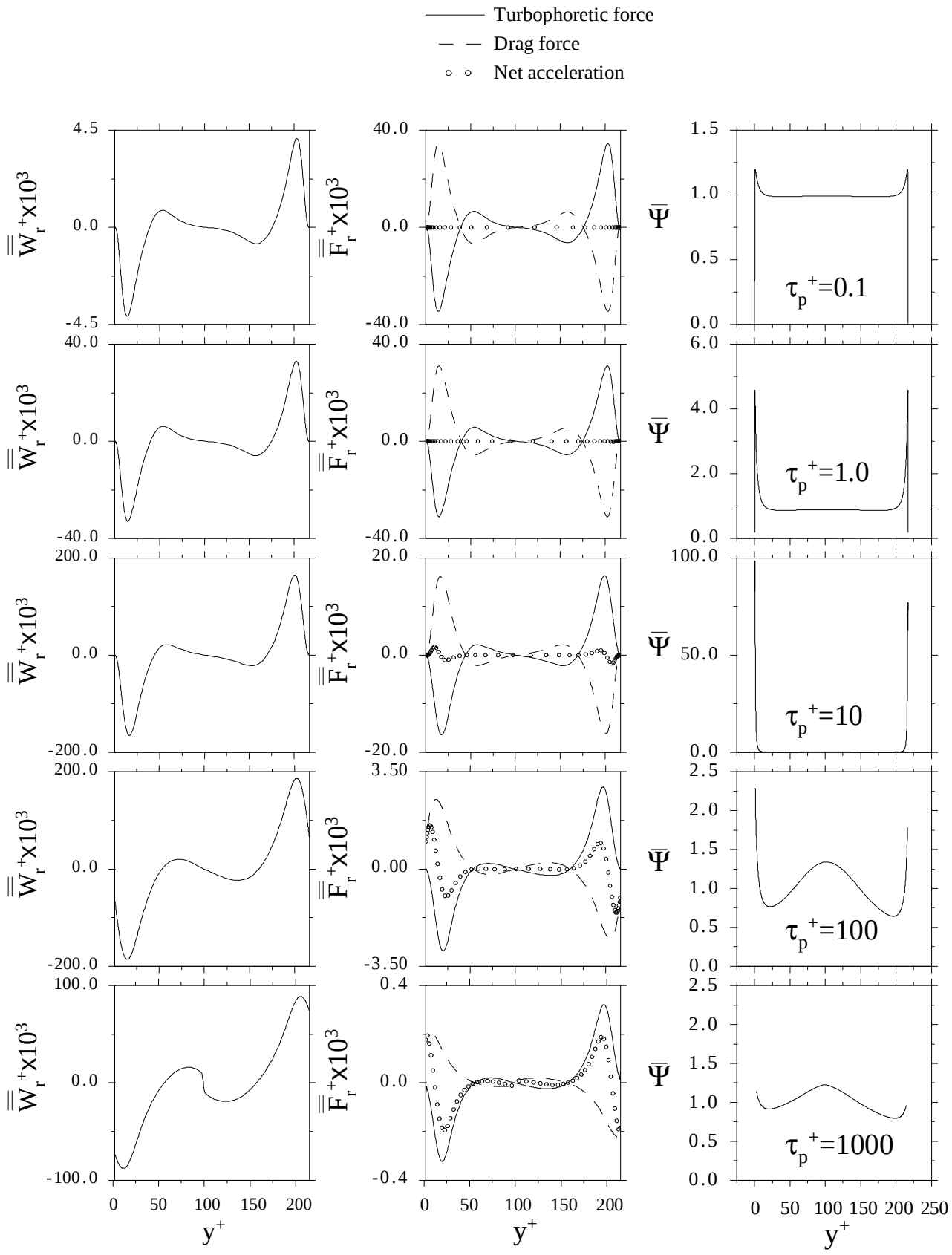

Figure 7.3: Particle behaviour neglecting the Saffman lift force: dimensionless profiles of radial particle velocity, radial forces and acceleration, and particle density

Particles with $\tau_p^+ = 0.1$ are in the diffusional deposition regime, particles with $\tau_p^+ = 1$, 10 and 100 represent the start, middle and end of the turbulent diffusion-eddy impaction regime, and particles with $\tau_p^+ = 1000$ are in the inertia moderated regime. These types of profiles have been discussed at length by Young & Leeming (1997) with regard to the manner in which particles of different sizes respond to turbulence, and how they deposit under the influence of diffusive or convective mechanisms, or a combination of both. The focus here is on the differences between the profiles with and without lift.

It can be seen that for $\tau_p^+ =$ 0.1 and 1, there is very little difference between the two cases, as can be expected from figure 7.1. The profiles for $\tau_p^+ =$ 10, 100 and 1000 are quite different however. In the absence of lift, peaks of $\overline{\psi}$ occur close to the walls, whereas the inclusion of lift results in the removal of these peaks, and much larger values of $\overline{\overline{W}_r}^+$ at the walls. This behaviour is not unexpected: Young & Leeming (1997) point out that the particle density profile should reflect the continuity requirement that the total radial particle flux (convective and diffusive) must remain almost exactly constant in the region $y^+ < 20$, and since convection dominates over diffusion for $10 < \tau_p^+ < 1000$, the continuity requirement is that $\overline{\psi}\,\overline{\overline{W}_r}^+$ should be nearly constant in the near-wall region. Hence, the increase in $\overline{\overline{W}_r}^+$ near the walls in the presence of lift requires a reduction in $\overline{\psi}$ (compared to the case without lift).

It has been shown that the lift force can have a significant influence on both V_d^+ and the profiles of $\overline{\overline{W}_r}^+$ and $\overline{\psi}$. However, the form of the lift force used (the Saffman formula) has been derived for a particle far from any boundaries, so that the presence of a wall may influence V_d^+ for particles of certain sizes. Wang *et al.* (1997) used an 'optimum' lift force which takes account of the presence of the wall. In fact, this 'optimum' force comprises a number of different expressions, the appropriate one depending on distance from the wall, and Reynolds numbers and length scales based on the slip velocity and fluid velocity gradient. The implementation of these expressions into the computational model proved difficult due to the large number of expressions, and it introduced numerical instabilities as the Reynolds number and length scales changed across the annulus, causing the form of the 'optimum' lift force to change suddenly (although this may be due to the present method's requirement for smooth profiles of fluid and particle properties, which will be explained in the next section). Wang *et al.* (1997) found that the use of the Saffman lift force led to an over-prediction of V_d^+, and large eddy simulations showed that the 'optimum' lift force was approximately three times smaller than the Saffman lift force. Accounting for the presence of the walls would lead to deposition velocities somewhere between those found without the lift force, and those found using the Saffman formula. Finding the correct form of the lift force is not be helped by the fact that the lift force has the greatest influence on V_d^+ in the region where the scatter of experimental data is the largest.

7.2.2 Fluid fluctuating velocity and eddy viscosity

In order to solve the particle equations, a knowledge of the fluid flow field is required. Validation of the particle solution depends on errors arising from the fluid solution being small, so that any differences between numerical and experimental deposition velocities can be attributed to the particle transport modelling rather than the fluid turbulence modelling. The information required by the particle equations is the radial variation of $\overline{U}_z$, $\overline{u_r' u_r'}$, $\nu_{g,T}$ (Sc_T is assumed equal to unity, $D_T \cong \nu_{g,T}$ and τ_g is a function of $\overline{u_r' u_r'}$ and $\nu_{g,T}$) and $\overline{T}$.

Slater (1999) carried out a sensitivity study of the deposition velocity to different methods of obtaining the fluid turbulence statistics. The closure methods investigated were $k-\epsilon$, full Reynolds stress, low Reynolds number $k-\epsilon$, and the use of experimental/DNS data. The limitation of these models was found to be their failure to predict the correct near-wall behaviour, with the result that deposition velocities were strongly dependent on the closure method used. The correct near-wall behaviour is that $\overline{u_r'^+ u_r'^+}^{1/2}$ varies with y^{+2}, and $\nu_{g,T}^+$ varies with y^{+3} (Chapman & Kuhn, 1986), where y^+ is the dimensionless distance from the wall.

The choice of gas turbulence model is also influenced by the stability requirements of the numerical scheme. Turbophoresis is governed by the term $-\partial(\overline{\overline{v_r'' v_r''}})/\partial r$, which is a function of $\overline{u_r' u_r'}$ and $\nu_{g,T}$ (through Γ). In order that the turbophoretic force has a smooth radial variation, $\overline{u_r' u_r'}$ and $\nu_{g,T}$ must be twice differentiable. The best method of meeting these requirements is the use of empirical models, which fit to available experimental (and/or DNS) data and represent the near-wall behaviour accurately, while also being continously differentiable. The empirical models used here are similar to those of Young & Leeming (1997), but with alterations to account for the change in geometry from a pipe to an annulus. They are described in detail in appendix D.1, along with other details of the fluid flow solver.

The only available data for an annulus, to which the empirical models may be fitted, appears to be the DNS data of Chung *et al.* (2002) for Re =8900 and Quadrio & Luchini (2002) for Re =11200. The experimental work of Kang *et al.* (2001) is unsuitable as it is for a vertical upflow of refrigerant (non-dimensionalisation is made difficult by this), and the Reynolds numbers used were much higher. Experimental and DNS data for turbulent pipe and channel flow indicates that there is a Reynolds number dependence in the near-wall region for low Re (see Manna & Vacca, 2001), and $Re \approx$ 5900 in the present experiments. Quadrio & Luchini (2002) investigated wall curvature effects on the turbulence statistics in an annulus, which were shown to have an effect even in the low-curvature range (the range of the present experiments), where a flow very similar to that over a plane surface was expected. As all of this creates a level of uncertainty in the prescription of $\overline{u_r' u_r'}$ and $\nu_{g,T}$, a sensitivity study was carried out on the effect of varying these quantities while maintaining a reasonable agreement with the available data (see appendix D.1 for justification of these variations).

Figure 7.4 shows the fluid fluctuating velocity and eddy viscosity, and their first derivatives. While the fluid fluctuating velocity profiles are plotted against y^+, the eddy viscosity profiles

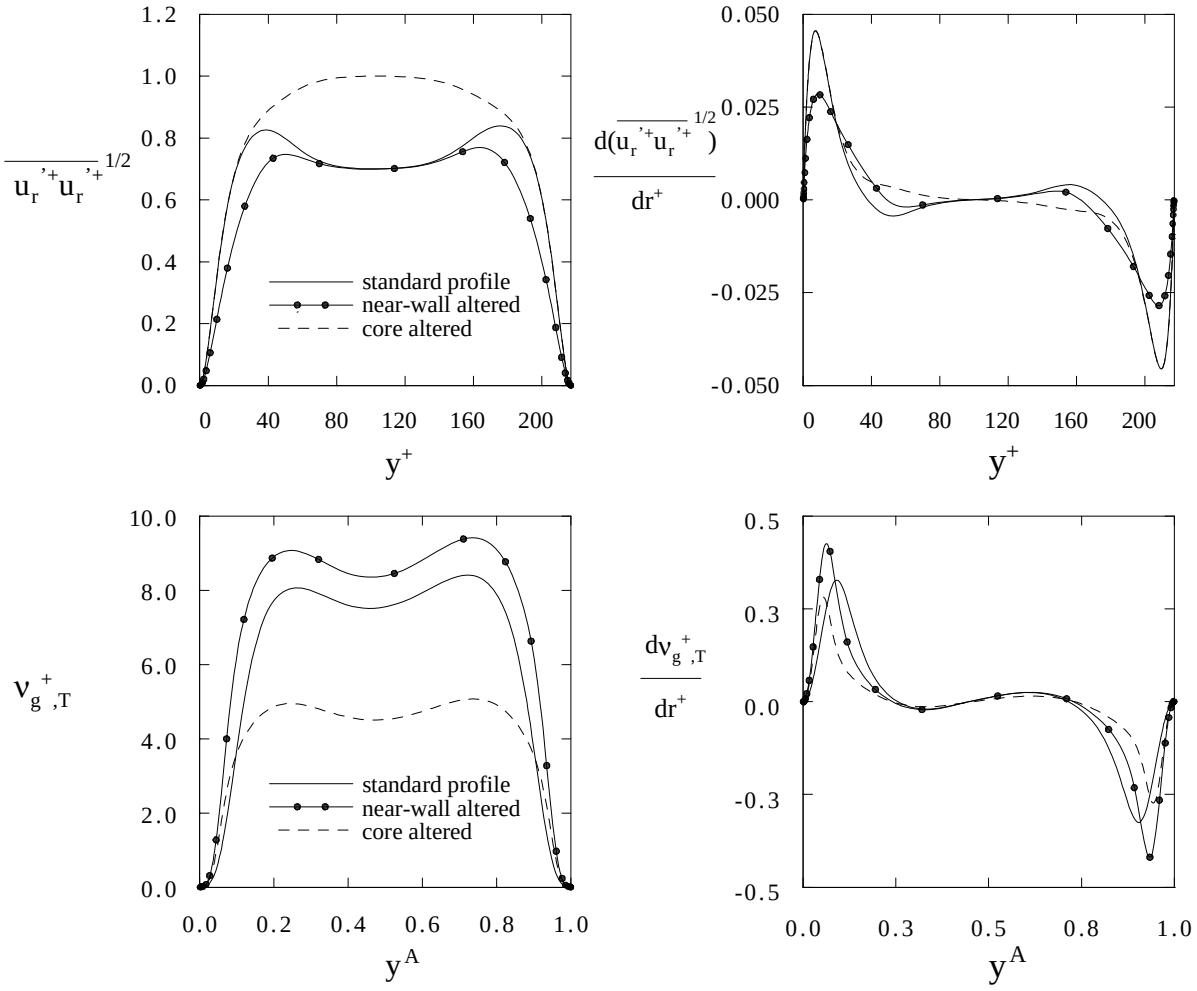

Figure 7.4: Fluid fluctuating velocity (above) and eddy viscosity (below) profiles and their first derivatives

	Standard	Near-wall	Core
$\overline{u_r'^+ u_r'^+}^{1/2}$			
Equation D.17	$\delta = 0.7$, $\gamma_{i/o} = 0.9$	$\delta = 0.7$, $\gamma_{i/o} = 0.9$	$\delta = 1.0$, $\gamma_{i/o} = 0.9$
Equation D.18	$\epsilon = 1.0$	$\epsilon = 1.7$	$\epsilon = 1.0$
$\nu_{g,T}^+$			
Equation D.12	$\kappa_{i/o} = 0.4$	$\kappa_{i/o} = 0.7$	$\kappa_{i/o} = 0.4$
Equation D.13	constant = 15	constant = 15	constant = 25

Table 7.1: Constants used to vary the profiles of fluid fluctuating velocity and eddy viscosity

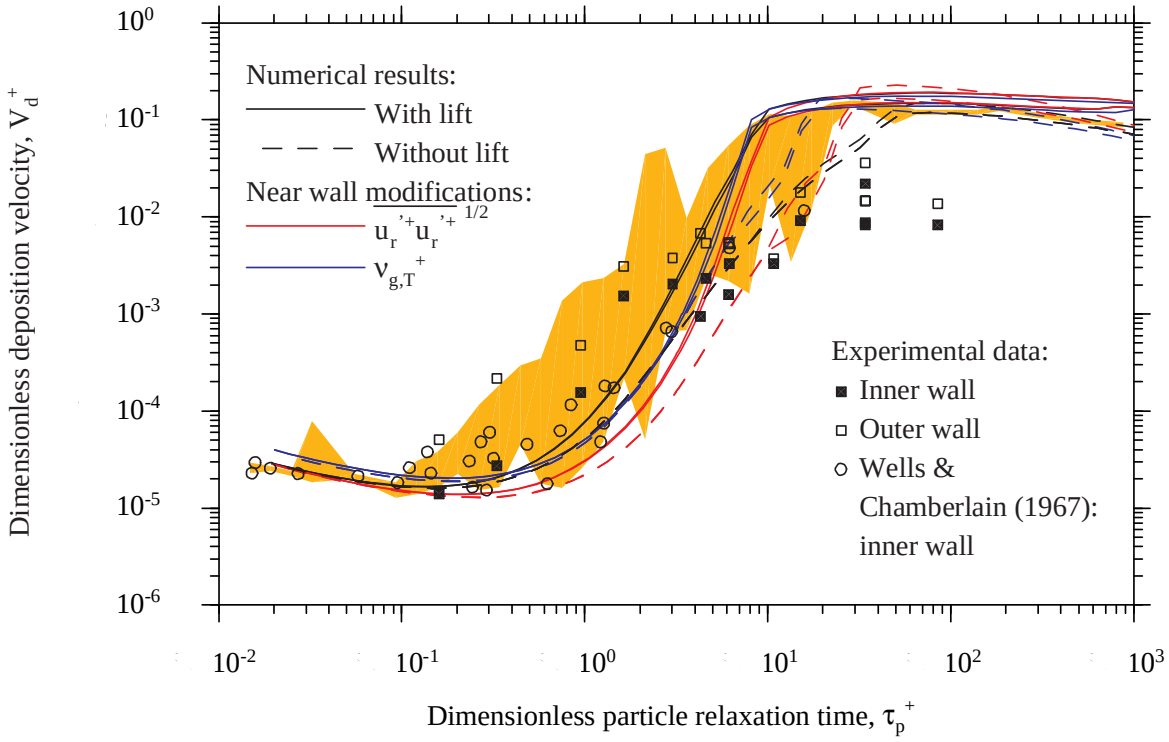

Figure 7.5: Isothermal particle deposition in a turbulent annulus with altered eddy viscosity and fluid fluctuating velocity profiles

are plotted against $y^A = (r - r_i)/(r_o - r_i)$ to allow for better comparison by avoiding changes in y^+ (through u_*) when $\nu_{g,T}$ is altered. Three different profiles are shown. The standard model, in each case, is the original empirical model that was used to obtain the results shown in figure 7.1, and represents the best fit to experimental data with a 'standard' choice of constants. The constants used in the empirical models of appendix D.1 were than varied, to obtain profiles that were altered in the near-wall and then, the core region. The different constants used are given in table 7.1.

Altering the turbulence statistics in the core of the flow, had a negligible effect on the deposition velocity (the results are not plotted), but the near-wall alterations exert more influence, as can be seen from figure 7.5. While there is a more pronounced change in particle velocity and density profiles (not shown), the change in deposition velocity is relatively small and confined mainly to the turbulent diffusion-eddy impaction regime, as was the case with the modifications to the lift force. The differences in V_d^+ are much smaller than the scatter associated with the experimental data in this range of τ_p^+. The 'standard' profiles of fluid fluctuating velocity and eddy viscosity will be used throughout the remainder of this study, and their prescription can be said to have only a minimal influence on V_d^+, in the sense that only vast and physically unrealistic changes in the fluid turbulence statistics would alter the values of V_d^+ sufficiently to fall outside of the scatter of experimental data for turbulent pipe flow.

7.2.3 Memory effects

Shin & Lee (2001) included a non-equilibrium 'memory effect' in the turbophoretic term, in an analysis valid in the absence of the Saffman lift force. When the particle relaxation time is much smaller than the characteristic time scale of the fluid flow, $\tau_p/\tau_g \ll 1$, particles follow the fluctuating fluid motion closely and the turbulence characteristics of the particle are almost the same as those of the fluid at the same position. When $\tau_p/\tau_g \gg 1$, the particle's inertia is such that its motion is only slightly altered by the turbulent eddy motion of the fluid over the small time interval of their interaction, and its turbulent characteristics are the result of its interactions over a longer period of time, i.e. a large particle has a longer memory. The expression given by Shin & Lee (2001) for the mean-square particle fluctuating velocity (towards the wall) accounting for this memory effect is:

$$\overline{\overline{v_r'' v_r''}} = \Gamma \overline{u_r' u_r'} - \frac{exp(-2\tau/\tau_p)}{1 - exp(-2\tau/\tau_p)} \tau \overline{\overline{W}}_r \frac{\partial}{\partial r}\left(\Gamma \overline{u_r' u_r'}\right) \tag{7.1}$$

where τ is an intermediate diffusion time scale, which may be given any value much smaller than τ_g. Thus, for small values of τ_p^+, the local equilibrium assumption still remains valid, while for large τ_p^+ the memory effect becomes significant and $\overline{\overline{v_r'' v_r''}}$ is altered from its local equilibrium value. The inclusion of the memory effect was found to induce an additional drift velocity towards the wall, alleviate the excessive build-up of particles near the wall, and enhance deposition.

Shin *et al.* (2003) carried out a further non-equilibrium analysis, this time in the presence of lift. The number of dispersion coefficients calculated represents a significant complication over the analysis in the absence of lift, and the deposition results vary depending on the choice of τ. An analysis was also carried out to investigate the effect of the choice of the particle turbulent diffusion coefficient. The local equilibrium model makes the assumption that $D_T \approx \nu_{g,T}$. Shin *et al.* (2003) modified this expression to take account of the 'crossing trajectory' [†] effect for large particles; large particles develop a slip velocity relative to the fluid, and particles drift out of their surrounding eddies, resulting in a reduction in the correlation between the particle velocity and the fluid velocity at the particle's 'previous' location, thus reducing D_T. While not altering the deposition results to a great extent, these alterations did result in better agreement with the experimental data of Liu & Agarwal (1974) in the inertia moderated regime, where V_d^+ begins to decrease with increasing τ_p^+ (which is often known as the 'roll-off' in deposition).

The effect of including the crossing trajectory effect on the roll-off in deposition can be explained by considering the local equilibrium definition of $\overline{\overline{v_r' v_r'}}$ and substituting $\tau_g = \nu_{g,T}/\overline{u_r' u_r'}$:

$$\overline{\overline{v_r'' v_r''}} = \frac{\nu_{g,T}\,\overline{u_r' u_r'}}{\nu_{g,T} + \overline{u_r' u_r'}\tau_p} \tag{7.2}$$

[†] Not be confused with the crossing trajectories of chapter 2.

Differentiating this:

$$\frac{\partial(\overline{\overline{v_r'' v_r''}})}{\partial r} = \frac{\tau_p}{(\tau_g + \tau_p)^2}\frac{\partial \nu_{g,T}}{\partial r} + \Gamma^2 \frac{\partial(\overline{u_r' u_r'})}{\partial r} \tag{7.3}$$

As $\tau_p \to 0$, $\Gamma \to 1$:

$$\frac{\partial(\overline{\overline{v_r'' v_r''}})}{\partial r} \cong \frac{\partial(\overline{u_r' u_r'})}{\partial r} \tag{7.4}$$

because small particles follow the fluid turbulence exactly. As $\tau_p \to \infty$, the fluid fluctuating velocity gradient term (of equation 7.3) scales with $1/\tau_p^2$ while the eddy viscosity gradient term scales with $1/\tau_p$, so that the eddy viscosity gradient term dominates and:

$$\frac{\partial(\overline{\overline{v_r'' v_r''}})}{\partial r} \cong \frac{1}{\tau_p}\frac{\partial \nu_{g,T}}{\partial r} \tag{7.5}$$

Over the range $1 < \tau_p^+ < 10$, the two terms of equation 7.3 are of roughly equal magnitude, but the fluid fluctuating velocity gradient term decreases while the eddy viscosity gradient term increases. In the region $10 < \tau_p^+ < 100$, the eddy viscosity gradient term dominates but gradually decreases with increasing τ_p^+ (so that V_d^+ decreases also). If D_T was modelled by $\nu_{g,T}$ minus the contribution due to crossing trajectories (as in Shin *et al.*, 2003), V_d^+ would be further reduced allowing the roll-off in deposition to be better captured. (It should be pointed out that the appearance of a diffusion coefficient in the description of particle motion at high τ_p^+, where convection dominates, may represent an undesirable characteristic of the modelling.)

7.2.4 Particle deposition in relation to particle transport

It has been shown over the preceeding pages that the fluid flow field may be altered, and that physically reasonable improvements may be made to the local equilibrium assumption without significant alteration to the overall shape of the deposition velocity curve (although the shape of particle velocity and density profiles are altered). The difficulties associated with measuring turbulence characteristics (even for the fluid phase) mean that, other than DNS data, there is very little validatory data for anything other than depositional studies, and so it is deposition that is of most interest in this thesis. The particle velocity and density profiles are intended to give an understanding of the mechanisms causing deposition, and the theory of Young & Leeming (1997) was formulated specifically for the case of deposition. There is a great volume of work in the literature more concerned with particle transport than deposition, i.e the particle properties throughout the flow rather than at the wall. While the work of each of these closely related fields is often mutually beneficial, it can sometimes lead to confusion.

One of the findings of the previous chapter was that the momentum equations derived using particle density-weighted averaging are essentially those obtained by Young & Leeming

(1997) using Reynolds averaging. Young & Leeming (1997) ignored a correlation involving the divergence of the particle velocity field, on the grounds that large gradients of particle density do not occur simultaneously with large convective velocities, and vice versa. Cerbelli *et al.* (2001) estimated the magnitude of this correlation and suggested that it can be significant, leading Slater *et al.* (2003) to suggest that there may be an inconsistency of comparable magnitude in the density-weighted turbulence modelling. The issue of the appearance or disappearance of this correlation highlights the importance of recognising the differences between studies of particle transport and those of particle deposition. Cerbelli *et al.* (2001) found that the particle density gradient can be large in the presence of large convective velocities, but only in the presence of perfectly reflecting walls (i.e. no deposition occurs). However, this is often a physically unrealistic case, and there is no need to take account of this correlation when particle deposition is being studied (although the assumption of perfect absorbing walls is also an idealisation, it is relevant to a wider variety of applications, and the particles in the experiments presented earlier had a coating of oleic acid to ensure adhesion).

Furthermore, the approach of Young & Leeming (1997) is not valid for such a case, as pointed out by Reeks (2003), who found inconsistencies in the closure approximations and the form of the transport equation, when applied to cases other than deposition in a turbulent pipe flow (or similar geometries). Reeks (2003) gives credit to the analysis of Young & Leeming (1997) for being aware of its own deficiencies and the conditions of its validity: for small particles, diffusion dominates or is comparable to convective mechanisms and the approximations for the diffusion coefficient and the gradient of fluctuating particle velocity are valid, while for large particles, convection dominates over diffusive mechanisms, so that the form of the diffusion coefficient is not vital, as long it is consistent with such behaviour. This is not the case when there is a perfectly reflecting boundary, as a balance of convective and diffusive mechanisms co-exist when τ_p^+ is large.

7.2.5 Direct numerical simulation of particle transport in wall-bounded flows

Recent computational advances have spawned a large number of studies involving direct numerical simulations (DNS), which resolve all of the relevant turbulent scales, without the need for turbulence closure models. Lagrangian tracking of the particles can then be performed. The development of the flow over time, coupled with the quality (in that there is no practical alternative means of obtaining such data) and quantity of information provided by such studies, has led them to be regarded as 'computational experiments' and the results are often used to validate new models and theories, in the absence of 'real' experimental data (e.g. Cerbelli *et al.*, 2001). Some of the earliest examples of this type of work are by McLaughlin (1989), Brooke *et al.* (1992), and Brooke *et al.* (1994) (often cited for its $\overline{v_r' v_r'}$ profiles).

One striking similarity between these studies and turbulent pipe flow experiments is the method by which the deposition velocity is calculated: the rate of particle depletion is plotted

against time (or distance along the pipe) and a deposition coefficient is found by determining the slope at the straight part of the curve (Uijttewaal & Oliemans, 1996). A straight portion of the curve forms after a period of time, the length of which depends on τ_p^+, and the particular conditions of the DNS study.

Nearly every DNS study since McLaughlin (1989) has reported the steady accumulation of particles in the near-wall region over time. Portela *et al.* (2001) found that it is in this near-wall region that the particle density takes longest to reach a stationary steady-state value, and Rouson & Eaton (1994) never reached a stationary value for particle density (instead running simulations until the particle velocity statistics alone became stationary in time).

Differences in the time to stationarity between different studies is hardly surprising. In certain cases (e.g. Rouson & Eaton, 1994; Marchioli *et al.*, 2003), particles that exit the flow domain through one boundary are reintroduced through the opposite boundary, while others (such as Brooke *et al.*, 1994) allow the particles simply to deposit. The particle density is calculated by dividing the flow domain into a number of 'bins' and averaging the number of particles resident in each bin over a time interval. Hence, the use of a greater number of particles (or reintroducing particles that have already 'deposited') should result in a stationary average being achieved over a shorter period of time (an alternative method for calculating particle density for laminar flows, that removes the need to use large numbers of particles, was discussed in part 1 of this thesis). Another discrepancy between various numerical studies, as pointed out by Pedinotti *et al.* (1992), is that it is impossible to match the particle Stokes numbers based on different scalings (e.g. Kolmogorov time scale and viscous wall time scale) for studies at different Reynolds number.

Differences in the time to stationarity for particles of different τ_p^+ can be expected, but there seems to be some conflict as to which particles take the longest times. Matida *et al.* (2000) found that for some intermediate sized particles ($\tau_p^+ \approx 5$, 10), the deposition velocity was still increasing at the end of the test section, and studied the influence of the inlet particle density distribution on deposition. However, Portela *et al.* (2001) found that a particle with $\tau_p^+ = 100$ took more than twice as long to reach a statistically steady-state concentration profile than a particle with $\tau_p^+ = 25$. They also estimated the length required for this to occur, and found that it could take as many as 300 pipe diameters. The particle density developing length is, in general, found to be much longer that the hydrodynamic developing length, particularly for large particles. In such cases, longer computational times, or longer experimental test-section lengths, are required.

Uijttewaal & Oliemans (1996) suggest that the discrepancy between computations (and experiments) of different Reynolds number for large τ_p^+ can be explained by a scaling argument (similar to that of Pedinotti *et al.* (1992)). They suggest that for small particles ($\tau_p^+ < 100$), since the motion is sensitive to the variation of turbulence properties in the near-wall layer, that the deposition velocity will scale properly with Reynolds number when non-dimensionalised with u_* and ν_g. Large particles hardly notice the presence of the near-wall layer, and it is considered more likely that they scale with an integral property of the turbulence. This was

found to be the case when their data was scaled with the turbulence integral time scale.

This brief look at particle studies using DNS has shown the value of such 'experiments', but also some possible sources for the discrepancies between different turbulent pipe flow studies, and between turbulent pipe and annulus experiments: the particle density profile may not have had sufficient length to develop, and the low Reynolds number (or even change in geometry) may require a change in dimensionless scaling.

7.2.6 Summary

Numerical results for particle deposition in an isothermal turbulent annulus have been presented, and were shown to be similar to those for an isothermal turbulent pipe. The fluid flow information required by the particle equations does not alter the deposition velocity significantly, but the inclusion of the Saffman lift force has a pronounced effect for certain sizes of particle, and alters the shape of particle velocity and density profiles across the annulus. The inclusion of some particle memory effects into the model has been examined. Although, there is a sound physical basis for their inclusion, there is little experimental evidence in the bulk of the particle flow to provide verification. The roll-off in deposition velocities found experimentally is captured well with this modification, but the overall effect on deposition velocities is small. By contrasting the interests of studies of particle transport (in the bulk of the flow) and particle deposition (on the wall), some conditions of applicability (or limitations) of the theory of Young & Leeming (1997) have been illustrated, and the usefulness of particle DNS studies have been shown with regard to some potential explanations for the variation in depositional behaviour of particles with large τ_p^+. An investigation into the scaling of V_d^+ for large τ_p^+ may result in a better collation of experimental and DNS data, in the same way that non-dimensionalisation of deposition results collated the results of the early deposition experiments (see the comment with regard to the work of Sehmel (1968) in section 3.4.2). Having established the mechanisms of deposition in an isothermal turbulent annulus, the numerical study of deposition in a turbulent annulus with a cross-stream temperature gradient will now be presented.

7.3 Thermophoretic particle deposition

The fluid flow solver (decribed in appendix D.1) was used to provide three solutions representative of the experimental conditions of chapter 5, where three different cross-stream temperature differences were imposed on a turbulent annular flow. The expression for the thermophoretic force derived by Brock (1962), using the constants of Talbot *et al.* (1980), was included in the Eulerian particle code of the previous chapter. The results are presented in figure 7.6, along with the experimental results from chapter 5. For small particles, the deposition velocity at the inner wall is approximately constant, and its magnitude increases with each increase in the temperature of the outer wall. The deposition velocity at the outer wall is negligible. In the range $1 < \tau_p^+ < 10$, the deposition velocities at both walls return to their isothermal values, and the deposition velocities of large particles are unaltered by thermophoresis. The agreement of $(V_d^+)_o$ with experimental data, as it recovers from a negligible level to its isothermal level, is very good considering the difficulty in measuring low levels of deposition to the outer wall of the annulus. It should also be remembered that the results at $\tau_p^+ \approx 8$ should be ignored, for the reasons stated in section 5.3.

While Romay *et al.* (1998) and Leeming (1995) (discussed in detail in chapter 3) found that their experimental results were greater than theoretical predictions (using the same expression for the thermophoretic force used here), figure 7.6 shows that the numerical predictions of this study are greater than the experimental results. The thermophoresis-turbulence interaction found experimentally is also reproduced.

Before investigating possible reasons for the discrepancy between experiment and prediction, dimensionless profiles of particle velocity, forces per unit mass of particles, and particle density will be presented, to highlight the changes compared with the isothermal case, and to illustrate the mechanisms behind the thermophoresis-turbulence interaction. The profiles are presented only for the largest temperate difference, $T_{ow,nom} - T_{iw} = 128°\text{C}$, and the Saffman lift force has been included in all predictions that will be presented in the remainder of this chapter.

7.3.1 Thermophoresis-turbulence interaction

Considering figure 7.7 for the case when $\tau_p = 0.01$, it can be seen that the negative thermophoretic force (in red) directs particles away from the hot outer wall (at $y^+ \approx 150$) and towards the cold inner wall (at $y^+ \approx 0$). As a result, (referring to figure 7.6) $(V_d^+)_o$ is negligible and $(V_d^+)_i$ is significantly increased from its isothermal value. The thermophoretic force also results in a finite radial particle convective velocity at either wall.

As τ_p^+ increases (and Kn decreases), the magnitude of the thermophoretic force decreases. Figure 7.6 shows that at $\tau_p^+ \approx 4$, $(V_d^+)_o$ has increased sharply to its isothermal value, and $(V_d^+)_i$ has also gradually attained its isothermal value. However, in the range $0.5 < \tau_p^+ < 4$, $(V_d^+)_i$ increases in value, rather than continuing at the constant value established below $\tau_p^+ \approx 0.5$. And this is despite the fact that figure 7.7 clearly shows that for $\tau_p^+ = 1$, the

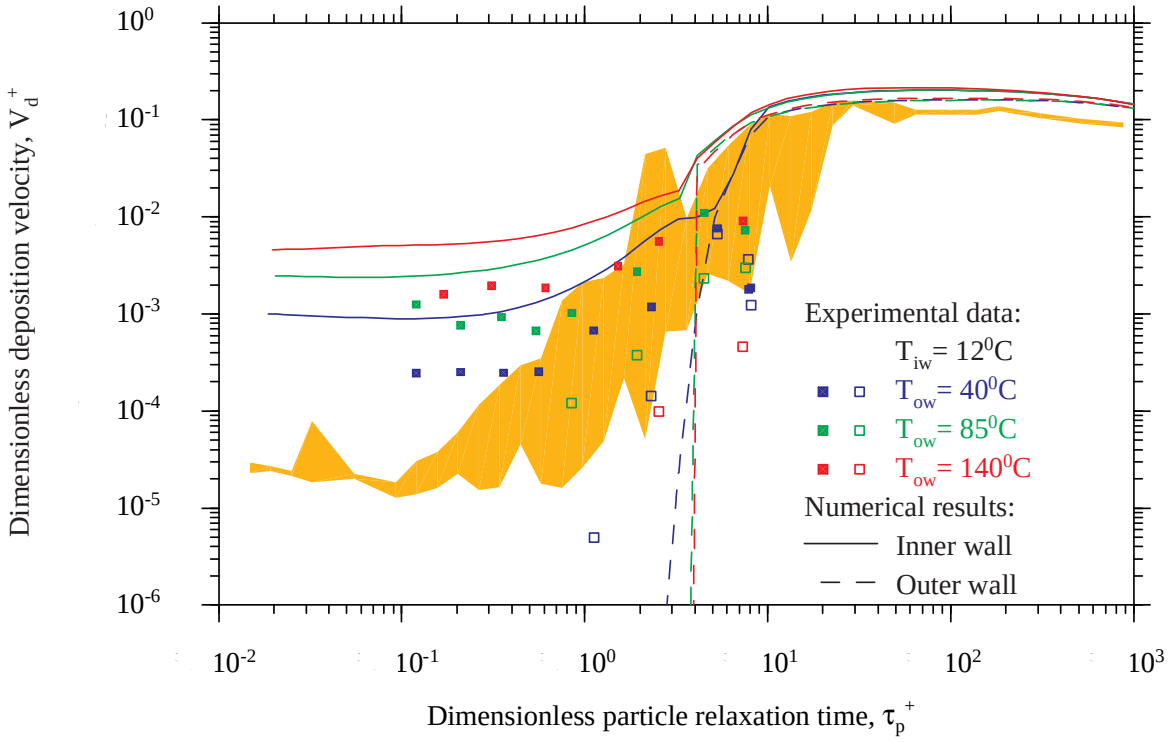

Figure 7.6: Thermophoretic particle deposition in a turbulent annulus with a cross-stream temperature gradient: comparison between experimental data and numerical results using the expression of Talbot *et al.* (1980)

thermophoretic force has become extremely small. This increase in deposition velocity with a decrease in thermophoretic force (with $(V_d^+)_i$ being more than an order of magnitude greater than its isothermal value), indicates a strong coupling between thermophoresis and turbulence, which has also been found experimentally.

Examining the force diagram in figure 7.7 for τ_p^+=1, apart from the now small thermophoretic force, the other forces are almost identical to the isothermal case (see figure 7.2). Under isothermal conditions, deposition in this size range would just be starting to be influenced by the increasing turbophoretic force. However, while the turbophoretic force decreases to zero at the wall, the small but finite thermophoretic force still has enough influence in the near-wall region to prevent significant deposition to the hot outer wall, and further enhance deposition to the cold inner wall. Even though the magnitudes of the deposition velocities vary between the experiments and numerical predictions, the rate of the increase due to the interaction of thermophoresis and turbophoresis is well-captured.

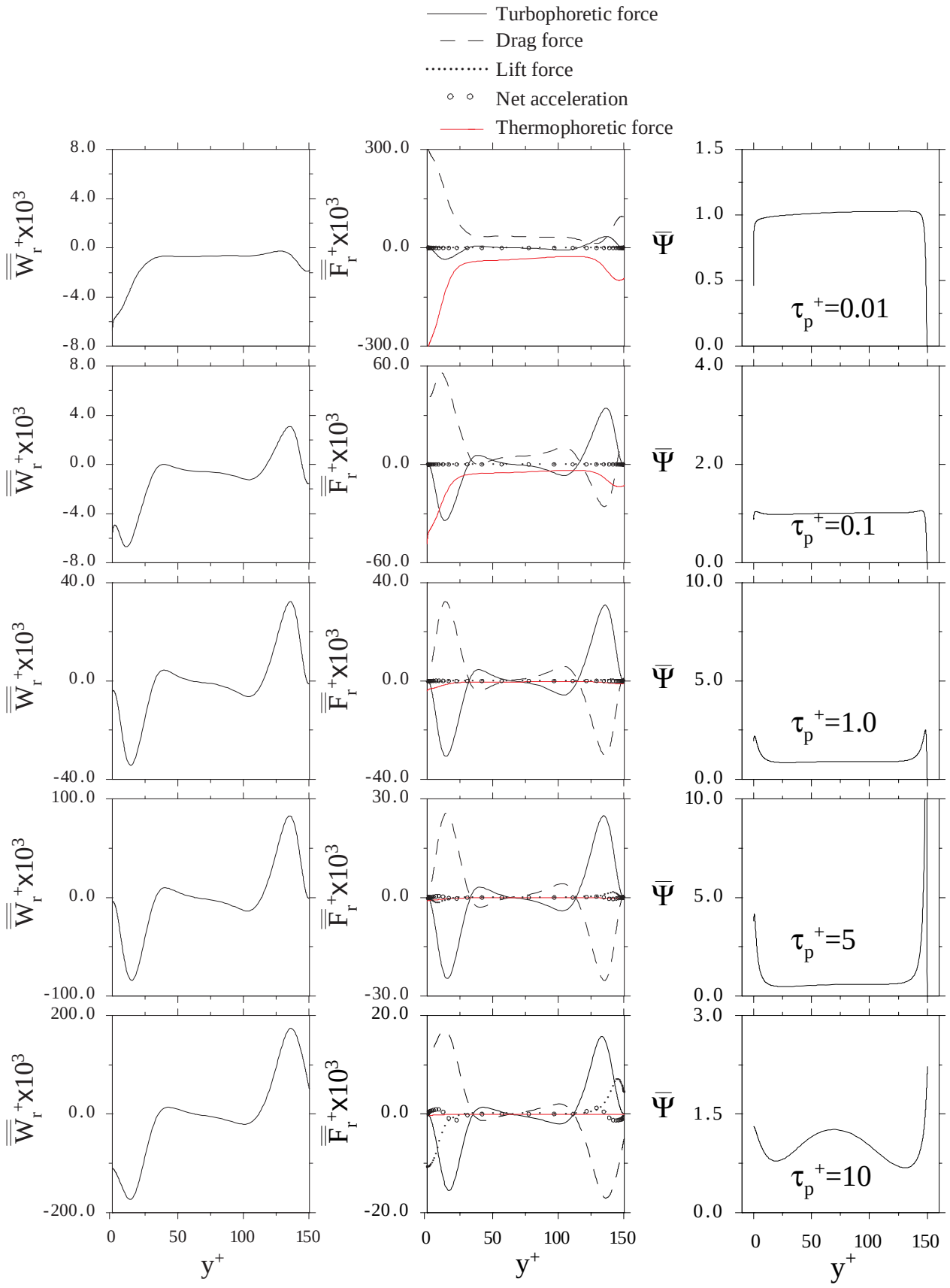

Figure 7.7: Particle behaviour under the influence of thermophoresis when $T_{ow,nom} = 140°C$: dimensionless profiles of radial particle velocity, radial forces and acceleration, and particle density

7.3.2 The discrepancy between experimental and numerical results

In order to understand the reasons for the differences between the experimental and numerical deposition velocities shown in figure 7.6, a number of possible sources were examined. Table 4.1 gives the thermal conductivities of uranine and oleic acid as 0.43 and 0.23 $Wm^{-1}K^{-1}$ respectively. While the thermal conductivity of a particle comprising these constituents should lie somewhere between their individual values, the individual values will also vary with changes in temperature. However, numerical results with a value of 0.43 or 0.23 $Wm^{-1}K^{-1}$ were identical (not shown) - it is the fact that this range of k_p is indicative of a particle of moderate to low thermal conductivity that is important, and slight changes will not significantly alter the ratio of gas to particle thermal conductivities.

The form of the closure model for the turbulent Prandtl number (Pr_T, equation D.15) was also found to be unimportant, and the use of other models that give quite different values of Pr_T in the near-wall region did not influence the deposition velocities (again, not shown). While there is no experimental data for flow in a turbulent annulus with a heated and cooled wall, there is DNS data for a turbulent channel flow with the walls at different temperatures (Kasagi *et al.*, 1992). This was used to show that the dimensionless temperature found using the annular flow solver conforms very closely to the universal profiles (see appendix D.1), and the slight differences were not found to influence the deposition velocities.

In the previous section, the effects of altering the fluid fluctuating velocity and eddy viscosity were examined. The only change in these quantities to have any effect on the thermophoretic deposition, was the alteration of the fluid fluctuating velocity profile in the near-wall region (ϵ=1.7 in table 7.1). The result of this (for $T_{ow,nom} = 40°$C) is shown in figure 7.8.

This alteration reduces the value of $(V_d^+)_i$ in the region of the thermophoresis-turbophoresis interaction, and reinforces the existence of the interaction by showing the influence of $\overline{u_r' u_r'}$ (and thus $\overline{\overline{v_r'' v_r''}}$) on $(V_d^+)_i$ over this range of τ_p^+, in the presence of thermophoresis. The bumpiness in values of $(V_d^+)_i$ in the region where $\tau_p^+ \approx 5$ is also smoothed by this alteration, but this particular range of τ_p^+ was found to require an increased grid resolution to achieve stability (even for the isothermal case), and little should be made of the lack of smoothness when $\epsilon = 1.0$.

Also shown in figure 7.8 is the result of using the constants of Brock (1962) instead of those suggested by Talbot *et al.* (1980) (for $T_{ow,nom} = 40°$C with $\epsilon = 1.7$). This involves the use of $C_s = 0.75$ in place of $C_s = 1.17$, in equation 3.50. The result was a small reduction in the value of $(V_d^+)_i$. For particles of low thermal conductivity in the Knudsen number range 0.01$< Kn <$0.1 (as is the case for these experiments), figure 3.5 shows that there is little difference in the magnitude of the thermophoretic force calculated by the different expresssions (except for that of Bakanov & Roldugin (1977)). One of the largest changes is when altering C_s from 1.17 to 0.75, but this does not reduce the magnitude of the numerical results for

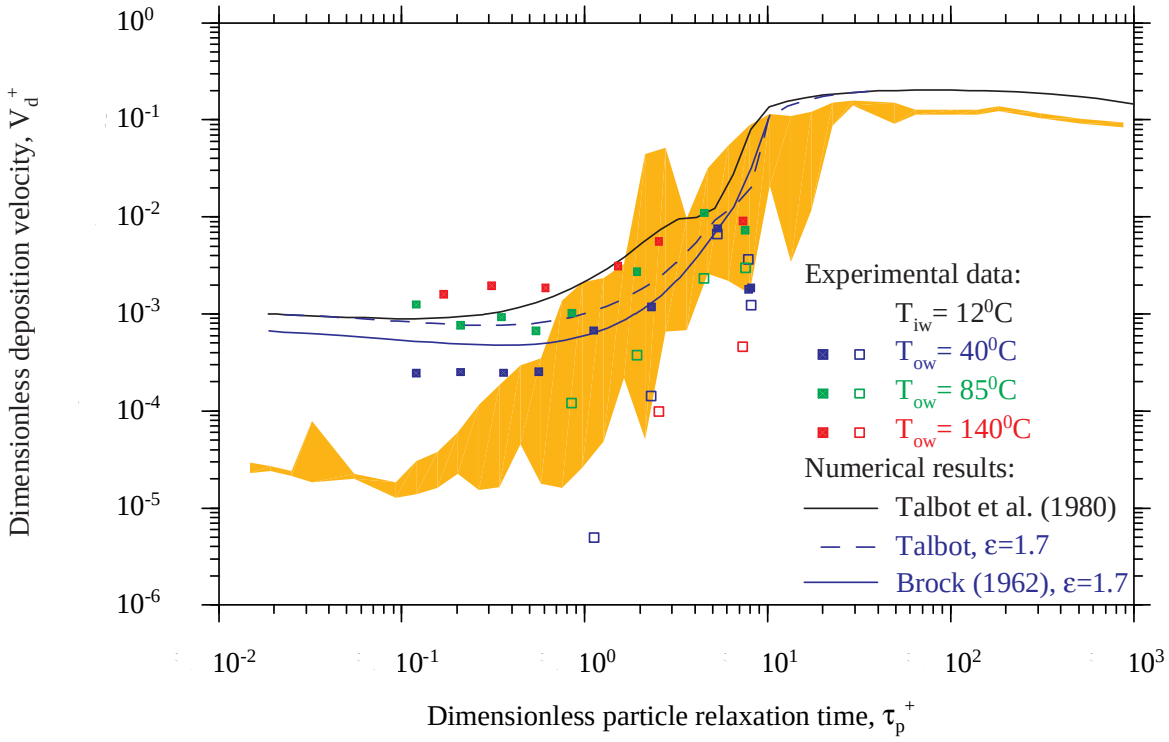

Figure 7.8: Thermophoretic particle deposition in a turbulent annulus with a cross-stream temperature gradient: numerical results for $T_{ow,nom} = 40°$C with a number of modifications, compared with experimental results

deposition velocity to the level of the experimental results.

There is the possbility that the temperature of the flow at either wall may have deviated from the values measured during the experiments. Figure 7.9 shows the effect of increasing the temperature of the inner wall by 5°C, and reducing the temperature of the outer wall by 5°C (but the mean temperature remains the same), for each temperature difference (using Brock's value for C_s). This would represent an extreme deviation from the measured conditions. Only the inner wall deposition velocities for small τ_p^+ are shown, and although the agreement with the experimental data is better, an even greater change in wall temperatures would be required to achieve a closer match. Even a 5°C deviation from the measured temperatures is considered highly unlikely.

7.3.3 Deficiency in the expression for the thermophoretic force

It has been established that there is a definite discrepancy between the deposition velocities that were measured during the experiments and those predicted in the numerical study, and various possible sources (both experimental and numerical) of the discrepancy have been investigated. The fluctuating temperature has been neglected in the calculation of the thermophoretic force, but the DNS study of Thakurta *et al.* (1998) on thermophoretic deposition

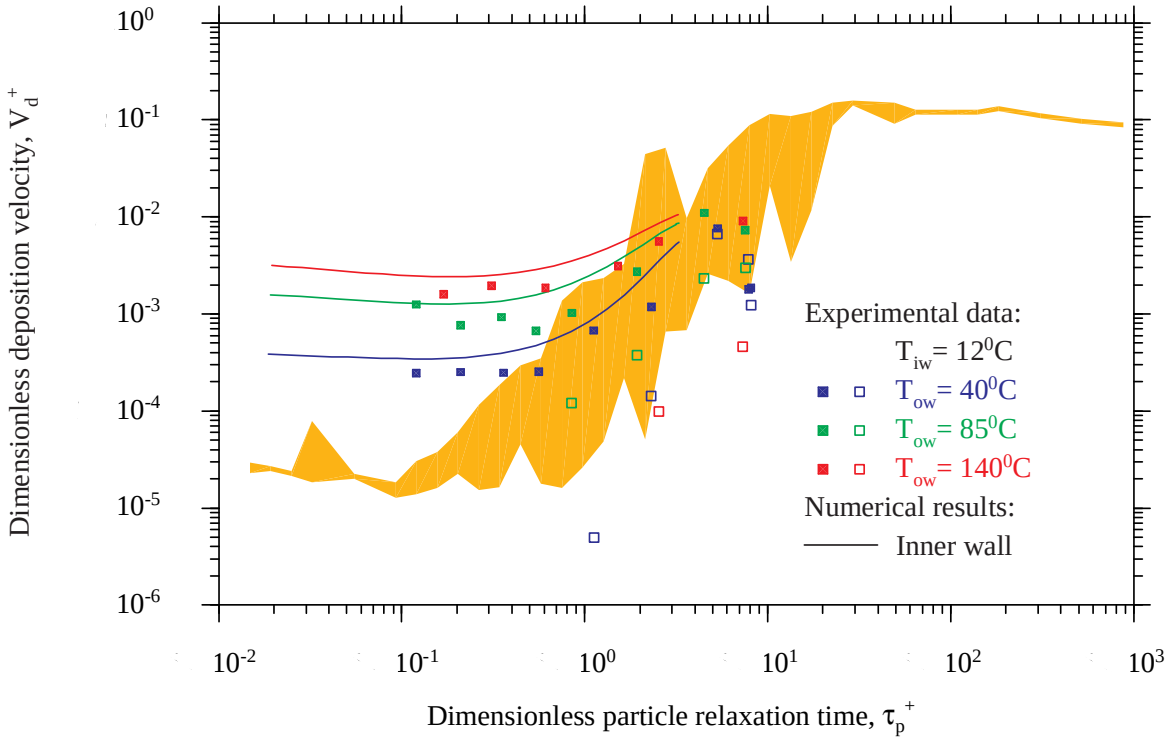

Figure 7.9: Thermophoretic particle deposition in a turbulent annulus with a cross-stream temperature gradient: numerical results for small τ_p^+ when each wall temperature is altered by 5°C, compared with experimental results

found that the inclusion of temperature fluctuations had virtually no effect. It is unclear how they included the temperature fluctuations, but adding the temperature fluctuations to the mean temperature (as done in the random-walk simulation of Kroger & Drossinos (2000)) was found to have no effect on the deposition velocities presented earlier. The remaining possibility is that the form of the thermophoretic force used in the numerical predictions might not be appropriate.

In section 3.5, it was concluded that the theory of Brock (1962) with the constants recommended by Talbot *et al.* (1980) probably represented the most accurate form for the thermophoretic force on a spherical particle. This was due to the fact that it can be applied over the full range of Knudsen numbers, it agrees with other theories in the limits of $Kn \ll 1$ and $Kn \gg 1$, and good qualitative agreement with experimental data was demonstrated; there also appears to be no alternative formulation that can be used with ease over the range of Kn. The theory of Bakanov & Roldugin (1977) (for small Kn) was found to inadequate, as it gave a thermophoretic force in the opposite direction to all other theories, and was overly sensitive to changes in the accommodation coefficients. For this reason, other studies that were similarly based on various approximations of the Boltzmann equation solutions, or on numerical calculations for the gas-kinetic model equations, were not considered any further.

Perhaps confusion and a lack of clarity have been introduced in the course of the translation

from Russian, but from the work of Beresnev & Chernyak (1995), it transpires that Bakanov & Roldugin (1977) (and Bakanov (1991), Bakanov (1992)) do not do justice to this type of study. Beresnev & Chernyak (1995) carried out an analysis on the basis of the linearised Bhatnagar-Gross-Krook (BGK) and S model kinetic equations. The thermophoretic force was found for arbitrary Knudsen number, accommodation coefficients, and ratio of gas to particle thermal conductivities. Before examining their expression for the thermophoretic force, an attempt will be made to clarify the different mechanisms that contribute to thermophoresis, and how these can bring about a reversal of the thermophoretic force. Paraphrasing Sone (1972):

> When gas and particle thermal conductivities are of similar magnitude, the side of the particle facing the hot region is heated more than the cold facing side and there is a temperature gradient, comparable to that of the gas, on the surface of the particle. A thermal creep flow of the gas is induced from the colder to the hotter region, and the particle is subjected to an equal and opposite force in the direction opposite to the temperature gradient (from hot to cold). This is the first thermophoresis mechanism.

It is this first thermophoresis mechanism that is of principle concern in this work ($k_g/k_p \approx 0.1$), and this mechanism was included in the hydrodynamic analysis of Brock (1962). However, certain other studies have found that when k_g/k_p and Kn are very small, the direction of the thermophoretic force may be reversed. Although these conditions did not exist in the present study, an explanation of this phenomenon is important in determining the credibility of any particular expression for the thermophoretic force. The most adequate explanation can be found from a combination of Sone (1972), Kogan (1992) and Beresnev & Chernyak (1995):

> When the thermal conductivity of the particle is much larger than the thermal conductivity of the gas, the temperature of the particle is almost uniform and the thermal creep flow is negligible. However, a temperature gradient exists in the gas, and molecules impinging obliquely on an element of the particle surface deliver more tangential momentum to the particle if they come from the hotter region of the gas. This unequal transfer of tangential momentum results in a shear stress exerted by the particle on the gas, and there is a flow of gas adjacent to the particle in the opposite direction to the temperature gradient - from the hotter to the colder region. The gas then exerts a reactive force on the particle towards the hotter region. This thermal stress slip flow is termed the second thermophoresis mechanism, and dominates over the first mechanism only for very small Kn and large k_p, resulting in reverse thermophoresis. As Kn increases (but is still much less than unity) the mechanisms compete, until further increases in Kn lead to the first mechanism dominating completely.

The second thermophoresis mechanism is predicted (alongside the first) by both the linearised Boltzmann equation and the BGK model. Beresnev & Chernyak (1995) graphically detail the competition between the two mechanisms with changes in Kn. The coefficient of thermophoresis for the S model (for complete thermal accommodation) was given by Beresnev & Chernyak (1995) as:

$$\eta_{TH} = \frac{2\pi\mu_g\nu_g r_p}{Kn} \frac{f_{11} + (k_p/k_g)f_{21}}{1 + [1 + (10/4)(k_p/k_g)Kn]f_{41}} \tag{7.6}$$

where the coefficients f_{11}, f_{21}, f_{41} depend only on Kn, and are presented in tabular form. However, an approximate expression for the thermophoretic force at $Kn \ll 1$ in the case of complete thermal accommodation is also given as:

$$\eta_{TH} = \frac{12\pi\mu_g\nu_g r_p C_s}{(k_p/k_g) + 2} \left[1 + Kn \left(A\frac{k_p}{k_g} + D' + \frac{C(k_p/k_g) + B}{1 + (1/2)(k_p/k_g)} \right) \right] \tag{7.7}$$

The force found using equation 7.6, its 'small Kn' approximation (equation 7.7), and the expression of Talbot *et al.* (1980) are shown in figure 7.10. In figure 7.10a, k_p/k_g is representative of the high thermal conductivity nickel particles for which the thermophoretic force was calculated in chapter 3, and in figure 7.10b, k_p/k_g is representative of the moderate thermal conductivity particles of uranine and oleic acid suspended in air that were used in the experiments carried out as part of the present study.

Figure 7.10 shows that equation 7.7 does not approximate equation 7.6 very well, except at $Kn \ll 1$, and figure 7.10a reveals that it behaves similarly to the expression of Bakanov & Roldugin (1977) in figure 3.5. So when Bakanov (1991) writes 'small Knudsen numbers', he is referring to the continuum regime, where $Kn \ll 1$. Therefore, the use of the Bakanov & Roldugin (1977) theory in chapter 3 at finite Kn was not valid, and the criticism of it was not entirely justified. This type of study (without making the approximation for $Kn \ll 1$) may prove to be useful over the entire range of Kn.

The results of studies using the kinetic equations have rarely produced an expression for the thermophoretic force, other than approximations for $Kn \ll 1$ and the free-molecule limit. As a consequence, the calculation of the thermophoretic force using such methods would be of a similar magnitude to the solution of the particle equations. The work of Beresnev & Chernyak (1995) is particularly welcome as it provides such an expression along with a table of the necessary coefficients. As interpolation between values of Kn is required to find the coefficients of equation 7.6, it may seem unsuitable for use as a formula over the range of Kn in the same manner as Talbot's expression. The results of figure 7.10 (for equation 7.6) were produced by fitting a sixth order polynomial to each coefficient, in each range of Kn (i.e $10^{-3} - 10^{-2}$, $10^{-2} - 10^{-1}$,$10^{-1} - 10^{0}$, etc). These polynomials are given in appendix D.1. It can be seen in figure 7.10a that there is a bump in the normalised thermophoretic force (calculated in this manner) at $Kn = 0.01$, and this is as a result of the shift between

ranges of Kn. Of much more interest, however, is that figure 7.10b shows that using the expression of Beresnev & Chernyak (1995) results in a reduced thermophoretic force when compared with the expression of Talbot *et al.* (1980), for the small Kn range. This is due to the action of the second thermophoresis mechanism.

The values of Kn for the turbulent annulus experiments where thermophoresis had the greatest effect (i.e. $10^{-1} < \tau_p^+ < 10^0$) were between 0.01 and 0.1. The use of this expression in the numerical study should result in a reduction in the deposition velocity in this range (again because of the inclusion of the second thermophoresis mechanism), and a closer fit with the experimental data. Beresnev & Chernyak (1995) also performed a sensitivity study on the effect of accommodation coefficients that deviate from unity.

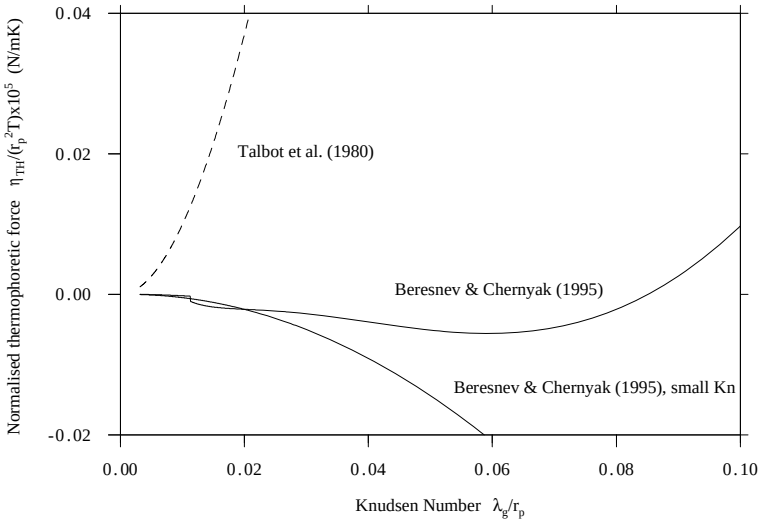

a)

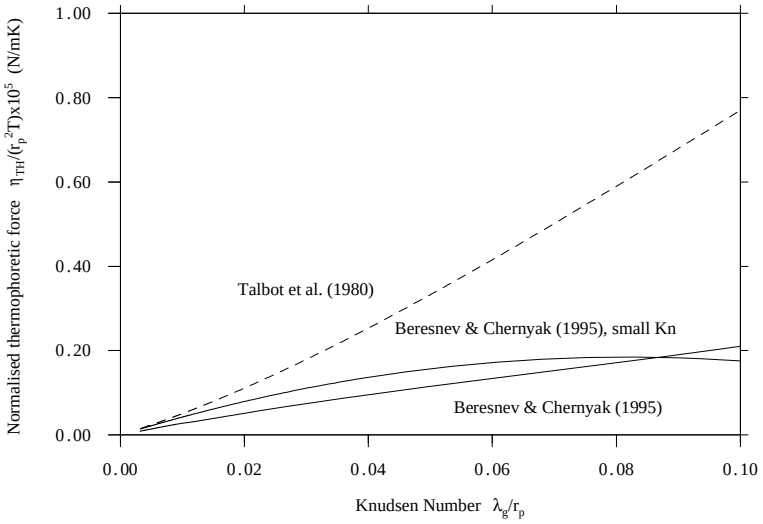

b)

Figure 7.10: The variation of normalised thermophoretic force with Knudsen number using difference expressions: a) k_p/k_g=3600; b) k_p/k_g=10.

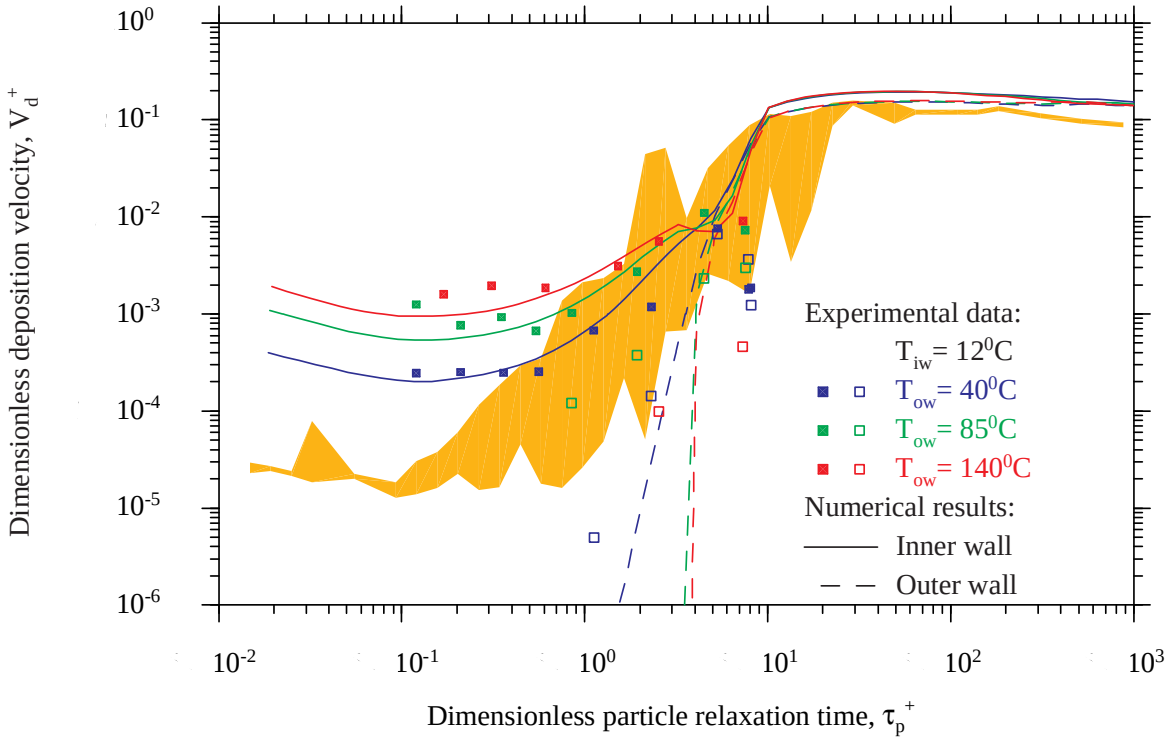

Figure 7.11: Thermophoretic particle deposition in a turbulent annulus with a cross-stream temperature gradient: comparison between experimental data and numerical results using the expression of Beresnev & Chernyak (1995)

The numerical results found by replacing Talbot's expression with that of Beresnev & Chernyak (1995) are shown in figure 7.11. The agreement with the experimental data in terms of the magnitude of the deposition velocity is much better, and within the uncertainty of the experimental data. V_d^+ first decreases slightly before increasing at the start of the turbulent diffusion-eddy impaction regime, in comparison with the behaviour found previously of a near constant V_d^+, followed by an increase. This may suggest that V_d^+ decreases as τ_p^+ increases and Kn decreases, and that the thermophoresis-turbulence interaction then occurs at smaller τ_p^+ than before, initiating the increase in V_d^+.

7.3.4 Summary

A set of experimental data for deposition in a turbulent annulus with different cross-stream gradients and constant thermophoretic force have been obtained. A numerical study has also been undertaken, and it has been found that the widely used expression resulting from the hydrodynamic analysis of Brock (1962), using the constants of Talbot *et al.* (1980), does not give the correct thermophoretic force for the range of Knudsen numbers used. The expression of Beresnev & Chernyak (1995) based on the linearised kinetic equations was found to give much better results, and includes mechanisms of thermophoresis not considered in the analysis

of Brock (1962), which makes it applicable to a broader range of situations. The expression of Beresnev & Chernyak (1995) can be included in particle calculations without significant computational penalties. The experimental and numerical studies also revealed the existence of an interaction between thermophoresis and turbophoresis. The evaluation of different expressions for the thermophoretic force, and the identification of the turbulence interaction has been made possible by the novel experimental set-up which allowed the imposition of a constant thermophoretic force (by maintaining a constant temperature difference and constant mean temperature) along the test section. These experimental results should provide a reliable datum for future studies of thermophoresis and its role in particle deposition in turbulent geometries.

Chapter 8

Conclusions and suggestions for further research

8.1 Part I - The Full Lagrangian Approach

The use of the Full Lagrangian approach (and more specifically, the Osiptsov Lagrangian approach) allows the direct calculation of particle density along particle pathlines in laminar fluid flows, reducing the number of particle pathlines required to achieve a stationary average of particle density, and increasing the computational efficiency of particle calculations. The Osiptsov Lagrangian approach had previously only been applied to analytical fluid flow fields, and the suitability of this approach for use with computationally generated fluid flow fields was assessed.

8.1.1 Conclusions

1. The Osiptsov Lagrangian approach has been shown to be capable of finding the particle density and velocity accurately using computationally generated fluid flow fields as well as analytical ones, by considering the case of gas-particle flow over a cylinder. It was found to give a better quality solution compared with the traditional Lagrangian approach, and had computational times that were between ten and twenty times smaller.

2. The Osiptsov Lagrangian approach was also applied to a practical flow application: gas-particle flow through a turbine cascade. An additional check on accuracy was tested, where in the limit of extremely small Stokes numbers the particle and gas density fields should be identical. The Osiptsov Lagrangian approach performed well.

3. A special technique was successfully developed for flows at low Stokes numbers which relieved the mathematical 'stiffness' of the equations and allowed solutions to be obtained without an increase in computational times.

4. A detailed study was made of the manner in which the Osiptsov Lagrangian approach

deals with crossing particle pathlines. At the crossing point, the particle density becomes infinite and this would usually cause numerical problems, but it is the Jacobian that is integrated along pathlines, and this passes smoothly through zero. The behaviour of a group of neighbouring particles was observed as they crossed in a flow over a cylinder, and it was shown that the Jacobian can increase or decrease along a particle pathline. This raises questions on the analysis of Robinson (1956) and the result that the particle density cannot decrease (i.e. the Jacobian increases) along a particle pathline in a potential flow.

8.1.2 Further research

1. In principle, there is no reason why the Osiptsov Lagrangian approach could not be extended to three-dimensional calculations. The reduction in the number of particle pathlines required means that the calculation would not be computationally prohibitive.

2. Eulerian approaches are generally employed for small Stokes numbers in turbulent fluid flows where turbulent/diffusive effects are important. At intermediate Stokes numbers, when large-scale inertial effects and turbulent/diffusive effects are important, a combination of both Eulerian and Lagrangian approaches would be desirable. The Osiptsov Lagrangian approach could be used to provide a solution of the particle flow field up to the edge of the boundary layer (outside of which turbulence has little effect on the particles), and an Eulerian approach could then be used to complete the calculation. Although this approach may not seem very elegant, the intricacy of the near-wall particle behaviour means that there is no justification for over-resolution of the entire flow field. Rather than viewing it as a 'mixed' calculation, the Lagrangian part may be thought of as an extra step between the solution of the fluid and particle flow fields, which provides a further input to the Eulerian boundary layer calculation. To this end, the Eulerian diffusion-inertia approach of Slater & Young (1998) should first be applied to a fluid boundary layer solution, and then an investigation into the matching of the two calculations at the edge of the boundary layer can be undertaken.

3. As both the Osiptsov Lagrangian and Eulerian components of such an approach are computationally efficient, extension of the combined approach to three-dimensional analyses is computationally feasible. Work is already under way to extend the Eulerian calculation to three-dimensions, and if the Osiptsov Lagrangian approach were similarly developed, this would allow the study of three-dimensional effects in turbomachinery flows, such as the influence of end wall boundary layers, passage vortices, and the blocking of turbine blade cooling holes by excess deposition.

8.2 Part II - Thermophoretic Deposition

The aim of the present experimental study was to provide data on the variation of deposition velocity with particle size over a range of temperature differences that were constant along the length of the test section, to provide a constant thermophoretic force (at a constant Reynolds number). Such data was required so that expressions for the thermophoretic force could be validated and used in other studies for which experimental data does not exist. This validation was considered necessary because of the considerable discrepancies between the many different expressions, despite the general acceptance of the expression of Talbot *et al.* (1980).

An experimental rig was designed to achieve a constant thermophoretic force. This was done by using an annular geometry with a cold inner wall and hot outer wall with the result that once the temperature was fully-developed, a constant temperature difference, a constant mean temperature and a constant thermophoretic force existed along the length of the test section. A numerical scheme was also developed based on the theory of Young & Leeming (1997), with modifications made for the change of geometry from a pipe to an annulus.

8.2.1 Conclusions

Experimental

1. Results in the diffusional deposition regime when a cross-stream temperature gradient was imposed, showed near constant values of deposition velocity at the inner wall as particle size was increased. When the temperature difference was increased, the value of the constant deposition velocity also increased. There was an area in the eddy impaction-turbulent diffusion regime where the deposition velocity at the inner wall increased beyond its constant value in the diffusional deposition regime, before reaching the same value as it would have in an isothermal flow. This provided experimental evidence of an interaction between thermophoresis and turbulence (i.e. turbophoresis). The outer wall deposition velocity was negligible in the diffusional deposition regime, but as particle size was increased, it increased towards its isothermal value.

2. Particle deposition in a turbulent isothermal annular flow was expected to be very similar to that in a turbulent isothermal pipe flow, and the experimental results showed this to be the case, except for particles in the inertia moderated regime where deposition velocities in the annulus were almost an order of magnitude lower than those in a pipe. For large particles, the large deposition velocities (and excessive deposition at the inlet to the test section) caused the mean particle concentration to be very low in some (or all) portions of the test section. If small satellite particles are present in the flow they will dominate depositional behaviour, giving smaller than expected deposition velocities.

Numerical

1. The work of Beresnev & Chernyak (1995) provided an expression for the thermophoretic force based on the linearised kinetic equations, and a table of coefficients for use at various values of Knudsen number. This expression, together with a number of polynomial fits to the coefficients over different ranges of Knudsen number, was used to obtain numerical results for turbulent flow in an annulus with a cross-stream temperature gradient, and these were compared with results obtained using the expression of Talbot *et al.* (1980). The expression of Beresnev & Chernyak (1995) performed much better than that of Talbot *et al.* (1980) in relation to the experimental data, at no extra computational cost.

2. The success of the expression of Beresnev & Chernyak (1995) over that of Talbot *et al.* (1980) is thought to be due to its inclusion of a second thermophoresis mechanism, which comes from the higher order solution of the model Boltzmann equation. For particles of high thermal conductivity at very small Knudsen numbers, this second mechanism can cause a reversal in the direction of the thermophoretic force. This mechanism was not included in the expression of Talbot *et al.* (1980), and with the moderate particle thermal conductivity and relatively small Knudsen numbers that existed experimentally, this second mechanism had the effect of reducing the overall thermophoretic force, thus improving agreement between the experimental data and numerical results, when the expression of Beresnev & Chernyak (1995) was used.

3. The thermophoresis-turbulence interaction was reproduced numerically, and explained by considering force profiles across the annulus. The turbophoresis force transports particles towards the wall, and the thermophoretic force (although very small at these values of τ_p^+ and Kn) is still of sufficient magnitude in the near-wall region to enhance deposition to the inner wall, and retard deposition to the outer wall.

8.2.2 Further research

1. A survey of experimental and DNS data has shown that there is some deviation in the values found for deposition velocity in the inertia moderated regime. A possible cause is the differences in the time/distance taken for a stationary particle density profile to be reached for different sized particles in different studies. Another is that large particles take little notice of the near-wall turbulence layer, and that non-dimensionalisation with an integral property of the turbulence (rather than wall variables) may result in a better correlation between different data. A comprehensive scaling study of DNS and experimental data would be useful to determine the most appropriate scaling for large particles, and establish limits of validity on the length of test section, or time of a calculation, required for particle densities to reach stationary values.

2. The attractiveness of turbulent pipe (and annulus) flow studies is due to the presence of all the deposition mechanisms that have so far been introduced, and the simplicity of the geometry. One of the greatest departures between this type of study and more practical applications is the effect of more complex geometries on particle deposition, especially when the flow is over a curved surface, as is the case for gas turbine blades. Konstandopoulos & Rosner (1995a) found that there was a significant interaction between thermophoresis and inertial effects due to streamline curvature for small particles in laminar boundary layer flows. While the interaction between thermophoresis and turbulence has been demonstrated in this thesis, if the theories developed are to be extended to more complex geometries, an understanding of the interaction between streamline curvature effects and turbophoresis is also required. For a range of particle sizes, there will be competition between the turbophoretic force and the centrifugal force, which may either enhance or oppose deposition (depending on whether the surface is concave or convex) and lead to local enrichment or depletion of the particle density near the surface. The annular test section of the experimental rig has now been replaced by a 90° curved duct, so that experiments can be carried out for a range of particles sizes and radii of curvature. This will allow an investigation of the streamwise curvature-turbulence interaction, and comparison with theory through a parallel numerical study.

Appendix A

Supplementary information to chapter 2

A.1 Two-dimensional stagnation point flow

The fluid streamlines for such a flow are shown in figure 2.6. The stream function equation is:

$$\Psi = -Axy, \quad \text{where} \quad U_x = \frac{\partial \Psi}{\partial y} = -Ax, \quad \text{and} \quad U_y = -\frac{\partial \Psi}{\partial x} = Ay \tag{A.1}$$

where A is a positive constant.

The analytical solution for the particle flow will now be derived. The particle equation of motion can be split into its $x-$ and $y-$components:

$$\frac{\partial V_x}{\partial \tau} = \beta(U_x - V_x) \quad \text{and} \quad \frac{\partial V_y}{\partial \tau} = \beta(U_y - V_y) \tag{A.2}$$

Substituting the relationships $V_x = \partial x_p/\partial \tau$ and $V_y = \partial y_p/\partial \tau$ into equation A.2 gives two second-order differential equations for x_p and y_p in terms of the time τ:

$$\frac{\partial^2 x_p}{\partial \tau^2} + \beta \frac{\partial x_p}{\partial \tau} + \beta A x_p = 0 \quad \text{and} \quad \frac{\partial^2 y_p}{\partial \tau^2} + \beta \frac{\partial y_p}{\partial \tau} - \beta A y_p = 0 \tag{A.3}$$

In order to solve these second-order differential equations, the roots of their auxiliary equations must be obtained. These are:

$$m_{x1,2} = -\frac{\beta}{2}\left(1 \pm \sqrt{1 - \frac{4A}{\beta}}\right) \quad \text{and} \quad m_{y1,2} = -\frac{\beta}{2}\left(1 \pm \sqrt{1 + \frac{4A}{\beta}}\right) \tag{A.4}$$

The y-direction equation has two real and different roots. The x-direction is more complicated, having three types of solution: when $\frac{4A}{\beta} < 1$, the roots are real and different, when $\frac{4A}{\beta} = 1$, the roots are real and equal, and when $\frac{4A}{\beta} > 1$, the roots are imaginary and different. The

solutions of each take the following form:

$$x_p = \begin{cases} C_1 e^{m_{x1}\tau} + C_2 e^{m_{x2}\tau} & \text{if } \frac{4A}{\beta} < 1 \\ (C_3 + C_4\tau)e^{m_{x1}\tau} & \text{if } \frac{4A}{\beta} = 1 \\ e^{-\beta\tau/2}\{C_5 cos(\frac{\beta}{2}\omega\tau) + C_6 sin(\frac{\beta}{2}\omega\tau)\} & \text{if } \frac{4A}{\beta} > 1 \end{cases} \tag{A.5}$$

$$y_p = \quad C_7 e^{m_{y1}\tau} + C_8 e^{m_{y2}\tau} \tag{A.6}$$

where $\omega = \sqrt{4A/\beta - 1}$. Differentiating with respect to τ gives the $x-$ and $y-$components of the particle velocity:

$$V_x = \begin{cases} C_1 m_{x1} e^{m_{x1}\tau} + C_2 m_{x2} e^{m_{x2}\tau} & \text{if } \frac{4A}{\beta} < 1 \\ (C_3 m_{x1} + C_4 m_{x1}\tau + C_4)e^{m_{x1}\tau} & \text{if } \frac{4A}{\beta} = 1 \\ -\frac{\beta}{2}e^{-\beta\tau/2}\{C_5 cos(\frac{\beta}{2}\omega\tau) + C_6 sin(\frac{\beta}{2}\omega\tau)\} & \text{if } \frac{4A}{\beta} > 1 \\ \quad +e^{-\beta\tau/2}\{-C_5\frac{\beta}{2}\omega sin(\frac{\beta}{2}\omega\tau) + C_6\frac{\beta}{2}\omega cos(\frac{\beta}{2}\omega\tau)\} & \end{cases} \tag{A.7}$$

$$V_y = \quad C_7 m_{y1} e^{m_{y1}\tau} + C_8 m_{y2} e^{m_{y2}\tau} \tag{A.8}$$

The constants in the above equations are dependent on the initial conditions of the particle flow. These are that the particles enter the flow from the x = -1 line with zero initial $x-$velocity slip ($V_{x,0} = U_{x,0} = -Ax_{p,0}$) and zero initial $y-$velocity ($V_{y,0} = 0$). Inserting these initial conditions into the above equations at time $\tau = 0$, gives the constants as:

$$\begin{aligned} C_1 &= \frac{x_{p,o}(m_{x1} + A)}{m_{x1} - m_{x2}} & C_2 &= \frac{-x_{p,o}(m_{x2} + A)}{m_{x1} - m_{x2}} \\ C_3 &= x_{p,o} & C_4 &= -x_{p,o}(m_{x1} + A) \\ C_5 &= x_{p,0} & C_6 &= \frac{x_{p,0}}{\omega}(1 - 2\frac{A}{\beta}) \\ C_7 &= \frac{y_{p,o} m_{y1}}{m_{y1} - m_{y2}} & C_8 &= \frac{-y_{p,o} m_{y2}}{m_{y1} - m_{y2}} \end{aligned} \tag{A.9}$$

Combining equations 2.16 and 2.17, two second-order differential equations may be written for the non-zero components of the Jacobian:

$$\frac{\partial^2 J_{xa}}{\partial\tau^2} + \beta\frac{\partial J_{xa}}{\partial\tau} + \beta A J_{xa} = 0 \quad \text{and} \quad \frac{\partial^2 J_{yb}}{\partial\tau^2} + \beta\frac{\partial J_{yb}}{\partial\tau} - \beta A J_{yb} = 0 \tag{A.10}$$

These equations can be solved in exactly the same manner as those for x_p and y_p, to give an analytical solution for the components of the Jacobian (and particle density), by using the initial conditions for J and w as described in section 2.3.3 to solve for the necessary constants.

The solutions are:

$$J_{xa} = \begin{cases} D_1 e^{m_{x1}\tau} + D_2 e^{m_{x2}\tau} & \text{if } \frac{4A}{\beta} < 1 \\ (D_3 + D_4\tau) e^{m_{x1}\tau} & \text{if } \frac{4A}{\beta} = 1 \\ e^{-\beta\tau/2}\{D_5 cos(\frac{\beta}{2}\omega\tau) + D_6 sin(\frac{\beta}{2}\omega\tau)\} & \text{if } \frac{4A}{\beta} > 1 \end{cases} \tag{A.11}$$

$$J_{yb} = \quad D_7 e^{m_{y1}\tau} + D_8 e^{m_{y2}\tau} \tag{A.12}$$

with constants:

$$\begin{aligned} D_1 &= \frac{-m_{x2}}{m_{x1} - m_{x2}} & D_2 &= \frac{m_{x1}}{m_{x1} - m_{x2}} \\ D_3 &= 1 & D_4 &= -m_{x1} \\ D_5 &= 1 & D_6 &= 1 \\ D_7 &= \frac{\beta\frac{U_{y,0}}{u_{x,0}} - m_{y,2}}{m_{y1} - m_{y2}} & D_8 &= \frac{m_{y,1} - \beta\frac{U_{y,0}}{u_{x,0}}}{m_{y1} - m_{y2}} \end{aligned} \tag{A.13}$$

A.2 Special treatment at low Stokes numbers in two-dimensions

The two particle velocity components are:

$$\begin{aligned} (V_x - U_x) &= (V_x - U_x)_0 e^{-\beta\Delta\tau} - \overline{\frac{\partial U_x}{\partial \tau}}\Big(\frac{1 - e^{-\beta\Delta\tau}}{\beta}\Big) \\ (V_y - U_y) &= (V_y - U_y)_0 e^{-\beta\Delta\tau} - \overline{\frac{\partial U_y}{\partial \tau}}\Big(\frac{1 - e^{-\beta\Delta\tau}}{\beta}\Big) \end{aligned} \tag{A.14}$$

The four Jacobian components are:

$$\begin{aligned} J_{xa} &= (J_{xa})_0 + (w_{xa})_0\left(\frac{1 - e^{-\beta\Delta\tau}}{\beta}\right) + \overline{\frac{\partial U_x}{\partial a}}\Big(\Delta\tau - \frac{1 - e^{-\beta\Delta\tau}}{\beta}\Big) \\ J_{xb} &= (J_{xb})_0 + (w_{xb})_0\left(\frac{1 - e^{-\beta\Delta\tau}}{\beta}\right) + \overline{\frac{\partial U_x}{\partial b}}\Big(\Delta\tau - \frac{1 - e^{-\beta\Delta\tau}}{\beta}\Big) \\ J_{ya} &= (J_{ya})_0 + (w_{ya})_0\left(\frac{1 - e^{-\beta\Delta\tau}}{\beta}\right) + \overline{\frac{\partial U_y}{\partial a}}\Big(\Delta\tau - \frac{1 - e^{-\beta\Delta\tau}}{\beta}\Big) \\ J_{yb} &= (J_{yb})_0 + (w_{yb})_0\left(\frac{1 - e^{-\beta\Delta\tau}}{\beta}\right) + \overline{\frac{\partial U_y}{\partial b}}\Big(\Delta\tau - \frac{1 - e^{-\beta\Delta\tau}}{\beta}\Big) \end{aligned} \tag{A.15}$$

and the four w-components are:

$$\begin{aligned} w_{xa} &= (w_{xa})_0 e^{-\beta\Delta\tau} + \overline{\frac{\partial U_x}{\partial a}}(1 - e^{-\beta\Delta\tau}) \\ w_{xb} &= (w_{xb})_0 e^{-\beta\Delta\tau} + \overline{\frac{\partial U_x}{\partial b}}(1 - e^{-\beta\Delta\tau}) \\ w_{ya} &= (w_{ya})_0 e^{-\beta\Delta\tau} + \overline{\frac{\partial U_y}{\partial a}}(1 - e^{-\beta\Delta\tau}) \\ w_{yb} &= (w_{yb})_0 e^{-\beta\Delta\tau} + \overline{\frac{\partial U_y}{\partial b}}(1 - e^{-\beta\Delta\tau}) \end{aligned} \tag{A.16}$$

where the gradients of fluid velocity are found using equation 2.18.

A.3 Deterministic Lagrangian tracking

The traditional Lagrangian calculations were performed using a code originally written by Slater (1999). The main features of this code are discussed here, because they also appear in the code written to perform the Osiptov Lagrangian calculations. This allowed the two methods to be compared on a fair and equal basis. Lagrangian tracking involves the repeated integration of the particle equations of motion. Using a temporal discretisation (first order accurate in $\Delta\tau$) gives:

$$\frac{\partial \mathbf{V}}{\partial \tau} = \beta(\mathbf{U} - \mathbf{V}) = \frac{\mathbf{V}_{new} - \mathbf{V}}{\Delta\tau} \tag{A.17a}$$

$$\mathbf{V} = \frac{\partial \mathbf{x}_p}{\partial \tau} = \frac{\mathbf{x}_{p,new} - \mathbf{x}_p}{\Delta\tau} \tag{A.17b}$$

The traditional Lagrangian method integrates only the particle equation of motion (equation A.17). If the initial conditions are known, i.e. particle velocity $\mathbf{V}$ and position $\mathbf{x}_p$, then the equation can be integrated to solve for the particle velocity $\mathbf{V}_{new}$ at the end of the time-step $\Delta\tau$. Slater (1999) points out that the use of this algorithm (which is first-order accurate in $\Delta\tau$), requires extremely small time-steps to minimise the statistical noise within the particle density field. This made the need for higher-order interpolations redundant.

The Osiptsov Lagrangian method also uses equation A.17, but in conjunction with the additional equations:

$$\frac{\partial \mathbf{w}}{\partial \tau} = \beta(\mathbf{J}\frac{\partial \mathbf{U}}{\partial \mathbf{x}} - \mathbf{w}) = \frac{\mathbf{w}_{new} - \mathbf{w}}{\Delta\tau} \tag{A.18a}$$

$$\mathbf{w} = \frac{\partial \mathbf{J}}{\partial \tau} = \frac{\mathbf{J}_{new} - \mathbf{J}}{\Delta\tau} \tag{A.18b}$$

These are integrated in the same manner as the particle equations of motion. If the inital values of $\mathbf{w}$, $\mathbf{J}$ and the fluid velocity gradient $\frac{\partial \mathbf{U}}{\partial \mathbf{x}}$ are known, then $\mathbf{w}_{new}$ at the end of the time-step can be found. If $\mathbf{w}$ and $\mathbf{J}$ are known, then $\mathbf{J}_{new}$ can be found, which then gives the

Figure A.1: Schematic of interpolation of data from Lagrangian trajectories to Eulerian grid

A.4 Plotting of particle density field

The Osiptsov Lagrangian approach provides detailed information about the particle density and velocity at every time-step along each particle pathline. Irregularly spaced data is extremely difficult to contour, so it must first be interpolated onto a regular grid. In this case, the Eulerian grid from the fluid phase calculation was used. Each particle pathline was dealt with individually. Figure A.1 shows two particle pathlines crossing Eulerian grid cells. Particle density and velocity were known at the points marked $\circ$. A two-dimensional bi-linear interpolation was performed between these points, and the particle density and velocity were calculated at the points (marked $\bullet$) where the particle pathlines intersect the dashed lines which join the cell centres to the centres of grid lines. A variable-power spline (Soanes, 1976) was then fitted to these points (marked $\bullet$) and values of particle density and velocity were

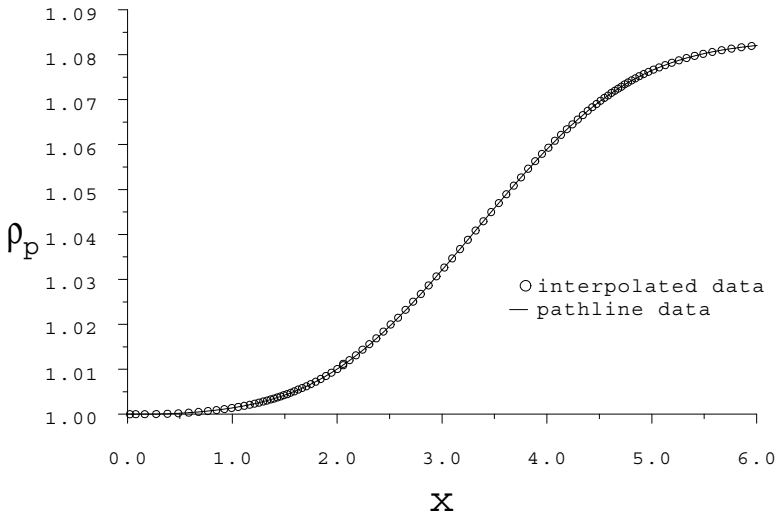

a) Interpolation along a particle pathline

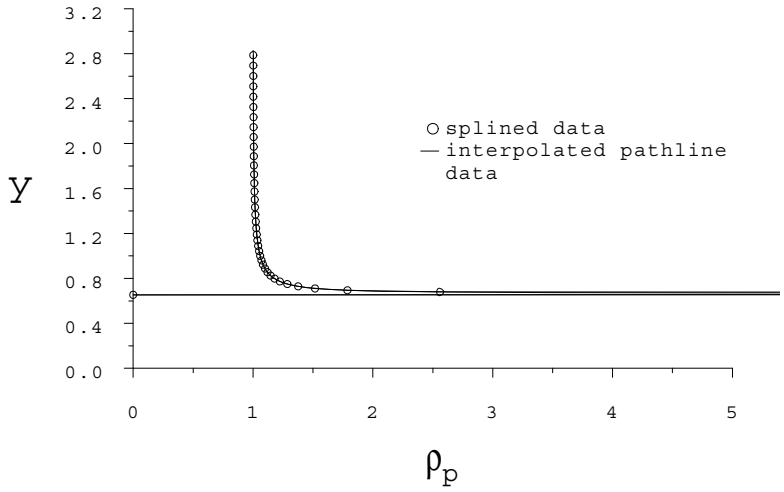

b) Splining across particle pathlines

Figure A.2: Interpolation of data from Lagrangian trajectories to Eulerian grid

found at the Eulerian grid cell centres (marked X). Figure A.2a shows the interpolation along a particle pathline (from $\circ$ to $\bullet$). Figure A.2b shows the variable-power spline across the particle pathlines (from $\bullet$ to X). The interpolation and splining can be seen to represent accurately the original particle pathline data.

Appendix B

Supplementary information to chapter 3

B.1 Drag term correction

The drag force per unit mass (equation 3.14) contains the term $\phi_D(Re_p)$, which is a correction for non-Stokesian behaviour. The Stokes drag coefficient (i.e. small Re_p) is given by $C_D = 24/Re_p$, but an empirical curve fit to experimental data may be used to extend the expression to finite values of Re_p. The correction is defined as:

$$\phi_D(Re_p) = C_D \frac{Re_p}{24} \tag{B.1}$$

and C_D is found for a range of values of Re_p from Morsi & Alexander (1972):

$$\begin{array}{lll}
C_D = \frac{24}{Re_p} & \text{for} & Re_p < 0.1 \\
C_D = \frac{22.73}{Re_p} + \frac{0.0903}{Re_p^2} + 3.69 & \text{for} & 0.1 < Re_p < 1.0 \\
C_D = \frac{29.1667}{Re_p} - \frac{3.8889}{Re_p^2} + 1.222 & \text{for} & 0.1 < Re_p < 1.0 \\
C_D = \frac{29.1667}{Re_p} - \frac{3.8889}{Re_p^2} + 1.222 & \text{for} & 1.0 < Re_p < 10.0 \\
C_D = \frac{46.5}{Re_p} - \frac{116.67}{Re_p^2} + 0.6167 & \text{for} & 10.0 < Re_p < 100.0
\end{array} \tag{B.2}$$

B.2 Lift term correction

Saffman's expression for the lift force (equation 3.16) is only valid when $Re_p \ll Re_{sh}$, $Re_p \ll 1$ and $Re_{sh} \ll 1$. McLaughlin (1991) and Dandy & Dwyer (1990) removed various restrictions, and Mei (1992) produced a curve fit incorporating these improvements. The lift force is now given as:

$$F_L = \phi_L F_{L,saff} \tag{B.3}$$

where $F_{L,saff}$ is the Saffman expression equation (3.16), and ϕ_L is given by Mei (1992) as:

$$\begin{aligned} \phi_L &= (1.0 - 0.3314\alpha^{1/2})exp(-\tfrac{Re_p}{10}) + 0.3314\alpha^{1/2} \quad \text{for} \quad Re_p \leq 40 \\ \phi_L &= 0.0524(\alpha Re_p)^{1/2} \quad \text{for} \quad Re_p \geq 40 \end{aligned} \tag{B.4}$$

where

$$\alpha = \frac{1}{2}\frac{Re_{sh}}{Re_p} \tag{B.5}$$

Appendix C

Supplementary information to chapters 4 and 5

C.1 Theoretical analysis of turbulent pipe deposition velocity

Consider a pipe flow with a radial coordinate r and an axial coordinate z. The particle density $\rho_p = \rho_p(r, z)$ and the mean particle density $\rho_{p,m} = \rho_{p,m}(z)$ is defined by:

$$\pi a^2 \rho_{p,m} = \int_0^a 2\pi r \rho_p dr \tag{C.1}$$

where a is the pipe radius. $V_z = V_z(r, z)$ is the particle axial velocity, and the mean particle axial velocity $V_{z,m} = V_{z,m}(z)$ is defined by:

$$\pi a^2 V_{z,m} = \int_0^a 2\pi r V_z dr \tag{C.2}$$

Defining $\psi = \rho_p/\rho_{p,m}$ and $\phi = V_z/V_{z,m}$:

$$\pi a^2 = \int_0^a 2\pi r \psi dr = \int_0^a 2\pi r \phi dr \tag{C.3}$$

The particle mass flow rate can now be written:

$$\dot{m}_p = \dot{m}_p(z) = \int_0^a 2\pi r \rho_p V_z dr = \pi a^2 \rho_{p,m} U_m \alpha \beta \tag{C.4}$$

where $\alpha = V_{z,m}/U_m$ and U_m is the mean gas velocity in the pipe, and β is defined by:

$$\pi a^2 \beta = \int_0^a 2\pi r \psi \phi dr \tag{C.5}$$

Generally, α and β are functions of z, and are constant for fully-developed particle flows. The product $\alpha\beta$ will be quite close to unity for most particle velocity and density profiles.

Remembering from equation 3.39, that $J_w = J_w(z)$ is the mass flux of particles to the wall per unit area, and is defined by:

$$J_w = \rho_{p,m} V_d \tag{C.6}$$

For fully-developed particle flow, theory shows the V_d is independent of z.

The change in particle mass flow rate in the axial direction is related to the mass of particles deposited on the wall, such that:

$$\frac{d\dot{m}_p}{dz} = \frac{d}{dz}\Big(\pi a^2 \rho_{p,m} U_m \alpha\beta\Big) = -2\pi a J_w = -2\pi a \rho_{p,m} V_d \tag{C.7}$$

Now consider a length of pipe over which α, β and V_d are approximately constant (not necessarily implying fully-developed particle flow). The particle conservation equation is:

$$\frac{d\rho_{p,m}}{dz} = -\frac{2}{a\alpha\beta}\frac{V_d}{U_m}\rho_{p,m} \tag{C.8}$$

By integrating from $z = z_1$ to $z = z_2$ where $z_2 - z_1 = L$,

$$ln\left(\frac{\rho_{p,m2}}{\rho_{p,m1}}\right) = -\frac{1}{\alpha\beta}\frac{2L}{a}\frac{V_d}{U_m} \tag{C.9}$$

Rearranging, gives the dimensionless deposition velocity V_d^+ as:

$$V_d^+ = \alpha\beta\frac{a}{2L}\frac{U_m}{u_*} ln\left(\frac{\rho_{p,m1}}{\rho_{p,m2}}\right) \tag{C.10}$$

Using equation 4.7 and the Blasius formula for a smooth pipe (Schlichting, 1968), rearrangement gives:

$$V_d^+ = 1.257\alpha\beta\left(\frac{d}{L}\right) Re^{0.125} ln\left(\frac{\rho_{p,m1}}{\rho_{p,m2}}\right) \tag{C.11}$$

Once the flow conditions of an experiment have been set, this expression can be used with a predicted value of V_d^+ to find the mean concentration drop along the length of the pipe. The expression $ln\left(\frac{C_{p,m1}}{C_{p,m2}}\right)$ may be used in place of $ln\left(\frac{\rho_{p,m1}}{\rho_{p,m2}}\right)$ as $\rho_{p,m} = m_p C_{p,m}$, and m_p is the same at positions 1 and 2.

C.2 Uncertainty analysis

Single-sample uncertainty analysis of the measurement of τ_p^+

The dimensionless particle relaxation time is:

$$\tau_p^+ = \frac{\rho_{p,mat} d_p^2}{18\mu_g} \frac{\rho_g u_*^2}{\mu_g} \tag{C.12}$$

Following Moffat (1988) and Leeming (1995), $\delta\tau_p^+$ is the uncertainty associated with τ_p^+, and may be expressed as:

$$\frac{\delta\tau_p^+}{\tau_p^+} = \left\{ \left[\frac{\delta\rho_g}{\rho_g}\right]^2 + 4\left[\frac{\delta u_*}{u_*}\right]^2 + 4\left[\frac{\delta\mu_g}{\mu_g}\right]^2 + 4\left[\frac{\delta d_p}{d_p}\right]^2 + \left[\frac{\delta\rho_{p,mat}}{\rho_{p,mat}}\right]^2 \right\}^{1/2} \tag{C.13}$$

where the individual uncertainties may be expressed as:

$$\begin{aligned}
\frac{\delta\rho_g}{\rho_g} &= \left\{ \left[\frac{\delta p}{p}\right]^2 + \left[\frac{\delta T}{T}\right]^2 + \left[\frac{\delta R}{R}\right]^2 \right\}^{1/2} \\
\frac{\delta u_*}{u_*} &= \left\{ \frac{65}{64}\left[\frac{\delta U_m}{U_m}\right]^2 + \frac{1}{4}\left[\frac{\delta f_{corr}}{f}\right]^2 + \frac{1}{64}\left[\frac{\delta\rho_g}{\rho_g}\right]^2 + \frac{1}{64}\left[\frac{\delta\mu_g}{\mu_g}\right]^2 + \frac{1}{64}\left[\frac{\delta d_h}{d_h}\right]^2 \right\}^{1/2} \\
\frac{\delta U_m}{U_m} &= \left\{ 4\left[\frac{\delta d_h}{d_h}\right]^2 + \left[\frac{\delta Q_a}{Q_a}\right]^2 + \left[\frac{\delta\rho_g}{\rho_g}\right]^2 + \left[\frac{\delta\rho_{g,rot}}{\rho_{g,rot}}\right]^2 + \left[\frac{\delta\mu_g}{\mu_g}\right]^2 \right\}^{1/2} \\
\frac{\delta\rho_{g,rot}}{\rho_{g,rot}} &= \left\{ \left[\frac{\delta p_{rot}}{p_{rot}}\right]^2 + \left[\frac{\delta T_{rot}}{T_{rot}}\right]^2 + \left[\frac{\delta R}{R}\right]^2 \right\}^{1/2} \\
\frac{\delta\mu_g}{\mu_g} &= \left\{ \left[\frac{\delta\mu_{g,corr}}{\mu_g}\right]^2 + \left[B(1)^2 + 4B(2)^2T^2 + 9B(3)^2T^3 + 16B(4)^2T^6\right]\left[\frac{\delta T}{T}\right]^2 \right\}^{1/2} \\
\frac{\delta Q_a}{Q_a} &= \left\{ \left[\frac{\delta Q_{ind}}{Q_{ind}}\right]^2 + \frac{1}{4}\left[\frac{\delta T_{rot}}{T_{rot}}\right]^2 + \frac{1}{4}\left[\frac{\delta p_{rot}}{p_{rot}}\right]^2 \right\}^{1/2}
\end{aligned} \tag{C.14}$$

where f_{corr} is the error due to the friction factor correlation (equation 4.11), and $\mu_{g,corr}$ is the error due to the correlation of Irvine & Liley (1984) used to find the dependence of μ_g on T, which introduces the constants $B(1)...B(4)$. The subscript $_{rot}$ indicates a quantity measured at the rotameter rather than in the test section, while the subscript $_{ind}$ refers to the flow rate indicated by the rotameter, before the correction for operating conditions that vary from calibration conditions (indicated by the subscipt $_{cal}$) has been made. The uncertainty in τ_p^+ is now a function of the following parameters:

$$\frac{\delta\tau_p^+}{\tau_p^+} = \frac{\delta\tau_p^+}{\tau_p^+}\left(d_h, d_p, f_{corr}, \mu_{g,corr}, p, p_{rot}, Q_{ind}, R, \rho_{p,mat}, T, T_{rot}\right) \tag{C.15}$$

Single-sample uncertainty analysis of the measurement of V_d^+

The dimensionless particle deposition velocity is:

$$(V_d^+)_{i/o} = \frac{U_m(d_o^2 - d_i^2)}{4\Delta x u_{*,i/o} d_{i/o}} \frac{M_{p,i/o}}{M_{p,i} + M_{p,o}} ln\frac{1}{P} \tag{C.16}$$

The uncertainty associated with this measurement may be expressed as:

$$\frac{\delta(V_d^+)_{i/o}}{(V_d^+)_{i/o}} = \left\{ \left[\frac{\delta U_m}{U_m}\right]^2 + \left[\frac{\delta u_{*,i/o}}{u_{*,i/o}}\right]^2 + 2\left[\frac{(d_o - d_i)}{(d_o + d_i)}\frac{\delta d_{i/o}}{d_{i/o}}\right]^2 + \left[\frac{\delta \Delta x}{\Delta x}\right]^2 + 2\left[\frac{\delta M_{p,i/o}}{M_{p,i} + M_{p,o}}\right]^2 + \left[\frac{1}{lnP}\frac{\delta P}{P}\right]^2 \right\}^{1/2} \tag{C.17}$$

The uncertainty in V_d^+ is a function of the following parameters:

$$\frac{\delta(V_d^+)_{i/o}}{(V_d^+)_{i/o}} = \frac{\delta(V_d^+)_{i/o}}{(V_d^+)_{i/o}} \left(\Delta x, d_{i/o}, f_{corr}, \mu_{g,corr}, M_{p,i/o}, p, p_{rot}, P, Q_{ind}, R, T, T_{rot} \right) \tag{C.18}$$

Uncertainty in the constituent variables - fixed uncertainties

The uncertainties in a number of the parameters do not vary from one run to the next. These will be dealt with first.

- The uncertainty in the concentration and volume of the constituent reagents of the aerosol solution, the solution feed rate, and the frequency of vibration of the orifice, are assumed to be insignificant. The particle material density, $\rho_{p,mat}$, is therefore known with negligible uncertainty, so that $\frac{\delta \rho_{p,mat}}{\rho_{p,mat}} = 0$. The particle diameter, d_p, is known with less certainty, because of the possibility of particle agglomeration producing doublets and triplets. Leeming (1995) assumed that the particle size distribution was similar to one produced during the calibration of the aerosol generator. 10% of the particles were doublets, increasing the mean particle diameter from d_p to $1.026 d_p$. Therefore, $\frac{\delta d_p}{d_p} = 0.026$.

- The nominal values for inside diameter, d_i, and outside diameter, d_o, (and thus the hydraulic diameter, d_h) are assumed to be within 1% of the real value, so that $\frac{\delta d_{i/o/h}}{d_{i/o/h}} = 0.01$.

- It is assumed that the washing can be carried out over 10 cm sections to an accuracy of $\pm$ 1 mm, so that $\frac{\delta \Delta x}{\Delta x} = 0.01$.

- The rotameter, from which Q_{ind} is read, is accurate to within 5% of its full-scale deflection (which is 180 lpm). Taking this as the worst case, $\frac{\delta Q_{ind}}{Q_{ind}} \leq 0.05$

- The correlation used for the friction factor was found to reduce the observed scatter of experimental data to approximately $\pm 5\%$ (Jones & Leung, 1981), so that $\frac{\delta f_{corr}}{f} = 0.05$.

- The correlation used for the variation of dynamic viscosity with temperature was accurate to within 1% for $T <$ 1500 K (Irvine & Liley, 1984), therefore $\frac{\delta \mu_{g,corr}}{\mu_g} = 0.01$. R = 287.1 Jkg^{-1}K^{-1} over the range of temperatures used so that $\frac{\delta R}{R} = 0$.

Multiple-sample analysis

The only remaining uncertainties required, are those associated with temperature, pressure and fractional penetration, and deposited mass (or luminosity reading). Temperature and pressure measurements were taken over the course of each experimental run, and the fractional penetration (and luminosity readings) was found for each section of the annulus. Therefore a multiple-sample analysis (again following Moffat (1988) and Leeming (1995)) was used to determine these uncertainties. The overall uncertainty in a result R at a 95% confidence level is given by:

$$(U_R)_{0.95} = \{(B_R)^2 + (t.S_R)^2\}^{1/2} \tag{C.19}$$

- B_R is the bias limit of a measurement, and provides an estimate of the maximum probable value of the fixed error arising from calibration or measurement.

- t is the Student's t multiplier for the number of degrees of freedom (equal to N-1, where N is the number of measurements taken), which may be found, for example, in Wonnacott & Wonnacott (1977).

- S_R is the precision index of the mean, and provides an estimate of the standard deviation of the mean of the set of N measurements. It is given by:

$$S_R = \frac{1}{\sqrt{N}} \left\{ \sum_{i-1}^{N} \frac{(X_i - \overline{X}_i)^2}{N-1} \right\}^{1/2} \tag{C.20}$$

The bias limit was taken as the uncertainty in the calibration of the relevant instrument (thermocouple, pressure transducer or luminescence spectrometer). Leeming (1995) took the bias limit for the uncertainty of the fractional penetration to be the uncertainty in the calibration of the luminescence spectrometer, but found this bias limit to be negligible. The bias limits for the fractional penetration and luminosity readings were therefore assumed negligible. The accuracy of the Druck DPI 610 pressure calibrator was 0.025 % of its full-scale deflection, which was 20 bar, so the bias limit for the pressure measurement was taken as 500 Nm^{-1}. The bias limit of the temperature measurement was taken as 2.5 K (see section 4.2.4).

C.3 Uncertainty for particle deposition in an isothermal turbulent annulus

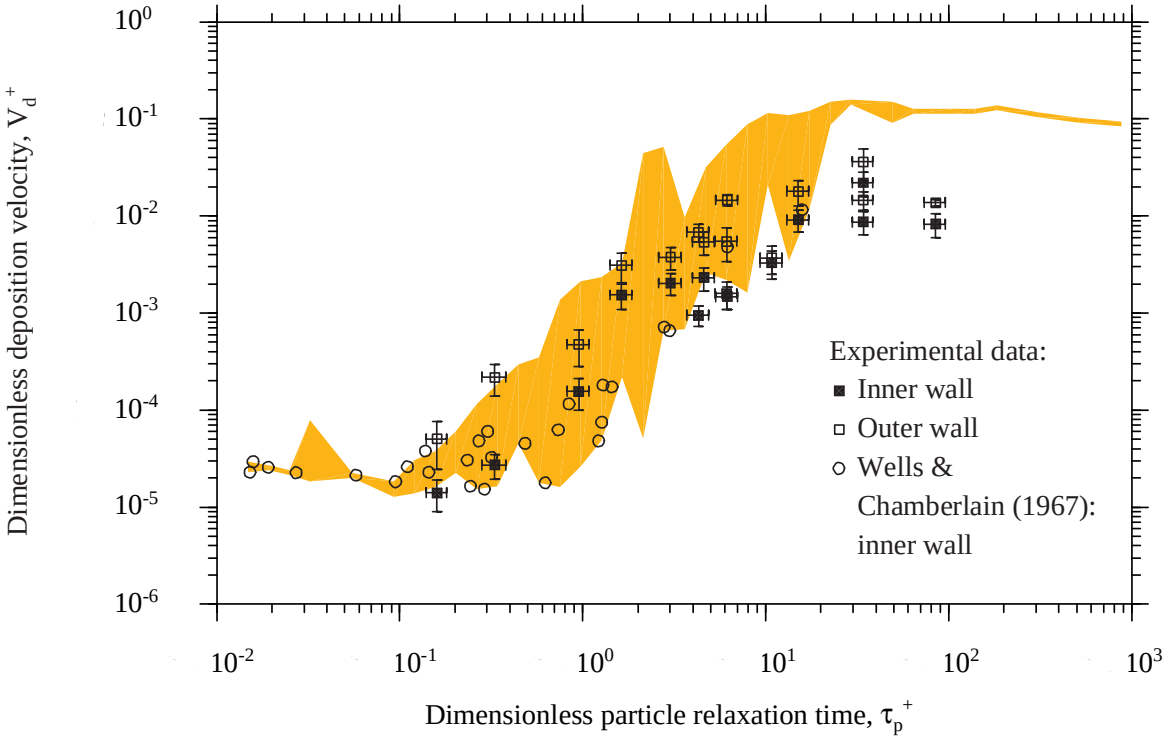

Figure C.1: Results for the isothermal experiments in turbulent annular flow with d_p found by measuring the particles impacted on a slide (with uncertainty level indicators)

Run Name	d_p calculated (μm)	Orifice size (μm)	Frequency (kHz)	d_p observed (μm)	Q_{ind} (lpm)	τ_p^+	$(V_d^+)_i$	$(V_d^+)_o$	Sc	$(\tau_p^+/Sc^2)^{1/3}$
annu5	1.20	10	50.00	1.20	170	0.16±0.02	(1.407±0.51)x10^{-5}	(5.034±2.58)x10^{-5}	7.77x10^5	6.37x10^{-5}
annu4	1.85	10	200.00	1.75	170	0.33±0.05	(2.710±0.77)x10^{-5}	(2.173±0.79)x10^{-4}	1.20x10^6	6.12x10^{-5}
annu3	2.96	10	250.00	3.10	170	0.95±0.13	(1.556±0.56)x10^{-4}	(4.748±1.95)x10^{-4}	1.92x10^6	6.37x10^{-5}
annu7	16.13	20	50.00	4.40	140	1.63±0.22	(1.532±0.44)x10^{-3}	(3.108±1.05)x10^{-3}	1.05x10^7	2.45x10^{-5}
annu2	18.88	20	50.00	5.28	170	3.02±0.42	(2.031±0.51)x10^{-3}	(3.759±0.98)x10^{-3}	1.22x10^7	2.72x10^{-5}
annu10	6.40	10	200.10	6.16	170	4.29±0.59	(9.503±2.26)x10^{-4}	(6.819±1.39)x10^{-3}	4.07x10^6	6.37x10^{-5}
annu12	13.70	35	29.50	6.30	170	4.59±0.63	(2.313±0.62)x10^{-3}	(5.399±1.47)x10^{-3}	8.63x10^6	3.95x10^{-5}
annu8	8.17	20	45.02	7.48	170	6.11±0.84	(1.586±0.50)x10^{-3}	(5.467±2.06)x10^{-3}	5.31x10^6	6.01x10^{-5}
annu11	13.33	35	32.04	7.12	170	6.15±0.84	(1.476±0.38)x10^{-3}	(5.301±1.89)x10^{-3}	8.23x10^6	4.49x10^{-5}
annu13	9.56	35	29.11	9.72	170	10.81±1.48	(3.298±1.07)x10^{-3}	(3.707±1.21)x10^{-3}	6.06x10^6	6.65x10^{-5}
annu1	11.78	20	50.00	11.78	170	15.06±2.07	(9.113±2.28)x10^{-3}	(1.801±0.53)x10^{-2}	7.63x10^6	6.37x10^{-5}
inert3	17.29	20	45.04	17.29	170	32.43±4.45	(8.681±2.33)x10^{-3}	(1.459±0.30)x10^{-2}	1.12x10^7	6.37x10^{-5}
inert4	17.29	20	45.03	17.29	170	32.43±4.45	(2.201±0.62)x10^{-2}	(3.632±1.32)x10^{-2}	1.12x10^7	6.37x10^{-5}
inert5	27.34	35	36.99	27.34	170	81.09±11.13	(8.230±2.28)x10^{-3}	(1.368±0.11)x10^{-2}	1.12x10^7	6.37x10^{-5}

Table C.1: A summary of the results, uncertainties and experimental conditions of the isothermal experiments

C.4 Results from the thermophoresis experiments

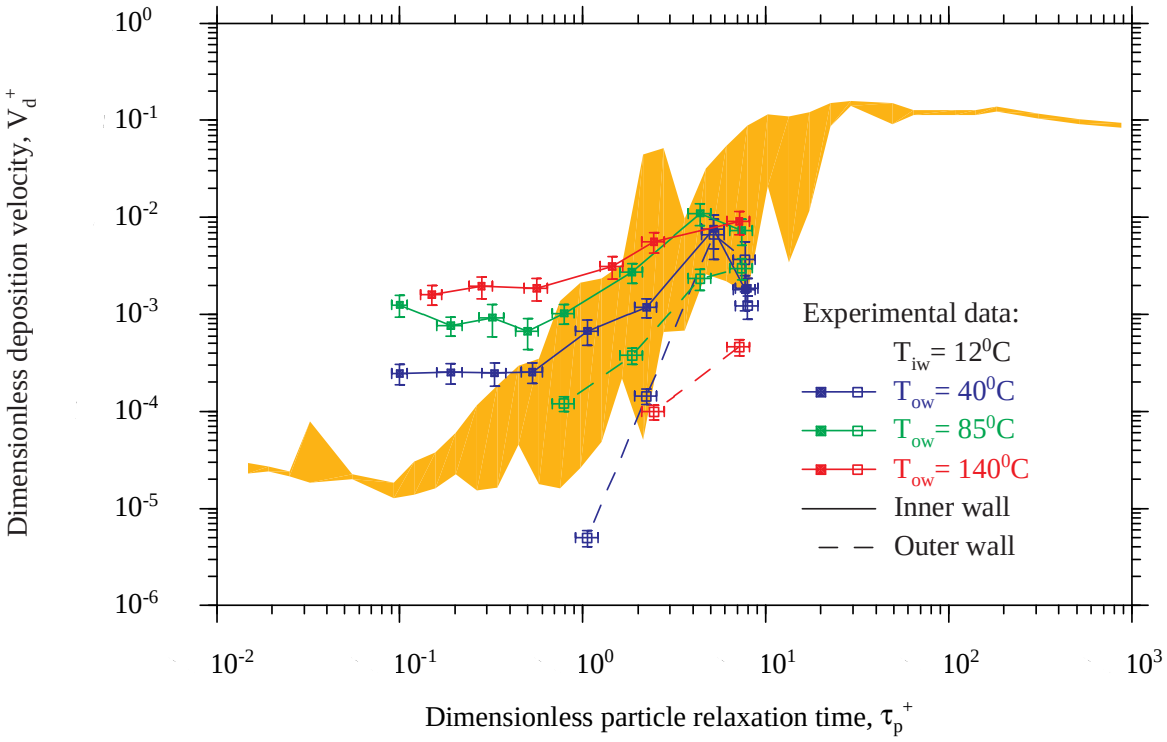

Figure C.2: Results for the thermophoresis experiments in turbulent annular flow with uncertainty level indicators

Run Name	d_p calculated (μm)	Orifice size (μm)	Frequency (kHz)	d_p observed (μm)	Q_{ind} (lpm)	τ_p^+	$(V_d^+)_i$	$(V_d^+)_o$	Sc	$(\tau_p^+/Sc^2)^{1/3}$
thermo6	1.07	10	201000.00	1.07	140	0.10±0.01	(2.468±0.60)x10^{-4}		7.04x10^5	5.93x10^{-5}
thermo1	1.46	10	201400.00	1.46	140	0.19±0.03	(2.521±0.60)x10^{-4}		9.58x10^5	5.92x10^{-5}
thermo5	1.94	10	200800.00	1.94	140	0.33±0.05	(2.478±0.66)x10^{-4}		1.31x10^6	5.75x10^{-5}
thermo3	2.42	10	201200.00	2.42	140	0.53±0.07	(2.544±0.61)x10^{-4}		1.59x10^6	5.94x10^{-5}
thermo4	3.04	10	202200.00	3.49	140	1.06±0.15	(6.742±1.94)x10^{-4}	(4.987±0.97)x10^{-6}	2.06x10^6	6.31x10^{-5}
thermo14	4.97	10	200200.00	4.97	140	2.23±0.31	(1.185±0.27)x10^{-3}	(1.431±0.26)x10^{-4}	3.23x10^6	5.98x10^{-5}
thermo15	7.59	10	200200.00	7.59	140	5.19±0.72	(7.616±2.90)x10^{-3}	(6.643±2.97)x10^{-3}	4.98x10^6	5.93x10^{-5}
thermo17	9.20	20	45000.00	9.20	140	7.71±1.07	(1.800±0.72)x10^{-3}	(3.652±1.94)x10^{-3}	6.08x10^6	5.93x10^{-5}
thermo18	9.23	10	200100.00	9.35	140	7.95±1.10	(1.856±0.50)x10^{-3}	(1.227±0.33)x10^{-3}	6.22x10^6	5.89x10^{-5}
thermo16	12.64	20	49980.00	5.34	140	2.58±0.36	(1.544±0.41)x10^{-3}	(1.092±0.28)x10^{-3}	8.25x10^6	3.36x10^{-5}

Table C.2: A summary of the results, uncertainties and experimental conditions of the thermophoresis experiments with $T_{ow,nom} = 40°$C

Run Name	d_p calculated (μm)	Orifice size (μm)	Frequency (kHz)	d_p observed (μm)	Q_{ind} (lpm)	τ_p^+	$(V_d^+)_i$	$(V_d^+)_o$	Sc	$(\tau_p^+/Sc^2)^{1/3}$
thermo10	1.07	10	200500.00	1.07	140	0.10±0.01	(1.252±0.32)x10^{-3}		7.85x10^5	5.47x10^{-5}
thermo9	1.46	10	200500.00	1.46	140	0.19±0.03	(7.639±1.71)x10^{-4}		1.07x10^6	5.49x10^{-5}
thermo8	1.94	10	200800.00	1.94	140	0.32±0.05	(9.275±3.45)x10^{-4}		1.46x10^6	5.31x10^{-5}
thermo7	2.42	10	200800.00	2.42	140	0.50±0.07	(6.668±2.35)x10^{-4}		1.81x10^6	5.35x10^{-5}
thermo11	3.04	10	200500.00	3.04	140	0.79±0.11	(1.024±0.23)x10^{-3}	(1.203±0.21)x10^{-4}	2.27x10^6	5.37x10^{-5}
thermo12	4.96	10	200500.00	4.96	150	1.86±0.26	(2.712±0.63)x10^{-3}	(3.766±0.71)x10^{-4}	3.63x10^6	5.20x10^{-5}
thermo13	7.59	10	200100.00	7.59	150	4.38±0.62	(1.098±0.28)x10^{-2}	(2.334±0.56)x10^{-3}	5.53x10^6	5.23x10^{-5}
thermo24	9.90	20	45010.00	9.90	150	7.39±1.04	(7.331±2.18)x10^{-3}	(2.984±0.73)x10^{-3}	7.14x10^6	5.25x10^{-5}

Table C.3: A summary of the results, uncertainties and experimental conditions of the thermophoresis experiments with $T_{ow,nom} = 85°$C

Run Name	d_p calculated (μm)	Orifice size (μm)	Frequency (kHz)	d_p observed (μm)	Q_{ind} (lpm)	τ_p^+	$(V_d^+)_i$	$(V_d^+)_o$	Sc	$(\tau_p^+/Sc^2)^{1/3}$
thermo21	1.43	10	200300.00	1.43	150	0.15±0.02	(1.604±0.37)x10^{-3}		1.19x10^6	4.73x10^{-5}
thermo19	1.94	10	200100.00	1.94	150	0.28±0.04	(1.943±0.49)x10^{-3}		1.58x10^6	4.80x10^{-5}
thermo20	2.77	10	200100.00	2.77	150	0.56±0.08	(1.865±0.48)x10^{-3}		2.31x10^6	4.72x10^{-5}
thermo22	4.44	10	200100.00	4.44	150	1.45±0.20	(3.129±0.84)x10^{-3}		3.64x10^6	4.78x10^{-5}
thermo23	6.02	10	200100.00	5.78	150	2.45±0.35	(5.614±1.36)x10^{-3}	(9.924±1.70)x10^{-5}	4.93x10^6	4.65x10^{-5}
thermo25	9.90	20	45010.00	9.90	150	7.17±1.01	(9.047±2.47)x10^{-3}	(4.603±0.88)x10^{-4}	7.96x10^6	4.83x10^{-5}
thermo26	14.59	20	45060.00	4.32	150	1.37±0.19	(5.936±1.48)x10^{-3}	(1.634±0.36)x10^{-3}	1.17x10^7	2.15x10^{-5}

Table C.4: A summary of the results, uncertainties and experimental conditions of the thermophoresis experiments with $T_{ow,nom} = 140°$C

Appendix D

Supplementary information to chapter 7

D.1 Turbulent annulus fluid flow solver

In order to solve the particle equations of motion, the fluid flow field must first be known. This section describes the manner in which the turbulent flow of air in an annulus was prescribed.

D.1.1 Momentum equation

In a fully-developed annular flow with constant density, continuity dictates that:

$$\overline{U}_r = 0 \qquad \frac{\partial \overline{U}_z}{\partial z} = 0 \qquad \overline{U}_z = \overline{U}_z(r) \tag{D.1}$$

where $\overline{U}$ is the time-mean fluid velocity in the radial (r) or axial (z) direction. Only the axial component of the momentum equation need be considered, and this reduces to:

$$-\frac{dp}{dz} + \frac{1}{r}\frac{d}{dr}\left[r(\mu_g + \mu_{g,T})\frac{d\overline{U}_z}{dr}\right] = 0 \tag{D.2}$$

where dp/dz is the pressure gradient along the annulus, and $\mu_{g,T}$ is the turbulent (or eddy) dynamic viscosity, defined by the relationship:

$$-\rho_g \overline{u_r' u_z'} = \mu_{g,T}\frac{\partial \overline{U}_z}{\partial r} \tag{D.3}$$

From equations 4.8 and 4.9:

$$\overline{\tau}_w = \rho_g u_*^2 = \frac{r_i\tau_{w,i} - r_o\tau_{w,o}}{r_o + r_i} = \frac{(r_o - r_i)}{2}\left(-\frac{dp}{dz}\right) \tag{D.4}$$

Non-dimensionalisation is carried out using the following variables:

$$r_{avg} = \frac{r_i + r_o}{2} \qquad r^A = \frac{r}{r_{avg}} \qquad y^A = \frac{r - r_i}{r_o - r_i} \qquad \nu^+_{g,T} = \frac{\nu_{g,T}}{\nu_g}$$

$$\overline{U}^A_z = \frac{\overline{U}_z}{U_m} \qquad \mu^A_g = \frac{\mu_g}{\mu_{g,m}} \qquad Re = \frac{\rho_g U_m 2(r_o - r_i)}{\mu_{g,m}} \qquad C_{f,i/o} = \frac{\tau_{w,i/o}}{\frac{1}{2}\rho_g U^2_m}$$

where $C_{f,i/o}$ is the skin friction coefficient at the inner or outer wall, $\mu_{g,m}$ is the mean dynamic eddy viscosity across the annulus, and the bulk mean velocity of the flow is given by:

$$U_m = \frac{2}{r^2_o - r^2_i} \int_{r_i}^{r_o} \overline{U}_z r dr \tag{D.5}$$

The radius r varies from r_i to r_o, so that y^A varies from 0 at the inner wall to 1 at the outer wall. Inserting equation D.4 into equation D.2 and non-dimensionalising gives:

$$r^A \frac{Re}{4}(r^A_i C_{f,i} - r^A_o C_{f,o}) + \frac{d}{dy^A}\left[r^A \mu^A_g (1 + \nu^+_{g,T}) \frac{d\overline{U}^A_z}{dy^A}\right] = 0 \tag{D.6}$$

By setting $b = r^A \mu^A_g (1+\nu^+_{g,T})$ and $\phi = \frac{d\overline{U}^A_z}{dy^A}$, the result is a system of two first-order equations. If the eddy viscosity profile is known, the resulting finite-difference equations can be written in matrix-vector form, and solved for the velocity profile using the block-tridiagonal-elimination method (see Cebeci & Bradshaw, 1984, chapter 13).

It is the flow field at a given Reynolds number that is required and the skin friction coefficients (from which the pressure gradient can be found) are unknown. Initially, $\nu^+_{g,T}$ is set equal to zero, $C_{f,i}$ and $C_{f,o}$ are found using the correlation of Jones & Leung (1981) (see equation 4.11), and an initial profile of $\overline{U}^A_z(y^A)$ is found. $\nu^+_{g,T}$ is then modelled (as described below), and an iterative procedure begins, where the velocity field is corrected by the pressure gradient, through the adjustment of $C_{f,i}$ and $C_{f,o}$, until $\overline{U}^A_m = 1$.

D.1.2 Energy equation

The temperature field in a turbulent annular flow can be said to be fully-developed when the dimensionless temperature T^A, defined by:

$$T^A = \frac{T - T_i}{T_o - T_i} \tag{D.7}$$

is independent of axial position (z) and depends only on radial position (r). The energy equation in a fully-developed annular flow with constant density reduces to:

$$r \rho_g \overline{U}_z c_p \frac{\partial \overline{T}}{\partial z} = \frac{\partial}{\partial r}\left[r(k_g + k_{g,T}) \frac{\partial \overline{T}}{\partial r}\right] \tag{D.8}$$

where c_p is the specific heat capacity of the gas, and k_g is the thermal conductivity of the gas, and $k_{g,T}$ is the turbulent (or eddy) conductivity, given by:

$$-\rho_g c_p \overline{u_r' T'} = k_{g,T} \frac{\partial \overline{T}}{\partial r} \tag{D.9}$$

Some additional dimensionless groups are:

$$Pr = \frac{c_{p,m}\mu_g}{k_g} \qquad Pr_T = \frac{c_{p,m}\mu_{g,T}}{k_{g,T}} \qquad c_p^A = \frac{c_p}{c_{p,m}} \tag{D.10}$$

where Pr and Pr_T are the Prandtl and turbulent Prandtl numbers respectively, and $c_{p,m}$ is the mean value of c_p across the annulus. The dimensionless form of equation D.8 is:

$$\frac{\partial}{\partial y}\left[r^A c_p^A \mu_g^A \left(\frac{1}{Pr} + \frac{\nu_{g,T}^+}{Pr_T} \right) \frac{\partial \overline{T}^A}{\partial y} \right] = 0 \tag{D.11}$$

Closure of this equation requires models for $\nu_{g,T}^+$ and Pr_T.

D.1.3 Turbulence modelling

Solution of the momentum and energy equations requires models for $\nu_{g,T}^+$ and Pr_T, and the solution of the particle equations also requires a model for $\overline{u_y'^+ u_y'^+}^{1/2}$.

Eddy viscosity

The eddy viscosity model is based on a form suggested by Michiyoshi & Nakajima (1968) which divides the flow cross-section into four regimes: a sublayer at the inner and outer annulus walls (denoted by $_{is}$ and $_{os}$), and a turbulent core region between each sublayer and the plane of zero shear (denoted by $_{ic}$ and $_{oc}$).

In each sublayer, the form of $\nu_{g,T}^+$ is based on a modified van Driest mixing length formula proposed by Granville (1990):

$$(\nu_{g,T}^+)_{is} = \kappa_i y^+ \left(1 - exp\left[-\left(\frac{y^+}{A^+} \right)^2 \right] \right) \tag{D.12a}$$

$$(\nu_{g,T}^+)_{os} = \kappa_o (a^+ - y^+) \left(1 - exp\left[-\left(\frac{a^+ - y^+}{A^+} \right)^2 \right] \right) \tag{D.12b}$$

where $y^+ = (r - r_i)u_*/\nu_g$. r is measured from the inner wall and varies between r_i and r_o, so that y^+ varies from 0 at the inner wall to a^+ (the dimensionless gap width) at the outer wall. $A^+ = 26$ (the value usually chosen), and the von Kármán constant, $\kappa_{i/o}$, for each wall

is chosen as 0.4, although some models assign different values to each wall (e.g. Michiyoshi & Nakajima, 1968; Azouz & Shirazi, 1997). This ensures that $\nu^+_{g,T}$ varies with y^{+3} near the wall (Chapman & Kuhn, 1986).

The expression of Michiyoshi & Nakajima (1968) for the inner turbulent core region is applied to both turbulent core regions with some modifications:

$$(\nu^+_{g,T})_{ic} = \frac{u_{*,o}}{u_*}\frac{r^+_o - r^+_{zs}}{15}(1-\eta_i^2)(1+2\eta_i^2)\left[1-\left(1-\frac{s_*}{\sqrt{\tau_*}})\right)\eta_i\right] \quad \text{(D.13a)}$$

$$(\nu^+_{g,T})_{oc} = \frac{u_{*,o}}{u_*}\frac{r^+_o - r^+_{zs}}{15}(1-\eta_o^2)(1+2\eta_o^2) \quad \text{(D.13b)}$$

where $\eta_i = \dfrac{r^+_{zs}-r^+}{r^+_{zs}-r^+_i}$, $\eta_o = \dfrac{r^+-r^+_{zs}}{r^+_o-r^+_{zs}}$; $s_* = \dfrac{r^+_{zs}-r^+_i}{r^+_o-r^+_{zs}}$ and $\tau_* = \dfrac{\tau_{w,o}}{\tau_{w,i}}$

where $r^+ = ru_*/\nu_g$, and r_{zs} is the radius of the plane of zero shear. When $r^+ = r^+_{zs}$, $(\nu^+_{g,T})_{ic} = (\nu^+_{g,T})_{oc}$. The blending relation of Granville (1990) is used to join each sublayer and turbulent core expression, such that:

$$(\nu^+_{g,T})_i = (\nu^+_{g,T})_{ic}\text{tanh}\frac{(\nu^+_{g,T})_{is}}{(\nu^+_{g,T})_{ic}} \quad \text{and} \quad (\nu^+_{g,T})_o = (\nu^+_{g,T})_{oc}\text{tanh}\frac{(\nu^+_{g,T})_{os}}{(\nu^+_{g,T})_{oc}} \quad \text{(D.14)}$$

where the subscripts i and o apply to the regions between the inner and outer walls and the radius of zero shear, respectively. The dependence of Γ on $\nu_{g,T}$ through τ_g, means that the profile of $\nu^+_{g,T}$ must be twice differentiable. Smooth derivatives at the radius of zero shear are enforced, by 'cutting-off' $(\nu^+_{g,T})_i$ and $(\nu^+_{g,T})_o$ at positions a small distance either side of the plane of zero shear, and connecting these two profiles with a function that has the same values of $\nu^+_{g,T}$ (and its first and second derivatives) at the 'cut-off' points.

Turbulent Prandtl number

Silva *et al.* (1999) and Kays (1994) have compared a number of different theories with DNS and experimental data for Pr_T. The evidence indicates that, for air, $0.9 < Pr_T < 1.5$ in the near-wall region, and Pr_T decreases to a value of approximately 0.9 in the core of the flow. The model of Wassel & Catton (1973) (from Silva *et al.*, 1999) followed this behaviour, and takes the form:

$$Pr_T = \frac{C_3\left[1-exp\left(\frac{-C_4}{\nu^+_{g,T}}\right)\right]}{C_1 Pr\left[1-exp\left(\frac{-C_2}{Pr\nu^+_{g,T}}\right)\right]} \quad \text{(D.15)}$$

where C_1=0.21, C_2=5.25, C_3=0.2 and C_4=5.0.

Radial rms fluctuating fluid velocity

The chosen model is very similar in form to that used by Young & Leeming (1997) and, as with the eddy viscosity model, the flow is split into four regimes. In the sublayer:

$$(\overline{u_y'^+ u_y'^+}^{1/2})_{is} = \alpha y^+ \left[1 - exp\left(-\frac{y^+}{\beta}\right)\right] \tag{D.16a}$$

$$(\overline{u_y'^+ u_y'^+}^{1/2})_{os} = \alpha(a^+ - y^+) \left[1 - exp\left(-\frac{(a^+ - y^+)}{\beta}\right)\right] \tag{D.16b}$$

α=0.0373 (the value used by Young & Leeming (1997)), and $\beta = \alpha/0.008$ results in $\overline{u_y'^+ u_y'^+}^{1/2}$ varying with $0.008y^{+2}$ near the wall. In the core:

$$(\overline{u_y'^+ u_y'^+}^{1/2})_{ic} = \delta + (\gamma_i - \delta)\left[1 - \frac{2}{\pi}\text{arctan}\left(\left[\frac{y^+}{y_{zs}^+ - y^+}\right]^2\right)\right] \tag{D.17a}$$

$$(\overline{u_y'^+ u_y'^+}^{1/2})_{oc} = \delta + (\gamma_o - \delta)\left[1 - \frac{2}{\pi}\text{arctan}\left(\left[\frac{(a^+ - y^+)}{y_{zs}^+ - y^+}\right]^2\right)\right] \tag{D.17b}$$

where γ_i and γ_o are the values of $\overline{u_y'^+ u_y'^+}^{1/2}$ at y^+ and $(a^+ - y^+) \approx 50$, and δ is the value of $\overline{u_y'^+ u_y'^+}^{1/2}$ in the core of the flow. y_{zs}^+ is the distance of the plane of zero shear from the inner wall, non-dimensionalised using wall units.

Again, a blending relation is used to join each sublayer and turbulent core expression:

$$(\overline{u_y'^+ u_y'^+}^{1/2})_i = (\overline{u_y'^+ u_y'^+}^{1/2})_{ic} \text{tanh} \frac{(\overline{u_y'^+ u_y'^+}^{1/2})_{is}}{\epsilon(\overline{u_y'^+ u_y'^+}^{1/2})_{ic}} \tag{D.18a}$$

$$(\overline{u_y'^+ u_y'^+}^{1/2})_o = (\overline{u_y'^+ u_y'^+}^{1/2})_{oc} \text{tanh} \frac{(\overline{u_y'^+ u_y'^+}^{1/2})_{os}}{\epsilon(\overline{u_y'^+ u_y'^+}^{1/2})_{oc}} \tag{D.18b}$$

where ϵ is a new constant to help capture experimental and DNS behaviour between the sublayer and core more accurately. The two blending relations meet smoothly at the radius of zero shear, where $\overline{u_y'^+ u_y'^+}^{1/2} \approx \delta$, so that even though $\overline{u_y'^+ u_y'^+}^{1/2}$ must be twice differentiable, there was no need to enforce this in the same manner as for $\nu_{g,T}^+$.

D.2 Validation of the fluid flow solver

Table D.1 compares some results of the fluid flow solver under isothermal conditions, with the radius ratio and Re set to match experimental data of Nouri *et al.* (1993) and the DNS data of Chung *et al.* (2002) for a turbulent annulus. Figures D.1a and D.1b show that the agreement between calculated values of axial velocity and Reynolds shear stress, and experimental/DNS data is excellent. Figures D.1c and D.1d plot the same quantities but with distance from the

wall on a log-scale, and the agreement is also good. Figure D.2 shows how the model for the fluctuating fluid radial velocity fits to given DNS data when adjusted through ϵ, $\gamma_{i/o}$ and δ.

Figures D.3a and D.3b show DNS and experimental data for $\overline{u_r' u_z'}$ and $\overline{u_r' u_r'}^{1/2}$ for pipe, channel and annulus flows over a range of Reynolds numbers. The aim of these figures is to show that evidence exists for a Re dependence of these quantities at small values of Re (see Manna & Vacca (2001) for a detailed study of this dependence). This establishes the uncertainty in the prescription of these quantities (due to Re and geometry), and the need for the sensitivity study to changes in these quantities carried out in chapter 7.

Table D.2 shows the conditions used by the fluid flow solver to match experimental conditions. Pr_T has been shown to agree with the DNS data of Kasagi *et al.* (1992). Figure D.4 shows the variation of the inner and outer wall temperatures compared with the universal profile in the sublayer, $\overline{\theta}^+ = Pry^+$. In studies of heat transfer in channel flows, $\overline{\theta}^+$ represents a local temperature difference $(T_w - T)$ non-dimensionalised using the friction temperature, $T_* = q_w/(\rho_g c_p u_*)$, where q_w (in $\mathrm{Wm^{-2}K^{-1}}$) is the time-averaged wall heat flux. In figure D.4, inner and outer non-dimensionalisation is required, such that:

$$\overline{\theta}_i^+ = \left| \frac{(T_{iw} - T)\rho_g c_p u_*}{q_{w,i}} \right| \qquad \text{and} \qquad \overline{\theta}_o^+ = \left| \frac{(T_{ow} - T)\rho_g c_p u_*}{q_{w,o}} \right| \tag{D.19}$$

It should be noted that in a channel flow, q_w is the same at either wall, but that for an annulus, the change in surface area between the inner radius and outer radius means that $q_{w,i} \neq q_{w,o}$.

	Nouri *et al.* (1993)	Chung *et al.* (2002)	Present study
Re	8900	8900	8900
a^+	-	297	296
r_i/r_o	0.5	0.5	0.5
$C_{f,i}$x10^{-3}	10.38	9.41	9.31
$C_{f,o}$x10^{-3}	10.38	8.49	8.41

Table D.1: Comparison of results found using annular flow solver with DNS and experimental data

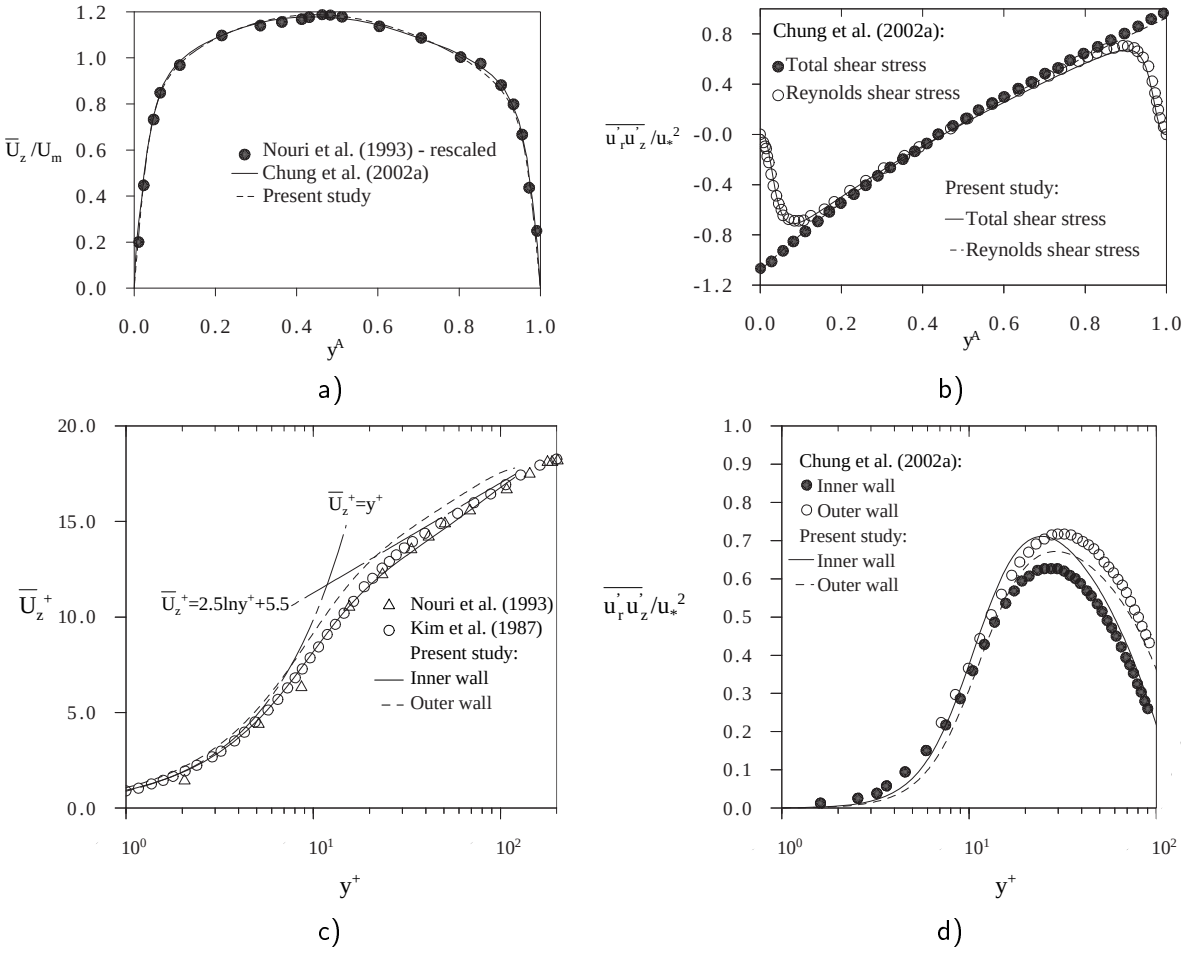

Figure D.1: Comparison of calculated mean fluid velocity and fluid fluctuating velocity correlations with DNS and experimental data with Re = 8900

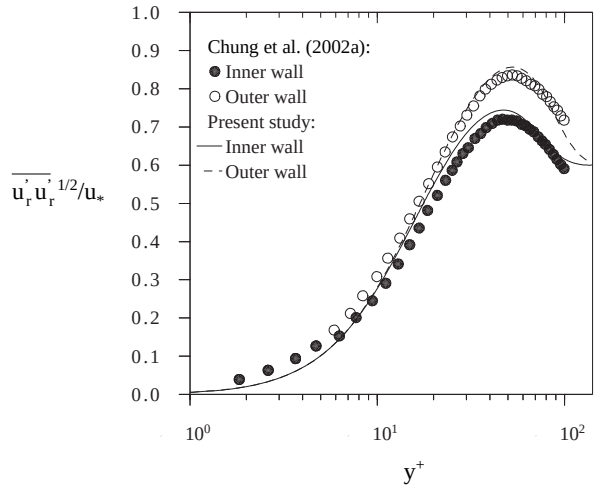

Figure D.2: Fluid fluctuating velocity in the radial direction adjusted to fit DNS data with Re = 8900

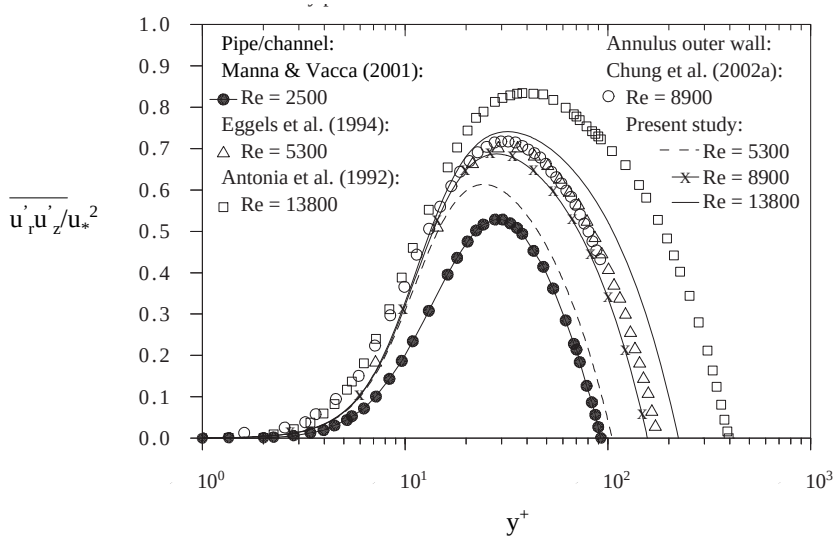

a)

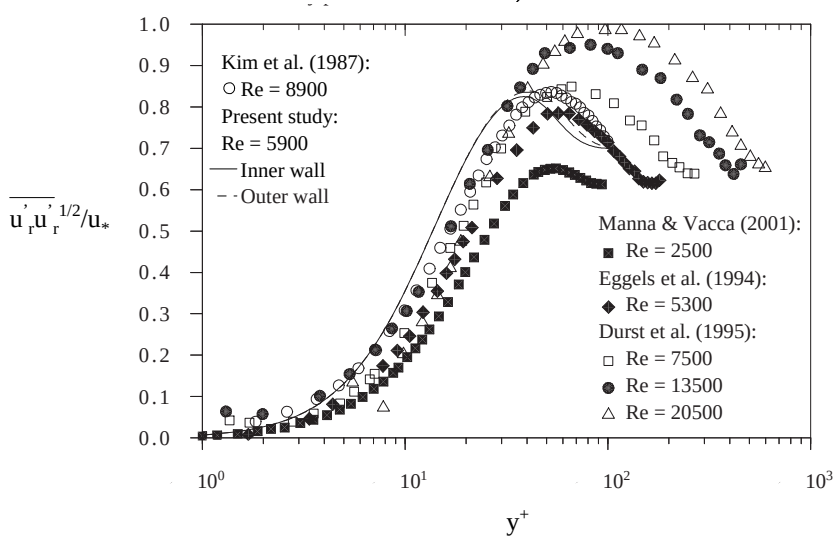

b)

Figure D.3: Comparison of fluid fluctuating velocity correlations with DNS and experimental data showing Re dependancy

	Isothermal	$T_{ow,nom} = 40°C$	$T_{ow,nom} = 85°C$	$T_{ow,nom} = 140°C$
Re	5900	4800	4500	4200
y^+	214	181	170	158
r^*	0.65	0.65	0.65	0.65
$C_{f,i}$x10^{-3}	11.02	12.44	13.15	13.91
$C_{f,o}$x10^{-3}	10.11	10.99	11.06	11.13
T_{ow}	293K	310K	350K	395K
T_{iw}	293K	285K	285K	285K

Table D.2: Details of numerical conditions to match experiments

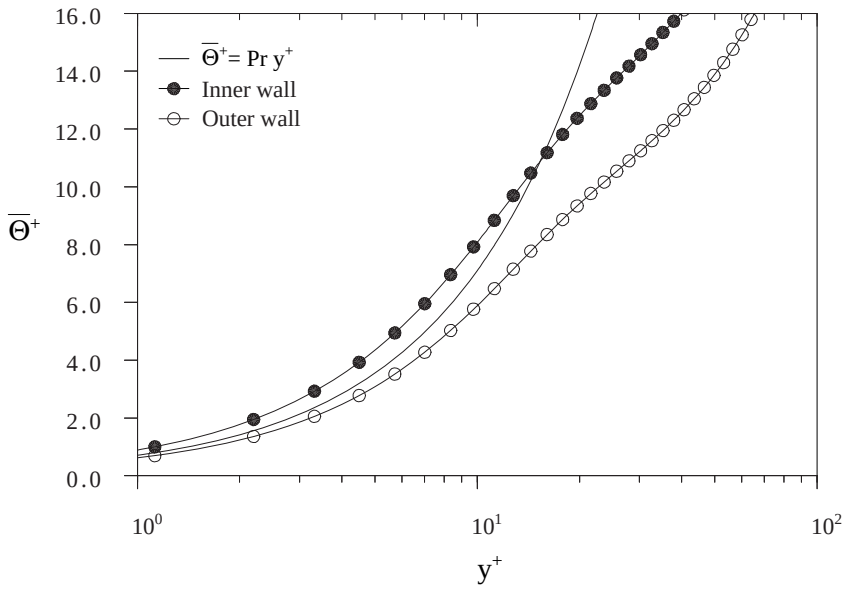

Figure D.4: Comparison of non-dimensional temperature profiles at each wall with the universal profile

D.3 Polynomial coefficients for fitting to the expression of Beresnev & Chernyak (1995)

The expression of Beresnev & Chernyak (1995) requires coefficients found from the kinetic equations. These were given in tabular form for specific values of Kn, and in between these values, some sort of interpolation is required. A different polynomial was fitted to the kinetic equation coefficients for different ranges of Kn. The polynomial was of the form:

$$f_{kj} = ax^6 + bx^5 + cx^4 + dx^3 + ex^2 + fx^1 + gx^0 \tag{D.20}$$

where the constants are given in table D.3.

	a	b	c	d	e	f	g
$Kn < 10^{-2}$							
f11	-4.8x10^{7}	1.0x10^{6}	-17448.0	121.91	-10.745	5.0x10^{-4}	- 2.0x10^{-7}
f21	-613.0	-201.27	12.212	0.9333	1.0x10^{-5}	-7.0x10^{-9}	2.0x10^{-12}
f41	3.0x10^{6}	- 2.0x10^{9}	4.0x10^{7}	-340371.0	1515.3	-6.8387	-0.998
$10^{-2} < Kn < 10^{-1}$							
f11	2040.3	-290.97	22.789	-10.503	-7.0x10^{-4}	1.0x10^{-5}	0
f21	-300.66	310.49	-113.32	10.681	-0.3548	0.0059	- 3.0x10^{-5}
f41	101488.0	-53444.0	10462.0	- 936.31	41.58	- 4.7178	- 0.9948
$10^{-1} < Kn < 10^{0}$							
f11	9.6226	-26.416	26.797	-11.84	0.0431	6.0x10^{-4}	0
f21	-8.7993	22.358	- 18.731	3.0629	- 0.1951	0.0046	0
f41	- 6.0197	15.502	- 15.884	10.079	-5.0632	- 0.9516	0
$Kn > 10^{0}$							
f11	2.0x10^{-5}	-8.0x10^{-4}	0.0177	- 0.1791	0.9206	-2.3861	0.0195
f21	-3.0x10^{-5}	0.0015	-0.0319	0.3166	-1.5624	- 2.2284	0.9817
f41	8.0x10^{-7}	-6.0x10^{-5}	0.0018	-0.0265	0.1962	-0.6987	-1.9209

Table D.3: Coefficients of polynomial fits to kinetic equation coefficients of Beresnev & Chernyak (1995)

Bibliography

Al-Azzawi, H.K., & Owen, I. 1984. Measuring the thermal conductivity of uranin. *Int. J. Heat & Fluid Flow*, **5**(1), 57–59.

Andreussi, P. 1983. Droplet transfer in two-phase annular flow. *Int. J. Multiphase Flow*, **9**(6), 697–713.

Azouz, I., & Shirazi, S.A. 1997. Numerical simulation of drag reducing turbulent flow in annular conduits. *J. Fluids Eng.*, **119**, 838–846.

Bakanov, S.P. 1991. Thermophoresis in gases at small Knudsen numbers. *Aerosol Sci. Technol.*, **15**, 77–92.

Bakanov, S.P. 1992. What kind of experiments are needed today on the thermophoresis of aerosols, and why? English Translation of *Kolloidnyi Zhurnal*, **54**(5), 39–42. (English pages: 679-681).

Bakanov, S.P., & Roldugin, V.I. 1977. Two methods for development of the theory of thermophoresis of large aerosol particles. English Translation of *Kolloidnyi Zhurnal*, **39**(6), 1027–1038. (English pages: 907-917).

Batchelor, G.K, & Shen, C. 1985. Thermophoretic deposition of particles in gas flowing over cold surfaces. *J. Colloid Interface Sci.*, **107**(1), 21–37.

Beresnev, S., & Chernyak, V. 1995. Thermophoresis of a spherical particle in a rarefied gas: Numerical analysis based on the model kinetic equations. *Phys. Fluids*, **7**(7), 1743–1756.

Berglund, R.N., & Liu, B.Y.H. 1973. Generation of monodisperse aerosol standards. *Environ. Sci. Technol.*, **7**, 147–153.

Biodata Ltd. 1986. *Microlink Hardware User Manual, Issue MH-11-08-86*. 10 Stocks Street, Manchester, Greater Manchester, M8 8RQ, UK.

Brighton, J.A., & Jones, J.B. 1964. Fully developed turbulent flow in annuli. *J. Basic Eng.*, 835–844.

Brock, J.R. 1962. On the theory of thermal forces acting on aerosol particles. *J. Colloid Sci.*, **17**, 768–780.

Brooke, J.W., Kontomaris, K., Hanratty, J.B., & McLaughlin, J.B. 1992. Turbulent deposition and trapping of aerosols at a wall. *Phys. Fluids A*, **4**(4), 825–834.

Brooke, J.W., Hanratty, J.B., & McLaughlin, J.B. 1994. Free-flight mixing and deposition of aerosols. *Phys. Fluids*, **6**(10), 3404–3415.

Byers, R.L., & Calvert, S. 1969. Particle deposition from turbulent streams by means of thermal force. *I & EC Fundam.*, **8**(4), 646–655.

Caporaloni, M., Tampieri, F., Trombetti, F., & Vittori, O. 1975. Transport of particles in nonisotropic air turbulence. *J. Atmos. Sci.*, **32**, 565–568.

Cebeci, T., & Bradshaw, P. 1984. *Physical and computational aspects of convective heat transfer*. Springer-Verlag.

Cerbelli, S., Giusti, A., & Soldati, A. 2001. ADE approach to predicting dispersion of heavy particles in wall-bounded turbulence. *Int. J. Multiphase Flow*, **27**, 1861–1879.

Cha, C.Y., & McCoy, B.J. 1974. Thermal force on aerosol particles. *Phys. Fluids*, **17**(7), 1376–1380.

Chapman, D.R., & Kuhn, G.D. 1986. The limiting behaviour of turbulence near a wall. *J. Fluid Mech.*, **170**, 265–292.

Chen, C., Riley, J.J., & McMurtry, P.A. 1991. A study of Favre averaging in turbulent flows with chemical reaction. *Combustion and Flame*, **87**, 257–277.

Chen, S.H. 1999. Thermophoretic deposition of a sphere normal to a plane surface. *Aerosol Sci. Technol.*, **30**, 364–382.

Chen, X., & Xu, D. 2002. Thermophoresis of a near-wall particle at great Knudsen numbers. *Aerosol Sci. Technol.*, **36**, 39–47.

Chiou, M.C., & Cleaver, J.W. 1996. Effect of thermophoresis on sub-micron particle deposition from a laminar forced convection boundary layer onto an isothermal cylinder. *J. Aerosol Sci.*, **27**(8), 1155–1167.

Chordá, R., Blasco, J.A., & Fueyo, N. 2002. An efficient particle-locating algorithm for application in arbitrary 2D and 3D grids. *Int. J. Multiphase Flow*, **28**, 1565–1580.

Chung, S.Y., Rhee, G.H., & Sung, H.J. 2002. Direct numerical simulation of turbulent concentric annular pipe flow - Part 1: Flow field. *Int. J. Heat Fluid Flow*, **23**, 426–440.

Crowe, C.T. 1982. Review - Numerical models for dilute gas-particle flows. *J. Fluids Eng.*, **104**, 297–303.

Crowe, C.T., Troutt, T.R., & Chung, J.N. 1996. Numerical models for two-phase turbulent flows. *Annu. Rev. Fluid Mech.*, **28**, 11–43.

Crowe, C.T., Sommerfeld, M., & Tsuji, Y. 1998. *Multiphase flows with droplets and particles*. CRC Press.

Cunningham, M.A. 1910. On the velocity of steady fall of spherical particles through fluid medium. *Proc. Roy. Soc. A*, **83**, 357–365.

Dandy, D.S., & Dwyer, H.A. 1990. A sphere in shear flow at finite Reynolds number: effect of shear on particle lift, drag, and heat transfer. *J. Fluid Mech.*, **216**, 381–410.

Dwyer, H.A. 1968. Thirteen-moment theory of the thermal force on a spherical particle. *Phys. Fluids*, **10**, 976–984.

Eckert, E.R.G., & Drake, R.M. 1959. *Heat and mass transfer*. McGraw-Hill, New York. Pages 276–279.

El-Shobokshy, M.S. 1983. Experimental measurements of aerosol deposition to smooth and rough surfaces. *Atmos. Environ.*, **17**(3), 639–644.

Elghobashi, S. 1994. On predicting particle-laden turbulent flows. *App. Sci. Res.*, **52**, 309–329.

Elsden, M.R., & Hutchinson, P. 1996. A joint Eulerian/Lagrangian model for dispersed turbulent two-phase flows. *ASME, Fluids Engineering Division (Publication)*, **236**(1), 57–63.

Fackrell, J.E., Brown, K., & Young, J.B. 1994. Modelling particle deposition in gas turbines employed in advanced coal-fired systems. *International Gas Turbine and Aeroengine Congress and Exposition*, June 13–16, The Hague, Netherlands.

Farmer, R., Griffith, P., & Rohsenow, W.M. 1970. Liquid droplet deposition in two-phase flow. *J. Heat Transfer*, **92**, 587–597.

Fernandez de la Mora, J., & Rosner, D.E. 1981. Inertial deposition of particles revisited and extended: Eulerian approach to a traditionally Lagrangian problem. *PhysioChemical Hydrodynamics*, **2**(1), 1–21.

Fisher Scientific UK. 2001. *The Fisher chemicals catalogue 2001-2002*.

Forney, L.J., & Spielman, L.A. 1974. Deposition of coarse aerosols from turbulent flow. *J. Aerosol Sci.*, **5**, 257–271.

Friedlander, S.K., & Johnstone, H.F. 1957. Deposition of suspended particles from turbulent gas streams. *Ind. Eng. Chem.*, **49**(7), 1151–1156.

Gallis, M.A., Rader, D.J., & Torczynski, J.R. 2002. Calculations of the near-wall thermophoretic force in a rarefied gas flow. *Phys. Fluids*, **14**(12), 4290–4301.

Ganic, E.N., & Mastanaiah, K. 1981. Investigation of droplet deposition from a turbulent gas stream. *Int. J. Multiphase Flow*, **7**, 401–422.

Geller, A.S., Rader, D.J., & Kempka, S.N. 1993. Calculation of particle concentration around aircraft-like geometries. *J. Aerosol Sci.*, **24**(6), 823–834.

Granville, P.S. 1990. A near-wall eddy viscosity formula for turbulent boundary layers in pressure gradients suitable for momentum, heat or mass transfer. *J. Fluids Eng.*, **112**, 240–243.

Gusev, I.N., Guseva, E.I., & Zaichik, L.I. 1990. Particle deposition on channel walls in a turbulent flow. English Translation of *Inzhenerno-Fizicheskii Zhurnal*, **59**(5), 735–742. (English pages: 1368-1375).

He, C., & Ahmadi, G. 1998. Particle deposition with thermophoresis in laminar and turbulent duct flows. *Aerosol Sci. Technol.*, **29**, 525–546.

Healy, D.P., & Young, J.B. 2003. Full Lagrangian methods for calculating particle density fields in non-turbulent flows. *Submitted to the Int. J. Multiphase Flow*.

Hinds, W.C. 1998. *Aerosol technology: properties, behaviour and measurement of airborne particles*. 2nd edn. Wiley-Interscience.

Irvine, T.F., Jr., & Liley, P. 1984. *Steam and gas tables with computer equations*. Academic Press.

Johansen, S.T. 1991. The deposition of particles on vertical walls. *Int. J. Multiphase Flow*, **17**(3), 355–376.

Jones, O.C., Jr., & Leung, J.C.M. 1981. An improvement in the calculation of turbulent friction in smooth concentric annuli. *J. Fluids Eng.*, **103**, 615–623.

Kang, S., Patil, B., Zarate, J.A., & Roy, R.P. 2001. Isothermal and heated turbulent upflow in a vertical annular channel - Part I. Experimental measurements. *Int. J. Heat Mass Transfer*, **44**, 1171–1184.

Kasagi, N., Tomita, Y., & Kuroda, A. 1992. Direct numerical simulation of passive scalar field in a turbulent channel flow. *J. Heat Transfer*, **114**, 598–606.

Kays, W.M. 1994. Turbulent Prandtl number - Where are we? The 1992 Max Jakob Memorial Award Lecture. *J. Heat Transfer*, **116**, 284–295.

Kennard, E.H. 1938. *Kinetic theory of gases*. McGraw-Hill, New York.

Kogan, M.N. 1992. Kinetic theory in aerothermodynamics. *Prog. Aerospace Sci.*, **29**(4), 271–354.

Konstandopoulos, A.G., & Rosner, D.E. 1995a. Inertial effects on thermophoretic transport of small particles to walls with streamwise curvature-I. Theory. *Int. J. Heat Mass Transfer*, **38**(12), 2305–2315.

Konstandopoulos, A.G., & Rosner, D.E. 1995b. Inertial effects on thermophoretic transport of small particles to walls with streamwise curvature-II. Experiment. *Int. J. Heat Mass Transfer*, **38**(12), 2317–2327.

Kroger, C., & Drossinos, Y. 2000. A random-walk simulation of thermophoretic particle deposition in a turbulent boundary layer. *Int. J. Multiphase Flow*, **26**, 1325–1350.

Lee, K.W., & Gieseke, J.A. 1994. Deposition of particles in turbulent pipe flows. *J. Aerosol Sci.*, **25**(4), 699–709.

Leeming, A.D. 1995. Particle deposition from turbulent flows. Ph.D. thesis, University of Cambridge.

Li, W., & Davis, E.J. 1995a. Measurement of the thermophoretic force by electrodynamic levitation: microspheres in air. *J. Aerosol Sci.*, **26**(7), 1063–1083.

Li, W., & Davis, E.J. 1995b. The effects of gas and particle properties on thermophoresis. *J. Aerosol Sci.*, **26**(7), 1085–1099.

Liu, B.Y.H., & Agarwal, J.K. 1974. Experimental observation of aerosol deposition in turbulent flow. *J. Aerosol Sci.*, **5**, 145–155.

Manna, M., & Vacca, A. 2001. Scaling properties of turbulent pipe flow at low Reynolds number. *Computers & Fluids*, **30**, 393–415.

Marchioli, C., Giusti, A., Salvetti, M.V., & Soldati, A. 2003. Direct numerical simulation of particle wall transfer and deposition in upward turbulent pipe flow. *Int. J. Multiphase Flow*, **29**, 1017–1038.

Matida, E.A., Nishino, K., & Torii, K. 2000. Statistical simulation of particle deposition on the wall from turbulent dispersed pipe flow. *Int. J. Heat Fluid Flow*, **21**, 389–402.

McLaughlin, J.B. 1989. Aerosol particle deposition in numerically simulated channel flow. *Phys. Fluids A*, **17**, 1211–1224.

McLaughlin, J.B. 1991. Inertial migration of a small sphere in linear shear flows. *J. Fluid Mech.*, **224**, 261–274.

Mei, R. 1992. An approximate expression for the shear lift force on a spherical particle at finite Reynolds number. *Int. J. Multiphase Flow*, **18**(1), 145–147.

Mei, R., Adrian, R.J., & Hanratty, T.J. 1991. Particle dispersion in isotropic turbulence under Stokes drag and Basset force with gravitational settling. *J. Fluid Mech.*, **225**, 481–495.

Menguturk, M., Gunes, D., Mimaroglu, H.K., & Sverdrup, E.F. 1983. Blade boundary layer effect on turbine erosion and deposition. *J. Fluids Eng.*, **105**, 270–276.

Michiyoshi, I., & Nakajima, T. 1968. Fully developed turbulent flow in a concentric annulus. *J. Nuclear Sci. Technol.*, **5**(7), 354–359.

Moffat, R.J. 1988. Describing the uncertainties in experimental results. *Exp. Therm. Fluid Sci.*, **1**, 3–17.

Montassier, N., Boulaud, D., Stratmann, F., & Fissan, H. 1990. Comparison between experimental study and theoretical model of thermophoretic particle deposition in laminar tube flow. *J. Aerosol Sci.*, **21**(S1), S85–S88.

Montassier, N., Boulaud, D., & Renoux, A. 1991. Experimental study of thermophoretic particle deposition in laminar tube flow. *J. Aerosol Sci.*, **22**(5), 677–687.

Montgomery, T.L., & Corn, M. 1970. Aerosol deposition in a pipe with turbulent airflow. *J. Aerosol Sci.*, **1**, 185–213.

Morsi, S.A., & Alexander, A.J. 1972. An investigation of particle trajectories in two-phase flow systems. *J. Fluid Mech.*, **55**(2), 193–208.

Nishio, G., Kitani, S., & Takahashi, K. 1974. Thermophoretic deposition of aerosol particles in a heat-exchanger pipe. *Ind. Eng. Chem., Process Des. Develop.*, **13**(4), 408–415.

Nomura, M., Morishita, T., & Susumu, K. 1997. An experiment of deposit formation on surface of an air-cooled gas-turbine blade. *Pages 566–573 of: Proceedings of the 1977 Tokyo Joint Gas Turbine Congress.*

Nouri, J.M., Umur, H., & Whitelaw, J.H. 1993. Flow of Newtonian and non-Newtonian fluids in concentric and eccentric annuli. *J. Fluid Mech.*, **253**, 617–641.

Olan-Figueroa, E., McFarland, A.R., & Ortiz, C.A. 1982. Flattening coefficients for DOP and oleic acid droplets deposited on treated glass slides. *AIHA Journal*, **43**(6), 395–399.

Osiptsov, A.N. 1984. Investigation of regions of unbounded growth of particle concentration in disperse flow. *Fluid Dynamics, (*English Translation of Izvestiya Akademii Nauk SSSR, Mekhanika Zhidkosti i Gaza*)*, **19**(3), 378–385.

Osiptsov, A.N. 1998. Modified Lagrangian method for calculating the particle concentration in dusty-gas flows with intersecting particle trajectories. *Third International Conference on Multiphase Flow - ICMF 1998*, June 8–12, Lyon, France.

Owen, I., El-Kady, A.A., & Cleaver, J.W. 1989. Deposition of sub-micrometre particles onto a heated surface with widely spaced roughness elements. *J. Aerosol Sci.*, **20**(6), 671–681.

Parker, G.J., & Ryley, D.J. 1970. Equipment and techniques for studying the deposition of sub-micron particles in turbine blades. *Proc. Instn. Mech. Engrs.*, **184**(3), 43–51.

Pedinotti, S., Mariotti, G., & Banerjee, S. 1992. Direct numerical simulation of particle behaviour in the wall region of turbulent flow in horizontal channels. *Int. J. Multiphase Flow*, **18**, 927–941.

Pershukov, V.A., Nigmatulin, B.I., & Zaichik, L.I. 1995. Modelling of dynamics and deposition of aerosols in two-phase turbulent flows. *Two-Phase Flow Modelling and Experimentation*, 1051–1058.

Pismen, L.M., & Nir, A. 1978. On the motion of suspended particles in stationary homogeneous turbulence. *J. Fluid Mech.*, **84**(1), 193–206.

Portela, L.M., Cota, P., & Oliemans, R.V.A. 2001. Numerical study of the near-wall behaviour of particles in turbulent pipe flows. *Fourth International Conference on Multiphase Flow - ICMF 2001*, May 27–June 1, New Orleans, LA, USA.

Quadrio, M., & Luchini, P. 2002. Direct numerical simulation of the turbulent flow in a pipe with annular cross section. *European Journal of Mechanics B/ Fluids*, **21**, 413–427.

Rambaud, P., Oesterlé, B., & Tanière, A. 2002. Assessment of integral time scales in a gas-solid channel flow with relevance to particle dispersion modelling. *Tenth Workshop on Two-Phase Flow Predictions*, April 9–12, Halle, Germany.

Ramshaw, J.D. 1979. Brownian motion in a flowing fluid. *Phys. Fluids*, **22**(9), 1595–1601.

Reeks, M.W. 1977. On the dispersion of small particles suspended in an isotropic turbulent fluid. *J. Fluid Mech.*, **83**(3), 529–546.

Reeks, M.W. 1983. The transport of discrete particles in inhomogeneous turbulence. *J. Aerosol Sci.*, **14**, 729–739.

Reeks, M.W. 1991. On a kinetic equation for the transport of particles in turbulent flows. *Phys. Fluids A*, **3**(3), 446–456.

Reeks, M.W. 1992. On the continuum equations for dispersed particles in nonuniform flows. *Phys. Fluids A*, **4**(6), 1290–1303.

Reeks, M.W. 1993. On the constitutive relations for dispersed particles in nonuniform flows. I: Dispersion in a simple shear flow. *Phys. Fluids A*, **5**(3), 750–761.

Reeks, M.W. 2003. Comparison of recent model equations for particle deposition in a turbulent boundary layer with those based on the PDF approach. *Proceedings of FEDSM'03 - Fourth ASME-JSME Joint Fluids Engineering Conference*, July 6–11, Honolulu, Hawaii, USA.

Rohsenow, W.M., & Choi, H.Y. 1961. *Heat, mass and momentum transfer*. Prentice-Hall, London. Pages 280–284.

Romay, F.J., Takagaki, S.S., Pui, D.Y.H., & Liu, B.Y.H. 1998. Thermophoretic deposition of aerosol particles in turbulent pipe flow. *J. Aerosol Sci.*, **29**(8), 943–959.

Rosner, D.E., & Fernandez de la Mora, J. 1982. Small particle transport across turbulent nonisothermal boundary layers. *J. Eng. Power*, **104**, 885–894.

Rouson, D.W.I., & Eaton, J.K. 1994. On the preferential concentration of solid particles in turbulent channel flow. *J. Fluid Mech.*, **272**, 349–381.

Ryley, D.J., & Davies, J.B. 1983. Effect of thermophoresis on fog droplet deposition on low pressure steam turbine guide blades. *Int. J. Heat Fluid Flow*, **4**(3), 161–167.

Saffman, P.G. 1965. The lift on a small sphere in a slow shear flow. *J. Fluid Mech.*, **22**(2), 385–400.

Saffman, P.G. 1968. The lift on a small sphere in a slow shear flow. *J. Fluid Mech.*, **31**(4), 624.

Schlichting, H. 1968. *Boundary-layer theory*. 6th edn. McGraw-Hill, New York.

Schwendiman, L.A., & Postma, A.K. 1961. Turbulent deposition in sampling lines. Tech. rept. TID-7627. USAEC. Seventh AEC Air Cleaning Conference.

Sehmel, G.A. 1963. The turbulent transport and deposition of particles within vertical tubes. Tech. rept. TID-7677. USAEC. Eighth AEC Air Cleaning Conference.

Sehmel, G.A. 1968. Aerosol deposition from turbulent airstreams in vertical conduits. Tech. rept. BNWL-578. Pacific Northwest Laboratory, Richland, Washington.

Shin, M., & Lee, J.W. 2001. Memory effect in the Eulerian particle deposition in a fully developed turbulent channel flow. *J. Aerosol Sci.*, **32**, 675–693.

Shin, M., Kim, D.S., & Lee, J.W. 2003. Deposition of inertia-dominated particles inside a turbulent boundary layer. *Int. J. Multiphase Flow*, **29**, 893–926.

Silva, M.C., De Lima, L.C., & Miranda, R.F. 1999. Comparative analysis of different models for the turbulent Prandtl number. *J. Heat Transfer*, **121**, 473–477.

Simonin, O., Deutsch, E., & Minier, J.P. 1993. Eulerian prediction of the fluid/particle correlated motion in turbulent two-phase flows. *App. Sci. Res.*, **51**, 275–283.

Slater, S.A. 1999. Particle transport in laminar and turbulent gas flows. Ph.D. thesis, University of Cambridge.

Slater, S.A., & Young, J.B. 1998. The calculation of inertial particle transport using an Eulerian formulation. *Proc. of ASME Fluids Engineering Division Summer Meeting 1998*, June 21–25, Washington, DC, USA.

Slater, S.A., Leeming, A.D., & Young, J.B. 2003. Particle deposition from two-dimensional turbulent gas flows. *Int. J. Multiphase Flow*, **29**, 721–750.

Soanes, Jnr., R.W. 1976. VP-splines, an extension of twice differentiable interpolation. *Proc. 1976 Army Numerical Analysis and Computers Conference*. A.R.O. Report 76-3, U.S Army Res. Office, P.O. Box 12211, Res. Triangle Park, N.C., 141-152.

Sone, Y. 1972. Flow induced by thermal stress in rarefied gas. *Phys. Fluids*, **15**(8), 1418–1423.

Sone, Y., & Aoki, K. 1981. Negative thermophoresis: thermal stress slip flow around a spherical particle in a rarefied gas. *Pages 489–503 of: Rarefied Gas Dynamics*. American Institute of Aeronautics and Astronautics, New York.

Stratmann, F., Otto, E., & Fissan, H. 1994. Thermophoretic and diffusional particle transport in cooled laminar tube flow. *J. Aerosol Sci.*, **25**(7), 1305–1319.

Talbot, L., Cheng, R.K., Schefer, R.W., & Willis, D.R. 1980. Thermophoresis of particles in a heated boundary layer. *J. Fluid Mech.*, **101**, 737–758.

Tarasova, N.V., & Tsirkunov, Yu.M. 2000. Full Lagrangian approach for numerical modelling of collisionless particle-phase flow field in the non-isothermal two-phase boundary layer. *Proc. 4th Summer Conf: Numerical Modelling in Continuum Mechanics*, 31 July–3 August, Prague, Czech Republic.

Thakurta, D.G., Chen, M., McLaughlin, J.B., & Kontomaris, K. 1998. Thermophoretic deposition of small particles in a direct numerical simulation of turbulent channel flow. *Int. J. Heat Mass Transfer*, **41**, 4167–4182.

TSI Inc. 1998. *Model 3450 Vibrating Orifice Aerosol Generator Instruction Manual*. 500 Cardigan Road, P.O. Box 64394, St. Paul, MN 55164, USA.

Tsirkunov, Yu.M. 2001. Gas-particle flows around bodies - key problems, modeling and numerical analysis. *Fourth International Conference on Multiphase Flow - ICMF 2001*, May 27–June 1, New Orleans, LA, USA.

Uijttewaal, W.S.J., & Oliemans, R.V.A. 1996. Particle dispersion and deposition in direct numerical and large eddy simulations of vertical pipe flows. *Phys. Fluids*, **8**(10), 2590–2604.

Ulke, A., & Rowleau, W.T. 1976. The effect of secondary flows on turbine blade erosion. *ASME Paper 76-GT-74*.

Vermes, G. 1979. Thermophoresis - enhanced deposition rates in combustion turbine blade passages. *J. Eng. Power*, **101**, 542–548.

Wang, Q., Squires, K.D., Chen, M., & McLaughlin, J.B. 1997. On the role of the lift force in turbulence simulations of particle deposition. *Int. J. Multiphase Flow*, **23**(4), 749–763.

Weast, R.C. (ed). 1967. *CRC handbook of chemistry and physics*. 48th edn. CRC Press Inc., Florida.

Weast, R.C. (ed). 1988. *CRC handbook of chemistry and physics*. 69th edn. CRC Press Inc., Florida.

Wells, A.C., & Chamberlain, A.C. 1967. Transport of small particles to vertical surfaces. *Brit. J. Appl. Phys.*, **18**, 1793–1799.

Wenglarz, R.A. 1981. An assessment of deposition in PFBC power plant turbines. *J. Eng. Power*, **103**, 552–559.

Wonnacott, T.H., & Wonnacott, R.J. 1977. *Introductory statistics*. 3rd edn. Wiley & Sons.

Wood, N.B. 1981a. The mass transfer of particles and acid vapour to cooled surfaces. *J. Inst. Energy*, **76**, 76–93.

Wood, N.B. 1981b. A simple method for the calculation of turbulent deposition to smooth and rough surfaces. *J. Aerosol Sci.*, **12**(3), 275–290.

Young, J.B. 1991. PARTICLE. A computer program for calculating the diffusion of small solid particles through two-dimensional boundary layers on gas turbine blades. Cambridge University Engineering Department.

Young, J.B., & Leeming, A.D. 1997. A theory of particle deposition in turbulent pipe flow. *J. Fluid Mech.*, **340**, 129–159.

Zaichik, L.I. 1997. Modelling of the motion of particles in non-uniform turbulent flow using the equation for the probability density function. *J. Appl. Maths Mechs*, **61**(1), 127–133.

Zhang, H., & Ahmadi, G. 2000. Aerosol particle transport and deposition in vertical and horizontal duct flows. *J. Fluid Mech.*, **406**, 55–80.

Zhou, Q., & Leschziner, M.A. 1999. An improved particle-locating algorithm for Eulerian-Lagrangian computations of two-phase flows in general coordinates. *Int. J. Multiphase Flow*, **25**, 813–825.